From Single Colloidal Particles to Coupled Plasmonic Systems

Dissertation

zur Erlangung des akademischen Grades eines

Doctor rerum naturalium
(Dr. rer. nat.)

vorgelegt dem Bereich
Mathematik und Naturwissenschaften
der Technischen Universität Dresden

von
M. Sc. **Martin Mayer**
geboren am 29. März 1989
in Augsburg

Eingereicht am 11. Juli 2019.
Verteidigt am 8. Oktober 2019.
Gutachter: Prof. Dr. Andreas Fery
Prof. Dr. Alexander Eychmüller

Angefertigt von September 2015 bis Juli 2019
unter der Betreuung von Prof. Dr. Andreas Fery
am Leibniz-Institut für Polymerforschung Dresden e.V.

”Study hard what interests you the most
in the most undisciplined, irreverent, and original manner possible.“
– Richard P. Feynman

Abstract

By down-sizing noble metals to the nanoscale, striking new optical properties arise—investigated in the scientific field of plasmonics. The steady rise of developments, innovations, and interest in plasmonics is directly linked with the much broader field of (colloidal) nanotechnology and its breakthroughs. In order to harvest the full potential of colloidal plasmonics, optimizing the synthesis of colloidal nanoparticles, controlling the subsequent assembly of them into complex architectures, and fully understanding the emerging plasmonic properties is inevitable. Wet-chemical seed-mediated growth of colloidal building blocks and colloidal self-assembly offer the tool-sets to tackle the challenges of plasmonic applications.

Due to the intrinsic properties of colloids and the resulting (coupled) assemblies, distinct differences are evident in comparison to top-down fabrication based plasmonics. Among these properties, this thesis focuses on the true three-dimensionality of colloids—in vast contrast, top-down processes always rely on stacking of layered architectures. Strong plasmonic coupling interactions are predominantly defined by the inter-particle distances and the geometry of the cross section area by which adjacent particles interact. Consequently, unique plasmonic features emerge from the three-dimensional structure of colloids and the possibility to tune the dielectric environment by surface functionalization.

The objective of this work is to investigate and understand the plasmonics of coupled colloidal systems. Following this scope, the first part of this thesis introduces a new synthetic concept, which thereby aims to provide colloidal building blocks for plasmonic assemblies. The optical quality and spectral range can be boosted by applying silver nanoparticles instead of gold as plasmonic material. Herein, a general synthetic concept is introduced resulting in monodispersed and shape-pure silver nanoparticles in a highly controlled manner. By transferring the concept of living polymerization reactions to nanoparticle growth, secondary nucleation is successfully suppressed and the particle dimensions are freely tunable. Finally, chemical stability toward oxidation and functionalization reactions is obtained by covering silver particles with a sub-skin depth gold shell.
The second part summarizes the plasmonic properties arising from coupled particle assemblies fabricated by colloidal self-assembly. Therefore, the complexity of the coupled systems was systematically increased to observe the transition from local to collective coupling interactions. Starting from metallic film-coupled gold nanorods, the presence of a highly sensitive magnetic mode and its impact on the magnetic permeability were investigated. Next, the transition from local to collective coupling was observed by stepwise increase of the number of particles in a linear gold nanoparticle chain revealing the formation of a plasmon band in quasi-infinite particle chains.

Consequently, this work aims to advance the field of colloidal metasurfaces by optimizing the building blocks and by further comprehending the plasmonic coupling effects in colloidal assemblies.

Kurzfassung

Durch das Herunterskalieren von (Edel-)Metallen in den Nanometerbereich entstehen neue optische Eigenschaften, die im Wissenschaftsfeld der Plasmonik untersucht werden. Die stetige Weiterentwicklung, Innovation, und das steigende Interesse an der Plasmonik ist direkt mit dem weiter gefassten Gebiet der (kolloidalen) Nanotechnologie verbunden. Um das Potenzial der kolloidalen Plasmonik voll ausschöpfen zu können, ist es unumgänglich, die Synthese kolloidaler Nanopartikel zu optimieren, deren anschließende Anordnung zu komplexen Architekturen gezielt zu steuern, und die entstehenden plasmonischen Effekte vollständig zu verstehen. Das nasschemische Keim-vermittelte Wachstum kolloidaler Bausteine und die kolloidale Selbstanordnung bieten die geeigneten Werkzeuge für plasmonische Anwendungen.

Aufgrund der intrinsischen Eigenschaften kolloidaler Partikel und den daraus resultierenden optischen Eigenschaften ihrer Anordnungen, ergeben sich deutliche Unterschiede zur Plasmonik von *Top-down* Systemen. Im Gegensatz zu diesen Systemen, die immer aus geschichteten Architekturen bestehen, handelt es sich bei kolloidalen Systemen um echte dreidimensionale Objekte. Starke plasmonische Kopplungswechselwirkungen werden hauptsächlich durch die Abstände zwischen Partikeln und die Geometrie des Querschnitts definiert, über die benachbarte Partikel interagieren. Folglich ergeben sich aus der dreidimensionalen Struktur von kolloidalen Nanopartikeln und der Möglichkeit, diese mit verschiedenen dielektrischen Umgebung zu funktionalisieren, einzigartige plasmonische Effekte.

Das übergeordnete Ziel dieser Arbeit besteht darin, die plasmonischen Effekte gekoppelter kolloidaler Systeme zu untersuchen und besser zu verstehen. Diesem Ziel folgend, wird im ersten Teil der Arbeit ein neues Synthesekonzept vorgestellt, das darauf abzielt geeignete kolloidale Bausteine für plasmonische Anordnungen zur Verfügung zu stellen. Verglichen mit Gold als Bausteinmaterial kann die optische Qualität und der Spektralbereich durch Nutzung der überlegenen plasmonischen Eigenschaften von Silbernanopartikeln gesteigert werden. Hier wurde ein allgemeines Synthesekonzept entwickelt, das auf kontrollierte Weise zu monodispersen und formreinen Silbernanopartikeln führt. Durch die Übertragung des Konzepts lebender Polymerisationsreaktionen auf das Nanopartikelwachstum, werden Nebenreaktionen (z.B. sekundäre Keimbildung) erfolgreich unterdrückt und die Partikelgröße wird dadurch genau einstellbar. Schließlich wurde durch die Überwachsung der Silberpartikel mit einer Goldschale unterhalb der Leitschichtdicke chemische Stabilität gegenüber Oxidations- und Funktionalisierungsreaktionen erhalten.

Im zweiten Teil werden die plasmonischen Eigenschaften gekoppelter Partikelanordnungen untersucht. Dafür wurde die Komplexität der gekoppelten Systeme systematisch erhöht, um den Übergang von lokalen zu kollektiven Kopplungsinteraktionen zu beobachten. Ausgehend von Goldstäbchen, die mit einem Metallfilm gekoppelt sind, wurde eine hochempfindliche magnetische Mode nachgewiesen und deren Einfluss auf die magnetische Permeabilität untersucht. Desweiteren wurde der direkte Übergang von lokaler zu kollektiver Kopplung durch schrittweise Erhöhung der Anzahl der Partikel in einer linearen Goldnanopartikelkette beobachtet, was zur Bildung eines Plasmonenbandes für quasi-unendlich lange Partikelketten führt.

Letztendlich ist das Ziel dieser Arbeit, kolloidale *Meta*oberflächen durch Optimierung der Bausteine und durch besseres Verständnis der plasmonischen Kopplungseffekte voranzubringen.

Table of

Contents

List of Publications

1. *"Controlled living nanowire growth: precise control over the morphology and optical properties of AgAuAg bimetallic nanowires"*
   Martin Mayer,‡ Leonardo Scarabelli,‡ Katia March, Thomas Altantzis, Moritz Tebbe, Mathieu Kociak, Sara Bals, F. Javier García de Abajo, Andreas Fery, and Luis M. Liz-Marzán*
   Nano Letters **2015**, 15, 5427–5437

2. *"Protein-assisted assembly of modular 3D plasmonic raspberry-like core/satellite nanoclusters: correlation of structure and optical properties"*
   Roland P.M. Höller, Martin Dulle, Sabrina Thomä, **Martin Mayer**, Anja Maria Steiner, Stephan Förster, Andreas Fery, Christian Kuttner,* and Munish Chanana*
   ACS Nano **2016**, 10, 5740–5750

3. *"Template-assisted colloidal self-assembly of macroscopic magnetic metasurfaces"*
   Martin Mayer, Moritz Tebbe, Christian Kuttner, Max J. Schnepf, Tobias A.F. König,* and Andreas Fery*
   Faraday Discussions **2016**, 191, 159–176

4. *"Nanorattles with tailored electric field enhancement"*
   Max J. Schnepf,‡ **Martin Mayer**,‡ Christian Kuttner, Moritz Tebbe, Daniel Wolf, Martin Dulle, Thomas Altantzis, Petr Formanek, Stephan Förster, Sara Bals, Tobias A.F. König,* and Andreas Fery*
   Nanoscale **2017**, 9, 9376–9385

5. *"Macroscopic Strain-Induced Transition from Quasi-infinite Gold Nanoparticle Chains to Defined Plasmonic Oligomers"*
   Anja Maria Steiner, **Martin Mayer**, Maximilian Seuss, Svetoslav Nikolov, Kenneth D. Harris, Alexander Alexeev, Christian Kuttner,* Tobias A.F. König,* and Andreas Fery*
   ACS Nano **2017**, 11, 8871–8880

6. *"Aqueous Gold Overgrowth of Silver Nanoparticles: Merging the Plasmonic Properties of Silver with the Functionality of Gold"*
   Martin Mayer,‡ Anja Maria Steiner,‡ Falk Röder, Petr Formanek, Tobias A.F. König,* and Andreas Fery*
   Angewandte Chemie International Edition **2017**, 56, 15866–15870

7. *"Colloidal Self-Assembly Concepts for Plasmonic Metasurfaces"*
   Martin Mayer, Max J. Schnepf, Tobias A.F. König,* and Andreas Fery*
   Advanced Optical Materials **2018**, 1800564–1800581

‡contributed equally
*corresponding author

8. *"Strong photoacoustic signal enhancement by coating gold nanoparticles with melanin for biomedical imaging"*
   Tatjana Repenko, Anne Rix, Alexander Nedilko, Jonas Rose, Alina Hermann, Rostislav Vinokur, Sheila Moli, Roberto Cao-Milàn, **Martin Mayer**, Gero von Plessen, Andreas Fery, Laura De Laporte, Wiltrud Lederle, Dmitry N. Chigrin, and Alexander J.C. Kuehne*
   Advanced Functional Materials **2018**, 28, 1705607–1705615

9. *"Seeded Growth Synthesis of Gold Nanotriangles: Size Control, SAXS Analysis, and SERS Performance"*
   Christian Kuttner, **Martin Mayer**, Martin Dulle, Ana Moscoso, Juan Manuel Lopez-Romero, Stephan Förster, Andreas Fery,* Jorge Perez-Juste, and Rafael Contreras-Caceres*
   ACS Applied Materials & Interfaces **2018**, 10, 11152–11163

10. *"Surface Plasmon Modes in Long Chains of Au Nanoparticles"*
    Pavel L. Potapov, **Martin Mayer**, Axel Lubk,* Darius Pohl, Johannes Schultz, Tobias A.F. König,* and Andreas Fery*
    Microscopy and Microanalysis **2018**, 24, 1748–1749

11. *"Ultranarrow Second-Harmonic Resonances in Hybrid Plasmon-Fiber Cavities"*
    Qi Ai,* Lili Gui,* Domenico Paone, Bernd Metzger, **Martin Mayer**, Ksenia Weber, Andreas Fery, and Harald Giessen*
    Nano Letters **2018**, 18, 5576–5582

12. *"DNA-assembled Plasmonic Waveguides for Nanoscale Light Propagation to a Fluorescent Nanodiamond"*
    Fatih N. Gür, Cillian Patrick, Thomas McPolin, Søren Raza, **Martin Mayer**, Diane J. Roth, Anja Maria Steiner, Markus Löffler, Andreas Fery, Mark L. Brongersma, Anatoly V. Zayats, Tobias A.F. König,* and Thorsten L. Schmidt*
    Nano Letters **2018**, 18, 7323–7329

13. *"Silver particles with rhombicuboctahedral shape and effective isotropic interactions with light"*
    Anja Maria Steiner,‡ **Martin Mayer**,‡ Daniel Schletz, Daniel Wolf, Petr Formanek, René Hübner, Martin Dulle, Stephan Förster, Tobias A.F. König,* and Andreas Fery*
    Chemistry of Materials **2019**, 31, 2822–2827

14. *"Direct Observation of Plasmon Band Formation and Delocalization in Quasi-Infinite Nanoparticle Chains"*
    Martin Mayer, Pavel L. Potapov, Darius Pohl, Anja Maria Steiner, Johannes Schultz, Bernd Rellinghaus, Axel Lubk,* Tobias A.F. König,* and Andreas Fery*
    Nano Letters **2019**, 19, 3854–3862

15. *"Active Chiral Plasmonics Based on Mechano-tunable Colloidal Metasurfaces"*
    Patrick T. Probst,‡ **Martin Mayer**,‡ Vaibhav Gupta, Anja Maria Steiner, Günter Auernhammer, Tobias A.F. König,* and Andreas Fery*
    in preparation

Awards

1. *ACS Nano Grand Poster Award*
   Nanax7, Philipps University Marburg, Germany **2016**

List of Figures

List of Tables

List of Abbreviations

α	polarizability
ε	permittivity
λ	wavelength
μ	permeability
ω	angular frequency
1D	one-dimensional
2D	two-dimensional
3D	three-dimensional
AFM	atomic force microscopy
AgAuAgNW	silver-gold-silver nanowire
AgEn	degree of silver elongation
AgNC	silver nanocube
AgRCO	silver nanorhombicuboctahedron
AR	aspect ratio
$AscH_2$	L-ascorbic acid
AuAgNC	gold protected silver nanocube
AuNC	gold nanocube
AuNR	gold nanorod
AuNSp	spherical single-crystalline gold nanoparticle
BdaC	benzyldimethylhexadecylammonium chloride
BEM	boundary-element method
BSA	bovine serum albumin / protein
CAPA	capillarity-assisted particle assembly
CLPR	controlled living polymerization reaction
CMC	critical micellar concentration
CtaB	hexadecyltrimethylammonium bromide
CtaC	hexadecyltrimethylammonium chloride
DDA	discrete dipole approximation
DFT	density functional theory
DLS	dynamic light scattering
DNA	deoxyribonucleic acid

DRA	diffuse reflection accessory
E	electric field
EDX	energy dispersive X-ray
EEL	electron energy-loss
EELS	electron energy-loss spectroscopy
EM	electric mode
f.c.	final concentration
FDTD	finite-difference time-domain method
FOM	figure of merit
FWHM	full width at half maximum
G	dipole-dipole interaction term
g	coupling parameter
H	magnetic field
HAADF	high-angle annular darkfield
HRTEM	high-resolution transmission electron microscopy
IR	infrared
IUPAC	International Union of Pure and Applied Chemistry
L	longitudinal
LC	inductor-capacitor
LSPR	localized surface plasmon resonance
μCP	micro-contact printing
MESME	multiple elastic scattering of multipole expansions model
MM	magnetic mode
MNPBEM	metallic nanoparticles using boundary element method
MSE	mean square error
MutaB	(11-mercaptoundecyl)trimethylammonium bromide
n	refractive index
NC	nanocube
NLLS	non-linear least square
NP	nanoparticle
NR	nanorod
NW	nanowire

P	particle dipole
PAA	poly(acrylic acid)
PDMS	poly(dimethylsiloxane)
PEG	poly(ethylenglycol)
PEI	poly(ethylenimine)
PMMA	poly(methyl)methacrylate
PNIPAm	poly(N-isopropylacrylamide)
PS	polystyrene
PT-AuNR	pentatwinned gold nanorod
PVA	poly(vinyl alcohol)
PVP	poly(vinyl pyrrolidone)
Q	extinction cross-section
q	wavevector
QF	quality factor
RCF	relative centrifugal force
RH	relative humidity
RMS	root mean square
RT	room temperature
S_{2D}	two-dimensional order parameter
RCO	rhombicuboctahedron
SAXS	small angle X-ray scattering
sCAPA	successive capillarity-assisted particle assembly
SEM	scanning electron microscopy
STEM	scanning transmission electron microscopy
T	transversal
TEM	transmission electron microscopy
TVM	total variation minimization technique
UMA	universal measurement accessory
UV-vis-NIR	ultraviolet-visible-near IR
vis-NIR	visible-near IR

Chapter

Introduction

Nanotechnology marks one of the next scientific revolutions due to its vast number of possible applications. The use of nanotechnology promises and already partially succeeds by offering faster computers, medical breakthroughs, smarter surfaces, and also expands the range of material properties, as in metamaterials.[1–3] In fact, miniaturization to and controlling of the nanoscale is a rather new scientific topic dating back to the famous lecture *There's plenty of room at the bottom* by Richard P. Feynman in 1959.[4] In this lecture, he envisions this field, which "[...] might tell us much of great interest about the strange phenomena that occur in complex situations."[4] Within his vision, he already defines the key challenge of nanotechnology, which is still valid: how to manipulate and control objects on the nanoscale in order to obtain the emergent properties of the nanoscale. One promising pathway to achieve this, is the wet-chemical fabrication of nanoscaled building blocks and then, assembling these colloids out of dispersion into the desired structures.[5]

In the field of nanotechnology, plasmonics of colloidal particles is particularly fascinating due to its possible impact on a wide range of applications,[2,6] like plasmonic heating,[7] sensing,[8] polarimetry,[9,10] plasmonic lasing,[11] or energy/information transport,[12] but also futuristic applications, like super lensing,[13] optical cloaking,[14] or more general, metamaterials.[15] By downsizing noble metals into colloidal particles, striking optical properties arise from the noble metal surface.[16] These properties originate from the so-called localized surface plasmon resonance (LSPR), which features extraordinary electric field enhancement, electrons in excited states, and light confinement far below the diffraction limit.[17] In general, a plasmon resonance is defined as the collective oscillation of conductance electrons excited by an external electromagnetic field.[16] Already in 1857, Michael Faraday was enthusiastic about the optical properties of gold colloids and their remarkable color change, while bringing them to the nanoscale.[18] But even before then, as early as the 4th-century, the vivid colors of gold and silver colloids were embraced in their use as color pigments, *e.g.*, in the famous Lycurgus Cup.[19]
In the last couple of decades, the field of modern plasmonics grew to one of the most active topics in nanotechnology due to its new, emergent properties, which arise from introducing short- and long-range coupling interactions between adjacent particles.[13,20,21]

In this context, the central challenge toward these applications is (again) to manipulate and control the shape, size, and material of the colloidal building blocks and to place them precisely at the nanoscale in order to use and understand their magnificent properties. Consequently, precise hierarchical assembly of nanoscale building blocks, *i.e.*, colloids, is inevitable to fully exploit the advantages of nanotechnology. Template-assisted colloidal self-assembly is the predominant bottom-up tool-set to fabricate plasmonically active surfaces with sub-wavelength unit cells, typically referred to as *metasurfaces*.[22,23] For this directed self-assembly process, templates are used in order to irreversibly and selectively trap nanoparticles from a colloidal dispersion.[24] Typically, the driving force, which brings the colloids in the energetic minima of the trap, are capillarity and capillary forces. Thus, scalability, but also final resolution, are limited by the template due to the shear amount of particles within a dispersion.

As compared to top-down processes, which are based on lithography techniques, such bottom-up assembly techniques feature several distinct advantages. The most dominantly named advantage is, that the final colloidal metasurface can be cost-efficiently scaled to macroscopic areas, if an adequate template is used.[25] One noteworthy template fabrication method is the exploitation of mechanical instabilities resulting in wrinkled templates with meter-squared extend, but simultaneously nanoscaled features.[26] For example by using such templates, gold nanoparticles with various morphologies can be assembled into perfectly linear particle chains, thereby obtaining huge optically anisotropic effects on square centimeters.[27–29]
But based on the intrinsic properties of colloids, plasmonics from colloidal building blocks have also less obvious advantages. Due to the defined crystallinity of the wet-chemically synthesized nanoparticles, the lack of surface roughness and grain boundaries yields lower damping and optical losses.[30] In order to employ these colloids, however, the synthetic protocols need to yield monodisperse particles, which allow for chemical surface functionalization. To date, only gold nanoparticles can comply with these synthetic requirements.[31] Furthermore, the stabilizing dielectric shell allows to render the immediate refractive index and its tunable thickness allows to tune the inter-particle distance in the range from microns down to nanometers.[32–35] Especially the latter one is far below the resolution limit of conventional top-down processes, but at the same time, essential to yield strong coupling interactions.[36]

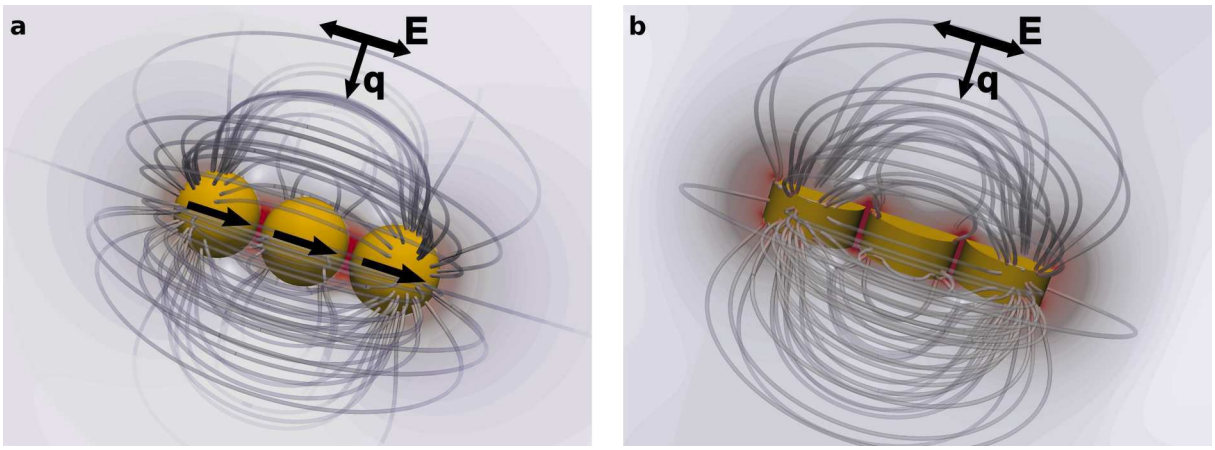

Figure I.1.: Electric field and electric field lines of linear trimers. (a) The linear coupling of the three-dimensional nanoparticles results in a point as the geometry of the cross section area, as shown by the high electric field between the particles (red). The electric field lines illustrate the dipolar character of the excited plasmon mode. (b) In case of three coupling disks, the geometry of the cross section area is a line and the electric field is influenced by the edges of the disks. The surface plasmons are excited by a planewave light source as indicated by the wavevector q with its external electric field E oriented parallel to the trimers.

This thesis, however, focuses on the tunable three-dimensional morphology of colloids—one of the most obvious, but often ignored features of colloids.[37] Some underappriciated challenges and features arise from their three-dimensionality for the plasmonic interaction of adjacent nanoparticles—not to mention the impact on the assembly process itself, which is not scope of this thesis. To illustrate this, the simple coupling of colloidal spheres in a line is a demonstrative example, as schematically shown in **Figure I.1a**. When such colloidal spheres couple, the cross section area of the coupling geometry between them is reduced to a point resulting in extraordinary high and focused field enhancement.[38]

Contrary, its top-down counterpart, a disk, results in a line as the geometry of the coupling cross section area (**Figure I.1b**), and also edge effects and surface roughness need to be considered.[30,39] Due to the nature of top-down techniques, they always end up with layered systems. Although quasi-three-dimensional structures are obtainable by stacking of various layers, the building blocks are cylinders with an arbitrarily shaped two-dimensional base and a height, which is fixed by its layer thickness.[30,40] A sphere is not a disk, a cube with its sharp corners and edges is not a rectangle, and a cylindrical rod is not a bar. In combination with its tunable dielectric shell, defined crystallinity, and the lack of surface roughness, the plasmonics of colloids differ distinctively from plasmonics of top-down processes—and *vice versa*.[41]

In this context, the objective of this thesis is (1) to design colloidal building blocks, which are able to highlight the aforementioned properties, and (2) to exploit and subsequently, comprehend the emerging plasmonic effects of the resulting colloidal metasurfaces.

(1) Compared to using the dominating gold as building blocks, the overall performance of colloidal metasurfaces can be boosted by **utilizing the superior plasmonic quality of silver nanoparticles.**[42,43] However, due to the lack of feasible aqueous synthesis concepts for silver colloids with sufficiently narrow size and shape distributions, the benefit from silver colloids is marginal.[43] Furthermore, silver is prone to oxidize and decompose, which limits its use in real-life applications.[44] Aim of the first part of this thesis is to design appropriate silver nanoparticles. Thus, in order to boost the performance of silver-based colloidal metasurfaces, a general synthesis concept will be introduced to yield **monodisperse and stable silver nanoparticles**, which are specifically designed as building blocks for template-assisted self-assembly.

(2) The second part of this thesis focuses on the **plasmonic properties arising from coupled particle assemblies made *via* colloidal self-assembly**. Within this study, the complexity of the investigated systems systematically increases **from local, isolated coupling effects up to the collective coupling** in a quasi-infinite long particle chain. The thereby observed effects will rely on the intrinsic properties of the employed colloids.

Consequently, the central aim of my work is to advance the field of colloidal based metasurfaces by optimizing the building blocks and by comprehending the plasmonic coupling effects of three-dimensional colloidal particles. The objected gain of fundamental understanding could then be exploited in various promising applications.

References

[1] L. Scarabelli, “Recent advances in the rational synthesis and self-assembly of anisotropic plasmonic nanoparticles”, *Pure and Applied Chemistry* **2018**, *90*, 1393.

[2] H. A. Atwater, “The promise of plasmonics”, *Scientific American* **2007**, *296*, 56–62.

[3] S. Zhang, R. Geryak, J. Geldmeier, S. Kim, V. V. Tsukruk, “Synthesis, Assembly, and Applications of Hybrid Nanostructures for Biosensing”, *Chemical Reviews* **2017**, *117*, 12942–13038.

[4] R. P. Feynman, “There’s plenty of room at the bottom”, *Engineering and Science* **1960**, *23*, 22–36.

[5] M. Grzelczak, L. M. Liz-Marzán, R. Klajn, “Stimuli-responsive self-assembly of nanoparticles”, *Chemical Society Reviews* **2019**, DOI 10.1039/C8CS00787J.

[6] N. Jiang, X. Zhuo, J. Wang, “Active Plasmonics: Principles, Structures, and Applications”, *Chemical Reviews* **2018**, *118*, 3054–3099.

[7] N. J. Hogan, A. S. Urban, C. Ayala-Orozco, A. Pimpinelli, P. Nordlander, N. J. Halas, “Nanoparticles Heat through Light Localization”, *Nano Letters* **2014**, *14*, 4640–4645.

[8] K. M. Mayer, J. H. Hafner, “Localized Surface Plasmon Resonance Sensors”, *Chemical Reviews* **2011**, *111*, 3828–3857.

[9] A. Martinez, “Polarimetry enabled by nanophotonics”, *Science* **2018**, *362*, 750–751.

[10] W. Ma, L. Xu, A. F. de Moura, X. Wu, H. Kuang, C. Xu, N. A. Kotov, “Chiral Inorganic Nanostructures”, *Chemical Reviews* **2017**, *117*, 8041–8093.

[11] D. Wang, W. Wang, M. P. Knudson, G. C. Schatz, T. W. Odom, “Structural Engineering in Plasmon Nanolasers”, *Chemical Reviews* **2018**, *118*, 2865–2881.

[12] F. N. Gür, F. W. Schwarz, J. Ye, S. Diez, T. L. Schmidt, “Toward Self-Assembled Plasmonic Devices: High-Yield Arrangement of Gold Nanoparticles on DNA Origami Templates”, *ACS Nano* **2016**, *10*, 5374–5382.

[13] N. Liu, H. Giessen, “Coupling Effects in Optical Metamaterials”, *Angewandte Chemie International Edition* **2010**, *49*, 9838–9852.

[14] X. Ni, Z. J. Wong, M. Mrejen, Y. Wang, X. Zhang, “An ultrathin invisibility skin cloak for visible light”, *Science* **2015**, *349*, 1310–1314.

[15] A. V. Kildishev, A. Boltasseva, V. M. Shalaev, “Planar Photonics with Metasurfaces”, *Science* **2013**, *339*, 1232009–1232009.

[16] S. A. Maier, *Plasmonics: Fundamentals and Applications*, Springer US, **2007**.

[17] J. A. Schuller, E. S. Barnard, W. Cai, Y. C. Jun, J. S. White, M. L. Brongersma, “Plasmonics for extreme light concentration and manipulation”, *Nature Materials* **2010**, *9*, 193–204.

[18] M. Faraday, “X. The Bakerian Lecture. – Experimental relations of gold (and other metals) to light”, *Philosophical Transactions of the Royal Society of London* **1857**, *147*, 145–181.

[19] L. M. Liz-Marzán, “In My Element: Gold”, *Chemistry – A European Journal* **2019**, *25*, 661–661.

[20] J. Krenn, “Surface plasmon resurrection”, *Nature Photonics* **2012**, *6*, Editorial, 707 EP.

[21] J. B. Khurgin, “How to deal with the loss in plasmonics and metamaterials”, *Nature Nanotechnology* **2015**, *10*, 2 EP.

[22] S. Ni, L. Isa, H. Wolf, “Capillary assembly as a tool for the heterogeneous integration of micro- and nanoscale objects”, *Soft Matter* **2018**, *14*, 2978–2995.

[23] T. Kraus, L. Malaquin, H. Schmid, W. Riess, N. D. Spencer, H. Wolf, “Nanoparticle printing with single-particle resolution”, *Nature Nanotechnology* **2007**, *2*, 570–576.

[24] M. Karg, T. A. König, M. Retsch, C. Stelling, P. M. Reichstein, T. Honold, M. Thelakkat, A. Fery, “Colloidal self-assembly concepts for light management in photovoltaics”, *Materials Today* **2015**, *18*, 185–205.

[25] M. Pretzl, A. Schweikart, C. Hanske, A. Chiche, U. Zettl, A. Horn, A. Böker, A. Fery, “A Lithography-Free Pathway for Chemical Microstructuring of Macromolecules from Aqueous Solution Based on Wrinkling”, *Langmuir* **2008**, *24*, 12748–12753.

[26] B. Glatz, A. Knapp, A. Fery, "Surface structured polymer objects and the procedure for their fabrication", *EP/PCT patent application*, **2017**.

[27] C. Hanske, M. Tebbe, C. Kuttner, V. Bieber, V. V. Tsukruk, M. Chanana, T. A. F. König, A. Fery, “Strongly Coupled Plasmonic Modes on Macroscopic Areas via Template-Assisted Colloidal Self-Assembly”, *Nano Letters* **2014**, *14*, 6863–6871.

[28] M. Tebbe, M. Mayer, B. A. Glatz, C. Hanske, P. T. Probst, M. B. Müller, M. Karg, M. Chanana, T. A. F. König, C. Kuttner, A. Fery, “Optically anisotropic substrates via wrinkle-assisted convective assembly of gold nanorods on macroscopic areas”, *Faraday Discussions* **2015**, *181*, 243–260.

[29] A. M. Steiner, M. Mayer, M. Seuss, S. Nikolov, K. D. Harris, A. Alexeev, C. Kuttner, T. A. König, A. Fery, “Macroscopic Strain-Induced Transition from Quasi-infinite Gold Nanoparticle Chains to Defined Plasmonic Oligomers”, *ACS Nano* **2017**, *11*, 8871–8880.

[30] A. Trügler, *Optical Properties of Metallic Nanoparticles*, Springer International Publishing, **2016**.

[31] Y. Xia, Y. Xiong, B. Lim, S. E. Skrabalak, “Shape-Controlled Synthesis of Metal Nanocrystals: Simple Chemistry Meets Complex Physics?”, *Angewandte Chemie International Edition* **2009**, *48*, 60–103.

[32] M. Mueller, M. Tebbe, D. V. Andreeva, M. Karg, R. A. Alvarez Puebla, N. Pazos Perez, A. Fery, “Large-Area Organization of pNIPAM-Coated Nanostars as SERS Platforms for Polycyclic Aromatic Hydrocarbons Sensing in Gas Phase”, *Langmuir* **2012**, *28*, 9168–9173.

[33] M. Tebbe, C. Kuttner, M. Männel, A. Fery, M. Chanana, “Colloidally Stable and Surfactant-Free Protein-Coated Gold Nanorods in Biological Media”, *ACS Applied Materials & Interfaces* **2015**, *7*, 5984–5991.

[34] I. Pastoriza-Santos, D. S. Koktysh, A. A. Mamedov, M. Giersig, N. A. Kotov, L. M. Liz-Marzán, "One-Pot Synthesis of Ag@TiO2 Core−Shell Nanoparticles and Their Layer-by-Layer Assembly", *Langmuir* **2000**, *16*, 2731–2735.

[35] A. Heuer-Jungemann, N. Feliu, I. Bakaimi, M. Hamaly, A. Alkilany, I. Chakraborty, A. Masood, M. F. Casula, A. Kostopoulou, E. Oh, K. Susumu, M. H. Stewart, I. L. Medintz, E. Stratakis, W. J. Parak, A. G. Kanaras, "The Role of Ligands in the Chemical Synthesis and Applications of Inorganic Nanoparticles", *Chemical Reviews* **2019**, DOI 10.1021/acs.chemrev.8b00733.

[36] C. Hanske, G. González-Rubio, C. Hamon, P. Formentín, E. Modin, A. Chuvilin, A. Guerrero-Martínez, L. F. Marsal, L. M. Liz-Marzán, "Large-Scale Plasmonic Pyramidal Supercrystals via Templated Self-Assembly of Monodisperse Gold Nanospheres", *The Journal of Physical Chemistry C* **2017**, *121*, 10899–10906.

[37] S. J. Tan, M. J. Campolongo, D. Luo, W. Cheng, "Building plasmonic nanostructures with DNA", *Nature Nanotechnology* **2011**, *6*, 268 EP.

[38] P. Nordlander, C. Oubre, E. Prodan, K. Li, M. I. Stockman, "Plasmon Hybridization in Nanoparticle Dimers", *Nano Letters* **2004**, *4*, 899–903.

[39] P. K. Jain, W. Huang, M. A. El-Sayed, "On the Universal Scaling Behavior of the Distance Decay of Plasmon Coupling in Metal Nanoparticle Pairs: A Plasmon Ruler Equation", *Nano Letters* **2007**, *7*, 2080–2088.

[40] M. R. Gonçalves, "Plasmonic nanoparticles: fabrication, simulation and experiments", *Journal of Physics D: Applied Physics* **2014**, *47*, 213001.

[41] P. K. Jain, M. A. El-Sayed, "Plasmonic coupling in noble metal nanostructures", *Chemical Physics Letters* **2010**, *487*, 153–164.

[42] F. Wang, Y. R. Shen, "General Properties of Local Plasmons in Metal Nanostructures", *Physical Review Letters* **2006**, *97*, 2068061–2068064.

[43] M. Rycenga, C. M. Cobley, J. Zeng, W. Li, C. H. Moran, Q. Zhang, D. Qin, Y. Xia, "Controlling the Synthesis and Assembly of Silver Nanostructures for Plasmonic Applications", *Chemical Reviews* **2011**, *111*, 3669–3712.

[44] A. Desireddy, B. E. Conn, J. Guo, B. Yoon, R. N. Barnett, B. M. Monahan, K. Kirschbaum, W. P. Griffith, R. L. Whetten, U. Landman, T. P. Bigioni, "Ultrastable silver nanoparticles", *Nature* **2013**, *501*, 399–402.

Chapter

II

Synopsis

II.1 Scope of the Thesis

The scope of this thesis is the investigation and understanding of coupled plasmonic systems built from colloidal nanoparticles. In this context, colloidal self-assembly offers a tool-set to fabricate coupled plasmonic systems in a controlled, reproducible, and scalable fashion. In comparison to top-down and lithographically produced plasmonic systems, colloidal nanotechnology features a set of apparent differences, but also some non-obvious ones.

Typically, when comparing to top-down methods, advantages such as scalability to macroscopic areas and cost-efficiency are being mentioned. However, the aim of this thesis is to focus on the intrinsic advantages of colloids and the resulting optical properties owed to them. Namely, this is the true three-dimensional structure of colloidal particles in combination with the possibility to tune the colloidal properties with thin stabilizing dielectric shells. The thin dielectric shell can be used to introduce novel functionality and/or to define the inter-particle distances, which drastically influence the resulting plasmonics.
The impact of the three-dimensional nature of a colloidal approach becomes more evident by recalling the contrast to top-down processes. Top-down processes rely always on layered structures. While within a layer the complexity of such structures is only limited by the resolution of the employed deposition method, the restriction to stacked layouts inhibits the fabrication of truly three-dimensional structures. Thus, in direct comparison to top-down processes, the colloidal approach aims for well-defined coupling geometries and nanometer ranged inter-particle distances in all principle directions.

As motivated in the **Introduction**, this thesis is divided into two main parts: (1) design of colloidal building blocks and (2) the plasmonics of coupled particle assemblies. The first part aims to introduce novel synthetic approaches, in order to emphasize and exploit the full potential of colloidal building blocks. This synthetic concept targets chemically stable particles with narrow size distributions combined with plasmonic resonances with a high quality factor. Thus, **monodisperse and stable silver nanoparticles** will be introduced.
The second part investigates the plasmonic properties of self-assembled colloidal systems. The plasmonics of these systems exploit and rely on the three-dimensional properties of the employed building blocks, which define the coupling geometry. Hence, plasmonic systems ranging **from local to collective coupling** will be studied.

The following sections summarize the content of the individual chapters and put them into context with the initial scope. Each section of the main chapters is written to form a self-contained story and is readable independent from the other chapters although being based on each other. In the last section of this chapter, all co-authors' contributions to the presented joint publications are specified.

II.2 Design of Colloidal Building Blocks

Chapter IV presents a new general synthetic approach to combine the intrinsic advantages of silver and gold. This is achieved in an environmentally friendly and versatile fully aqueous system. In terms of plasmonic and optical properties, silver is the superior material. This is because of the high quality factor and the accessibility to the complete optical range of the induced plasmon resonance. But then, gold colloids feature several experimental advantages. In general their synthesis is by far more controlled in respect to crystallinity, shape-, and size distribution control, but gold additionally exhibits chemical stability and a wide range of functionality. **Figure II.1** summarizes the developed synthesis pathway. Briefly: well-established gold colloids are used as seeds for epitaxial silver overgrowth in order to pass their crystallinity and dispersity to the resulting silver nanoparticles (**Section IV.1**). Next, the targeted silver plasmonics are protected by a sub-skin depth gold layer, which offers chemical stability and simultaneously allows for functionalization (**Section IV.2**). **Section IV.3** gives a brief excursion to morphology tuning *via* oxidative reactions.

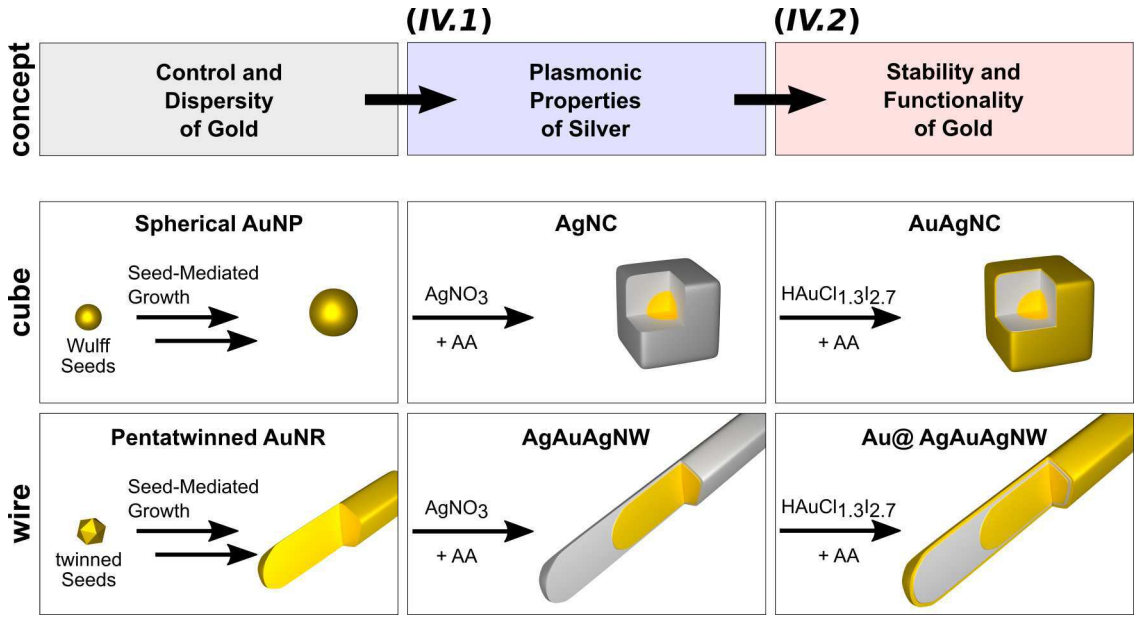

Figure II.1.: General synthesis concept for the designed colloidal silver nanoparticles. The controlled synthesis of narrowly distributed and pure gold nanoparticles are exploited as seeds in this synthesis concept. By the introduced living silver growth conditions, these features can be inherited to particles with the superior plasmonic properties of silver (IV.1). Finally, the silver is protected by an optically invisible gold layer in order to suppress oxidation reactions (IV.2). Adapted with permission.[1] Copyright 2017, Wiley-VCH.

Section IV.1 introduces a novel silver overgrowth concept, which can be understood as the consequent further development of seed-mediated growth. Externally enforcing reaction kinetics increases control of the overgrowth step (process) unprecedentedly. This is crucial to suppress any side reactions and secondary nucleation, and to avoid unnecessary broadening of the particle size distribution. Due to the close analogy of these requirement to polymer synthesis, the concept of *controlled living polymerization reactions* (CLPR) is employed to seed-mediated silver growth.

To emphasize this analogy and to better illustrate the synthesis concept, the new concept of *controlled living silver growth* was introduced on the example of one-dimensional colloidal particles, *i.e.,* nanowire growth. As defined by the International Union of Pure and Applied Chemistry (IUPAC),[2] a living polymerization is "a chain polymerization from which chain transfer and chain termination are absent. In many cases, the rate of chain initiation is fast compared with the rate of chain propagation, so that the number of kinetic-chain carriers is essentially constant throughout the polymerization."
As shown in **Figure II.2a**, pentatwinned gold nanorods were used as seeds, or—to keep the polymerization analogy—as bifunctional initiators. By efficiently stabilizing the lateral {100} facets of these nanocrystals with chloride, the silver precursor is preferentially reduced at the less stable {111} facets at the tip of the nanorods. Thereby, active reaction sides are formed. Thus, further silver ions are only reduced at these active sides resulting in the proposed one-dimensional growth (**Figure II.2b–e**).

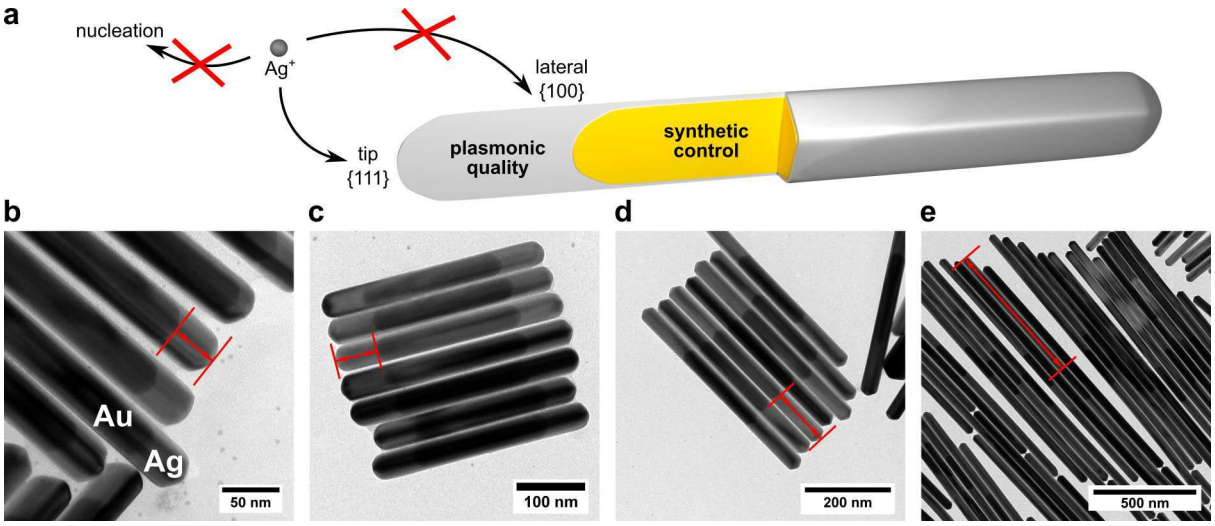

Figure II.2.: Employing living reaction conditions to silver nanowire growth. The effect of the living reaction conditions (a) can be best tracked in the one-dimensional growth of silver nanowires (AgAuAgNWs; b–e). Due to the employed conditions strictly selective silver deposition occurs on the nanorod tips resulting in elongation. As shown in (e) several micrometers length are achievable without side reactions. Adapted under the terms of ACS AuthorChoice license.[3] Copyright 2015, American Chemical Society.

Living reaction conditions are achieved by externally controlling the reaction kinetics and thus, limiting the available precursor. The precursor addition rate needs to be set below the actual reaction rate, thereby, enforcing a linear zero-order kinetic. Tracking of the nanowire length and longitudinal plasmon resonance wavelength proofed the linearity of the growth kinetic. As a control, even slight increasing the addition rate, above the actual reaction rate, results in secondary nucleation, growth into width, and accumulation of silver precursor in huge silver chloride agglomerates.
The extraordinary quality and the low polydispersity of the resulting nanowires allows to detect up to nine distinguishable plasmonic modes (for an exemplary 900 nm nanowire) in ensemble averaged UV-vis-NIR measurements. By performing electron energy loss spectroscopy and mapping of the electron energy loss, the nature of those modes on the single particle level is assigned and directly linked them to the plasmon modes of the colloidal solution. Furthermore,

by probing the spatial distribution of plasmon modes along the wires, the negligible influence of the initial gold onto the plasmonic properties of the final particle was shown. Consequently, seeding with a gold core facilitates the synthesis of highly controlled silver colloids.

In **Section IV.2**, the concept of *controlled living silver growth* is successfully extended to cubic particles, starting from single crystalline gold spheres. Further, by adding a sub-skin depth gold layer, silver is protected from oxidation reactions, and are thereby expanding their surface functionality. The concept of the designed particle system is exemplified for a nanocube in **Figure II.3a**. Once again, a general synthetic pathway is developed and later on, transferred to silver nanowires to proof the independence from the initial silver particle shape.

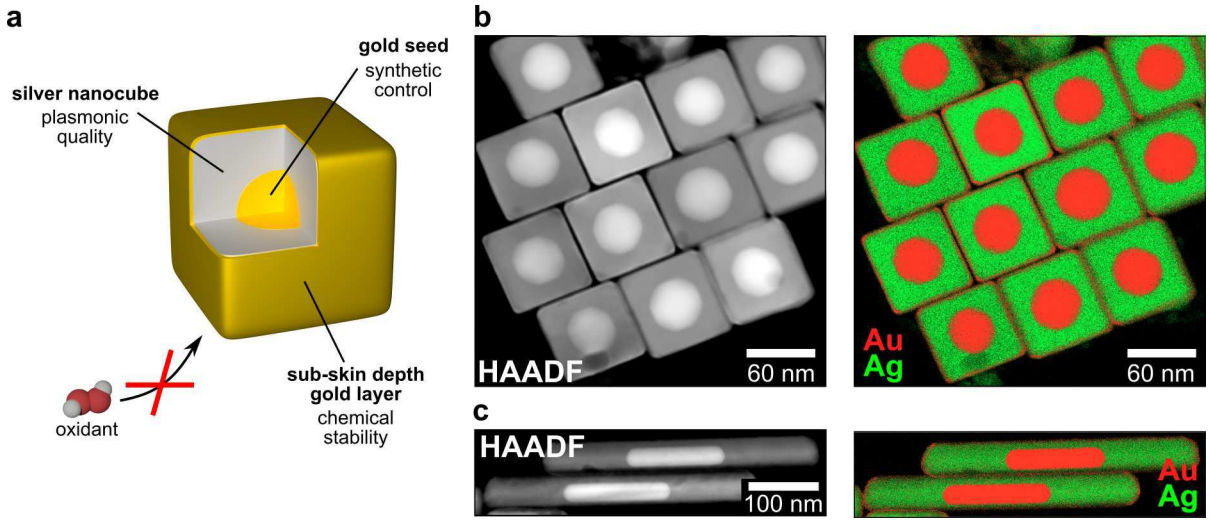

Figure II.3.: Aqueous gold overgrowth acting as protection layer. Protecting the silver with a thin gold layer enables oxidant stability and surface functionality of this system without altering the silver-based optical properties (a). As shown in the elemental maps (b & c), a homogeneous and closed gold shell can be achieved independent of the particle morphology. Adapted with permission.[1] Copyright 2017, Wiley-VCH.

Due to the high sensitivity of sharp corners and edges in terms of oxidation stability as well as plasmonic properties, nanocubes mark the perfect environment to test the influence of a thin gold shell on plasmonic and chemical properties of silver colloids.
The main challenge in gold overgrowth of silver colloids is to avoid galvanic replacement reactions and oxidative etching by the employed gold precursor. Since gold is the most noble metal, these reactions are preferred to overgrowth. Thus, to yield a homogeneous layer, the reduction potential of the gold precursor needs to be drastically lowered. Pre-complexation of the gold ions with iodide allows for sufficient reduction of this potential. Due to the high affinity and resulting passivation of iodide on noble metal surfaces, the iodide-to-gold concentration needs to be balanced in order to avoid oxidation as well as passivation. To be able to control the kinetics and thermodynamics of the reaction, external kinetic control, comparable to the introduced living reaction conditions is inevitable. By externally controlling these parameters, we were able to directly tune and show the importance of the reduction potentials in nanocrystals growths. As shown in **Figure II.3b & c**, an iodide-to-gold ratio of 2.7:1 results in the formation of homogeneous and closed gold layer for nanocubes and nanowires with a thickness of approximately

1 nm. Deviation from this ratio shifts the reaction equilibrium either to oxidative reactions, or to passivation of the surface with iodide.
As revealed by statistical TEM image analysis and UV-vis-NIR spectroscopy, the morphology of particles, especially their edges and corners, as well as the plasmonic properties of silver are only negligible damped by the gold protection layer. However, the thickness of the gold layer needs to be well-below the skin-depth of the plasmons in order to render it “optically invisible”. The experimentally obtained 1 nm layer is by a factor of almost five below the theoretical skin depth for this system. By electromagnetic simulations, this observation was validated for the near-field properties of both morphologies, nanocubes and nanowires.
Long-term stability tests against oxidants in both dispersed and also dried state showed the efficient protection properties of the gold shell for several months. On the contrary, unprotected silver nanocubes oxidized and ultimately degraded under oxidative environments within minutes and hours in dispersion and dried state, respectively. The obtained oxidation stability reasons also the gained stability toward surface functionalization. Due to the chemical stability of gold, chemically reactive functional groups are not able to oxidize the surface, while performing exchange reactions of the stabilizing ligands. Therefore, the chemical advantages are successfully combined with the plasmonic properties of silver colloids.

The brief excursion in **Section IV.3** describes two opposing pathways to change the morphology of silver colloids *via* oxidative reactions. The first method presents the catalytic etching by a copper catalyst resulting in an isotropic plasmonic response, while the rhombicubeoctahedral shape supports high crystallinity and low polydispersity (see **Figure II.4a**). Monodisperse silver rhombicubeoctahedra are obtained by balanced etching and simultaneous growing of silver nanocubes. Such isotropically behaving silver nanoparticles are of great importance for fundamental studies including plasmonic applications, since they make the optical range below 500 nm accessible for applications. Furthermore, the plasmonics of silver exhibits a remarkable high quality factor in this spectral range.

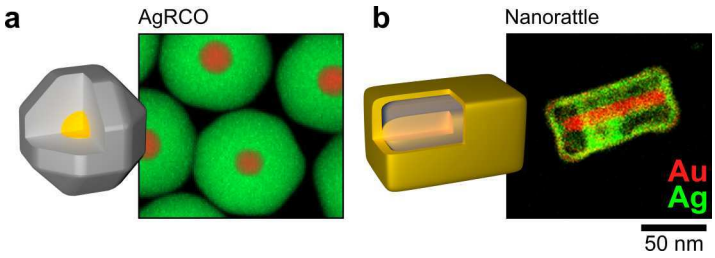

Figure II.4.: Silver rhombicubeoctahedra and axisymmetric nanorattles *via* oxidative reactions (a) Monodisperse silver rhombicubeoctahedra *via* oxidative etching of silver nanocubes. (b) Nanorattles with well-defined cavities by galvanic replacement of silver@gold cuboids. (a) Adapted with permission and (b) under the terms of CC-BY-NC license.[4,5] Copyright 2019 & 2017, American Chemical Society and Royal Society of Chemistry, respectively.

The second method is galvanic replacement by gold(III) yielding a cavity in axisymmetric nanorattles (see **Figure II.4b**). The obtained plasmonic cavity renders the plasmonics absorption dominated and features high electric field enhancement. Due to the highly selective growth of Ag@Au cuboids, the central rod of the final nanorattles is fixed resulting in axisymmetric particles with a well-defined nanosized cavity.

II.3 Coupled Particle Assemblies

The key aspect of **Chapter V** is the plasmonic coupling of colloidal particles assemblies. The presented coupled systems rely on the features of three-dimensional colloids and the presence of a homogeneous dielectric shells around them. As **Figure II.5** summarizes, the complexity of theses systems is gradually increased within the sections. The investigated samples are prepared *via* templated colloidal self-assembly to ensure macroscopic detection of the effects and to form reproducible unit cells with nanometer precision. In order to obtain simple and robust plasmonic coupling, the same monodisperse gold particles, which are used as seeds in **Chapter IV**, are employed as building blocks for the herein investigated coupled systems.

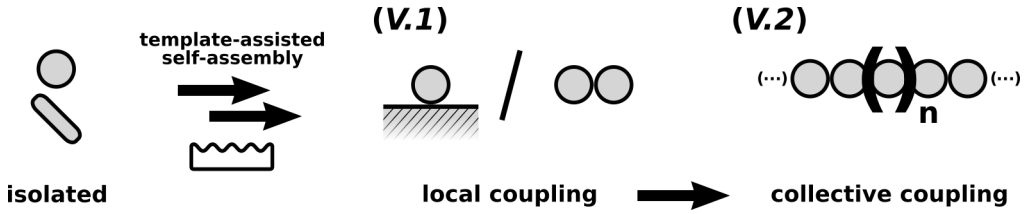

Figure II.5.: Self-assembly concepts for coupled particle assemblies. The coupling complexity of the studied particle assemblies is gradually increased by the addition of further particles. Firstly, the sensitivity of a gold nanorod by local coupling with gold film is observed (V.1). Next, systematically the transition from local coupling of a particle dimer to the collective coupling of a quasi-infinite particle chain (V.2). Adapted with permission.[6] Copyright 2018, Wiley-VCH.

The first level of complexity is the coupling of colloidal nanoparticle with a smooth metallic film. The effects, as presented in **Section V.1**, rely on the lateral flattened morphology of a pentatwinned nanorod and its nanometer sized dielectric corona. In **Section V.2**, starting from a dimer, the number of particles in a chain is systematically increased in a linear fashion and thereby, studies the transition of a particle chain from local coupling to collective coupling by crossing the *infinite chain limit*.

In **Section V.1**, the optical properties of metallic film supported gold nanorods are investigated. Therefore, pentatwinned gold nanorods were assembled into linear structures by exploiting wrinkled-templates. The tip-to-tip orientation of the gold nanorods results in a highly anisotropic optical respond, which allows for selective transversal excitation of the array. Due to the lateral dimensions of the array over several square millimeters, the optical effects can be detected by conventional UV-vis spectroscopy methods. To yield a homogeneous optical response, pentatwinned gold nanorods, as introduced as seeds in **Section IV.1**, were selected due to several morphological advantages. Most importantly, the flattened lateral side of the pentagonal cross section allows for a well-defined and reproducible plasmonic coupling to the gold film. The overall performance of the final metasurface is further improved by the bigger size, in comparison to single crystalline gold nanorods, resulting in a higher extinction cross section and their high aspect ratio separating the optical and geometrical axis.

As shown in **Figure II.6a**, template-assisted self-assembly on the metallic film into line arrays enables efficient separation of the plasmonic response and an isolated transversal mode, while keeping a high filling rate. The targeted separation of the modes was evidenced by the averaged deviation Θ to the principle alignment direction $\langle\sigma_\Theta\rangle$ of only 2.69°. Hence, the resulting two-dimensional order parameter was determined to be close to unity (0.99).

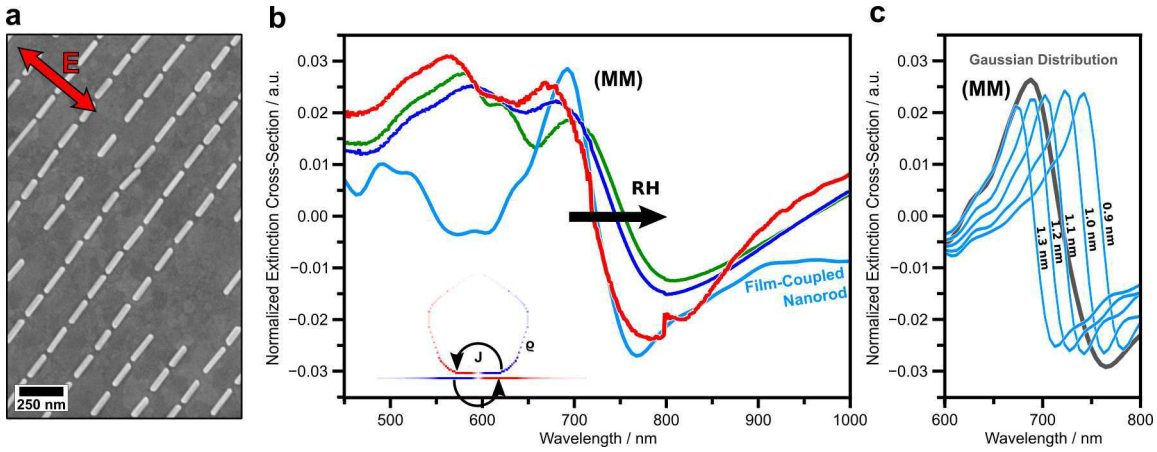

Figure II.6.: Sensitivity of gold film coupled gold nanorods. The self-assembly in particle lines (a) allows for macroscopic UV-vis-NIR measurement of the induced magnetic mode (b). Due the high sensitivity of the magnetic mode (MM) toward particle-film-distance changes, changes in the relative humidity are observable (c) and can be explained by matching with electromagnetic simulations (e). Adapted under the terms of CC-BY-NC license.[7] Copyright 2016, Royal Society of Chemistry.

Similar to the well-known hybridization model,[8] the plasmonic coupling with the gold film leads into splitting of the (transversal) mode into a bonding (magnetic) and into an anti-bonding (electric) mode. Due to the plasmonic support film, this coupling can be described as the coupling of a particle with its induced mirror charges. This coupling scenario induces a circular current flow, which is educible to a classical inductor-capacitor (LC) model for resonant circuits. Following Lenz's law, a magnetic field is induced counteracting the external magnetic field of the incidence electromagnetic wave. Thus, this magnetic field is the eponym for the induced magnetic mode.
The featured magnetic mode exhibits an exceptional sensitivity toward distance variations. As determined by electromagnetic simulations, the obtained experimental particle-to-film distance was as low as 1.1 nm with a standard deviation of approximately 0.2 nm for ensemble-averaged measurements (see **Figure II.6b–c**). Due to the Fano-like line shape of the magnetic mode, the plasmonic shift was easily tracked by its point of inflection. As a proof of concept, the high sensitivity of the mode was experimentally proven by changing of the surrounding relative humidity (RH). The used protein corona around the particles swells upon humidity changes due to its hydrophilic nature resulting in directly altering the dielectric media around the particles. Consequently, the magnetic mode offers the required sensitivity to track the conformal changes of protein monolayers upon environmental changes.
To probe the macroscopic magnetic metasurface aspect, the induced magnetic mode is linked to changes of the effective magnetic permeability *via* electromagnetic simulations based on the LC model. Indeed, the nanorod on metallic mirror configuration was able to tune the effective magnetic permeability proofing the presence of a true magnetic mode.

This section was able to demonstrate, that the fabricated metasurface strictly relies on colloidal concepts and on the well-defined 3D structure of the gold nanorod. Consequently, the proposed metasurface aims for reproducibility, narrow distributions, and robustness.

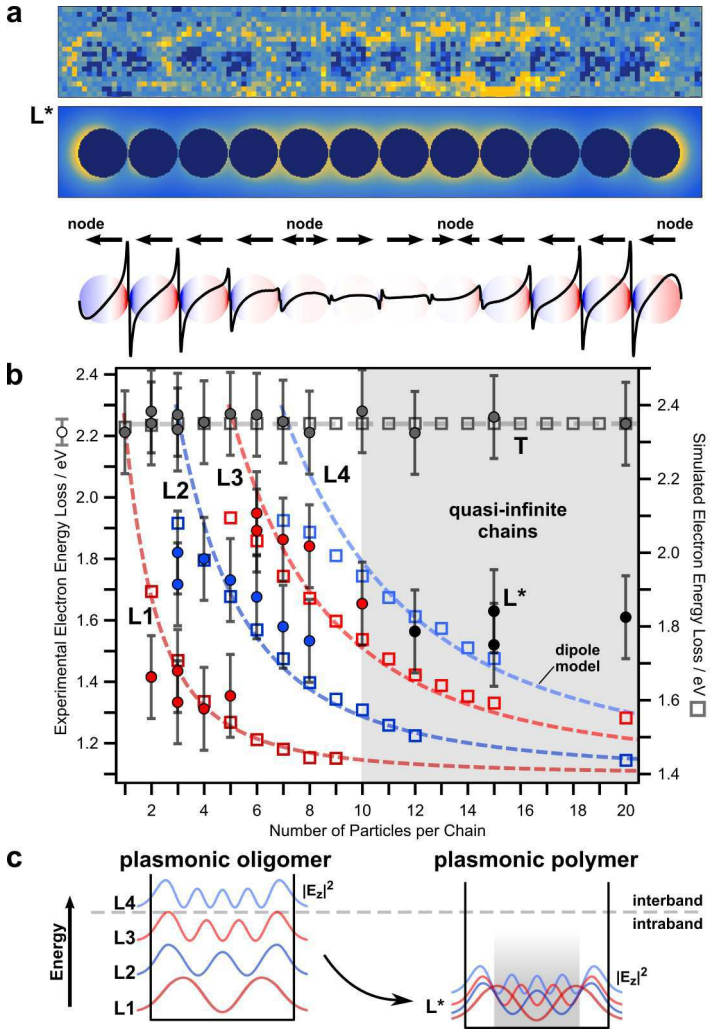

Figure II.7.: Formation of degenerated plasmon modes in quasi-infinite linear particle chains. For particle chains above the *infinite chain limit*, an energy band is formed in the central part of the chains (a; top down: experimental and simulated maps of electron energy loss and simulated surface charge map, respectively). This degenerated L* mode results from merging of several longitudinal modes, as shown by the spectral positions of all plasmonic modes and schematically sketched in (c). Adapted with permission. Copyright 2019,[9] American Chemical Society.

Section V.2 examines the near-field properties of linear particle chains. By electron energy loss spectroscopy and electromagnetic modeling, the formation of the degenerated L* mode was identified as the near-field cause of the so-called *infinite chain limit*. Such particle lines and their optical properties depend strongly on colloidal aspects.
By colloidal self-assembly, inter-particle distances of 1–2 nm are achievable, which are required to boost the plasmonic effects in order to detect them. The low dispersity, high sphericity, and single-crystallinity of the in **Section IV.2** used gold particles is exploited in this section to obtain reducible coupling scenarios. Furthermore, due the spherical shape of the gold particles, the

coupling cross section between neighboring particles is reduced to a point cross section. Thus, a sphere can be approximated by a singe dipole and a particle chain treated as a line of interacting, *i.e.*, plasmonically coupling, dipoles.

Starting from a simple dimer, the complexity of investigated linear particle chains is gradually increased by adding additional particles to the chain. As previously shown, adding particles results in a gradual red-shift of the predominant plasmon mode (L1). The near-field of these so-called plasmonic oligomer is dominated by the formation of dipolar non-degenerated modes, spanning over the complete particle chain. Spectroscopically, the red-shift decreases per particle and the position of the L1 mode converges to a specific wavelength. This is typically reached at about 10 particles and until now, defined the *infinite chain limit*.

By the transition from the isolated L1 modes of plasmonic oligomers to plasmonic polymers, a degenerated collective L* mode emerges (see **Figure II.7a**). The observed L* mode is dominated by the formation of a band structure in the central part of the chain, restricted by standing surface charge waves at the chain ends. The convergence of the longitudinal plasmonic modes into the L* mode is visualized in **Figure II.7b** by their spectral positions.

By introducing a simplified discrete dipole model, the formation of the degenerated L* mode by the spectral overlap of plasmonic modes is explained. This model approximates each particle of the chain with a single discrete dipole, coupling mainly with the nearest neighboring dipoles, *i.e.*, particles. As simplified in the sketch in **Figure II.7c**, the formation of the central band origins in the out-of-phase overlap of the L1 to LX modes, which form the L* mode. Consequently, the *infinite chain limit* can be defined by the appearance of the degenerated L* mode, which simultaneously is the cause of the *infinite chain limit* in the near-field.

To highlight the substantial importance of the degenerated L* mode in the plasmonics of linear particle chains, its impact on energy transport was investigated in a proof-of-principle study. Plasmonic energy transport is typically described as one of the most promising applications for particle chains and its effect is dominated by near-field effects. As shown *via* theoretical simulations, the degenerated L* modes overlapping with the energy band support efficient energy transport along the chains.

References

[1] M. Mayer, A. M. Steiner, F. Röder, P. Formanek, T. A. F. König, A. Fery, “Aqueous Gold Overgrowth of Silver Nanoparticles: Merging the Plasmonic Properties of Silver with the Functionality of Gold”, *Angewandte Chemie International Edition* **2017**, *56*, 15866–15870.

[2] In *IUPAC Compendium of Chemical Terminology*, (Eds.: M. Nič, J. Jirát, B. Košata, A. Jenkins, A. McNaught), IUPAC, Research Triagle Park, NC, **2009**.

[3] M. Mayer, L. Scarabelli, K. March, T. Altantzis, M. Tebbe, M. Kociak, S. Bals, F. J. García de Abajo, A. Fery, L. M. Liz-Marzán, “Controlled Living Nanowire Growth: Precise Control over the Morphology and Optical Properties of AgAuAg Bimetallic Nanowires”, *Nano Letters* **2015**, *15*, 5427–5437.

[4] A. M. Steiner, M. Mayer, D. Schletz, P. Formanek, R. Hübner, M. Dulle, S. Förster, S. Bals, T. A. F. König, A. Fery, “Silver particles with rhombicuboctahedral shape and effective isotropic interactions with light”, *Chemistry of Materials* **2019**, *31*, 2822–2827.

[5] M. J. Schnepf, M. Mayer, C. Kuttner, M. Tebbe, D. Wolf, M. Dulle, T. Altantzis, P. Formanek, S. Förster, S. Bals, T. A. F. König, A. Fery, “Nanorattles with tailored electric field enhancement”, *Nanoscale* **2017**, *9*, 9376–9385.

[6] M. Mayer, M. J. Schnepf, T. A. F. König, A. Fery, “Colloidal Self-Assembly Concepts for Plasmonic Metasurfaces”, *Advanced Optical Materials* **2018**, 1800564–1800581.

[7] M. Mayer, M. Tebbe, C. Kuttner, M. J. Schnepf, T. A. F. König, A. Fery, “Template-assisted colloidal self-assembly of macroscopic magnetic metasurfaces”, *Faraday Discussions* **2016**, *191*, 159–176.

[8] Y. S. Joe, A. M. Satanin, C. S. Kim, “Classical analogy of Fano resonances”, *Physica Scripta* **2006**, *74*, 259–266.

[9] M. Mayer, P. L. Potapov, D. Pohl, A. M. Steiner, J. Schultz, B. Rellinghaus, A. Lubk, T. A. F. König, A. Fery, “Direct Observation of Plasmon Band Formation and Delocalization in Quasi-Infinite Nanoparticle Chains”, *Nano Letters* **2019**, *19*, 3854–3862.

Contribution to Joint Publications

The results and content presented in this thesis are results of various collaborations and research projects. Thus, the included chapters are adopted from and based on several peer reviewed joint publications. In the following, the contributions of all involved authors and cooperation partners to these projects are addressed chapter-wise.

III Colloidal self-assembly concepts for plasmonic metasurfaces

This chapter is based on the Progress Report in *Advanced Optical Materials* **2018**, 18000564–18000581.

By Martin Mayer, Max J. Schnepf, Tobias A.F. König, and Andreas Fery**

I performed the main writing of the manuscript and literature research. Max J. Schnepf proof-read the manuscript and assisted structuring the manuscript. Tobias A.F. König wrote the introduction and the original theoretical aspects of the first chapters. Andreas Fery contributed in developing of the concept and writing of the manuscript.

IV.1 Controlled living silver growth

This section is published in *Nano Letters* **2015**, *15*, 5427–5437.

*By Martin Mayer,‡ Leonardo Scarabelli,‡ Katia March, Thomas Altantzis, Moritz Tebbe, Mathieu Kociak, Sara Bals, F. Javier García de Abajo, Andreas Fery, and Luis M. Liz-Marzán**

I performed the synthesis, optical characterization, developed the generalization of the synthesis concept and wrote the manuscript. Leonardo Scarabelli equally contributed by also performing of syntheses, writing the manuscript, and performing of optical characterization and TEM measurements. Katia March, Thomas Altantzis, Mathieu Kociak, and Sara Bals performed the advanced TEM measurements, including the 3D reconstructions and EELS measurements. Moritz Tebbe supported the development of the synthesis concept and writing of the manuscript. F. Javier García de Abajo performed electromagnetic simulations and clarified the theoretical background. Andreas Fery and Luis M. Liz-Marzán supervised the project, were involved in scientific discussion, and proof-read the manuscript.

IV.2 Aqueous gold overgrowth of silver nanoparticles

This section is published in *Angewandte Chemie International Edition* **2017**, *56*, 15866–15870.

By Martin Mayer,‡ Anja Maria Steiner,‡ Falk Röder, Petr Formanek, Tobias A.F. König, and Andreas Fery**

Anja Maria Steiner and I equally contributed in carrying out the synthesis, developing the synthetic concept and writing of the manuscript. Falk Röder and Petr Formanek contributed in TEM and EDX experiments. Supported by Tobias A.F. König, I also performed the electromagnetic simulations and theoretical considerations. Andreas Fery contributed in development of the concept and writing of the manuscript.

---

*corresponding author

‡contributed equally

IV.3 Tailoring the plasmonics of silver nanoparticles

This section is based on publications in *Chemistry of Materials* **2019**, *31*, 2822–2827 and *Nanoscale* **2017** *9*, 9376–9385.

First part by Anja Maria Steiner,‡ Martin Mayer,‡ Daniel Schletz, Daniel Wolf, Petr Formanek, René Hübner, Martin Dulle, Stephan Förster, Tobias A.F. König, and Andreas Fery**

Second part by Max J. Schnepf,‡ Martin Mayer,‡ Christian Kuttner, Moritz Tebbe, Daniel Wolf, Martin Dulle, Thomas Altantzis, Petr Formanek, Stephan Förster, Sara Bals, Tobias A.F. König, and Andreas Fery**

In the first part, Anja Maria Steiner and I equally contributed in preparing of the manuscript, and developing of the synthesis concept. Anja Maria Steiner mainly performed the synthesis supported by Daniel Schletz and myself. I performed the DRA characterization, the SAXS evaluation, electromagnetic simulations, and basic TEM measurements. Daniel Wolf performed the HRTEM measurements and the TEM tomography. René Hübner and Petr Formanek contributed in TEM and EDX experiments. Martin Dulle, Stephan Förster carried out the SAXS measurements and supported their evaluation with the theoretical background. Tobias A.F. König supported the electromagnetic simulations. Andreas Fery contributed in development of the concept and writing of the manuscript.

In the second part, Max J. Schnepf and I equally contributed in preparing the manuscript, and development of the synthesis concept. Max J. Schnepf performed the synthesis of the colloidal particles and the embedding in the PVA film. I performed the optical characterization, the SAXS evaluation, electromagnetic simulations, and basic TEM measurements. Christian Kuttner and Moritz Tebbe supported writing of the manuscript and were involved in scientific discussions. Daniel Wolf and Petr Formanek supported the TEM measurements and evaluation. Thomas Altantzis and Sara Bals performed the EELS and EDX measurements. Christian Kuttner, Martin Dulle, Stephan Förster carried out the SAXS measurements and were involved in discussion of their evaluation. Tobias A.F. König and Andreas Fery contributed in developing of the concept and writing of the manuscript.

V.1 Self-Assembly of macroscopic magnetic metasurfaces

This section is published in *Faraday Discussions* **2016**, *191*, 159–176.

By Martin Mayer, Moritz Tebbe, Christian Kuttner, Max J. Schnepf, Tobias A.F. König, and Andreas Fery**

I carried out all experimental tasks (synthesis, functionalization, self-assembly, and transfer) and performed TEM, SEM, and the optical characterization. Additionally, I carried out basic electromagnetic simulations and wrote the manuscript. Moritz Tebbe was involved in in-depth discussion during all stages of the project. Christian Kuttner was involved in discussions about the theoretical background and the simulations, and contributed writing the manuscript. Max J. Schnepf assisted the self-assembly of the nanorods. Tobias A.F. König performed advanced FDTD modeling, clarified the theoretical background, was involved in scientific discussion, and wrote parts of the manuscript. Andreas Fery supervised the project, was involved in scientific discussion, and proof-read the manuscript.

V.2 Plasmon band formation and delocalization in quasi-infinite chains

This section is published in *Nano Letters* **2019**, 19, 3854–3862.

By Martin Mayer, Pavel L. Potapov, Darius Pohl, Anja Maria Steiner, Johannes Schultz, Bernd Rellinghaus, Axel Lubk, Tobias A.F. König,* and Andreas Fery**

I performed the electromagnetic simulations *via* the boundary elemental method (BEM) and also *via* the finite-difference time-domain method (FDTD). Additionally I carried out the transfer to the TEM grid, developed the concept, and wrote the manuscript. Pavel L. Potapov performed the experimental EELS evaluation. Darius Pohl, Johannes Schultz, and Bernd Rellinghaus are responsible for the experimental EELS measurements. Anja Maria Steiner fabricated the sample and supported the subsequent transfer. Axel Lubk was involved in scientific discussions, developed the analytical model, and wrote the respective part of the manuscript. Tobias A.F. König was involved in scientific discussions and supervised the simulations. Andreas Fery supervised the project, was involved in scientific discussions, and proof-read the manuscript.

Chapter

III

Theory and Status of the Field

Colloidal Self-Assembly Concepts for Plasmonic Metasurfaces

This chapter is based on the publication *Advanced Optical Materials* **2018**, 18000564–18000581.

By Martin Mayer,[a,b] Max J. Schnepf,[a] Tobias A.F. König,[a,b,*] and Andreas Fery[a,b,c,*]

[a]Leibniz-Institut für Polymerforschung Dresden e.V., Institute of Physical Chemistry and Polymer Physics, Hohe Str. 6, 01069 Dresden, Germany

[b]Cluster of Excellence Center for Advancing Electronics Dresden, Technische Universität Dresden, 01062 Dresden, Germany

[c]Department of Physical Chemistry of Polymeric Materials, Technische Universität Dresden, Hohe Str. 6, 01069 Dresden, Germany

* corresponding author

III.1 Plasmonics and Wet-Chemical Synthesis to Fabricate Colloidal Plasmonic Metasurfaces

III.1.1. Optical Properties and Synthesis of Plasmonic Particles

Plasmonic nanoparticles facilitate a variety of applications, including coloring agents (*e.g.*, colored glass[1]), electronics (*e.g.*, plasmonic solar cells[2]), optics (*e.g.*, overcoming the diffraction limit[3]), medicine (*e.g.*, cancer treatment[4]), and sensing (signal/sensitivity enhancement[5]). Although all of these effects are present in isolated, individual plasmonic nanoparticles, these effects can be further boosted and better controlled by plasmonically coupling of such colloids in assemblies. Plasmonic coupling imparts tunable interactions with electromagnetic radiation and new emergent properties. Examples include strong electromagnetic field enhancement,[6] hybridized plasmon modes,[7] and a dramatic color change when varying the distance between coupled nanoparticles.[8] Thus, assembling nanoparticles into dimers already results in superior field enhancement and improved sensitivity in Raman scattering spectroscopy.[9] Moreover, advancements in theory, simulations, and computing power have facilitated the rational design of complex nanoparticles and well-defined assemblies.[10]

In this first section, the basics of plasmonics, design rules, and experimental approaches for tailoring the optical properties of isolated, *i.e.*, non-interacting, nanoparticles will be introduced. The herein presented theory has been selected to align with the types and properties of nanoparticles that are readily obtained *via* wet-chemical synthesis. Coupling of plasmonic particles and their fabrication will be introduced in the next sections.

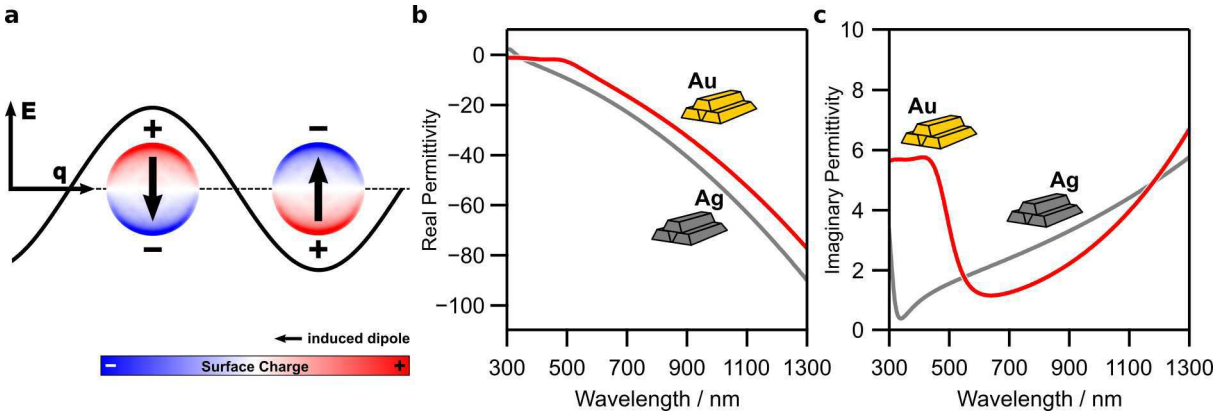

Figure III.1.: Basics of plasmonics: excitation of a subwavelength nanoparticle (a) The electric field of an incident electromagnetic field, *e.g.,* a light wave with the wavevector q, results in a coherent oscillation of the conductance electrons in a metal nanoparticle, as analytically described by Mie theory. (b) Real part of the permittivity and (c) imaginary part of the permittivity for bulk gold and silver (dielectric d taken from Johnson and Christy[11] and Hagemann *et al.*,[12] respectively).

In metals, incident light can excite coherent oscillations of the quasi-free conductance electrons at its interface. The resonance condition of this oscillation, known as surface plasmon resonance, depends on excitation wavelength, polarization, angle of incidence of the light, *e.g.,* q-vector of the light, as well as the thickness of the metallic film.[13] In the case of colloidal nanoparticles, the wavelength of incident light is much larger than the particle dimension.[14] The spacial con-

finement of the quasi-free electrons results in localization of the induced oscillation within the nanoparticles and thereby, to charge separation (**Figure III.1a**). Thus, an oscillating net dipole moment is formed by the electric field of the charges.

The plasmonics of a spherical metal nanoparticle in a dielectric medium can be analytically expressed by the theory of Mie.[15] As described above, the incident light induces a charge separation by polarizing the particle. The respective polarizability α reads for a metallic particle as follows:

$$\alpha = 4\pi r^3 \frac{\varepsilon_m - \varepsilon_d}{\varepsilon_m + 2\varepsilon_d} \tag{III.1}$$

with the radius of the metallic particle r, complex dielectric function of the metal ε_m, and of the dielectric environment ε_d, respectively. In order to excite the plasmons, the real part of the dielectric function needs to be negative, which is the case for metals. The imaginary part influences mainly the linewidth of the excited plasmonic resonance, *i.e.*, the damping of the oscillation. Examples for the dielectric functions of gold and silver, which are plasmonically active in the optical range, are shown in **Figure III.1b&c**. Exciting a metallic particle with an incident light beam (*i.e.,* q-vector $q = {}^{2\pi}/_{\lambda}$) results in scattering (σ_{sct}) and absorption (σ_{abs}) in dependency of their polarizability α:

$$\sigma_{sct} = \frac{1}{6\pi} q^4 |\alpha|^2 = \frac{8\pi}{3} q^4 r^6 \left| \frac{\varepsilon_m - \varepsilon_d}{\varepsilon_m + 2\varepsilon_d} \right|^2 \tag{III.2}$$

$$\sigma_{abs} = q\ \mathrm{imag}[\alpha] = 4\pi q r^3\ \mathrm{imag}\left[\frac{\varepsilon_m - \varepsilon_d}{\varepsilon_m + 2\varepsilon_d} \right] \tag{III.3}$$

The final extinction (σ_{ext}) of the particle is defined by the sum of scattering and absorption (equation III.4). Thus, as described by equations III.2 & III.3, the ratio of scattering and absorption depends on the particle radius r; *e.g.*, small particles are dominated by absorption and big particles by scattering.

$$\sigma_{ext} = \sigma_{sct} + \sigma_{abs} \tag{III.4}$$

The impact of size, dielectric environment, particle geometry, and plasmonic material is discussed in more detail on the following pages.

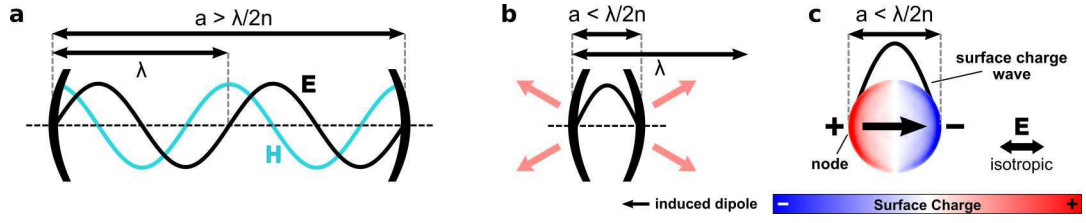

Figure III.2.: Basics of plasmonics: conservation of energy in photonic and plasmonic systems. (a) In a simple photonic cavity with a dimension larger than the half wavelengths (λ / 2n), a self-sustaining oscillation of a light wave is possible. (b) For a subwavelength cavity, however, this is impossible and hence, the energy cannot be contained in the cavity, *i.e.*, it radiates out. (c) In the case of plasmonic particles, the conductance electrons act as free carriers, thereby allowing a coherent oscillation of the plasmons and confinement of light below the diffraction limit. Thus, the incident light excites a coherent oscillation of the conductance electrons resulting in the formation of an oscillating dipole moment. This dipole moment is typically visualized by either an arrow, plotting of the surface charges (red and blue), or schematically by its surface charge wave. The zero crossing of such surface charge waves marks a node of the induced plasmon mode.

A more intuitive model of plasmonics can be formulated by looking at the energy balance and the conservation of energy in such structures, as recently presented by Jacob Khurgin.[16] As shown in **Figure III.2a**, in an optical (photonic) cavity of a dimension well-above the exciting wavelength ($a > \lambda/2n$; with wavelengths λ and refractive index n), the energy is transferred from the electric field energy to the magnetic field energy after every half period and back. Similar to a simple gravity pendulum, in which the energy is transferred from potential energy to kinetic energy and back, a self-sustaining oscillation is formed, and thereby, conserving the energy.[16]
When the size of the cavity is decreased below half of the wavelength ($a < \lambda/2n$; **Figure III.2b**), the energy can no longer be efficiently converted from the electric field to the magnetic field. In order to comply with the conservation of energy, the energy needs to radiate out of such a cavity, as illustrated by the red arrows. Thus, a self-sustaining oscillation is impossible—consistent with the diffraction limit.[17]
In a plasmonic particle, however, the free conductance electrons of the noble metal can store the energy. Instead of magnetic energy, kinetic energy of the induced collective electron oscillation is used to comply with the conservation of energy. As summarized in **Figure III.2c**, this electron oscillation results in the formation of a net dipole moment. Thus, the localized surface plasmon resonances (LSPR) allow localization of electromagnetic fields below the diffraction limit. However, due to the motion of the electrons in the metal, the resulting plasmon mode is strongly damped and lossy.[16,18]

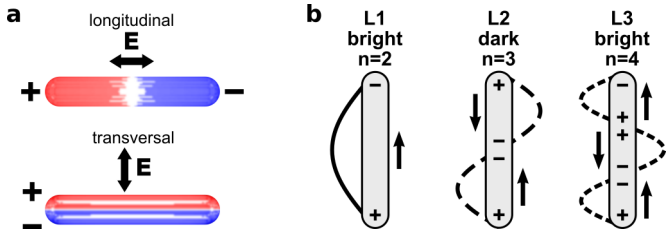

Figure III.3.: Basics of plasmonics: excitation and higher order plasmon modes of anisotropic nanoparticles. (a) For anisotropic particles, fundamental modes exist for each geometric main axes of the particle. In case of a nanorod, longitudinal (L) and transversal (T) modes can be excited. (b) In addition to the fundamental modes (L/T1), also higher order longitudinal modes (L2··X) can be excited at higher energies, forming additional nodes.

The fundamental plasmon mode of an isolated sphere has the character of a single dipole (D1) and is hence, energetically degenerated. For anisotropic particles the fundamental mode splits into a separate dipolar mode for each geometric axis—thus, the anisotropy lifts the degeneracy. For a nanorod, a longitudinal and transversal dipolar mode (L1 and T1) can be excited, as shown in **Figure III.3a**. The resulting excitation wavelength scales with the polarizability of the plasmon mode, *i.e.*, (typically) the T1 resonance condition is met at higher energies / lower wavelengths. If the polarizability of a plasmon mode is high enough, higher order modes (L/T2··X) can be excited, resulting in the formation of additional nodes in the “surface charge wave“, which schematically represents the polarization field of the respective plasmonic modes (**Figure III.3b**). Plasmon modes, which have a non-vanishing net dipole moment, can be excited by a plane wave (*e.g.* classical non-focused light), and consequently, are referred to as ”bright modes“. In reverse, if the net dipole moment cancels out, like in L2, the mode is called ”dark mode“. Furthermore, the scattering and absorption properties of plasmonic nanoparticles can be tailored by controlling their composition, size, geometry, and/or environment.[19,20]

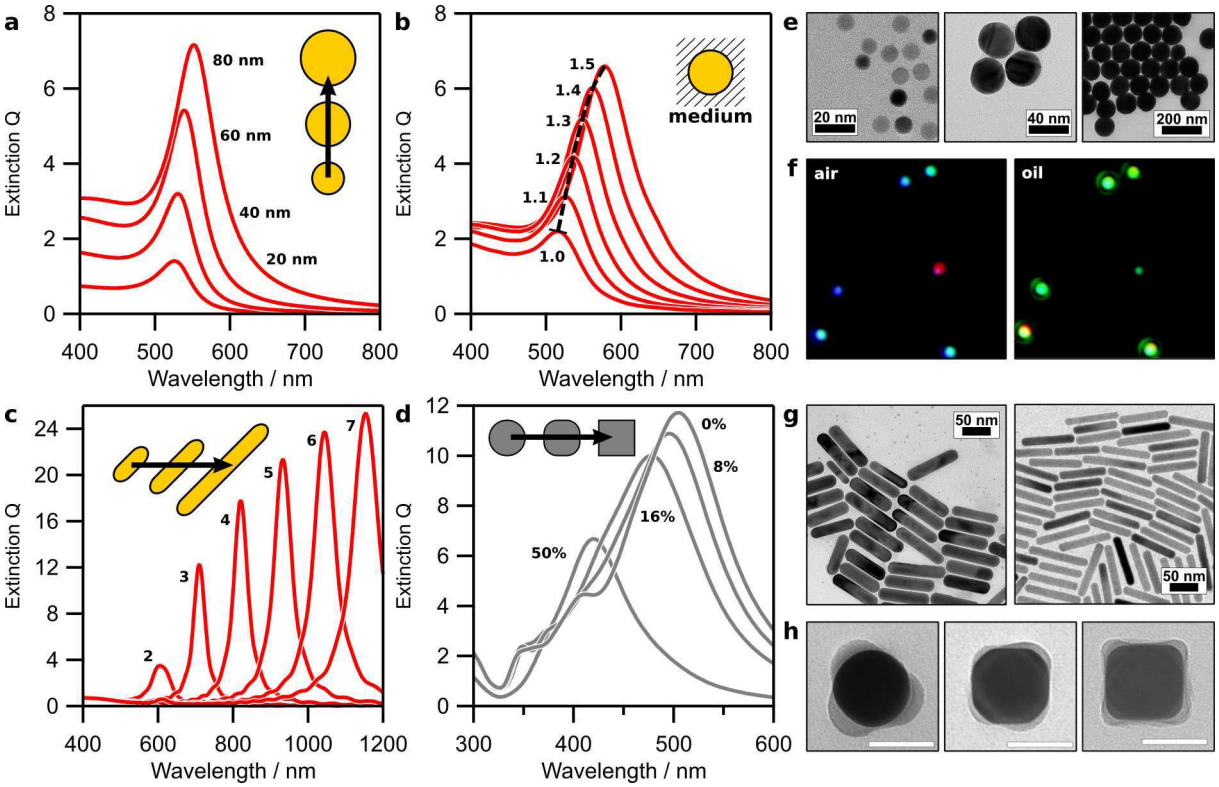

Figure III.4.: Design principles and colloidal plasmonic building blocks. The optical properties of an isolated plasmonic nanoparticle depend mainly on the following features: (a) particle dimension (40–80 nm), (b) refractive index of the surrounding media, (c) particle shape (*e.g.*, anisotropy), and (d) presence of tips, edges and sharp corners. For (a–c) gold is used as nanoparticle material and for (d) silver. (a, c–d) surrounding medium is water (n = 1.33). (e–h) Exemplary particles visualizing the aforementioned properties: (e) spherical particles with varying size (left: 8 nm; middle: 40 nm; right: 70 nm), (f) refractive index changes visualized in darkfield images (left: air; right: oil), (g) gold nanorods with varying aspect ratio (AR = length / width; left: 3.9; right: 6.3), (h) and edge rounding of gold nanocubes (left: 50%; middle: 40%; right: 25%, scale bars: 50 nm). (e) Adapted with permission. Copyright 2019, Anja Maria Steiner. (f) Adapted with permission.[21] Copyright 2003, American Chemical Society. (g, right) Adapted under the terms of CC-BY license.[22] Copyright 2017, Royal Society of Chemistry. (h) Adapted with permission.[23] Copyright 2017, American Chemical Society.

The optical response of an isolated nanoparticle is the starting point toward designing complex assemblies. **Figure III.4** summarizes the basic design principles of plasmonic building blocks and their correlated optical response.

Increasing the diameter of the nanoparticle causes a red-shift of the plasmon resonance (toward lower energy) and an increase in the effective absorption cross section. Mie theory calculations of spherical gold particle with diameters of 20–80 nm in water (n = 1.33) illustrate this effect (**Figure III.4a**). The effective extinction cross section Q is defined by the intensity of extinction cross section divided by the cross sectional area of the scattering nanoparticle. This definition holds for all of the calculations discussed in this chapter, and the effective extinction cross section makes the optical responses from different types of metal nanoparticles comparable.

When the refractive index n of the dielectric environment is varied, the optical responses can also be tuned, as shown in **Figure III.4b**. Increasing the refractive index of the surrounding results in an excitation at lower energy and an increase in effective extinction, since the polarizability is increased and damping (of the oscillation) lowered.[24] This is exemplified in **Figure III.4f** by the scattering response of spherical particles in different media (air and oil; n=1.44).

Colloidal particles in dispersions, formed by wet-chemical synthesis methods, are employed in a wide range of applications.[2] As shown in **Figure III.5**, a huge variety of different morphologies is achievable in dispersion. Hence, wet-chemical methods allow tuning of the optical response of plasmonic nanoparticles in a cost-efficient manner. Although methods for synthesizing simple gold colloids are already well established, utilizing these nanoparticles as building blocks for assemblies on plasmonic metasurfaces requires fulfillment of additional criteria: Dispersity in size and shape leads to undesired broadening of the plasmonic peak extinction due to superposition of the optical response of all (different) nanoparticles in the ensemble.[25,26] Nowadays, modern synthesis, however, can reach theoretical limits of optical quality in colloidal ensembles. For example, González-Rubio *et al.* impressively showed that the optical linewidth of gold nanorods can be reduced close to the theoretical limit by post-synthesis reshaping.[27]

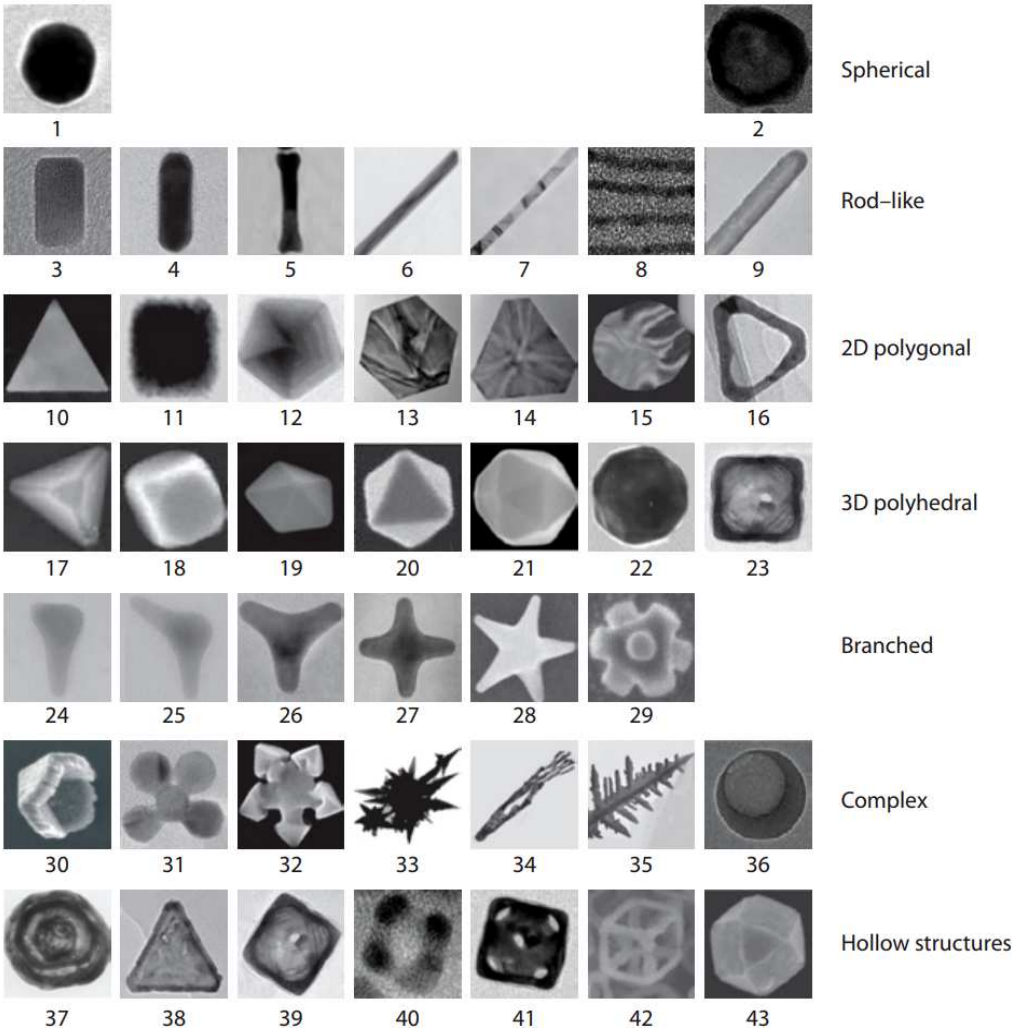

Figure III.5.: Overview of various obtainable building block morphologies. By wet-chemical synthesis, a huge database of various morphologies is accessible. From top to bottom, the complexity of the presented morphology types is increased. From left to right, the aspect ratios, number of sides and facets, or number of branches are increased and the last particle of each row is the respective hollow structure. Adapted with permission.[28] Copyright 2011, Springer Nature.

Especially, seed-mediated growth has proven to result in small size and shape variations meeting the requirements of high optical quality (**Figure III.4e**).[29] In this synthesis approach, the

nucleation of the particles, known as the seeding, and growth are completely separated from each other. Typically, such seeds (diameter <5 nm) are formed by a fast reduction with a strong reducing agent, followed by a slow and controlled overgrowth to achieve the final size and shape under mild conditions.[30] Since the dispersity of the final particles is inherited from the initial seeds, this synthesis approach can yield particle size distributions with standard deviations of the diameter well-below 5%.[31] Although the size dispersion is rather low, even small amounts of morphological by-product can hinder assembly processes and give inconsistent optical properties that often appear as broadening of spectral features. This size and shape distributions can often be improved by additional purification steps, such as exploiting depletion forces.[32–34] Since some particle geometries, like nanotriangles, can only be synthesized in mixtures with other shapes purification is crucial to obtain a highly pure sample.[34]

This purification method relies on attractive, short-range depletion forces between colloidal particles. The depletion forces arise when the separation distance between the colloids and the size of a second smaller, more abundant species*, e.g.,* surfactant micelles, are in the same order of size. The depletion of the surfactant micelles from the volume between the colloids results in an attractive osmotic pressure. As described in equation III.5, the depletion potential depends on the excluded volume V_e between the colloids and the resulting osmotic pressure Π_m:

$$|U| = -V_e\Pi_m = \underbrace{A2r_m}_{-V_e}\underbrace{\frac{C - C_{CMC}}{n}N_A k_B T}_{\Pi_m} \tag{III.5}$$

where r_m, C_{CMC}, C and n are respectively the radius, the critical micellar concentration (CMC), the analytical concentration and the aggregation number of the selected surfactant, N_A is the Avogadro constant, and A is the area of interaction between two adjacent particles. The excluded volume can be ascribed to the area of interaction, given by dimension and shape of the particles, and the size of the micelles. The osmotic pressure depends on the surfactant concentration, under consideration of the micellar aggregation number and CMC.

Consequently, depending on the particle type and the employed surfactant concentration, colloids can be selectively and reversibly agglomerated and then, separated *via* sedimentation. A detailed description of the purification process, exemplified with the help of an example and experimental data, can be found in **Section IV.1**.

The introduction of nanoparticles with anisotropic shapes is an exciting development that extends the accessible range of excitation wavelengths. Furthermore, the increased polarizability allows higher sensitivity in comparison to spherical particles (**Figure III.4c**).[35–38] Anisotropic shapes result in anisotropic surface plasmon resonances with more complex and tunable optical properties.[22] As a consequence of such more complex geometries, the number of induceable plasmon modes increases, since the incident electric field is able to polarize the nanoparticles in more different ways. **Figure III.4g** depicts exemplary nanorods, which can be excited by the electric field vector parallel (longitudinal mode) or perpendicular (transverse mode) to the long axis of the nanorod (see above).

Methods for synthesizing nanoparticles with anisotropic shapes or geometric features with high curvature are well established.[39] In seed-mediated growth, the nanoparticle shape is controlled by passivation and selective stabilization of specific crystal facets.[40] Most prominently, surfac-

tants containing halides act as shape-directing agents by energetically favoring growth of certain facets.[41–43] In the special case of gold nanorods, halides are combined with silver ions to increase the efficiency of the symmetry break.[40] Facet-selective growth gives rise to a variety of morphologies including spheres, triangles, cubes, and rods (see also **Figure III.5**).[44]
Nanocubes are another commonly used particle morphology in various studies, which can be obtained by overgrowth processes or polyol processes.[45–49] The latter are usually one-pot reactions, based on passivation by polymers, and will be not discussed in detail in this thesis. But in general, the herein presented synthetic concepts are also valid for polyol reactions, *e.g.*, the passivation by halides as shape directing agent.[48,50] Analogously to nanorods, the optical properties of cubes (**Figure III.4d**) are defined by the following rules: As shown in **Figure III.4d** the plasmon resonance shifts red for lower symmetries due to the increased polarizability of sharp edges and corners. Furthermore, multipolar modes can be excited easier (see **Figure III.4d** <450 nm; see the next section for the impact of silver)[47]
Electromagnetic simulations can be used as a tool to interpret spectroscopic data obtained for nanoparticles formed by wet-chemical synthesis. By comparing experimental spectra to simulations, the size and shape of the plasmonic nanoparticles can be estimated. *E.g.*, the presence of undesired anisotropy and edges would lead to additional broadening and/or a red shift of the LSPR, as discussed in the following paragraphs.

For electromagnetic simulations of spherical, isolated nanoparticles the analytical Mie equations are used within this thesis.[15,51,52] For all non-spherical nanoparticles and also coupling spherical nanoparticles, a commercial-grade simulator based on the finite-difference time-domain (FDTD) method (Lumerical FDTD)[53] is used herein, due to its efficient access to complex particle geometries and to the resulting electric fields. For investigating the scattering behavior of the plasmonic nanoparticles, a source designed for scattering behavior of objects (total-field scattered-field source) is utilized to isolate the scattering field from the incident field. A balance between the computational effort and accuracy (validated by comparison with Mie theory calculations) is required considering for this finite-element method. Thus, the frequency points are set to half of the wavelength span and the mesh size to 1 nm. For objects smaller than 20 nm, even smaller mesh sizes are necessary. Finally, the injected electromagnetic field must converge during the defined simulation time.
For the dielectric properties of gold, the sample data from Johnson and Christy usually show the best match between simulated and experimental optical response.[11] For silver, the approximation by Hagemann *et al.* matches best to experiments.[12]
Similar results can also be achieved by using other, non-commercial solutions. The boundary element method (BEM) follows a different approach, since it only considers the dielectric-metal surfaces.[54,55] The calculation of the spectral response from the surface charges in the frequency-domain makes this method complementary to FDTD in terms of efficiency. Thus, BEM is used to simulate electron energy loss (EELS) in **Section V.2**.
An other, herein not used, example is the discrete dipole approximation (DDA), in which materials are approximated by a set of (almost atomically sized) discrete dipoles.[56] However, the DDA method has a significant disadvantage in computational effort when surfaces are added, since these surfaces must be approximated also by dipoles. But a simplified DDA model will be introduced in **Section V.2** to explain plasmonic coupling in linear particle chains.

Such analytical and semi-analytical methods contribute to a better understanding of optics and plasmonics because of their computation efficiency in comparison with numerical methods, as discussed in the review article by García de Abajo *et al.*[57]

III.1.2. Excitation Across the Entire Visible Spectrum: From Gold to Silver

The optical and chemical properties vary widely among plasmonic materials. In this section, the optical properties and wet-chemical syntheses of colloids are compared for the most commonly used plasmonic materials, which are as well subject of this thesis: gold and silver. Despite their promising plasmonic properties, alternative metals, like aluminum, still play a minor role in colloidal plasmonics due to the lack of feasible nanoparticle synthesis protocols—but with recent advancements in their synthesis, especially aluminum becomes more and more popular.[58–60]
For plasmonic excitation in the full visible range (380–750 nm), silver is generally the preferred material for colloids rather than gold. The reason is visualized by the quality factor (QF), which was introduced by Shen *et al.* and is defined as QF= $\omega(\mathrm{d}\varepsilon'/\mathrm{d}\omega)/(2\varepsilon'')$, where ε' and ε'' are the real and imaginary parts of the dielectric function (ε) of the metal.[61] Thus, a large QF is obtained when ε'' is small and the change in ε' is large.
As shown in **Figure III.6a**, silver has a large QF in the violet (<450 nm), and has a significant QF across the entire visible spectrum, while the QF of gold vanishes in the blue (<500 nm). The observed effect is also correlated with the band transition from intraband to interband of silver (at 326 nm) and gold (at 515 nm).[12] The influence of the QF on the spectral line width and the extinction efficiency is directly visualized in **Figure III.6b** by comparing gold and silver spheres of varying size (40 nm and 80 nm, respectively). Because of the distinct optical properties of silver and gold, the expected dipolar resonances for silver and gold nanocubes (**Figure III.6c**) occur at 505 nm and 595 nm. It should be noted that the energetically lowest modes for silver and gold are both dipolar. For clarity in **Figure III.6c**, the plasmonic modes are only labeled and illustrated for silver. Gold only exhibits a single dipolar mode, which is similar to (I) of silver. Due to the high QF of silver in the violet range, energetically higher plasmonic modes can be observed as well. These higher plasmonic modes are potentially useful for energy propagation because of their lower radiative damping.

The sensitivity of silver to oxidation makes the synthesis of durable silver nanoparticles challenging and creates some experimental limitations. Gold, in contrast, is the most noble metal and is least prone to oxidize upon contact with ligands or the environment. Furthermore, the size and shape of gold nanoparticles can be readily controlled following a vast range of well-established synthetic protocols.[45] Consequently, gold is the common material of choice for nanoparticles in proof-of-concept realizations of plasmonic metasurfaces.[62] Despite the superior optical properties of silver, the number of reproducible and tunable protocols that result in a narrow distribution of nanoparticles as well as high yield of shaped nanoparticles is limited.[63] These protocols typically involve chemical-passivation of the particle-surface by polymer layers like polyvinylpyrrolidone (PVP).[63,64] The drawback of passivation by a polymeric layer can be overcome through recent advances in surfactant-based synthesis[63] and/or the use of well-defined gold particles as seeds for the silver deposition,[45,64,65] depicted in **Figure III.6d–g**.

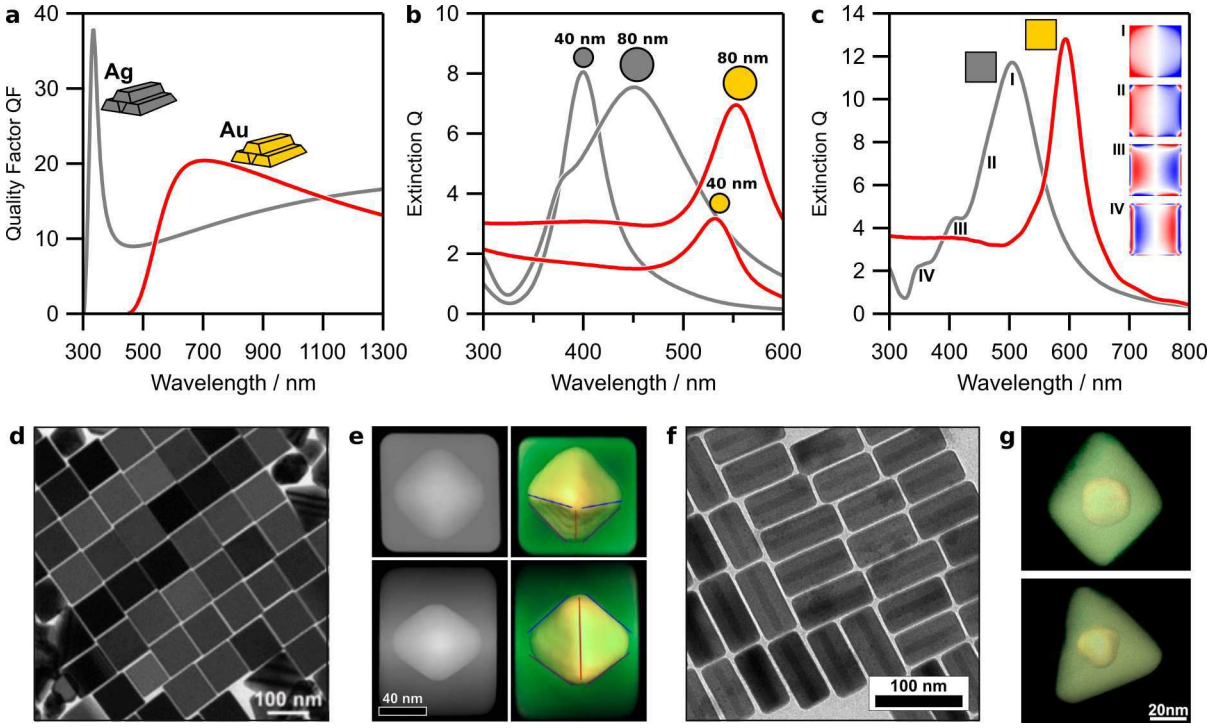

Figure III.6.: Plasmonic quality factor and examples of well-defined silver nanoparticles. (a) Wavelength-dependent quality factor (QF) for bulk silver and gold in the visible range. (b) Spectroscopic response of silver and gold nanoparticle with varying size. (c) gold and silver nanocubes and surface charge images of plasmonic modes for silver. For (b–c), the surrounding media is water (n = 1.33). (d) Finely-tuned surfactant-based silver nanocube synthesis as shown by Xia and coworkers. Alternatively, (e–g) silver overgrowth from gold particle seeds inherit their size distribution and crystal structure, exemplarily shown for cubes, cuboids, and bipyramids. The abbreviations are defined as follows: effective extinction cross section (Q) and wavelength (λ). (d, e) Adapted with permission.[45,63] Copyright 2016/2013, American Chemical Society. (f) Adapted under the terms of CC-BY license.[22] Copyright 2017, Royal Society of Chemistry. (g) Adapted under the terms of CC-BY license.[66] Copyright 2017, Royal Society of Chemistry.

In the latter approach, the narrow size distribution of gold cores is templated into a highly uniform silver shell, which dominates the optical properties by masking the gold core.[67] By combining the superior optical properties of silver and the synthetic advantages of gold in this manner, wires, cubes, bipyramids and cuboidal morphologies with outstanding optical properties can be achieved.[22,45,66] These shapes have in common, that they are predominantly covered by {100} facets, the thermodynamically most stable facet. Due to the high absorption energy of halides on low index facets of silver the formation of {100} facets is enforced in silver (over)growth.[45,68] The in **Chapter IV** introduced synthesis protocols are based on this approach and **Section IV.1** includes a more detailed discussion of it.

III.1.3. Plasmonic Coupling in Colloidal Metasurfaces

With the optical properties of non-interacting nanoparticles and methods for synthesizing and engineering the optical properties of plasmonic nanoparticles established, this section is dedicated to understanding the properties of local and collective coupling effects between adjacent nanoparticles. The plasmonic hybridization that occurs in coupling systems is important for understanding the properties of plasmonic metasurfaces.

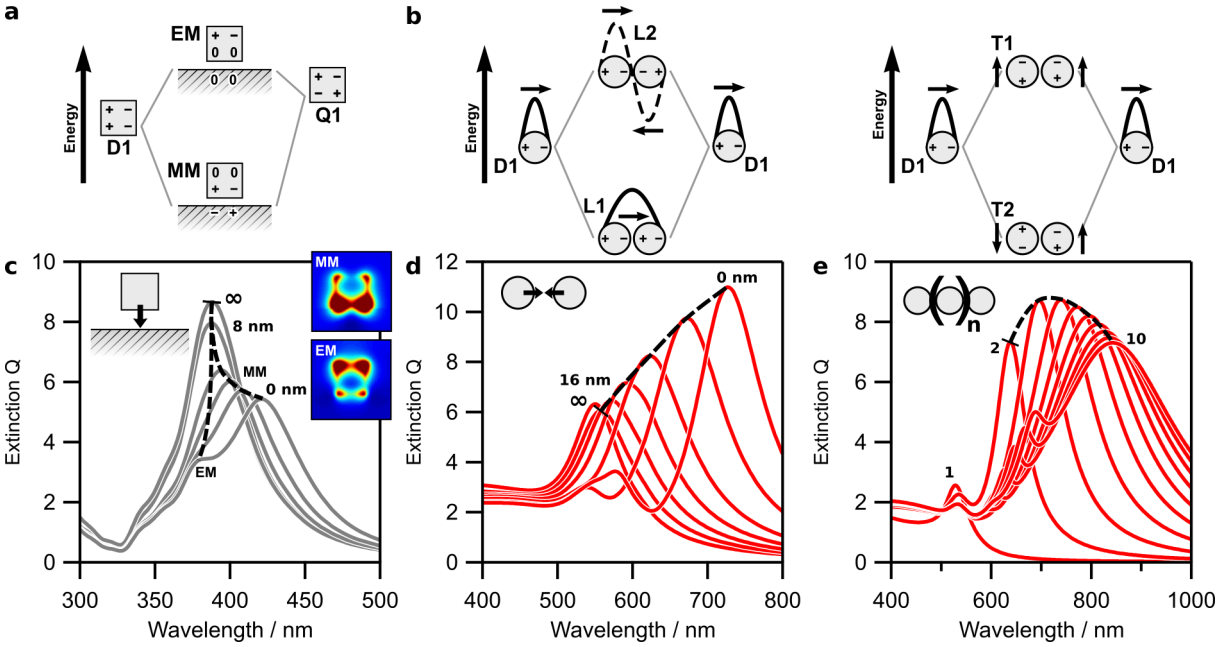

Figure III.7.: Principles of plasmonic coupling. Plasmonic hybridization mode for cube to substrate coupling (a) and hybridization for a plasmonic dimer (b, longitudinal and transversal excitation, respectively). (c) Simulations of plasmonic hybridization when a silver cube approaches a dielectric substrate, (d) for two approaching nanoparticles forming a dimer, and (e) a linear particle chain formed by the gradual addition of more particles.

Since the symmetry of the dielectric environment is broken by placing a plasmonic nanoparticle onto a substrate, it has a pronounced impact on the spectroscopic properties of the system (**Figure III.7a & c**). As shown in the hybridization model (**Figure III.7a**), the dipolar mode (D1) of the exemplary cube couples with its quadrupolar mode (Q1), while approaching the surface.[69] This coupling results in splitting of the modes into a bonding magnetic mode (MM) and an anti-bonding electric mode (EM), as shown in the resulting electric field distributions. The hybridization model describes this splitting of the initial degenerated modes into hybridized modes by the linear combination of the isolated modes.[7,70] The anti-bonding mode is useful for applications in sensing because of enhanced electric field facing toward the environment.[71] Controlling the plasmonic field enhancement in the gap between the nanoparticle and substrate is important to exploit radiative processes in such plasmonic cavities.[72–75] **Section V.1** investigates the plasmonics of such systems. A limiting factor in colloid-based approaches is the presence of stabilizing ligands (∼2 nm thickness) around the nanoparticle, which can limit charge transfer and the gap size. Despite the possibility of removing this dielectric shell by plasma cleaning, heat, or chemical treatment,[76–78] it is usually preferable to functionalize the particles with adequate alternative ligands (see also **Section III.2 I**).

Analogously, the coupling of two (identical) plasmonic particles results in a more complex hybridization of the modes. As shown in the hybridization model in **Figure III.7b**, two different scenarios arise: polarization of the incident light along or perpendicular to the particles (longitudinal and transversal, left and right, respectively).[7] In both cases, the dipolar modes of the individual particles interact with each other resulting in splitting of the mode. An energetically favorable anti-symmetric L1/T2 mode, which features an increased dipole moment, and an energetically less favorable symmetric L2/T1 mode with a vanishing net dipole moment (dark mode) emerge. The coupling of this particle dimer is extremely sensitive toward the interparticle distance (see **Figure III.7d**). Due to this distance sensitivity, this system is often referred to as plasmon ruler.[8] Examples of such dimers include a dramatic color change when varying the distance between coupled nanoparticles,[8] strong electromagnetic field enhancement,[6] and hybridized plasmon modes.[7] Thus, simply assembling nanoparticles into dimers can already result in superior field enhancement and improved sensitivity, *e.g.*, in surface enhanced Raman scattering spectroscopy.[9]

In each of these examples, two or more plasmon resonances overlap and interact with each other. These interactions may result in an asymmetric line-shape (so-called Fano resonance), where the extinction of the coupled particles has a distinct minimum and maximum arising from the coupling. Because of the wide range of possible interactions, Fano line shapes are commonly observed in many plasmonic systems. The sharpness of the Fano resonance makes it highly appealing for several applications. For example, colors from plasmonic coupling can be brighter than pigmentary colors, are immune to photo bleaching, and can be tuned dynamically, if the system is mounted on a flexible substrate.[79] Non-linear effects, such as lasing, can be achieved when the plasmonic effect is coherently coupled to a gain medium, like fluorescent emitters.[80] Further applications include highly sensitive refractive index sensors[81] and selective injection of hot electrons.[82] For further reading about Fano resonances at plasmonic metasurfaces, the review from Chong *et al.* gives a more detailed overview.[83]

The logical continuation of a plasmonic dimer is to add more particles to it, thereby, forming a linear particle chain. As exemplified in **Figure III.7e**, additional particles lead to a red shift of the predominant dipolar L1 mode.[84–86] The spectral position of this mode converges to a specific wavelength, which depends on the interparticle spacing, particle size, particle morphology, and surrounding media.[84,87–89] This effect is explained by the *infinite chain limit* and for spherical particles, is described in literature at 8–12 particles.[84,85,90] Due to the collective, coherent coupling within such particle chains and the high electric field enhancement in the hotspots between the particles, plasmonic particle chains are a candidate for the integration of colloids in various applications, like waveguiding, energy transport, and sensing.[84,87,91,92] Linear particle chains will be discussed in-depth in **Section V.2.**

III.2 Principles of Colloidal Self-Assembly

Self-assembly is the spontaneous organization of pre-existing components into complex organized structures.[93] This process is controlled by the chemical and physical properties of nanoparticles, surfaces, and their interactions.[2] The driving force for the organization of these structures is the reduction of free energy to approach local equilibrium. Approach a specific local equilibrium can be externally aided or modulated by exploiting directing fields and/or confinement effects. In the directed self-assembly processes, templates, external fields, or directing agents are typically used to induce selective clustering of colloids and spatial order. For template-assisted colloidal self-assembly—the primary method for bottom-up fabrication of colloidal metasurfaces—capillarity and capillary forces drive self-assembly process on the interface of templates (*i.e.*, surface-modified objects with selective binding sites). Recent developments in colloidal science have enabled the precise self-assembly of plasmonic nanoparticle, resulting in well-controlled emergent properties through plasmon coupling. In particular, simultaneous progress in surface modification, miniaturization of features, and improved scalability of template fabrication in the last decade have led to significant advances in self-assembly.[20,94–97] The improved reproducibility and fine control now available through templated self-assembly provide a strong and necessary foundation for complex spatial organization that is required for applications. The field of template-assisted self-assembly has matured to a point, where efficient scalability, how to obtain precise control, and subsequent system integration need to be considered early in the development of self-assembly processes.

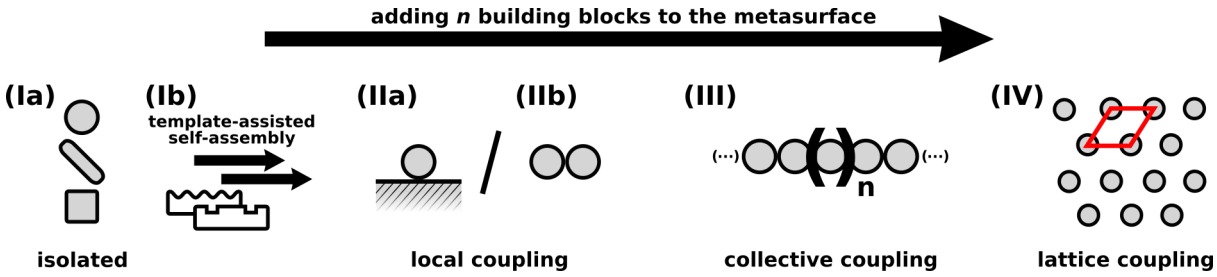

Figure III.8.: Self-assembly concepts for colloidal metasurfaces *via* incremental increase in the number of particles in the unit cell. (I) Colloidal particles with well-defined morphology (a) and templates (b) as building blocks for the self-assembly; (II) unit cells from (a) surface-coupled colloids or (b) few closely-placed colloids, both dominated by near-field coupling; (III) 1D plasmonic "polymers" from spheres acting as quasi-finite chains by collective coupling within the particle cluster; (IV) 2D lattices with long-distance order resulting in surface lattice plasmons.

Following the theory of plasmon hybridization, complex materials can be constructed from their primary components by step-wise introduction of additional nanoparticles to a plasmonic metasurface, increasing its size. As visualized in **Figure III.8**, for large, periodic assemblies obtained in this manner, long-range lattice effects can dominate the properties. Hence, hierarchical plasmonic metasurfaces can be designed by assembling the colloidal building blocks in a rational manner.[28,98] Within this thesis, colloidal self-assembly acts as tool-set for the fabrication of plasmonic systems. This section gives a broad overview about self-assembly processes in general, although only few methods from this tool-set are experimentally used.

(I) As represented by nanospheres, nanocubes, and nanorods in **Figure III.8 Ia**, colloidal (noble metal) nanoparticles constitute the primary component. **Chapter IV** deals with the defined synthesis of adequate building blocks for self-assembly. Their optical properties are defined by the composition and shape of the nanoparticles, as discussed in previous sections. The resulting metasurfaces from a stepwise increased number of interacting particles in the unit cell can be grouped as follows:

(II) A group consisting of a few building blocks support additional properties such as Fano-resonances and/or electric/magnetic resonances. Therefore, they are dominated by the local coupling, which is dependent on the coupling strength and the number of particles. The most basic motif is a closely-coupled particle dimer (IIb), which can be further simplified to a single particle coupled to a dielectric or metal surface that breaks its symmetry (IIa), as illustrated in **Figure III.8** (group II). **Section V.1** investigates the plasmonics from systems based on group IIa.

(III) For linear particle chains or plasmonic polymers, the optical response is independent of the number of particles in the chain due to the radiative damping—thereby distinguishing them from smaller clusters.[90,99,100] Linear particle chains are particularly interesting for sub-wavelength energy and information transport applications or applications in strain sensing, as a result of their directional and anisotropic optical properties.[92,100] **Section V.2** studies in-depth the near-field properties of such linear particle chains.

(IV) In the case of plasmonic crystals, the building blocks are arranged in a period array to exploit the collective coupling effects induced by the long-range ordering of well-separated nanoparticles. The resulting Fano resonances are sharp because they combine coherent coupling of the individual plasmon modes and Bragg diffraction of the lattices. The plasmonics of lattices are not within the scope of this thesis.

(Ia) Role of surface functionalization of individual nanoparticles

For achieving well-controlled colloidal self-assembly, several requirements of the building blocks and the templates need to be met. Hence, the surface properties of the colloids, defined by their chemical functionalization, are essential for the self-assembly process and need to be matched to the chosen assembly technique. The main requirements are (1) colloidal stability in solution, (2) suitable properties of the spacer material between adjacent building blocks, and (3) the ability to form connections between the template and the directing fields and/or confinement effects during the assembly process. These features are determined by the (typically organic) ligand stabilizing the nanoparticles, which is either employed as the capping agent during synthesis or can be modified or exchanged later *via* functionalization or ligand exchange in an additional step. Several examples of functionalization for assembly are summarized in **Table III.1**.

(1) The colloidal stability of nanoparticles is especially important during the self-assembly process: The ligand has to prevent irreversible agglomeration, even in situations when external forces acting during the assembly process bring the nanoparticles into contact with each other.[101] Colloidal stability needs to be attained at high concentrations in order to prevent uncontrolled agglomeration. The assembly process can be accompanied by changes in ionic strength and pH. Thus, the nanoparticles need to be stable over a

range of pH and ionic strength. This can be achieved by electrostatic or steric (or both combined: electro-steric) interactions.[102,103] Typically, colloidal stability is provided by the capping-agent used in the synthesis, *e.g.*, cetyltrimethylammonium bromide (CtaB) or polyvinylpyrrolidone (PVP). Unfortunately, these ligands often lack functionality and/or are incompatible with assembly processes. Replacing the initial capping-agent *via* functionalization with polymeric ligands can introduce the required properties/functionality, for example the inversion of surface charges.

(2) Beyond providing colloidal stability, ligands can act as a dielectric spacer in the plasmonic metasurface and introduce tunability and responsiveness, thereby enabling and affecting the optical properties of the metasurface.[104] Synergistic effects between colloids and spacers or substrates can be introduced *via* "smart" ligands. A few examples include (semi-)conducting polymers, poly(N-isopropylacrylamide) (PNIPAm) as temperature responsive polymer, or fluorescently labeled DNA/protein.[105–108] By employing smart ligand, properties such as conductivity, environmental responsiveness, (*e.g.*, pH or temperature), and optical effects like fluorescence can be introduced into the system.[109–111]

(3) Most of the different self-assembly processes, which are discussed later, require optimizing interactions between the colloidal nanoparticles and the surface, as well as wetting of the colloidal dispersion. Surface modification of the nanoparticles can be used to render both their interactions and wetting behavior compatible with the assembly process. Examples for tuning wettability can be found in References [101, 104, 112]. As explained in References [101, 112], the contact angle of the wetting solution defines the strength of the capillarity, which is exploited for the assembly process. In Reference [104] the colloids are rendered surface active by a polymeric shell, in order to freely float the on the water-air interface. Examples for the significance of particle-surface interactions can be found in References [89, 113–115]. In these examples assembly on the templates is achieved *via* hydrophobic-hydrophobic interactions,[113] electrostatic interactions,[89,114] and chemical linking.[115] Surface functionalization guides the interactions with the template, which can include complementary charges or highly selective groups, such as DNA.

Table III.1.: Surface functionalization of nanoparticles for self-assembly.

Cat.	Purpose	Type of Functionalization	Example	Thickness	Reference
(1)	Capping agent	Surfactant from synthesis	CtaB, CtaC	<5 nm	[41–43]
(1)	Capping agent	Polymer from synthesis	PVP / Polyol	<5 nm	[63, 64]
(2)	Responsive spacer	Responsive polymer / hydrogel	PNIPAm, PVP-Gel	<1 µm	[104, 108, 109]
(2)	Spacer	Inorganic (+label)	SiO_2	>5 nm	[75, 116]
(2)	Conductive spacer	Conductive polymer	PEDOT:PSS, PANI	<50 nm	[107, 111]
(2)	(Responsive) spacer	(Labeled) protein / DNA	BSA, DNA	<10 nm	[103, 105]
(3)	Wetting modification	Surfactant for assembly	SDS / Triton	–	[101]
(3)	Hydrophobic linking	Polymer for assembly	PSS / P2VP	<5 nm	[113]
	Electrostatic linking		PAH / PVP	<5 nm	[117]
	Wetting modification		PEG-SH	<2 nm	[118]
(3)	Chemical linking	DNA	ssDNA, DNA	∼1 nm	[119, 120]

(Ib) Role of the template

The role of the template is to direct the forces guiding self-assembly to produce hierarchically ordered nanoparticle assemblies.[96] Templates have specific binding sites for the approaching colloids, which employ chemical linkers to form bonds or attractive interactions, spacers that provide repulsive interactions, or topographical traps. Templates are often designed to engineer specific interactions with nanoparticles, based on the size, shape, and chemistry of the nanoparticles. An overview of templates that have already been employed for template-assisted self-assembly is provided in the next section. The examples are sorted from those giving high positional control for the assembly to those that are scalable and cost efficient—which is the general sorting scheme in this chapter. These selected examples were chosen for the outstanding and/or recent results of assembled nanoparticles without respect to the novelty of the method for fabricating the template.

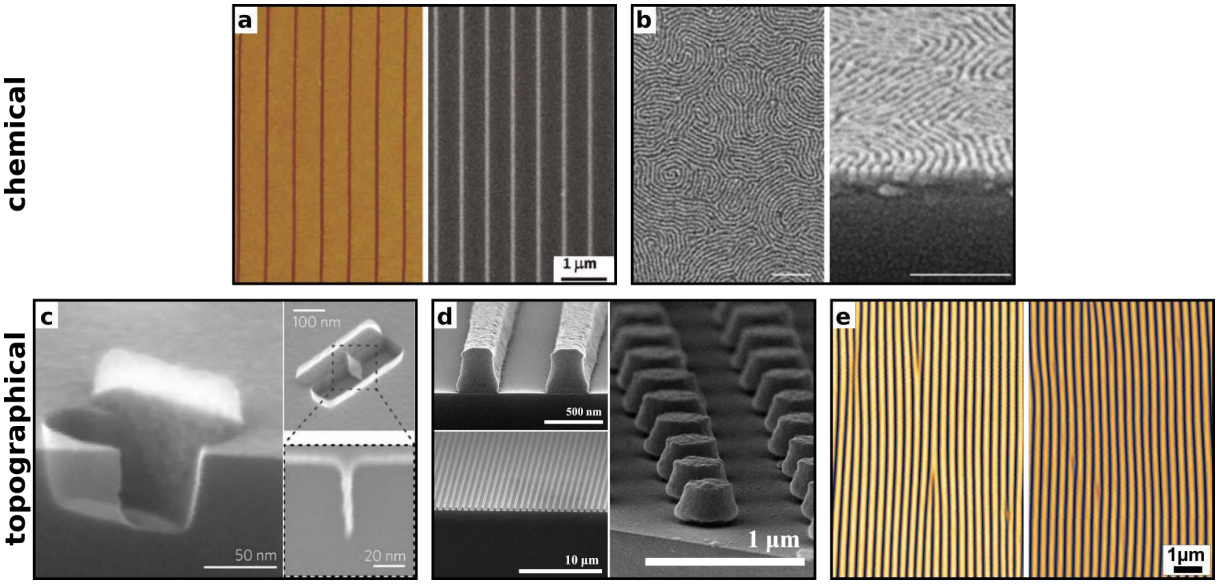

Figure III.9.: Chemical (top) or topographical (bottom) templates for colloidal self-assembly. (a) Micro-contact printing (µCP) to stamp chemical contrast onto a target: polyelectrolytes. (b) Micro-phase separation of block-polymers featuring chemical contrast (scale bars: 100 nm). (c) Topographic traps fabricated *via* high-resolution electron beam lithography. (d) Laser interference lithography to form channels and more complex structures. (e) Periodically wrinkled templates formed by mechanical instabilities due to modulus mismatch between an elastomer slab and its surface layer. (a) Adapted with permission.[113] Copyright 2012, American Chemical Society. (b) Adapted with permission.[121] Copyright 2017, American Chemical Society. (c) Adapted with permission.[35] Copyright 2016, Springer Nature. (d) Adapted with permission.[122] Copyright 2011, Elsevier. (e) Adapted under the terms of CC-BY license.[88] Copyright 2015, Royal Society of Chemistry.

For chemically structured templates (**Figure III.9a–b**, top line), sub-micron-sized chemical contrast is crucial for providing attractive and repulsive regions for phys- or chemisorption. Exploiting the dielectric shell encapsulating the colloids as spacer is commonly employed for obtaining ordered (mono)layers. The shell serves as a template for close-packed films, allowing tuning of the inter-particle distance *via* the shell thickness and its hydrophobicity.[102,104,123–125]
Chemically structured templates can be fabricated by nano/micro-contact printing. In this process, chemical contrast is printed using a topographic stamp by transferring/removing binding

sides onto/from a target surface. The resolution of the template primarily depends on the resolution of the stamp, and a several different types of chemical contrast are commonly used, including charge, hydrophobicity, and reactive linking groups.[113,126] Micro-phase separation can also be used to provide contrast on templates. A common method is tailoring and fabricating block-copolymers of with contrast embedded in the different blocks.[127,128] However, controlled formation of grains and domains needs to be considered for the scalability of this approach. By selective etching of one component of the micro-phase, the chemical template can also be converted into topographical structures, thus bridging chemical and topographical template approaches.[129]

Topographical templates (**Figure III.9c–e**) can provide excellent control over the self-assembly process, resulting in highly ordered structures by providing local energy minima. The selectivity of topographical templates is determined by the geometry of the features and their dimensions.[35,36,88,112] Templates fabricated *via* electron beam lithography or focused ion beam milling have the highest degree of control and versatile trap geometries. This flexibility to create arbitrary template structures comes at a relatively high cost, however, and generally lacks efficient scalability to macroscopic areas. Therefore, these kinds of templates are only well suited for the proof-of-concept plasmonic metasurfaces. Laser interference lithography is a scalable alternative to these methods, whose resolution is limited by the diffraction limit of light. Topography is constructed by interference of multiple laser beams at a photoresist, utilizing the phase of light. The types of patterns that can be fabricated by interference lithography range from periodic lines and elliptical holes to holes/pillars in hexagonal or square lattices.

Arrays of periodic lines can be fabricated in an extraordinarily inexpensive and scalable manner, as compared to conventional lithographic methods. Centimeter-scale wrinkled structures can be formed through mechanical instabilities in polymer films, as explained in detail in the reviews and book chapters by Schweikart *et al.*[130,131] For example, periodicities down to 200 nm can be fabricated by simply stretching a flat slab of an elastomer, polydimethylsiloxane (PDMS), followed by introducing elastic modulus mismatch by plasma hardening of the surface layer and subsequent relaxation of the PDMS.[88,132] The wrinkled structures that result (**Figure III.9f**) are well suited as templates for colloidal self-assembly of nanoparticles into macroscopic plasmonic metasurfaces and thus, are used in this thesis as the template for self-assembly. In summary, several different methods are available for template self-assembly of plasmonic nanoparticles, and the precision of the assembly, scalability, and cost are key considerations.

(IIa) Building plasmonic metasurfaces from single nanoparticle assemblies on substrates

One limiting behavior of plasmonic metasurfaces is individual clusters that do not rely on interactions between neighboring unit cells, but obtain their optical properties by local coupling (depicted schematically in **Figure III.8 IIa & b**). The only plasmonic coupling is within clusters of nanoparticle particles, *e.g.*, dimers deposited from solution or formed during deposition, or coupling to a dielectric/metallic substrate, which enhances its electromagnetic field.

Formation of particle assemblies on surfaces will typically use the surface as an element in guiding the assembly process, in contrast to bulk solution fabrication, which is not dis-

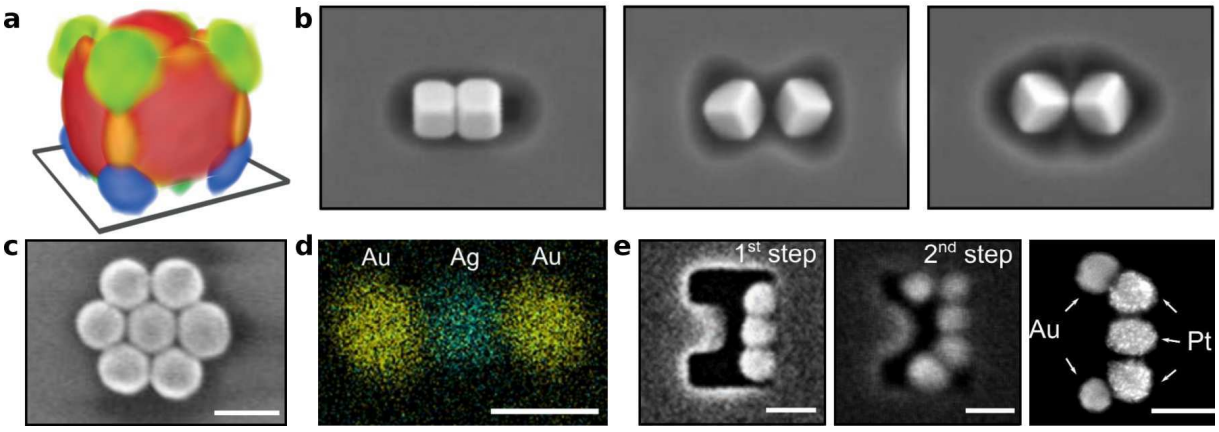

Figure III.10.: Plasmonic metasurfaces dominated by local coupling within plasmonically isolated unit cells. (a) Plasmonic modes of an isolated nanoparticle coupled to a substrate, a simple and common design motif; (b) Coupling scenarios for nanocube dimers; (c) Circular heptamer supporting a hybridized plasmonic mode (scale bar: 200 nm); (d) Heterotrimer consisting of two terminal gold particles and a central silver colloid (scale bar: 100 nm); (e) Multi-metallic U-shaped pentamer consisting of gold and platinum particles *via* successive assembly steps (scale bar: 100 nm). (a) Adapted with permission.[133] Copyright 2013, Springer Nature. (b) Adapted with permission.[35] Copyright 2016, Springer Nature. (c) Adapted with permission.[99] Copyright 2013, American Chemical Society. (d–e) Adapted with permission.[101] Copyright 2018, Royal Society of Chemistry.

cussed here. One of the most basic concepts is coupling a single plasmonic nanoparticle with a surface, either a dielectric surface to induce symmetry breaking,[47,134] or a metal film to induce plasmon coupling with the induced image charges.[135–137] Nanoparticles can be deposited on substrates through many common techniques, such as drop-casting,[138] spin coating,[125,135] and Langmuir-Schaefer techniques.[104,139] Hybridized plasmon modes,[47] magnetic resonances,[140] and high sensitivity can results from the formation of plasmonic cavities.[140,141] A key feature of such systems is the high sensitivity and tunability of the plasmonic response by varying the distance between the nanoparticle and substrate. One of the most common structures is the coupling of a nanocube to a substrate (**Figures III.8 IIa & III.10a**),[133] which does not require fabrication of lateral features in the templates. The quality and smoothness of the substrate are important, however, for reproducible coupling, and the dielectric spacer can be exploited to introduce responsiveness to external triggers.[109–111,142] An recent example is the tuning of the distance between a gold nanoparticle and gold mirror by a thermoresponsive PNIPAm shell.[109]

(IIb) Plasmonic metasurfaces from finite colloidal assemblies

Moving beyond substrate effects, interparticle coupling also has an important role in the formation of plasmonic metasurfaces (**Figure III.8 III & IV**). Thereby, the template provides steric hindrance for selective linking reactions resulting in anisotropic and more selective coupling scenarios. For example, plasmonic necklaces and dimer formations are feasible, as shown by Bach *et al.* and Yoon *et al.*, respectively.[143,144]

Capillarity-assisted particle assembly (CAPA) is a technique that provides precise positional ordering of the building blocks, even for complex designs.[99,145,146] The required topographic template imposes limits on the design, resolution, and the scalability of CAPA. Electron beam

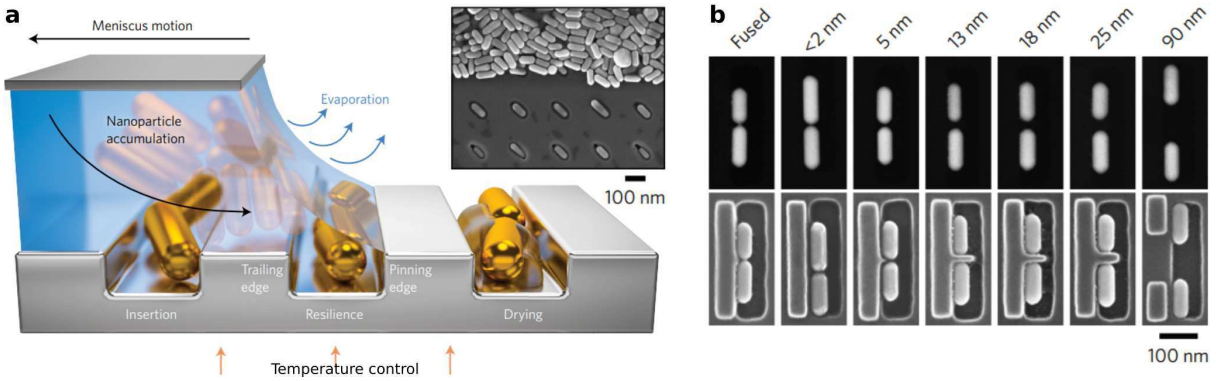

Figure III.11.: Capillarity-assisted particle assembly (CAPA). (a) Assembly is triggered by pulling a colloidal dispersion over a topographic template. Nanoparticle accumulation is triggered by the evaporation process, resulting in nearly complete filling with nanorods. (inset) Assembled nanorods and freeze-dried meniscus shows the high particle concentration in the accumulation zone. (b) Electron beam lithography proves highly precise manufacturing of dimers. Adapted with permission.[35] Copyright 2016, Springer Nature.

lithography is the predominant substrate fabrication method for CAPA because of its high precision and well established protocols.[35] Self-assembly is triggered by pulling a meniscus of the colloidal dispersion droplet by a doctor-blade-like setup across the template (see **Figure III.11a**). Nanoparticles are concentrated in the accumulation zone of the meniscus *via* convective flow. The concentration in the accumulation zone is controlled by the rate of evaporation of the meniscus front. The topographic features of the template define minima of the free energy and selectively trap the particles.[101,147] For CAPA the choice of stabilizing ligand is largely irrelevant, since trapping is triggered by capillary forces. Controlling the contact-angle of the moving meniscus, however, is critically important for directing capillary forces, while maintaining colloidal stability in the accumulation zone. The contact angle can be set by adding surfactants, which are typically also used as stabilizing ligands or need to be compatible with the ligands already on the nanoparticles.[101] CtaB—also in combination with co-surfactants—is sufficient for stabilizing the colloids.[148] Tuning the forces by controlling the contact angle and trap geometry allows trapping of single nanoparticles and successive assembly (sCAPA) of different types of nanoparticles, giving rise to complex multimetallic plasmonic clusters, shown by Ni *et al.*[101] Such multimetallic clusters hold great potential for several applications, such as charge and information transfer processes.[149] Selected examples of (s)CAPA are shown in **Figure III.10b–f**, and many more details about this method can be found the recent review article by Wolf and coworkers:[148] (b) simple dimeric nanorod antennas with tunable distance,[35] (c) corner-connected nanocubes,[35] (d) circular heptamers,[99] and (e) multimetallic U-shaped assemblies.[101]

(III) Regularly spaced nanoparticle chains

Plasmonic polymers are closely related to smaller clusters of plasmon-coupled nanoparticles. The transition between those two types of nanoparticle clusters is rather smooth (**Figure III.8**). To define this term more precisely, the definition of polymers by International Union of Pure and Applied Chemistry (IUPAC) is employed: A molecule can be regarded as polymer "(...) if the addition or removal of one or a few of repeat units has a negligible effect on the molecular properties."[150] By analogy, plasmonic polymers are defined by the sensitivity of their opti-

cal properties to the number of constituting nanoparticles. If the dominating plasmonic resonance (the super-radiant mode) does not change upon addition (or removal) of one or a few nanoparticles to the chain, such a linear colloidal cluster is a plasmonic polymer.[91] The critical number, above which a particle chain is a plasmonic polymer, is commonly referred to the *infinite chain limit*.[91] For linear chain-like plasmonic polymers, this threshold of repeat units is typically reached within 8–10 particles.[90,151] Below the *infinite chain limit*, (linear) clusters are referred to plasmonic oligomers.[100] The nature of the plasmonic modes in a linear assembly can be considered in analogy to the particle-in-a-box model from quantum mechanics. In this model, the end of the chain defines the potential barrier, and the plasmonic chain modes correspond to the energy eigenstates.[86] Results from classical electromagnetic simulations using coupled-dipole approximation methods can be used to get a qualitative understanding of these modes.[152] Quantitative results can be obtained from FDTD modeling or the efficient boundary element method (BEM).[54,55] An important feature of these complex nanoparticle assemblies is the high field enhancement in hot spots, the gaps between nanoparticles, and their anisotropic optical response, shown in **Figure III.12d–e** for chains composed of spherical and rod-shaped nanoparticles.[84,88] Linear plasmonic polymers are especially interesting for sub-wavelength information transport and light harvesting applications.[86] Controlling the degree of coupling between individual nanoparticles requires a precisely defined spacer material. The ligands used as spacers serve several functions simultaneously, because they provide colloidal stability in solution and during the self-assembly process, and they also keep the nanoparticles separated with controlled gaps after assembly.

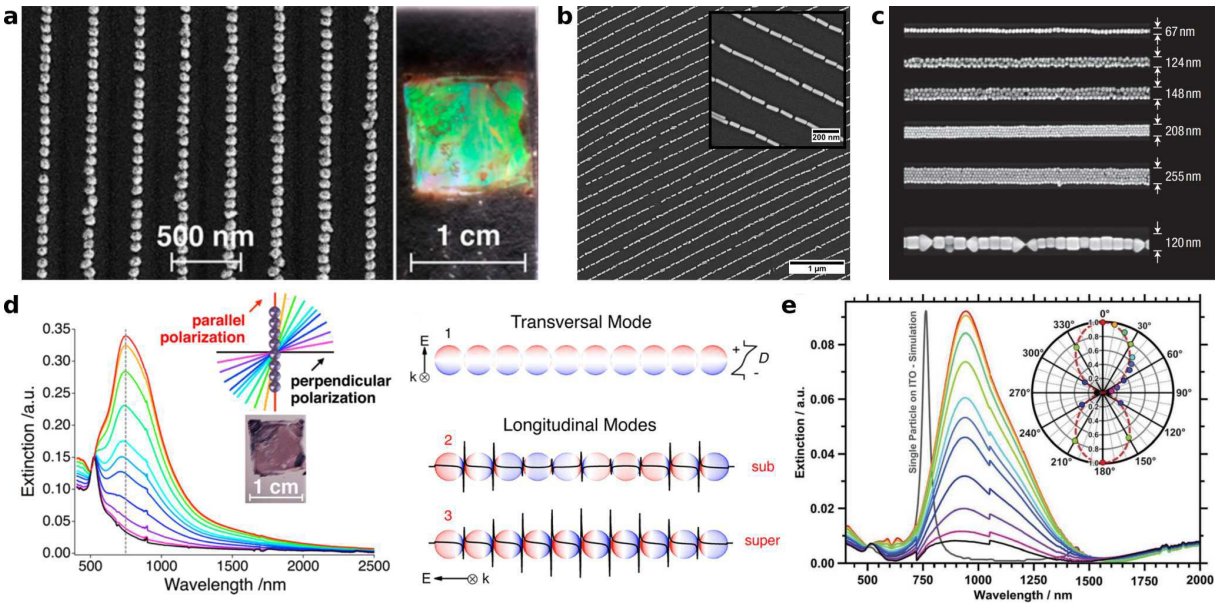

Figure III.12.: Structure and optical properties of plasmonic polymers. (a) Periodic single particle lines from spin coating and (b) periodic nanorod lines from dip coating using wrinkled PDMS substrates as templates. (c) Particle lines of varying thickness and morphologies by CAPA. (d) Optical response and respective plasmonic modes of a linear quasi-infinite line of nanoparticles, as shown in (a), for different polarization angles. (e) Optical response of linearly aligned gold nanorods as shown in (b). (a,d) Adapted with permission.[84] Copyright 2014, American Chemical Society. (b,e) Adapted under the terms of CC-BY license.[82] Copyright 2015, Royal Society of Chemistry. (c) Adapted with permission.[97] Copyright 2007, Springer Nature.

Many methods are available and commonly used for depositing dispersions onto templates with chemical or topographical features such that the template will guide the self-assembly process. The last part of this section is focused on techniques using templates to guide the formation of plasmonic polymers. Templates are important for providing positional and orientation control of nanoparticles and for directing the shape of the clusters into lines. Thus, the methods for assembling long linear chains of nanoparticles can be sorted from those that are highly scalable to those that provide the best positional control and allow assembly of the most complex geometries.

Spray coating is one of the most scalable and simplest methods for particle assembly and can be combined with templates to fabricate plasmonic polymers. The colloidal dispersion is sprayed onto the template and the colloids are assembled by chemical trapping or directed topographically.[153] Spraying with grazing incidence allows large-area fabrication of monolayers with optical anisotropy.[117,154]

In drop casting, the colloidal dispersion is placed onto the template, confinement in the template provides the external trigger during the drying process for the assembly. The templates can have chemical binding sides and/or topographic traps.[90,155] The control and reproducibility of drop-casting is limited, since the assembly process during drying is typically dictated by the uncontrolled laboratory environment.

Spin coating, however, provides greater control over the drying rate and the amount of material deposited through setting the acceleration and rotational velocity. Highly regular and perfectly linear arrays of plasmonic polymers can be fabricated using centimeter-squared templates, as shown in **Figure III.12a**.[84] Macroscopic wrinkled templates provide the required topography and do not limit the scalability of the assembly method, thus enabling conventional optical characterization of strong plasmonic effects.[84,88] Interparticle distances are similarly tuned *via* the spacer material.[100] PNIPAm and protein coatings, depending on the targeted interparticle spacing, have proven suitable for self-assembly through spin coating, because they impart high colloidal stability and can be used in the absence additional surfactants.[84,87,156] Spin coating lacks orientational control of anisotropic nanoparticles, but dip coating is a closely related method that can give control over the orientation of nanoparticles.[157] The system, which will be investigated in **Section V.2**, relies on this assembly method.

In dip coating, the directed movement of the drying front allows orientation of anisotropic particles into the grooves of the templates by capillary forces, as shown for gold nanorods in **Figure III.12b**.[88,136] **Section V.1** uses this assembly method to fabricate linear nanorod assemblies on a gold substrate.

As mentioned above, CAPA provides the most controlled assembly of plasmonic polymers. The well-controlled movement of the meniscus directs the colloids into the traps in the template. Consequently, a wide range of nanoparticle morphologies, nanoparticle sizes, and various materials of the dielectric shell are feasible to be assembled by CAPA. This is shown by Kraus *et al.* in **Figure III.12c** for different sizes and for spherical as well as for cubic particles.[36,97] CAPA, however, relies on traps with exact and perfectly-matching geometry. Thus far, this demand is only fulfilled by lithographic methods like electron beam lithography, which typically lack cost-efficient scalability.

(IV) Plasmonic two-dimensional ordered arrays

For the sake of completeness, collective coupling of a two-dimensional colloidal lattice can be achieved by long-range interactions between unit cells with domain sizes larger than the diffraction limit (*i.e.*, several micrometers).[158]

As a rule of thumb, coupling occur between two gold nanoparticles when their separation is less than 2.5 times their diameter (or 5 times the diameter for silver nanoparticles).[159] If the interparticle distances are too large to give plasmon coupling the plasmon resonance (broad band) can still couple to the first order Bragg diffraction resonance (narrow band), resulting in a surface lattice Fano resonance, as shown in **Figure III.13**.[160] The wavelength location of the first Bragg mode (D_{01}) is proportional to the lattice constant a and the refractive index n of the surrounding media ($D_{01} \propto n \times a$),[158] which results in tunability of the surface lattice resonance by changing the periodicity. Recently, Gérard *et al.* identified the resulting hybridized lattice modes as delocalized "photonic-like" (energetically lower resonance) and localized "plasmonic-like" (energetically higher resonance) modes.[161] The tunability of surface lattice resonances makes them attractive for structural color[72] or for strong coupling in lasing applications.[162,163]

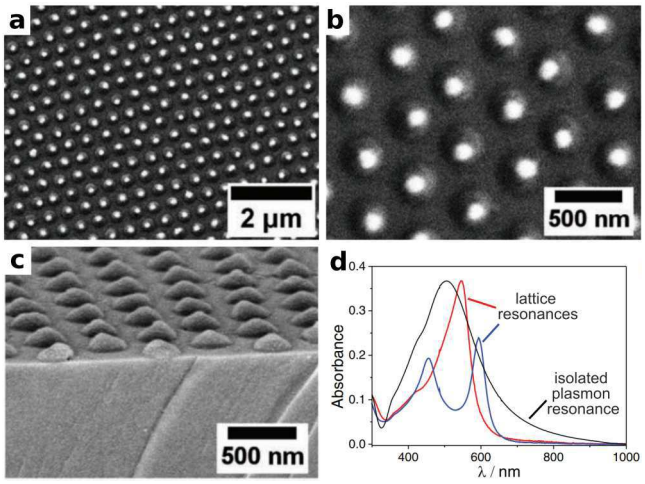

Figure III.13.: 2D lattices of plasmonic colloids supporting surface lattice resonances. (a–c) SEM images of close-packed silver particles using PNIPAm as spacer material. (d) Extinction spectra of isolated particles (black line), a close-packed nanoparticle film (red line) and index-matched close-packed particle film supporting a Fano resonance (blue line) due to the coupling of the Bragg lattice with the plasmon resonance. Adopted with permission.[160] Copyright 2017, Wiley-VCH.

Thus, the lattice constant needs to cause first-order Bragg diffraction that energetically match the plasmon of the colloids for effective coupling. Therefore, the design relies on the precise packing of the self-assembled plasmonic building blocks into a plasmonic crystal. The experimental lattice constant is commonly defined by the thickness of the dielectric shell. Periodic nanoparticle monolayers can be prepared by spin coating, dip coating or transfer of floating layers of nanoparticles from the liquid-air interface, *e.g.*, *via* Langmuir-Blodgett or related systems.[104,160] These techniques result in close-packed lattices as shown in **Figure III.13a–c**. For example, PVP and polystyrene (PS) support short interparticle distances, and for larger distances, PNIPAm has shown to be sufficiently surface-active due to its hydrophobicity for forming closed-packed plasmonic crystals when floating at the water-air interface.[104,164–166]

System integration *via* subsequent transfer

For many potential applications of functional plasmonic metasurfaces, integrating nanoparticle assemblies with other materials or systems is crucial. Two strategies are showing the greatest feasibility thus far, depending on the assembly method and the desired complexity. Either the template for self-assembly serves as the final substrate, or the self-assembled unit cells need to be transferred onto another "target" structure. As a general rule for transfer processes, the target substrate needs to be "stickier" than the template.[156] This stickiness can be realized under wet and dry μ-contact printing conditions and can be practically achieved through various approaches, including hydrophilic-hydrophobic interactions,[167] selective phys- or chemisorption of the dielectric spacer itself, addition of an adhesive promoter (*e.g.*, polyethylenimine; PEI),[84,88,97,168,169] or transfer into a polymer heated above its glass-transition temperature (*e.g.*, poly(methyl)methacrylate, PMMA).[36]

Acknowledgements This project was financially supported by the Volkswagen Foundation through a Freigeist Fellowship to TAFK. The authors acknowledge the Deutsche Forschungsgemeinschaft (DFG) within the Cluster of Excellence 'Center for Advancing Electronics Dresden' (cfaed) for financial support. We thank Joseph B. Tracy from the North Carolina State University, Charlene Ng, and Yannic Brasse for valuable discussion of the manuscript.

References

[1] S. J. Tan, L. Zhang, D. Zhu, X. M. Goh, Y. M. Wang, K. Kumar, C.-W. Qiu, J. K. W. Yang, "Plasmonic Color Palettes for Photorealistic Printing with Aluminum Nanostructures", *Nano Letters* **2014**, *14*, 4023–4029.

[2] M. Karg, T. A. König, M. Retsch, C. Stelling, P. M. Reichstein, T. Honold, M. Thelakkat, A. Fery, "Colloidal self-assembly concepts for light management in photovoltaics", *Materials Today* **2015**, *18*, 185–205.

[3] J. A. Schuller, E. S. Barnard, W. Cai, Y. C. Jun, J. S. White, M. L. Brongersma, "Plasmonics for extreme light concentration and manipulation", *Nature Materials* **2010**, *9*, 193–204.

[4] X. Huang, I. H. El-Sayed, W. Qian, M. A. El-Sayed, "Cancer Cell Imaging and Photothermal Therapy in the Near-Infrared Region by Using Gold Nanorods", *Journal of the American Chemical Society* **2006**, *128*, 2115–2120.

[5] K. M. Mayer, J. H. Hafner, "Localized Surface Plasmon Resonance Sensors", *Chemical Reviews* **2011**, *111*, 3828–3857.

[6] J. M. Romo-Herrera, R. A. Alvarez-Puebla, L. M. Liz-Marzán, "Controlled assembly of plasmonic colloidal nanoparticle clusters", *Nanoscale* **2011**, *3*, 1304.

[7] P. Nordlander, C. Oubre, E. Prodan, K. Li, M. I. Stockman, "Plasmon Hybridization in Nanoparticle Dimers", *Nano Letters* **2004**, *4*, 899–903.

[8] P. K. Jain, W. Huang, M. A. El-Sayed, "On the Universal Scaling Behavior of the Distance Decay of Plasmon Coupling in Metal Nanoparticle Pairs: A Plasmon Ruler Equation", *Nano Letters* **2007**, *7*, 2080–2088.

[9] R. Kodiyath, S. T. Malak, Z. A. Combs, T. Koenig, M. A. Mahmoud, M. A. El-Sayed, V. V. Tsukruk, "Assemblies of silver nanocubes for highly sensitive SERS chemical vapor detection", *Journal of Materials Chemistry A* **2013**, *1*, 2777.

[10] G. Veronis, S. Fan in *Surface Plasmon Nanophotonics*, *Vol. 131*, (Eds.: M. L. Brongersma, P. G. Kik), Springer Netherlands, Dordrecht, **2007**, pp. 169–182.

[11] P. B. Johnson, R. W. Christy, "Optical Constants of the Noble Metals", *Physical Review B* **1972**, *6*, 4370–4379.

[12] H.-J. Hagemann, W. Gudat, C. Kunz, "Optical constants from the far infrared to the x-ray region: Mg, Al, Cu, Ag, Au, Bi, C, and Al_2O_3", *Journal of the Optical Society of America* **1975**, *65*, 742.

[13] H. Raether in *Surface Plasmons on Smooth and Rough Surfaces and on Gratings*, *Vol. 111*, Springer Berlin Heidelberg, Berlin, Heidelberg, **1988**, pp. 4–39.

[14] S. Link, M. A. El-Sayed, "Spectral Properties and Relaxation Dynamics of Surface Plasmon Electronic Oscillations in Gold and Silver Nanodots and Nanorods", *The Journal of Physical Chemistry B* **1999**, *103*, 8410–8426.

[15] G. Mie, "Beiträge zur Optik trüber Medien, speziell kolloidaler Metallösungen", *Annalen der Physik* **1908**, *330*, 377–445.

[16] J. B. Khurgin, "How to deal with the loss in plasmonics and metamaterials", *Nature Nanotechnology* **2015**, *10*, 2 EP.

[17] A. Trügler, *Optical Properties of Metallic Nanoparticles*, Springer International Publishing, **2016**.

[18] K. A. Willets, R. P. Van Duyne, "Localized Surface Plasmon Resonance Spectroscopy and Sensing", *Annual Review of Physical Chemistry* **2007**, *58*, 267–297.

[19] N. J. Halas, S. Lal, W.-S. Chang, S. Link, P. Nordlander, "Plasmons in Strongly Coupled Metallic Nanostructures", *Chemical Reviews* **2011**, *111*, 3913–3961.

[20] M. Rycenga, C. M. Cobley, J. Zeng, W. Li, C. H. Moran, Q. Zhang, D. Qin, Y. Xia, "Controlling the Synthesis and Assembly of Silver Nanostructures for Plasmonic Applications", *Chemical Reviews* **2011**, *111*, 3669–3712.

[21] J. J. Mock, D. R. Smith, S. Schultz, "Local Refractive Index Dependence of Plasmon Resonance Spectra from Individual Nanoparticles", *Nano Letters* **2003**, *3*, 485–491.

[22] M. J. Schnepf, M. Mayer, C. Kuttner, M. Tebbe, D. Wolf, M. Dulle, T. Altantzis, P. Formanek, S. Förster, S. Bals, T. A. F. König, A. Fery, "Nanorattles with tailored electric field enhancement", *Nanoscale* **2017**, *9*, 9376–9385.

[23] E. Galati, M. Tebbe, A. Querejeta-Fernández, H. L. Xin, O. Gang, E. B. Zhulina, E. Kumacheva, "Shape-Specific Patterning of Polymer-Functionalized Nanoparticles", *ACS Nano* **2017**, *11*, 4995–5002.

[24] V. Myroshnychenko, J. Rodríguez-Fernández, I. Pastoriza-Santos, A. M. Funston, C. Novo, P. Mulvaney, L. M. Liz-Marzán, F. J. García de Abajo, "Modelling the optical response of gold nanoparticles", *Chemical Society Reviews* **2008**, *37*, 1792.

[25] N. G. Bastús, J. Comenge, V. Puntes, "Kinetically Controlled Seeded Growth Synthesis of Citrate-Stabilized Gold Nanoparticles of up to 200 nm: Size Focusing versus Ostwald Ripening", *Langmuir* **2011**, *27*, 11098–11105.

[26] J. Turkevich, P. C. Stevenson, J. Hillier, "A Study of the Nucleation and Growth Processes in the Synthesis of Colloidal Gold", *Discussions of the Faraday Society* **1951**, *11*, 55–&.

[27] G. González-Rubio, P. Díaz-Núñez, A. Rivera, A. Prada, G. Tardajos, J. González-Izquierdo, L. Bañares, P. Llombart, L. G. Macdowell, M. Alcolea Palafox, L. M. Liz-Marzán, O. Peña-Rodríguez, A. Guerrero-Martínez, "Femtosecond laser reshaping yields gold nanorods with ultranarrow surface plasmon resonances", *Science* **2017**, *358*, 640–644.

[28] S. J. Tan, M. J. Campolongo, D. Luo, W. Cheng, "Building plasmonic nanostructures with DNA", *Nature Nanotechnology* **2011**, *6*, 268–276.

[29] N. R. Jana, L. Gearheart, C. J. Murphy, "Seeding Growth for Size Control of 5−40 nm Diameter Gold Nanoparticles", *Langmuir* **2001**, *17*, 6782–6786.

[30] G. González-Rubio, T. M. de Oliveira, T. Altantzis, A. La Porta, A. Guerrero-Martínez, S. Bals, L. Scarabelli, L. M. Liz-Marzán, "Disentangling the effect of seed size and crystal habit on gold nanoparticle seeded growth", *Chemical Communications* **2017**, *53*, 11360–11363.

[31] Y. Zheng, X. Zhong, Z. Li, Y. Xia, “Successive, Seed-Mediated Growth for the Synthesis of Single-Crystal Gold Nanospheres with Uniform Diameters Controlled in the Range of 5-150 nm”, *Particle & Particle Systems Characterization* **2014**, *31*, 266–273.

[32] N. R. Jana, “Nanorod shape separation using surfactant assisted self-assembly”, *Chemical Communications* **2003**, 1950.

[33] K. Park, H. Koerner, R. A. Vaia, “Depletion-Induced Shape and Size Selection of Gold Nanoparticles”, *Nano Letters* **2010**, *10*, 1433–1439.

[34] L. Scarabelli, M. Coronado-Puchau, J. J. Giner-Casares, J. Langer, L. M. Liz-Marzán, “Monodisperse Gold Nanotriangles: Size Control, Large-Scale Self-Assembly, and Performance in Surface-Enhanced Raman Scattering”, *ACS Nano* **2014**, *8*, 5833–5842.

[35] V. Flauraud, M. Mastrangeli, G. D. Bernasconi, J. Butet, D. T. L. Alexander, E. Shahrabi, O. J. F. Martin, J. Brugger, “Nanoscale topographical control of capillary assembly of nanoparticles”, *Nature Nanotechnology* **2016**, *12*, 73–80.

[36] A. Rey, G. Billardon, E. Lörtscher, K. Moth-Poulsen, N. Stuhr-Hansen, H. Wolf, T. Bjørnholm, A. Stemmer, H. Riel, “Deterministic assembly of linear gold nanorod chains as a platform for nanoscale applications”, *Nanoscale* **2013**, *5*, 8680.

[37] L. Vigderman, B. P. Khanal, E. R. Zubarev, “Functional Gold Nanorods: Synthesis, Self-Assembly, and Sensing Applications”, *Advanced Materials* **2012**, *24*, 4811–4841.

[38] L. Vigderman, E. R. Zubarev, “High-Yield Synthesis of Gold Nanorods with Longitudinal SPR Peak Greater than 1200 nm Using Hydroquinone as a Reducing Agent”, *Chemistry of Materials* **2013**, *25*, 1450–1457.

[39] Y. Xia, Y. Xiong, B. Lim, S. E. Skrabalak, “Shape-Controlled Synthesis of Metal Nanocrystals: Simple Chemistry Meets Complex Physics?”, *Angewandte Chemie International Edition* **2009**, *48*, 60–103.

[40] S. E. Lohse, N. D. Burrows, L. Scarabelli, L. M. Liz-Marzán, C. J. Murphy, “Anisotropic Noble Metal Nanocrystal Growth: The Role of Halides”, *Chemistry of Materials* **2014**, *26*, 34–43.

[41] S. Jessl, M. Tebbe, L. Guerrini, A. Fery, R. A. Alvarez-Puebla, N. Pazos-Perez, “Silver-Assisted Synthesis of Gold Nanorods: the Relation between Silver Additive and Iodide Impurities”, *Small* **2018**, 1703879.

[42] L. Scarabelli, A. Sánchez-Iglesias, J. Pérez-Juste, L. M. Liz-Marzán, “A “Tips and Tricks” Practical Guide to the Synthesis of Gold Nanorods”, *The Journal of Physical Chemistry Letters* **2015**, *6*, 4270–4279.

[43] M. Tebbe, C. Kuttner, M. Mayer, M. Maennel, N. Pazos-Perez, T. A. König, A. Fery, “Silver-Overgrowth-Induced Changes in Intrinsic Optical Properties of Gold Nanorods: From Noninvasive Monitoring of Growth Kinetics to Tailoring Internal Mirror Charges”, *The Journal of Physical Chemistry C* **2015**, *119*, 9513–9523.

[44] J. Zeng, Y. Zheng, M. Rycenga, J. Tao, Z.-Y. Li, Q. Zhang, Y. Zhu, Y. Xia, “Controlling the Shapes of Silver Nanocrystals with Different Capping Agents”, *Journal of the American Chemical Society* **2010**, *132*, 8552–8553.

[45] S. Gómez-Graña, B. Goris, T. Altantzis, C. Fernández-López, E. Carbó-Argibay, A. Guerrero-Martínez, N. Almora-Barrios, N. López, I. Pastoriza-Santos, J. Pérez-Juste, S. Bals, G. Van Tendeloo, L. M. Liz-Marzán, "Au@Ag Nanoparticles: Halides Stabilize 100 Facets", *The Journal of Physical Chemistry Letters* **2013**, *4*, 2209–2216.

[46] Q. Zhang, W. Li, C. Moran, J. Zeng, J. Chen, L.-P. Wen, Y. Xia, "Seed-Mediated Synthesis of Ag Nanocubes with Controllable Edge Lengths in the Range of 30−200 nm and Comparison of Their Optical Properties", *Journal of the American Chemical Society* **2010**, *132*, 11372–11378.

[47] S. Zhang, K. Bao, N. J. Halas, H. Xu, P. Nordlander, "Substrate-Induced Fano Resonances of a Plasmonic Nanocube: A Route to Increased-Sensitivity Localized Surface Plasmon Resonance Sensors Revealed", *Nano Letters* **2011**, *11*, 1657–1663.

[48] Z. Chen, J. W. Chang, C. Balasanthiran, S. T. Milner, R. M. Rioux, "Anisotropic Growth of Silver Nanoparticles Is Kinetically Controlled by Polyvinylpyrrolidone Binding", *Journal of the American Chemical Society*, null.

[49] T. A. F. König, P. A. Ledin, J. Kerszulis, M. A. Mahmoud, M. A. El-Sayed, J. R. Reynolds, V. V. Tsukruk, "Electrically Tunable Plasmonic Behavior of Nanocube-Polymer Nanomaterials Induced by a Redox-Active Electrochromic Polymer", *ACS Nano* **2014**, *8*, 6182–6192.

[50] Z. Chen, T. Balankura, K. A. Fichthorn, R. M. Rioux, "Revisiting the Polyol Synthesis of Silver Nanostructures: Role of Chloride in Nanocube Formation", *ACS Nano* **2019**, *13*, 1849–1860.

[51] C. Mätzler, "MATLAB functions for Mie scattering and absorption", **2002**.

[52] Y.-l. Xu, B. Å. Gustafson, "A generalized multiparticle Mie-solution: further experimental verification", *Journal of Quantitative Spectroscopy and Radiative Transfer* **2001**, *70*, Light Scattering by Non-Spherical Particles, 395–419.

[53] Lumerical Inc., CA, **2018**, `http://www.lumerical.com/tcad-products/fdtd/` (visited on 11/06/2018).

[54] F. J. García de Abajo, A. Howie, "Retarded field calculation of electron energy loss in inhomogeneous dielectrics", *Physical Review B* **2002**, *65*, DOI `10.1103/PhysRevB.65.115418`.

[55] U. Hohenester, "Simulating electron energy loss spectroscopy with the MNPBEM toolbox", *Computer Physics Communications* **2014**, *185*, 1177–1187.

[56] B. T. Draine, P. J. Flatau, "Discrete-Dipole Approximation For Scattering Calculations", *Journal of the Optical Society of America A* **1994**, *11*, 1491–1499.

[57] R. Yu, L. M. Liz-Marzan, F. J. Garcia de Abajo, "Universal analytical modeling of plasmonic nanoparticles", *Chemical Society Reviews* **2017**, *46*, 6710–6724.

[58] M. W. Knight, N. S. King, L. Liu, H. O. Everitt, P. Nordlander, N. J. Halas, "Aluminum for Plasmonics", *ACS Nano* **2014**, *8*, 834–840.

[59] S. Lu, H. Yu, S. Gottheim, H. Gao, C. J. DeSantis, B. D. Clark, J. Yang, C. R. Jacobson, Z. Lu, P. Nordlander, N. J. Halas, K. Liu, "Polymer-Directed Growth of Plasmonic Aluminum Nanocrystals", *Journal of the American Chemical Society* **2018**, *140*, 15412–15418.

[60] C. J. DeSantis, M. J. McClain, N. J. Halas, "Walking the Walk: A Giant Step toward Sustainable Plasmonics", *ACS Nano* **2016**, *10*, 9772–9775.

[61] F. Wang, Y. R. Shen, "General Properties of Local Plasmons in Metal Nanostructures", *Physical Review Letters* **2006**, *97*, DOI 10.1103/PhysRevLett.97.206806.

[62] N. Liu, H. Giessen, "Coupling Effects in Optical Metamaterials", *Angewandte Chemie International Edition* **2010**, *49*, 9838–9852.

[63] S. Zhou, J. Li, K. D. Gilroy, J. Tao, C. Zhu, X. Yang, X. Sun, Y. Xia, "Facile Synthesis of Silver Nanocubes with Sharp Corners and Edges in an Aqueous Solution", *ACS Nano* **2016**, *10*, 9861–9870.

[64] M. Mayer, L. Scarabelli, K. March, T. Altantzis, M. Tebbe, M. Kociak, S. Bals, F. J. García de Abajo, A. Fery, L. M. Liz-Marzán, "Controlled Living Nanowire Growth: Precise Control over the Morphology and Optical Properties of AgAuAg Bimetallic Nanowires", *Nano Letters* **2015**, *15*, 5427–5437.

[65] X. Zhuo, X. Zhu, Q. Li, Z. Yang, J. Wang, "Gold Nanobipyramid-Directed Growth of Length-Variable Silver Nanorods with Multipolar Plasmon Resonances", *ACS Nano* **2015**, *9*, 7523–7535.

[66] G. González-Rubio, T. M. de Oliveira, T. Altantzis, A. La Porta, A. Guerrero-Martínez, S. Bals, L. Scarabelli, L. M. Liz-Marzán, "Disentangling the effect of seed size and crystal habit on gold nanoparticle seeded growth", *Chemical Communications* **2017**, *53*, 11360–11363.

[67] Y. Xia, K. D. Gilroy, H.-C. Peng, X. Xia, "Seed-Mediated Growth of Colloidal Metal Nanocrystals", *Angewandte Chemie International Edition* **2017**, *56*, 60–95.

[68] K. D. Gilroy, A. Ruditskiy, H.-C. Peng, D. Qin, Y. Xia, "Bimetallic Nanocrystals: Syntheses, Properties, and Applications", *Chemical Reviews* **2016**, *116*, 10414–10472.

[69] Y. S. Joe, A. M. Satanin, C. S. Kim, "Classical analogy of Fano resonances", *Physica Scripta* **2006**, *74*, 259–266.

[70] E. Prodan, C. Radloff, N. J. Halas, P. Nordlander, "A hybridization model for the plasmon response of complex nanostructures", *Science* **2003**, *302*, 419–22.

[71] T. König, R. Kodiyath, Z. A. Combs, M. A. Mahmoud, M. A. El-Sayed, V. V. Tsukruk, "Silver Nanocube Aggregates in Cylindrical Pores for Higher Refractive Index Plasmonic Sensing", *Particle & Particle Systems Characterization* **2014**, *31*, 274–283.

[72] C. Ng, J. J. Cadusch, S. Dligatch, A. Roberts, T. J. Davis, P. Mulvaney, D. E. Gómez, "Hot Carrier Extraction with Plasmonic Broadband Absorbers", *ACS Nano* **2016**, *10*, 4704–4711.

[73] R. Chikkaraddy, B. de Nijs, F. Benz, S. J. Barrow, O. A. Scherman, E. Rosta, A. Demetriadou, P. Fox, O. Hess, J. J. Baumberg, "Single-molecule strong coupling at room temperature in plasmonic nanocavities", *Nature* **2016**, *535*, 127–130.

[74] A. Rose, T. B. Hoang, F. McGuire, J. J. Mock, C. Ciracì, D. R. Smith, M. H. Mikkelsen, "Control of Radiative Processes Using Tunable Plasmonic Nanopatch Antennas", *Nano Letters* **2014**, *14*, 4797–4802.

[75] M. J. Schnepf, Y. Brasse, F. R. Goßler, A. M. Steiner, J. Obermeier, M. Lippitz, A. Fery, T. A. König, "Single Particle Spectroscopy of Radiative Processes in Colloid-to-Film-Coupled Nanoantennas", *Zeitschrift für Physikalische Chemie* **2018**, DOI 10.1515/zpch-2018-1109.

[76] R. A. Alvarez-Puebla, A. Agarwal, P. Manna, B. P. Khanal, P. Aldeanueva-Potel, E. Carbo-Argibay, N. Pazos-Perez, L. Vigderman, E. R. Zubarev, N. A. Kotov, L. M. Liz-Marzan, "Gold nanorods 3D-supercrystals as surface enhanced Raman scattering spectroscopy substrates for the rapid detection of scrambled prions", *Proceedings of the National Academy of Sciences* **2011**, *108*, 8157–8161.

[77] S. Jaber, M. Karg, A. Morfa, P. Mulvaney, "2D assembly of gold–PNIPAM core–shell nanocrystals", *Physical Chemistry Chemical Physics* **2011**, *13*, 5576.

[78] J. A. Lopez-Sanchez, N. Dimitratos, C. Hammond, G. L. Brett, L. Kesavan, S. White, P. Miedziak, R. Tiruvalam, R. L. Jenkins, A. F. Carley, D. Knight, C. J. Kiely, G. J. Hutchings, "Facile removal of stabilizer-ligands from supported gold nanoparticles", *Nature Chemistry* **2011**, *3*, 551–556.

[79] S. Song, X. Ma, M. Pu, X. Li, K. Liu, P. Gao, Z. Zhao, Y. Wang, C. Wang, X. Luo, "Actively Tunable Structural Color Rendering with Tensile Substrate", *Advanced Optical Materials* **2017**, *5*, 1600829.

[80] J.-H. Choi, Y.-S. No, J.-P. So, J. M. Lee, K.-H. Kim, M.-S. Hwang, S.-H. Kwon, H.-G. Park, "A high-resolution strain-gauge nanolaser", *Nature Communications* **2016**, *7*, 11569.

[81] M. Mesch, T. Weiss, M. Schäferling, M. Hentschel, R. S. Hegde, H. Giessen, "Highly Sensitive Refractive Index Sensors with Plasmonic Nanoantennas−Utilization of Optimal Spectral Detuning of Fano Resonances", *ACS Sensors* **2018**, *3*, 960–966.

[82] S. Simoncelli, Y. Li, E. Cortés, S. A. Maier, "Imaging Plasmon Hybridization of Fano Resonances via Hot-Electron-Mediated Absorption Mapping", *Nano Letters* **2018**, *18*, 3400–3406.

[83] B. Luk'yanchuk, N. I. Zheludev, S. A. Maier, N. J. Halas, P. Nordlander, H. Giessen, C. T. Chong, "The Fano resonance in plasmonic nanostructures and metamaterials", *Nature Materials* **2010**, *9*, 707–715.

[84] C. Hanske, M. Tebbe, C. Kuttner, V. Bieber, V. V. Tsukruk, M. Chanana, T. A. F. König, A. Fery, "Strongly Coupled Plasmonic Modes on Macroscopic Areas via Template-Assisted Colloidal Self-Assembly", *Nano Letters* **2014**, *14*, 6863–6871.

[85] S. J. Barrow, A. M. Funston, D. E. Gómez, T. J. Davis, P. Mulvaney, "Surface Plasmon Resonances in Strongly Coupled Gold Nanosphere Chains from Monomer to Hexamer", *Nano Letters* **2011**, *11*, 4180–4187.

[86] S. J. Barrow, D. Rossouw, A. M. Funston, G. A. Botton, P. Mulvaney, “Mapping Bright and Dark Modes in Gold Nanoparticle Chains using Electron Energy Loss Spectroscopy.”, *Nano Letters* **2014**, *14*, 3799–3808.

[87] M. Mueller, M. Tebbe, D. V. Andreeva, M. Karg, R. A. Alvarez Puebla, N. Pazos Perez, A. Fery, “Large-Area Organization of pNIPAM-Coated Nanostars as SERS Platforms for Polycyclic Aromatic Hydrocarbons Sensing in Gas Phase”, *Langmuir* **2012**, *28*, 9168–9173.

[88] M. Tebbe, M. Mayer, B. A. Glatz, C. Hanske, P. T. Probst, M. B. Müller, M. Karg, M. Chanana, T. A. F. König, C. Kuttner, A. Fery, “Optically anisotropic substrates via wrinkle-assisted convective assembly of gold nanorods on macroscopic areas”, *Faraday Discussions* **2015**, *181*, 243–260.

[89] A. Klinkova, H. Thérien-Aubin, A. Ahmed, D. Nykypanchuk, R. M. Choueiri, B. Gagnon, A. Muntyanu, O. Gang, G. C. Walker, E. Kumacheva, “Structural and Optical Properties of Self-Assembled Chains of Plasmonic Nanocubes”, *Nano Letters* **2014**, *14*, 6314–6321.

[90] L. S. Slaughter, B. A. Willingham, W.-S. Chang, M. H. Chester, N. Ogden, S. Link, “Toward Plasmonic Polymers”, *Nano Letters* **2012**, *12*, 3967–3972.

[91] B. Willingham, S. Link, “Energy transport in metal nanoparticle chains via sub-radiant plasmon modes”, *Optics Express* **2011**, *19*, 6450.

[92] F. N. Gür, C. P. T. McPolin, S. Raza, M. Mayer, D. J. Roth, A. M. Steiner, M. Löffler, A. Fery, M. L. Brongerma, A. V. Zayats, T. A. F. König, T. L. Schmidt, “Self-assembled plasmonic waveguides for excitation of fluorescent nanodiamonds”, *arXiv:1712.09141 [physics]* **2017**.

[93] M. Grzelczak, J. Vermant, E. M. Furst, L. M. Liz-Marzán, “Directed Self-Assembly of Nanoparticles”, *ACS Nano* **2010**, *4*, 3591–3605.

[94] N. Gaponik, S. G. Hickey, D. Dorfs, A. L. Rogach, A. Eychmüller, “Progress in the Light Emission of Colloidal Semiconductor Nanocrystals”, *Small* **2010**, *6*, 1364–1378.

[95] A. Guerrero-Martínez, J. Pérez-Juste, E. Carbó-Argibay, G. Tardajos, L. M. Liz-Marzán, “Gemini-Surfactant-Directed Self-Assembly of Monodisperse Gold Nanorods into Standing Superlattices”, *Angewandte Chemie International Edition* **2009**, *48*, 9484–9488.

[96] T. Kraus, D. Brodoceanu, N. Pazos-Perez, A. Fery, “Colloidal Surface Assemblies: Nanotechnology Meets Bioinspiration”, *Advanced Functional Materials* **2013**, *23*, 4529–4541.

[97] T. Kraus, L. Malaquin, H. Schmid, W. Riess, N. D. Spencer, H. Wolf, “Nanoparticle printing with single-particle resolution”, *Nature Nanotechnology* **2007**, *2*, 570–576.

[98] J. Lee, J.-H. Huh, K. Kim, S. Lee, “DNA Origami-Guided Assembly of the Roundest 60-100 nm Gold Nanospheres into Plasmonic Metamolecules”, *Advanced Functional Materials* **2018**, *28*, 1707309.

[99] J. A. Fan, K. Bao, L. Sun, J. Bao, V. N. Manoharan, P. Nordlander, F. Capasso, “Plasmonic Mode Engineering with Templated Self-Assembled Nanoclusters”, *Nano Letters* **2012**, *12*, 5318–5324.

[100] A. M. Steiner, M. Mayer, M. Seuss, S. Nikolov, K. D. Harris, A. Alexeev, C. Kuttner, T. A. König, A. Fery, "Macroscopic Strain-Induced Transition from Quasi-infinite Gold Nanoparticle Chains to Defined Plasmonic Oligomers", *ACS Nano* **2017**, *11*, 8871–8880.

[101] S. Ni, H. Wolf, L. Isa, "Programmable Assembly of Hybrid Nanoclusters", *Langmuir* **2018**, *34*, 2481–2488.

[102] M. Karg, T. Hellweg, P. Mulvaney, "Self-Assembly of Tunable Nanocrystal Superlattices Using Poly-(NIPAM) Spacers", *Advanced Functional Materials* **2011**, *21*, 4668–4676.

[103] M. Tebbe, C. Kuttner, M. Männel, A. Fery, M. Chanana, "Colloidally Stable and Surfactant-Free Protein-Coated Gold Nanorods in Biological Media", *ACS Applied Materials & Interfaces* **2015**, *7*, 5984–5991.

[104] K. Volk, J. P. S. Fitzgerald, M. Retsch, M. Karg, "Time-Controlled Colloidal Superstructures: Long-Range Plasmon Resonance Coupling in Particle Monolayers", *Advanced Materials* **2015**, *27*, 7332–7337.

[105] M. Chanana, P. RiveraGil, M. A. Correa-Duarte, L. M. Liz-Marzán, W. J. Parak, "Physicochemical Properties of Protein-Coated Gold Nanoparticles in Biological Fluids and Cells before and after Proteolytic Digestion", *Angewandte Chemie International Edition* **2013**, *52*, 4179–4183.

[106] E. W. Edwards, M. Chanana, D. Wang, H. Möhwald, "Stimuli-Responsive Reversible Transport of Nanoparticles Across Water/Oil Interfaces", *Angewandte Chemie International Edition* **2008**, *47*, 320–323.

[107] J.-W. Jeon, P. A. Ledin, J. A. Geldmeier, J. F. Ponder, M. A. Mahmoud, M. El-Sayed, J. R. Reynolds, V. V. Tsukruk, "Electrically Controlled Plasmonic Behavior of Gold Nanocube@Polyaniline Nanostructures: Transparent Plasmonic Aggregates", *Chemistry of Materials* **2016**, *28*, 2868–2881.

[108] M. Karg, I. Pastoriza-Santos, J. Pérez-Juste, T. Hellweg, L. M. Liz-Marzán, "Nanorod-Coated PNIPAM Microgels: Thermoresponsive Optical Properties", *Small* **2007**, *3*, 1222–1229.

[109] S. Cormier, T. Ding, V. Turek, J. J. Baumberg, "Actuating Single Nano-Oscillators with Light", *Advanced Optical Materials* **2018**, *6*, 1701281.

[110] M. A. Noginov, G. Zhu, A. M. Belgrave, R. Bakker, V. M. Shalaev, E. E. Narimanov, S. Stout, E. Herz, T. Suteewong, U. Wiesner, "Demonstration of a spaser-based nanolaser", *Nature* **2009**, *460*, 1110–1112.

[111] B. Reiser, L. González-García, I. Kanelidis, J. H. M. Maurer, T. Kraus, "Gold nanorods with conjugated polymer ligands: sintering-free conductive inks for printed electronics", *Chemical Science* **2016**, *7*, 4190–4196.

[112] L. Malaquin, T. Kraus, H. Schmid, E. Delamarche, H. Wolf, "Controlled Particle Placement through Convective and Capillary Assembly", *Langmuir* **2007**, *23*, 11513–11521.

[113] D. Nepal, M. S. Onses, K. Park, M. Jespersen, C. J. Thode, P. F. Nealey, R. A. Vaia, "Control over Position, Orientation, and Spacing of Arrays of Gold Nanorods Using Chemically Nanopatterned Surfaces and Tailored Particle–Particle–Surface Interactions", *ACS Nano* **2012**, *6*, 5693–5701.

[114] Q. Chen, S. C. Bae, S. Granick, "Directed self-assembly of a colloidal kagome lattice", *Nature* **2011**, *469*, 381–384.

[115] G. González-Rubio, J. González-Izquierdo, L. Bañares, G. Tardajos, A. Rivera, T. Altantzis, S. Bals, O. Peña-Rodríguez, A. Guerrero-Martínez, L. M. Liz-Marzán, "Femtosecond Laser-Controlled Tip-to-Tip Assembly and Welding of Gold Nanorods", *Nano Letters* **2015**, *15*, 8282–8288.

[116] M. N. Sanz-Ortiz, K. Sentosun, S. Bals, L. M. Liz-Marzán, "Templated Growth of Surface Enhanced Raman Scattering-Active Branched Gold Nanoparticles within Radial Mesoporous Silica Shells", *ACS Nano* **2015**, *9*, 10489–10497.

[117] P. T. Probst, S. Sekar, T. A. F. König, P. Formanek, G. Decher, A. Fery, M. Pauly, "Highly Oriented Nanowire Thin Films with Anisotropic Optical Properties Driven by the Simultaneous Influence of Surface Templating and Shear Forces", *ACS Applied Materials & Interfaces* **2018**, *10*, 3046–3057.

[118] C. Hanske, G. González-Rubio, C. Hamon, P. Formentín, E. Modin, A. Chuvilin, A. Guerrero-Martínez, L. F. Marsal, L. M. Liz-Marzán, "Large-Scale Plasmonic Pyramidal Supercrystals via Templated Self-Assembly of Monodisperse Gold Nanospheres", *The Journal of Physical Chemistry C* **2017**, *121*, 10899–10906.

[119] F. N. Gür, F. W. Schwarz, J. Ye, S. Diez, T. L. Schmidt, "Toward Self-Assembled Plasmonic Devices: High-Yield Arrangement of Gold Nanoparticles on DNA Origami Templates", *ACS Nano* **2016**, *10*, 5374–5382.

[120] V. A. Turek, R. Chikkaraddy, S. Cormier, B. Stockham, T. Ding, U. F. Keyser, J. J. Baumberg, "Thermo-Responsive Actuation of a DNA Origami Flexor", *Advanced Functional Materials* **2018**, 1706410.

[121] A. P. Lane, X. Yang, M. J. Maher, G. Blachut, Y. Asano, Y. Someya, A. Mallavarapu, S. M. Sirard, C. J. Ellison, C. G. Willson, "Directed Self-Assembly and Pattern Transfer of Five Nanometer Block Copolymer Lamellae", *ACS Nano* **2017**, *11*, 7656–7665.

[122] E.-M. Park, J. Choi, B. H. Kang, K.-Y. Dong, Y. Park, I. S. Song, B.-K. Ju, "Investigation of the effects of bottom anti-reflective coating on nanoscale patterns by laser interference lithography", *Thin Solid Films* **2011**, *519*, 4220–4224.

[123] J. Deng, C. Zhao, J. P. Spatz, Q. Wei, "Nanopatterned Adhesive, Stretchable Hydrogel to Control Ligand Spacing and Regulate Cell Spreading and Migration", *ACS Nano* **2017**, *11*, 8282–8291.

[124] J. Guasch, J. Diemer, H. Riahinezhad, S. Neubauer, H. Kessler, J. P. Spatz, "Synthesis of Binary Nanopatterns on Hydrogels for Initiating Cellular Responses", *Chemistry of Materials* **2016**, *28*, 1806–1815.

[125] M. B. Müller, C. Kuttner, T. A. F. König, V. V. Tsukruk, S. Förster, M. Karg, A. Fery, "Plasmonic Library Based on Substrate-Supported Gradiential Plasmonic Arrays", *ACS Nano* **2014**, *8*, 9410–9421.

[126] M. Pretzl, A. Schweikart, C. Hanske, A. Chiche, U. Zettl, A. Horn, A. Böker, A. Fery, "A Lithography-Free Pathway for Chemical Microstructuring of Macromolecules from Aqueous Solution Based on Wrinkling", *Langmuir* **2008**, *24*, 12748–12753.

[127] Z. Liu, T. Chang, H. Huang, T. He, "Gold nanoparticle arrays assembled on the reconstructed surface of block copolymer thin films", *RSC Advances* **2013**, *3*, 20464.

[128] S. Sanwaria, S. Singh, A. Horechyy, P. Formanek, M. Stamm, R. Srivastava, B. Nandan, "Multifunctional core–shell polymer–inorganic hybrid nanofibers prepared via block copolymer self-assembly", *RSC Advances* **2015**, *5*, 89861–89868.

[129] S. B. Darling, "Directing the self-assembly of block copolymers", *Progress in Polymer Science* **2007**, *32*, 1152–1204.

[130] A. Schweikart, A. Fery, "Controlled wrinkling as a novel method for the fabrication of patterned surfaces", *Microchimica Acta* **2009**, *165*, 249–263.

[131] A. Schweikart, A. Horn, A. Böker, A. Fery in *Complex Macromolecular Systems I*, *Vol. 227*, (Eds.: A. H. E. Müller, H.-W. Schmidt), Springer Berlin Heidelberg, Berlin, Heidelberg, **2009**, pp. 75–99.

[132] B. A. Glatz, M. Tebbe, B. Kaoui, R. Aichele, C. Kuttner, A. E. Schedl, H.-W. Schmidt, W. Zimmermann, A. Fery, "Hierarchical line-defect patterns in wrinkled surfaces", *Soft Matter* **2015**, *11*, 3332–3339.

[133] O. Nicoletti, F. de la Peña, R. K. Leary, D. J. Holland, C. Ducati, P. A. Midgley, "Three-dimensional imaging of localized surface plasmon resonances of metal nanoparticles", *Nature* **2013**, *502*, 80–84.

[134] H. Chen, L. Shao, T. Ming, K. C. Woo, Y. C. Man, J. Wang, H.-Q. Lin, "Observation of the Fano Resonance in Gold Nanorods Supported on High-Dielectric-Constant Substrates", *ACS Nano* **2011**, *5*, 6754–6763.

[135] Y. Brasse, M. B. Müller, M. Karg, C. Kuttner, T. A. F. König, A. Fery, "Magnetic and Electric Resonances in Particle-to-Film-Coupled Functional Nanostructures", *ACS Applied Materials & Interfaces* **2018**, *10*, 3133–3141.

[136] M. Mayer, M. Tebbe, C. Kuttner, M. J. Schnepf, T. A. F. König, A. Fery, "Template-assisted colloidal self-assembly of macroscopic magnetic metasurfaces", *Faraday Discussions* **2016**, *191*, 159–176.

[137] H. Wang, K. O'Dea, L. Wang, "Selective absorption of visible light in film-coupled nanoparticles by exciting magnetic resonance", *Optics Letters* **2014**, *39*, 1457.

[138] T. B. Hoang, G. M. Akselrod, C. Argyropoulos, J. Huang, D. R. Smith, M. H. Mikkelsen, "Ultrafast spontaneous emission source using plasmonic nanoantennas", *Nature Communications* **2015**, *6*, DOI 10.1038/ncomms8788.

[139] T. A. F. König, P. A. Ledin, J. Kerszulis, M. A. Mahmoud, M. A. El-Sayed, J. R. Reynolds, V. V. Tsukruk, "Electrically Tunable Plasmonic Behavior of Nanocube–Polymer Nanomaterials Induced by a Redox-Active Electrochromic Polymer", *ACS Nano* **2014**, *8*, 6182–6192.

[140] J. B. Lassiter, F. McGuire, J. J. Mock, C. Ciracì, R. T. Hill, B. J. Wiley, A. Chilkoti, D. R. Smith, "Plasmonic Waveguide Modes of Film-Coupled Metallic Nanocubes", *Nano Letters* **2013**, *13*, 5866–5872.

[141] T. A. F. König, P. A. Ledin, M. Russell, J. A. Geldmeier, M. A. Mahmoud, M. A. El-Sayed, V. V. Tsukruk, "Silver nanocube aggregation gradient materials in search for total internal reflection with high phase sensitivity", *Nanoscale* **2015**, *7*, 5230–5239.

[142] J. Clara-Rahola, R. Contreras-Caceres, B. Sierra-Martin, A. Maldonado-Valdivia, M. Hund, A. Fery, T. Hellweg, A. Fernandez-Barbero, "Structure and plasmon coupling of gold-poly(N-isopropylacrylamide) core–shell microgel arrays with thermally controlled interparticle gap", *Colloids and Surfaces A: Physicochemical and Engineering Aspects* **2014**, *463*, 18–27.

[143] H. Cha, J. H. Yoon, S. Yoon, "Probing Quantum Plasmon Coupling Using Gold Nanoparticle Dimers with Tunable Interparticle Distances Down to the Subnanometer Range", *ACS Nano* **2014**, *8*, 8554–8563.

[144] Y. Zheng, T. Thai, P. Reineck, L. Qiu, Y. Guo, U. Bach, "DNA-Directed Self-Assembly of Core-Satellite Plasmonic Nanostructures: A Highly Sensitive and Reproducible Near-IR SERS Sensor", *Advanced Functional Materials* **2013**, *23*, 1519–1526.

[145] T. Chen, B. M. Reinhard, "Assembling Color on the Nanoscale: Multichromatic Switchable Pixels from Plasmonic Atoms and Molecules", *Advanced Materials* **2016**, *28*, 3522–3527.

[146] N. J. Greybush, I. Liberal, L. Malassis, J. M. Kikkawa, N. Engheta, C. B. Murray, C. R. Kagan, "Plasmon Resonances in Self-Assembled Two-Dimensional Au Nanocrystal Metamolecules", *ACS Nano* **2017**, *11*, 2917–2927.

[147] S. Ni, J. Leemann, H. Wolf, L. Isa, "Insights into mechanisms of capillary assembly", *Faraday Discussions* **2015**, *181*, 225–242.

[148] S. Ni, L. Isa, H. Wolf, "Capillary assembly as a tool for the heterogeneous integration of micro- and nanoscale objects", *Soft Matter* **2018**, *14*, 2978–2995.

[149] E.-M. Roller, L. V. Besteiro, C. Pupp, L. K. Khorashad, A. O. Govorov, T. Liedl, "Hotspot-mediated non-dissipative and ultrafast plasmon passage", *Nature Physics* **2017**, *13*, 761–765.

[150] In *IUPAC Compendium of Chemical Terminology*, (Eds.: M. Nič, J. Jirát, B. Košata, A. Jenkins, A. McNaught), IUPAC, Research Triagle Park, NC, **2009**.

[151] L. S. Slaughter, L.-Y. Wang, B. A. Willingham, J. M. Olson, P. Swanglap, S. Dominguez-Medina, S. Link, "Plasmonic polymers unraveled through single particle spectroscopy", *Nanoscale* **2014**, *6*, 11451–11461.

[152] W. Cai, R. Sainidou, J. Xu, A. Polman, F. J. García de Abajo, "Efficient Generation of Propagating Plasmons by Electron Beams", *Nano Letters* **2009**, *9*, 1176–1181.

[153] S. Sekar, V. Lemaire, H. Hu, G. Decher, M. Pauly, “Anisotropic optical and conductive properties of oriented 1D-nanoparticle thin films made by spray-assisted self-assembly”, *Faraday Discussions* **2016**, *191*, 373–389.

[154] H. Hu, M. Pauly, O. Felix, G. Decher, “Spray-assisted alignment of Layer-by-Layer assembled silver nanowires: a general approach for the preparation of highly anisotropic nano-composite films”, *Nanoscale* **2017**, *9*, 1307–1314.

[155] N. Pazos-Pérez, W. Ni, A. Schweikart, R. A. Alvarez-Puebla, A. Fery, L. M. Liz-Marzán, “Highly uniform SERS substrates formed by wrinkle-confined drying of gold colloids”, *Chemical Science* **2010**, *1*, 174.

[156] A. Castelli, A. Striolo, A. Roig, C. Murphy, J. Reguera, L. Liz-Marzán, A. Mueller, K. Critchley, Y. Zhou, M. Brust, A. Thill, L. Scarabelli, L. Tadiello, T. A. F. König, B. Reiser, M. A. López-Quintela, M. Buzza, A. Deák, C. Kuttner, E. Gonzalez Solveyra, L. Pasquato, D. Portehault, H. Mattoussi, N. A. Kotov, E. Kumacheva, K. Heatley, J. Bergueiro, G. González, W. Tong, M. N. Tahir, B. Abécassis, O. Rojas-Carrillo, Y. Xia, M. Mayer, D. Peddis, “Anisotropic nanoparticles: general discussion”, *Faraday Discussions* **2016**, *191*, 229–254.

[157] J. Huang, A. R. Tao, S. Connor, R. He, P. Yang, “A General Method for Assembling Single Colloidal Particle Lines”, *Nano Letters* **2006**, *6*, 524–529.

[158] J. P. S. Fitzgerald, M. Karg, “Plasmon resonance coupling phenomena in self-assembled colloidal monolayers: Plasmonic coupling in self-assembled monolayers”, *physica status solidi (a)* **2017**, *214*, 1600947.

[159] S. K. Ghosh, T. Pal, “Interparticle Coupling Effect on the Surface Plasmon Resonance of Gold Nanoparticles: From Theory to Applications”, *Chemical Reviews* **2007**, *107*, 4797–4862.

[160] K. Volk, J. P. S. Fitzgerald, P. Ruckdeschel, M. Retsch, T. A. F. König, M. Karg, “Reversible Tuning of Visible Wavelength Surface Lattice Resonances in Self-Assembled Hybrid Monolayers”, *Advanced Optical Materials* **2017**, *5*, 1600971.

[161] D. Khlopin, F. Laux, W. P. Wardley, J. Martin, G. A. Wurtz, J. Plain, N. Bonod, A. V. Zayats, W. Dickson, D. Gérard, “Lattice modes and plasmonic linewidth engineering in gold and aluminum nanoparticle arrays”, *Journal of the Optical Society of America B* **2017**, *34*, 691.

[162] A. I. Väkeväinen, R. J. Moerland, H. T. Rekola, A.-P. Eskelinen, J.-P. Martikainen, D.-H. Kim, P. Törmä, “Plasmonic Surface Lattice Resonances at the Strong Coupling Regime”, *Nano Letters* **2014**, *14*, 1721–1727.

[163] W. Zhou, M. Dridi, J. Y. Suh, C. H. Kim, D. T. Co, M. R. Wasielewski, G. C. Schatz, T. W. Odom, “Lasing action in strongly coupled plasmonic nanocavity arrays”, *Nature Nanotechnology* **2013**, *8*, 506–511.

[164] J. Henzie, M. Grünwald, A. Widmer-Cooper, P. L. Geissler, P. Yang, “Self-assembly of uniform polyhedral silver nanocrystals into densest packings and exotic superlattices”, *Nature Materials* **2011**, *11*, 131–137.

[165] M. T. Perez Cardenas, C. Kong, J. He, S. Litvin, M. L. Meyerson, Z. Nie, “Immobilized Seed-Mediated Growth of Two-Dimensional Array of Metallic Nanocrystals with Asymmetric Shapes”, *ACS Nano* **2018**, *12*, 1107–1119.

[166] K. J. Si, D. Sikdar, Y. Chen, F. Eftekhari, Z. Xu, Y. Tang, W. Xiong, P. Guo, S. Zhang, Y. Lu, Q. Bao, W. Zhu, M. Premaratne, W. Cheng, “Giant Plasmene Nanosheets, Nanoribbons, and Origami”, *ACS Nano* **2014**, *8*, 11086–11093.

[167] C. Hanske, M. B. Müller, V. Bieber, M. Tebbe, S. Jessl, A. Wittemann, A. Fery, “The Role of Substrate Wettability in Nanoparticle Transfer from Wrinkled Elastomers: Fundamentals and Application toward Hierarchical Patterning”, *Langmuir* **2012**, *28*, 16745–16750.

[168] C. Kuemin, L. Nowack, L. Bozano, N. D. Spencer, H. Wolf, “Oriented Assembly of Gold Nanorods on the Single-Particle Level”, *Advanced Functional Materials* **2012**, *22*, 702–708.

[169] M. Müller, M. Karg, A. Fortini, T. Hellweg, A. Fery, “Wrinkle-assisted linear assembly of hard-core/soft-shell particles: impact of the soft shell on the local structure”, *Nanoscale* **2012**, *4*, 2491.

Chapter IV

Design of Colloidal Building Blocks

IV.1 Controlled Living Silver Growth

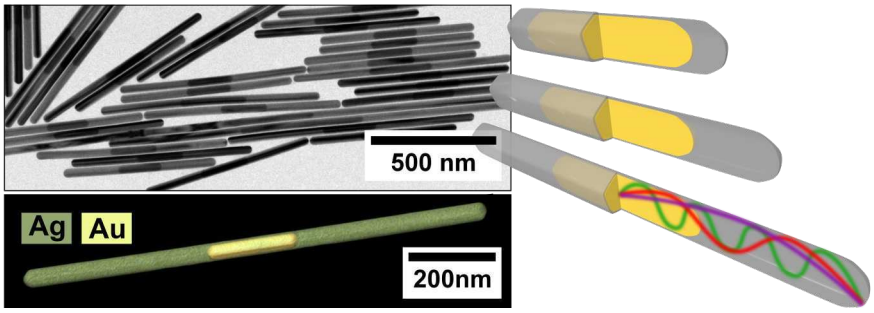

This section is based on the publication *Nano Letters* **2015**, *15*, 5427–5437. Adapted under the terms of ACS AuthorChoice license.

By Martin Mayer,[a,‡] Leonardo Scarabelli,[b,‡] Katia March,[c] Thomas Altantzis,[d] Moritz Tebbe,[a] Mathieu Kociak,[c] Sara Bals,[d] F. Javier García de Abajo,[e,f] Andreas Fery,[a] and Luis M. Liz-Marzán[b,g,*]

[a]Physical Chemistry II, University of Bayreuth, Universitätsstraße 30, 95440 Bayreuth, Germany
[b]CIC biomaGUNE, Paseo de Miramón 182, 20009 Donostia / San Sebastián, Spain
[c]Laboratoire de Physique des Solides CNRS, University Paris-Sud, Orsay 91405, France
[d]EMAT, University of Antwerp, Groenenborgerlaan 171, 2020 Antwerp, Belgium
[e]ICFO, Mediterranean Technology Park, 08860 Castelldefels, Spain
[f]ICREA, Passeig Lluís Companys 23, 08010 Barcelona, Spain
[g]Ikerbasque, Basque Foundation for Science, 48011 Bilbao, Spain
‡ contributed equally
* corresponding author

Abstract. Inspired by the concept of living polymerization reaction, silver-gold-silver nanowires are produced with precise control over their total length and plasmonic properties, by establishing a constant silver deposition rate on the tips of pentatwinned gold nanorods used as seed cores. Consequently, the length of the wires increases linearly in time. The nanowire lengths can be tune up to several microns in a highly controlled manner, corresponding to aspect ratios above 100, while the low polydispersity of the product allows to detect up to nine distinguishable plasmonic resonances in a single colloidal dispersion. Finally, the spatial distribution and the nature of the plasmons is investigated by electron energy loss spectroscopy and excellent agreement is obtained between measurements and electromagnetic simulations, clearly demonstrating that the presence of the gold core plays a marginal role, except for relatively short wires or high-energy modes.

Plasmons—the collective excitations of conduction electrons supported by metallic nanostructures—enable the confinement of electromagnetic radiation on a subwavelength nanometer scale. This phenomenon holds great potential for a vast range of applications in optics, including metamaterials design,[1–3] biosensing,[4,5] therapeutics,[6,7] solar energy harvesting,[8] and photocatalysis.[9] Alongside the continued progress in the synthesis of noble metal nanoparticles with new exotic shapes and increased monodispersity, the manufacture of bimetallic nanostructures represents an alternative strategy to enrich the library of plasmonic structures at our disposal.[10] Epitaxial seeded growth is one of the most widely used approaches for the preparation of such structures, where one or more metal precursors are reduced or co-reduced on the surface of a previously prepared core of a different metal.[11] The geometry of the obtained bimetallic system mainly depends on the lattice matching of the metal species involved,[12,13] on the seed morphology,[14] and on the growth mode on different crystallographic facets, which can be influenced by facet-specific capping agents.[15] The particular case of Au@Ag bimetallic nanoparticles has attracted much attention from the scientific community because of their complementary properties: while gold nanoparticles can be easily modulated in shape and size,[16–19] the lower optical losses of silver render a better plasmonic performance, for example in the amplification of weak optical processes such as Raman scattering,[20] fluorescence[21] and IR spectroscopy.[22] Among many other examples, Seo *et al.* reported the preparation of silver-gold-silver pentatwinned nanorods through epitaxial growth of silver on a pentatwinned gold nanorod core in an ethylene glycol solution of polyvinylpyrrolidone.[23] Recently, Li *et al.* performed the same reaction in water,[24] which was further studied by Gómez-Graña *et al.* to elucidate the growth mechanism behind the formation of the silver shell using high-resolution electron microscopy in combination with density functional theory (DFT) calculations.[19] Is important to underline that the production of high aspect ratio nanowires relies on the selective deposition of Ag on {111} tip facets, whereas a similar overgrowth reaction with gold would lead to a decrease in aspect ratio (AR), as previously reported.[25] Such elongated structures can be regarded as the plasmonic analogues of radiofrequency antennas, but with the resonance shifted into the visible-near IR (vis-NIR) range of the electromagnetic spectrum.[26] Like their radiofrequency counterparts, optical antennas are characterized by several multipolar plasmon oscillations, which can be separated into bright and dark modes, depending on their ability to couple efficiently (bright) or not (dark) to incident/scattered far-field radiation.[27,28] While the former can be exploited in the development of signal processing devices[29] and Raman/IR/fluorescence-based sensors, the latter is useful for enhanced absorption spectroscopy and photothermia.[30]
In order to efficiently engineer the near-field electromagnetic confinement and implement the application of optical antennas, it is useful to have a detailed understanding of the relationship between the antenna structure and the spatial/spectral distributions of the different plasmon modes.[31,32] In this respect, the near-field properties of pure gold and silver nanorods have been investigated by different research groups, both theoretically[28,33] and experimentally, using different imaging techniques that exploit either resonant optical illumination (*e.g.*, dark-field spectroscopy,[34,35] apertureless scanning near-field optical microscopy[36–38] (aSNOM), and photoemission electron microscopy[39,40]) or fast electrons (cathodoluminescence[41] and electron energy-loss spectroscopy[27,42–44] (EELS)). In contrast, detailed studies of the plasmon near-field behavior of Au@Ag bimetallic nanostructures have not been reported. Rodríguez-

González *et al.* studied the effect of a silver shell on the plasmonic behavior of gold nanodumbbell cores, describing a complex plasmonic scenario where the transversal mode of the core-shell system cannot be directly related to an equivalent silver nanorod.[45] To the best of our knowledge, the only available study of the plasmonic properties of silver-gold-silver nanorods is the work by Ahn *et al.* using dark-field spectroscopy, which indicated no influence of the gold core.[35] The most important prerequisites for a precise engineering of the plasmonic properties of noble metal nanoparticles are monodispersity and size tunability. As maintaining a narrow size distribution becomes more difficult when anisotropy is increased, we developed, as we report here, the concept of controlled living nanowire growth for the production of monodisperse silver-gold-silver nanowires (AgAuAgNWs), by analogy with *controlled living polymerization reactions*.[46] The general synthesis concept is summeraized in **Figure IV.1a**. Controlling the addition of silver precursors by means of a syringe pump device, we managed to achieve a linear growth rate of silver on the gold cores. This procedure allowed us to prevent the nucleation of silver nanoparticles during nanowire growth, to significantly improve the monodispersity of the product, and to accurately predict the final dimensions of the bimetallic system. As a result, AgAuAgNW colloids were obtained which display up to nine well-defined plasmon resonance peaks spreading over the entire vis-NIR wavelength range, with a tight control on the total nanowire (NW) length up to several microns, corresponding to aspect ratios above 100. Direct electron-microscopy-based visualization of the plasmon near-field spatial distributions provided essential information toward eventual optimization and rational application of this bimetallic system. We thus present here a complete optical-extinction and EELS analysis of plasmon modes supported by AgAuAgNWs, which are compared to boundary-element method (BEM) electromagnetic simulations,[47,48] allowing us to assess the influence of the central gold nanorod. We show that the presence of the gold core influences the high-energy spectral range, while it becomes progressively irrelevant in the vis-NIR region, where the spectroscopic behavior resembles that of a monometallic silver nanowire.

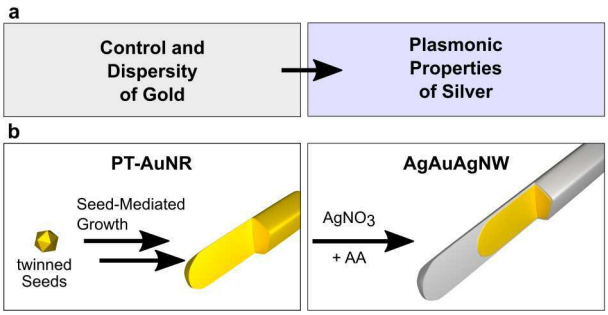

Figure IV.1.: General synthesis pathway for controlled living silver overgrowth. (a) The controlled and well-established seeding of gold as well as its stable and functional surface chemistry are merged with the strong plasmonic properties of silver. (b) Exemplarily: synthesis of pentatwinned gold AuNRs by seed-mediated growth. Followed by facet-selective silver overgrowth to form AgAuAgNWs in a living manner.

To push the quality of AgNW synthesis beyond the existing limits, any side reactions and secondary nucleation should be suppressed completely. Thus, the aims in NW synthesis are similar to those in polymer synthesis, where a small polydispersity index is desired. Consequently, we can apply the well-known concept of *controlled living polymerization reactions* (CLPR) to an one-dimensional NW growth reaction. The criteria for CLPR as defined by IUPAC standards involve

the complete suppression of termination and side reactions and a constant number of actively growing chains throughout the polymerisation.[46] Furthermore, the initiation reaction should be much faster than the propagation reaction. As a consequence, the degree of polymerization—and thus the resulting chain length—is determined only by the ratio of monomer to initiator concentrations $P_n = [M_0]/[I_0]$. In the following, we introduce the concept of controlled living nanowire growth, which allows us to synthesize bimetallic AgAuAgNWs with remarkably narrow size distributions and nanometer precision in length.

As previously described by various groups, epitaxial silver overgrowth of pentatwinned gold nanorods (PT-AuNRs) in the presence of surfactants with chloride counter-ions leads to one-dimensional growth of bimetallic AgAuAg rods/wires, as sketched in **Figure IV.1b**.[19,24,35] This can be explained by the adsorption of chloride onto the lateral {100} facets resulting in less favored silver reduction. Consequently, silver is only reduced and deposited epitaxially on the {111} facets at the NR tips, so the PT-AuNR seeds can act as bifunctional initiators bearing two initiation sites. After deposition of the very first silver monolayer the initiator becomes an active species that is subsequently overgrown in one-dimensional fashion by continuous reduction of silver ions at the metal surface during NW growth. We identify the following requirements to obtain a living controlled nanocrystal growth mechanism: (i) the initiation of crystal growth takes place simultaneously and much faster than the continuous reduction of Ag^+ ions at the metal surface of the active species; (ii) all particles have to persist as active growing species for selective deposition of Ag atoms throughout the complete experiment; and (iii) the reduction and deposition of Ag^+ must be quantitative, so that the growth of the particles is proportional to the amount of added silver precursor and a precise control over the final NW dimensions can be achieved.

(i) The first condition is met by using PT-AuNRs with a narrow size distribution as seeds, uncoupling completely nucleation and elongation. Furthermore, the *ex-situ* synthesis of the PT initiator guarantees a homogeneous and simultaneous initiation at both ends upon addition of silver precursor. Consequently, the preparation of high quality PT-AuNR seeds is of primary importance toward a precise growth of monodisperse AgAuAgNWs. PT-AuNRs with average length of 210 ± 10 nm and width of 34 ± 1 nm were prepared as previously described by Pérez-Juste *et al.*, with minor modifications (see Experimental Section).[49]

Since the presence of byproducts (nanoparticles with different shapes) ultimately limits the use of PT-AuNRs as seeds for silver overgrowth, a purification step was required to separate nanorods from other nanoparticles. Shape-dependent separation can be achieved by exploiting depletion interaction forces.[50–52] A depletion force is an effective attractive force that arises between large colloidal particles that are suspended in a dilute solution of depletants, which are smaller solutes that are preferentially excluded from the vicinity of the large particles. In our case the depletants are hexadecyltrimethylammonium chloride (CtaC) micelles and the depletion potential can be modulated according to the following equation:

$$|U| = \frac{2 r_m A \, N_A (C - C_{CMC})}{n} k_B T \qquad \text{(IV.1)}$$

where r_m, C_{CMC}, C and n are respectively the radius, the critical micellar concentration (CMC), the analytical concentration and the aggregation number of the selected surfactant, N_A is the Avogadro constant, and A is the area of interaction between two adjacent particles. The choice

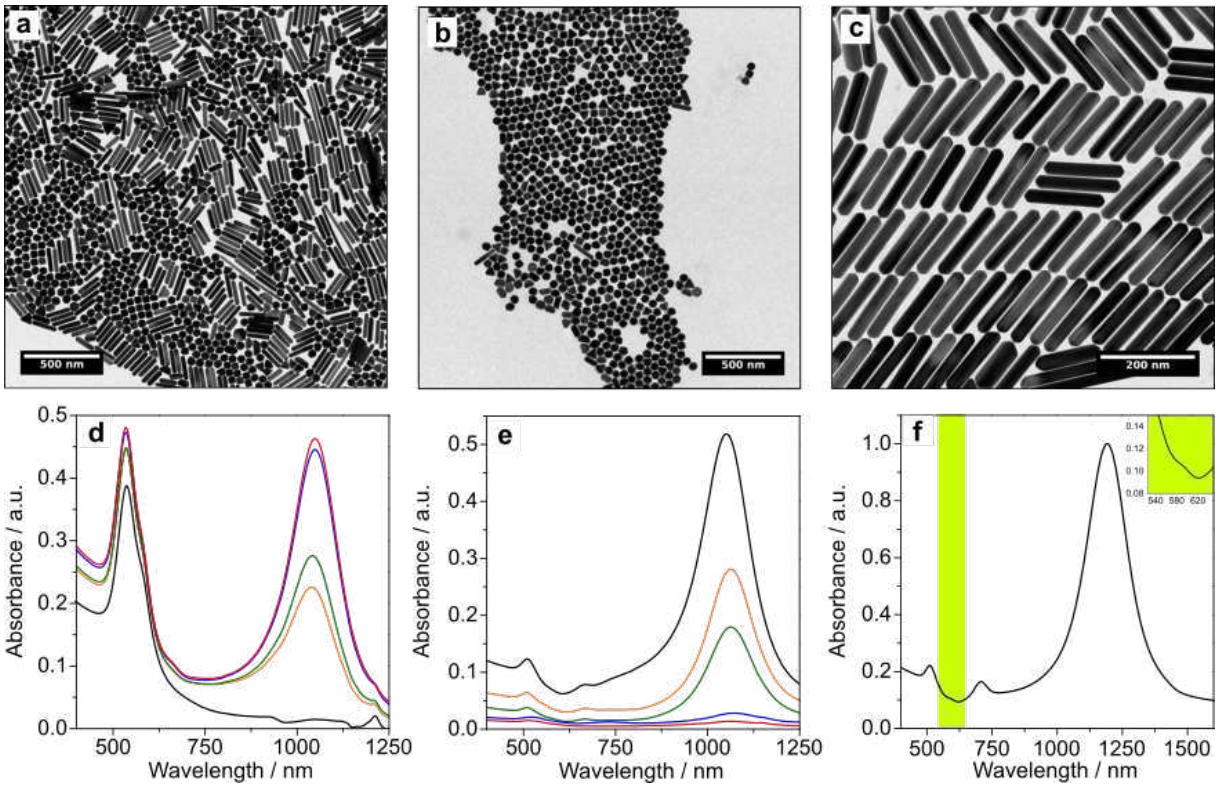

Figure IV.2.: Synthesis and purification of PT-AuNR used as core for controlled living nanowire growth. (a) TEM image of as-synthesized PT-AuNRs. (b) TEM image from the supernatant containing the synthesis by-product. (c) TEM image of purified PT-AuNRs. D: UV-vis analysis of the supernatant obtained 16 hours after addition of CtaC solutions; [CtaC] = 0.12 M (black curve), 0.10 M (orange curve), 0.08 M (green curve), 0.06 M (blue curve) and 0.04 M (red curve). (e) UV-vis analysis of the precipitate obtained 16 hours after the addition of CtaC stock solution. The curve colors correspond to those in (d). (f) UV-vis spectra of a purified PT-AuNRs solution; inset: zoom of the highlighted area discerning the octupolar mode.

of CtaC arises from its high water solubility compared to CtaB or BdaC; since CtaC only varies from CtaB in the counter-ion, the surfactant used for PT-AuNR synthesis, and considering that it is present with a concentration as low as 8 mM, no washing is required prior to surfactant exchange, *i.e.* the required CtaC amount was added directly to the PT-AuNR solution. To obtain the highest possible purification degree, different surfactant concentrations between 0.05 M and 0.15 M were screened for each PT-AuNR batch (**Figure IV.2d–e**). To calculate the amount of CtaC stock solution needed to reach a desired final concentration it is enough to solve the following equation:

$$V_x = \frac{V_{in}(C_{fin} - C_{in})}{C_{stock} - C_{fin}} \tag{IV.2}$$

where V_x is the volume of CtaC stock solution (of concentration C_{stock}) needed to reach the desired final concentration C_{fin} from a solution of nanoparticles with an initial volume V_{in} and an initial concentration C_{in}. We assume that the initial concentration was that of CtaB: even though CtaB and CtaC present different CMC values, we consider this an acceptable simplification considering the low concentration of CtaB used for the PT-AuNR growth. After screening different CtaC concentrations, a concentration around 0.1 M was found to lead to selective flocculation and precipitation of PT-AuNRs within 12 hours.

The purified PT-AuNRs show a shape yield around 99%, (**Figure IV.2a–c**) and can be used as seeds after redispersion in 10 mM benzyldimethylhexadecylammonium chloride (BdaC). As evidenced by UV-vis-NIR spectroscopy (**Figure IV.2f**), the characteristic transversal and longitudinal dipolar, as well as longitudinal quadrupolar plasmon modes can be identified for the pure PT-AuNR dispersion. Further inspection of the high-energy region reveals the presence of an octupolar mode as a shoulder below 600 nm (inset **Figure IV.2f**). The narrow dipolar plasmon band, with a quality factor of 6.45 (**Supporting Figure A.IV.1**), and the high intensity ratio between dipolar and transversal modes confirms the narrow size distribution of the PT-AuNR.
(ii) The second requirement can be fulfilled through careful adjustment of a low silver reduction rate to facilitate anisotropic growth.[10,53] Therefore, the silver overgrowth reaction conditions were set according to the following three conditions: (1) slow silver reduction at slightly acidic conditions and elevated temperature;[19] (2) BdaC as surfactant, which drastically reduces the reduction rate as compared to non-aromatic surfactants;[54] and most importantly, (3) continuous addition of silver nitrate and ascorbic acid by means of a microfluidic pump setup from separated reservoirs. The continuous and slow addition prevents the accumulation of unreacted Ag^+ within the growth solution leading to secondary nucleation and non-specific silver deposition.
UV-vis-NIR extinction spectra after various reaction times during NW growth were correlated with TEM images. All spectra were collected after transferring the NWs into heavy water, so as to expand the detection window up to 2500 nm, avoiding the strong absorbance of water around 1 350 nm (see Experimental Section). We observed an initial blue shift of about 20 nm, along with a slight reduction of the overall aspect ratio when a thin silver layer (approximately 2 nm) grows on all facets (sides and tips). However, after coverage of the PT-AuNR cores with this initial thin layer, silver deposits on the nanowire tips only. This results in a significant and gradual red-shift of all plasmon modes, while multipolar, higher energy plasmon modes emerge as silver deposition continues. Optical extinction spectra of the resulting length-controlled AgAuAgNWs are shown in **Figure IV.3a**-top, along with representative TEM images for selected sizes (**Figure IV.3d–h**), illustrating the striking monodispersity typically achieved by the growth method described above (see **Table A.IV.1** and **Supporting Figure A.IV.2**). In particular, the plasmon spectral features are narrow and mainly limited by intrinsic absorption and radiative losses, rather than by particle size dispersion (see below). The corresponding BEM calculated extinction spectra (**Figure IV.3a**-bottom solid lines, see Methods) show an excellent agreement with the experimental spectra, as well as a gradually increasing similarity with spectra calculated for pure AgNWs with the same overall dimensions (**Figure IV.3a**-bottom dashed lines).
The quality factor (QF) is the characteristic figure of merit (FOM) of any resonator, as it indicates how many oscillations are undergone by a particular oscillator. During silver elongation, the QF of the dipolar mode decays exponentially (**Supporting Figure A.IV.1**), which can be explained considering that radiative coupling to the far-field increases with the length of the antenna, together with the relative dissipation, causing the peaks to broaden.[55] When comparing the experimental QFs with the ones obtained from the BEM simulated spectra of **Figure IV.3a**, the calculated ones are found to be only 25% higher compared to the experimental ones. This clearly emphasizes the low polydispersity of the samples. Interestingly, the decay slope is similar in both experiment and theory, suggesting again that there is no significant increase in the polydispersity of AgAuAgNWs during silver growth.

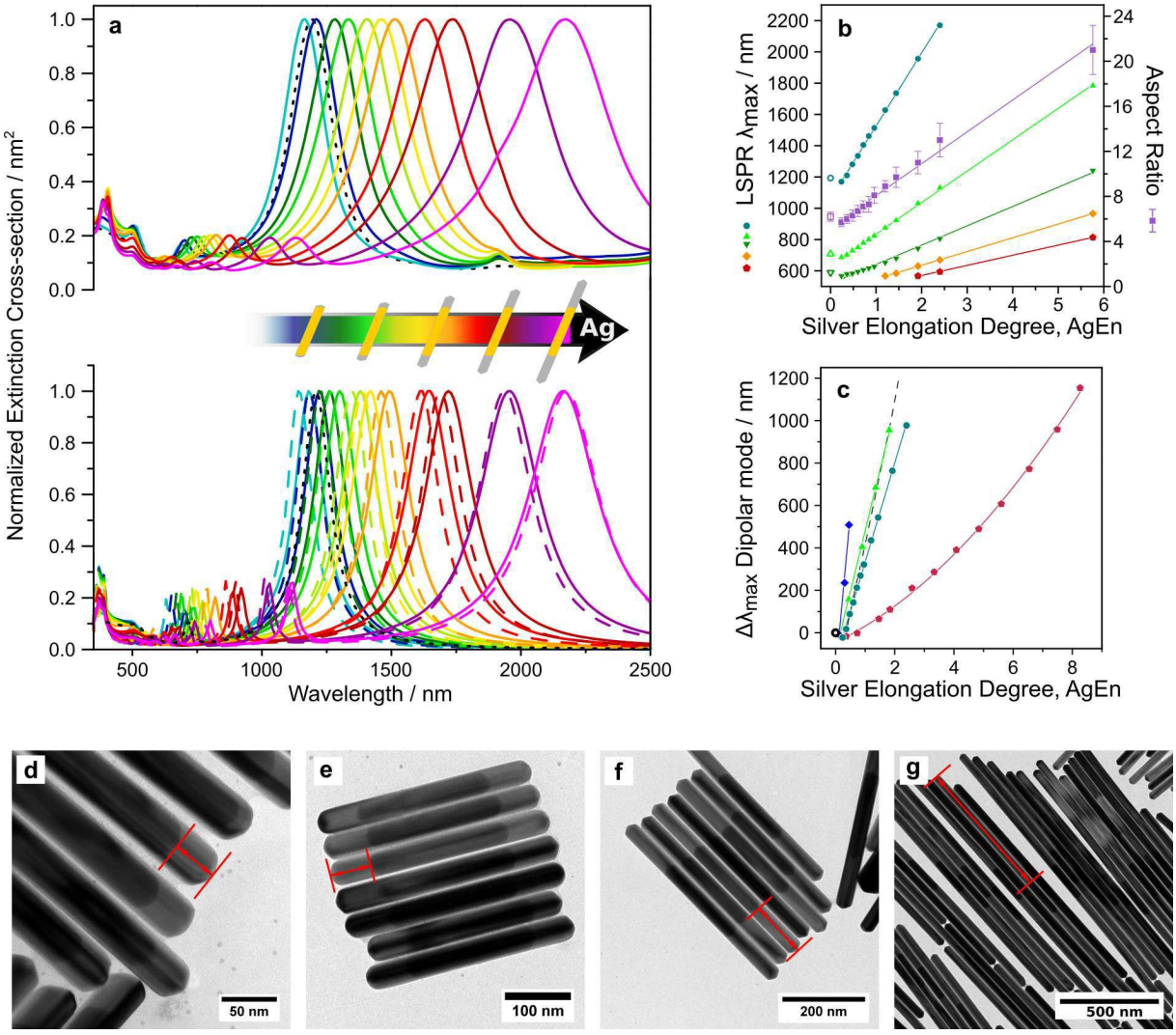

Figure IV.3.: Spectral and morphological evolution of controlled living silver overgrowth. (a) Upper panel: vis-NIR spectra recorded during silver growth; the PT-AuNR core is displayed as a black dotted curve; Lower panel: calculated (BEM) extinction spectra of AgAuAg (solid curves) and pure Ag (dashed curves) NWs with dimensions corresponding to the experimental ones (same color code). (b) Resonance wavelengths for the dipolar (cyan) and 2nd–5th order multipolar modes (green, dark green, orange, and red, respectively) *vs.* AgEn. The aspect ratio (purple) is also plotted for reference. Solid lines are linear fits to the data. The position of the corresponding modes for the PT-AuNR cores are plotted as open symbols. (c) Wavelength shift of the dipolar plasmon mode for growth with a faster addition rate (red), and for the standard rate on PT-AuNRs with different dimensions (180×34 nm, blue; 180×32 nm, green; 210×32 nm, cyan). The dashed gray line represents a theoretical estimation, using the silver-to-gold volume ratio in one nanowire as AgEn. The open black circle is the common origin. (d–g) Representative TEM images at four different values of AgEn = 0.72, 1.2, 2.4, 11.52, corresponding to a silver elongations per tip of 33 ± 6 nm, 61 ± 9 nm, 130 ± 20 nm, and 660 ± 90 nm, and a longitudinal dipolar plasmon resonances at 1 405 nm, 1 630 nm, and 2 170 nm, respectively. The dipolar plasmon for (g) lies beyond the spectral window of the measurement.

Overall, the resulting polydispersity of the product is remarkably narrow and clearly emphasized by the narrowness of the plasmon bands in **Figure IV.3a**. In order to achieve a more meaningful comparison between the widths of experimental and calculated spectra, we used TEM analysis to predict the contribution of the polydispersity to the full width at half maximum (FWHM), which

Table IV.1.: Total length distribution for AgAuAgNWs with increasing elongation degrees AgEn, evaluated by TEM analysis (ΔL_{TEM}) and comparing experimental and calculated optical spectra (ΔL_{opt}).

AgEn	ΔL_{TEM} / nm	ΔL_{OPT} / nm
0.24	20.3	17.6
0.36	19.5	18.7
0.48	19.8	24.3
0.72	21.9	27.5
0.84	29.2	29.7
1.20	36.3	29.7
1.92	39.8	34.2
2.40	42.9	39.1

is missing in the calculation. In fact, the FWHM of the experimental peaks is constituted by a Lorentzian component, intrinsically related to the nanoparticle properties, and a Gaussian component, related to the size distribution in the colloidal solution. The latter is what we normally evaluate using different techniques like transmission electron microscopy (TEM), dynamic light scattering (DLS) or small angle X-ray scattering (SAXS). The finite size distribution within each sample accounts for a moderate increase in FWHM of the observed plasmon features (see **Supporting Figure A.IV.3**). A more precise assessment is provided by comparing the wavelength width of the measured ($\Delta\lambda_{exp}$) and theoretical ($\Delta\lambda_{th}$) spectra, assuming that the excess in the former one originates from the finite size distribution of NW sizes for each given sample (ΔL). We then have $\Delta\lambda_{exp} \sim \Delta\lambda_{th} + \Delta m$, where m is the slope of the plot of plasmon wavelength peak *vs.* NW length, extracted from **Figure IV.3b**. In **Table IV.1** the values of ΔL extracted from this analysis of the optical spectra (ΔL_{opt}) are compared with the size distributions obtained from TEM analysis (ΔL_{TEM}). The results show an acceptable agreement, considering that the number of NWs measured by TEM for each sample is much smaller than those contributing to UV-vis-NIR spectra.

(iii) The last requirement to achieve a living polymerization reaction (linear growth) can be met by selecting an addition rate that is slower than the reaction rate. In this way, a linear zero-order kinetic path is enforced and the resonance wavelengths of the longitudinal modes, as well as the corresponding aspect ratios evaluated from TEM measurements (see **Supporting Table A.IV.1**), turn out to scale linearly with time. Furthermore, as the conversion rate for silver is close to 100%, the linear shifts are directly proportional to the amount of added Ag^+. This proportionality is referred to in what follows as the degree of silver elongation, AgEn, defined as the molar ratio of added silver salt to gold seeds (*i.e.* $[Ag^+]$ / $[Au^0]$), in analogy to the concept of degree of polymerization. We plotted in **Figure IV.3b** the resonance wavelengths for all the longitudinal plasmons that were recorded within our measurement spectral window (ranging from the dipolar mode up to the 5th order mode) *vs.* AgEn. Note that we disregarded some high-energy spectral features that cannot be clearly resolved apart from the transverse mode. This plot clearly reveals a linear slope for all modes, up to aspect ratios above 20 and AgEn value of almost 6. In other words, this plot indicates that the reaction proceeds according to zero order kinetics and that no termination or passivation occurs. The corresponding regression fits (solid lines) yield a Pearson R^2 above 0.999 for all the modes and for the aspect ratio. As a control experiment, we increased the rate of Ag^+ addition by a factor of 1.25. The resulting plasmon shifts were plotted

in **Figure IV.3c** (red dots), showing that the faster addition rate leads to non-linear shifts. Since the reaction does not comply with a slow addition rate, the apparent AgEn increases significantly faster than the plasmon band shift, which represents the actual growth rate. Furthermore, under these conditions, excess silver nitrate accumulates in solution, leading to secondary nucleation, formation of AgCl nuclei, non-specific deposition of silver on the growing particle surface, and uncontrolled increase of the reaction rate. All these effects reduce the amount of available silver ions for deposition on the NW tips and consequently compromise the linear growth and impair an accurate prediction of the final length of the produced AgAuAgNWs. Interestingly, spherical particles with diameters around 500 nm were observed upon TEM inspection of the resulting colloid, which are likely due to crystallization of AgCl present in solution upon drying of the dispersion on the TEM grid (**Supporting Figure A.IV.4**). We also found that the thickness of the NWs was significantly larger than expected, in contrast to living reaction conditions (see **Table A.IV.2**). An increase of the reaction temperature also leads to faster reaction rates and uncontrolled growth, so we conclude that the living reaction conditions are highly sensitive to changes in reaction kinetics, either induced by increased temperature or faster precursor addition. The generality of this method was confirmed by carrying out different experiments under controlled living nanowire growth conditions but starting with different PT-AuNR core dimensions, which also led to linear growth and reproducible evolution of the plasmonic features (**Figure IV.3c**). We used the silver to gold volume ratio of a single bimetallic nanowire as the AgEn parameter for BEM simulations (**Figure IV.3a**-bottom), so as to estimate the theoretical linear behavior (dashed line in **Figure IV.3c**). The observed deviation can be explained taking into account the presence of a small amount of Au byproducts (different particle shapes), on which silver is also reduced, as well as some uncertainty in the initial Au nanorod concentration, due to the purification step ([Au^0] was estimated using the absorbance at 400 nm, as detailed in the Experimental Section). The obtained agreement is a strong confirmation that all silver ions added were reduced and selectively deposited on the AgAuAgNW tips. It is worth noting that we have not found any limitation in the final length of the NWs, our longest experiment resulting in 3.4 µm NWs (corresponding to a AgEn of 40.32; **Supporting Figure A.IV.5**).

We selected two samples with significantly different NW lengths to discuss the influence of the PT-AuNR core on the optical properties of the bimetallic particles. We analyzed the optical extinction spectra from NWs in heavy water solution (**Figure IV.4**) and carried out a detailed EELS analysis (**Figures IV.5 & IV.6**). Both experimental methods were supported by BEM calculations. The first sample had AgEn = 0.5, corresponding to a total aspect ratio of 6.7, and 25 nm Ag extending beyond each tip of the PT-AuNR core. We compare in **Figure IV.4a** the vis-NIR spectrum (black solid curve) with the calculated extinction spectrum of a NW with the average dimensions, either containing the PT-AuNR core (red-dotted curve) or being made of pure Ag (blue dash-dotted curve). The simulations reveal in this case a clear influence of the PT-AuNR core on all the plasmon modes, particularly in the short wavelength (high energy) region. The second sample corresponds to AgEn = 5.3, aspect ratio 25, and 360 nm of Ag from each tip. The 3D reconstructed volume of the two samples obtained by the Total Variation Minimization (TVM)[56] technique, applied to a tilt series of high-angle annular darkfield scanning transmission electron microscopy (HAADF-STEM) images (**Figure IV.4b&c**) clearly shows that the PT-AuNR core is located in the center, with 2 nm of silver on the lateral facets (also considered for the simulations).

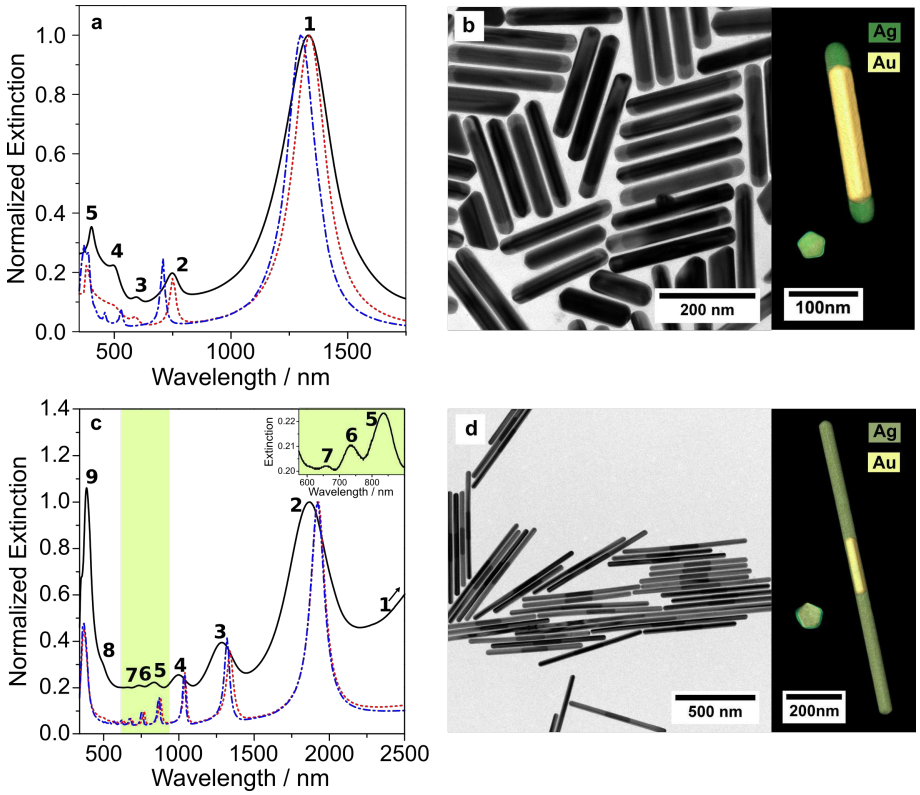

Figure IV.4.: Characterization of exemplary short and long AgAuAgNWs. (a) Vis-NIR spectrum of a colloid of short (AgEn = 0.5) AgAuAgNWs (black line) compared to simulated spectra in the presence (red) and absence (blue) of the PT-AuNR core. (b) Representative TEM image showing the high monodispersity of the sample. (c&d) Same as (a&b) for a sample of longer NWs (AgEn 5.3). Inset of (c) zoom of the highlighted area discerning high order modes 5, 6, and 7. At the right subpanels of (b) and (d), 3D TEM visualizations of the reconstructed nanowires are presented (green and yellow correspond to silver and gold, respectively), both from one tip (left) and along their length (right).

The pentagonal cross section of the particle—characteristic for PT-NRs—is preserved, as evidenced by the cross section in **Figure IV.4b** & **IV.4d**. Remarkably, the low polydispersity of the synthesized AgAuAgNWs allowed us to detect nine LSPR bands in solution (**Figure IV.4c**), and we find again a good agreement with the BEM simulated extinction spectrum. In this case however, the differences between simulations with and without the gold core are significantly smaller, and mainly observed in the high-energy region. It should be noted that the permittivities of silver and gold are well described through a common Drude expression $\varepsilon(\omega) = \varepsilon_b - \omega_p^2/\omega(\omega + i\gamma)$ in the IR region, where the so-called classical plasma energy is given by $\hbar\omega_p \sim 9$ eV,[57] as determined by the density of s conduction electrons (*i.e.* the same in both metals, because each atom contributes with one s electron and their atomic densities are nearly identical). The difference between these two metals lies in the level of losses ($\hbar\gamma$ = 25 meV for silver and 71 meV for gold) and in the background screening produced by d-band polarization (ε_b = 4 in silver and 9.5 in gold). Consequently, in the infrared spectral region (*i.e.* $\lambda > 1000$ nm), the second term dominates in the Drude expression, the precise value of ε_b becomes irrelevant, and both silver and gold behave in a similar fashion, except that the latter produces more inelastic optical losses (through a larger damping rate γ). Besides these intrinsic material properties, which lead to similar optical behavior in the NIR, there is a geometrical effect associated with the NW: for a given

mode order (*e.g.* the lowest-order dipolar mode), the wavelength shifts deeper into the IR with increasing NW length, and eventually the mode size becomes comparable to $\lambda/2$, giving rise to a relatively larger contribution of radiative damping, which again makes the two metals look more similar. These considerations explain why the AgAuAg bimetallic NWs have similar properties to those of pure Ag wires with the same outer geometry, particularly for infrared modes and long NWs (**Figure IV.3a**).

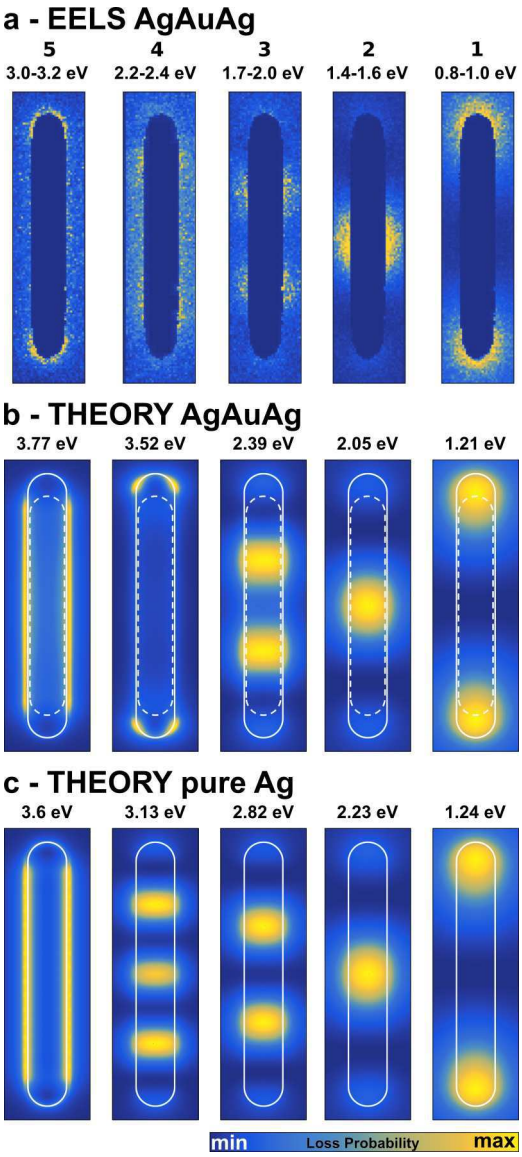

Figure IV.5.: Near-field characterization of exemplary short AgAuAgNW. (a) spatial distribution of plasmon modes for a short AgAuAgNW (AgEn = 0.5) as measured by EELS; the numbers refer to the same modes as in the vis-NIR spectrum of **Figure IV.4a**. (b) BEM simulations of EELS maps associated to the plasmon modes shown in (a), for a NW containing the PT-AuNR core. (c) Simulations for an AgNW with the same dimensions. The simulated maps are normalized to the maximum intensity in each case. The silver (gold) surface is indicated with solid (broken) white lines in the calculated maps.

To confirm these observations, we carried out a detailed near-field study by EELS, also supported by BEM calculations. Plasmon mapping confirmed the symmetry and standing-wave nature of the modes under study. We summarize in **Figure IV.5** and **Supporting Figure A.IV.7**

the results for the short NWs (AgEn = 0.5): all of the extinction bands observed in the far-field vis-NIR spectrum are also found in EELS (**Figure IV.5a**). The spatial distribution of the plasmons clearly indicates the even or odd nature of each mode: modes (1–3) are the dipolar, quadrupolar, and octupolar longitudinal modes, respectively, while modes (4–5) are the accumulation of several modes (see below). Incidentally, only odd modes can be excited using light incident with its electric field parallel to the NW, in contrast to EELS in which even modes are also excited due to the multipolar character of the electron exciting field. This conclusion can be actually extended to NWs of arbitrary orientation relative to the externally applied field when they are sufficiently small as to neglect retardation effects (*e.g.* an $\exp(i2\pi r/\lambda)$ dependence on position r and light wavelength λ). However, we are dealing here with long NWs, with lengths that are comparable to λ, so there is strong retardation and this is the reason why our optical spectra reveal modes with both odd and even symmetry.[30,37,41,58] The EELS experimental maps were compared to numerically computed maps using BEM. Simulations were carried out both in the presence (mid panel) and in the absence (bottom panel) of the PT-AuNR core. Although the agreement between theoretical and experimental plasmon energies in the optical measurements is excellent (see above), the EELS modes are noticeably redshifted with respect to theory, presumably because of the effect of the substrate, which is not accounted for in our simulations. However, the features in the measured and calculated EELS spectra are in good mutual agreement (see **Supporting Figure A.IV.6**), and we argue that the spatial distribution of the plasmon excitation should not be too sensitive to the observed shift. This intuition is corroborated when comparing modes of the same symmetry, which yield very similar spatial distributions in theory and experiment. Is important to keep in mind that the highest-order modes observed in EELS (modes 4 and 5 in **Figure IV.5**) are in fact the accumulation of several modes, which are integrated over the finite energy range covered within the energy-filtered images. Note that we are instead showing monochromatic maps in the calculations, so that these high-order maps are understandably different from those experimentally acquired. Additionally, the number of plasmon modes (an infinite, discrete set) has an accumulation point toward the electrostatic planar surface plasmon (signaled by $\varepsilon = -1$ in vacuum), as they undergo fast oscillations, so that the surface is locally seen as flat. This explains the rather uniform distribution of the observed map at that energy (3.7 eV for the silver-vacuum interface). The theoretical calculations also allow us to explore the role of the PT-AuNR core in the plasmonic response, which essentially produces a redshift of the plasmon energies, along with additional broadening in the EELS spectra (see **Supporting Figure A.IV.6**). It is thus not surprising that the silver NW has better-defined higher-order modes (second maps from the left in **Figure IV.5b&c**).

For a long NW (**Figure IV.6** and **Supporting Figure A.IV.8**, AgEn = 5.3), EELS characterization did allow us to identify the dipolar longitudinal mode (1), as well as six additional multipolar modes (2–7 corresponding to increasing order, *i.e.* number of sign changes in the associated induced charge along the wire), whereas the last two peaks (8–9) correspond to an accumulation of several modes, as discussed above for short NWs. In this case, the effect of the PT-AuNR core is qualitatively similar, but nearly marginal for low energy modes. In particular, the lowest-order dipolar plasmon involves high plasmon strength (larger enhancement of the near field) near the NW tips, and consequently the near field plot looks nearly identical for the calculated AgAuAg (**Figure IV.6b**) and the pure AgNW (**Figure IV.6c**), also in excellent agreement with the

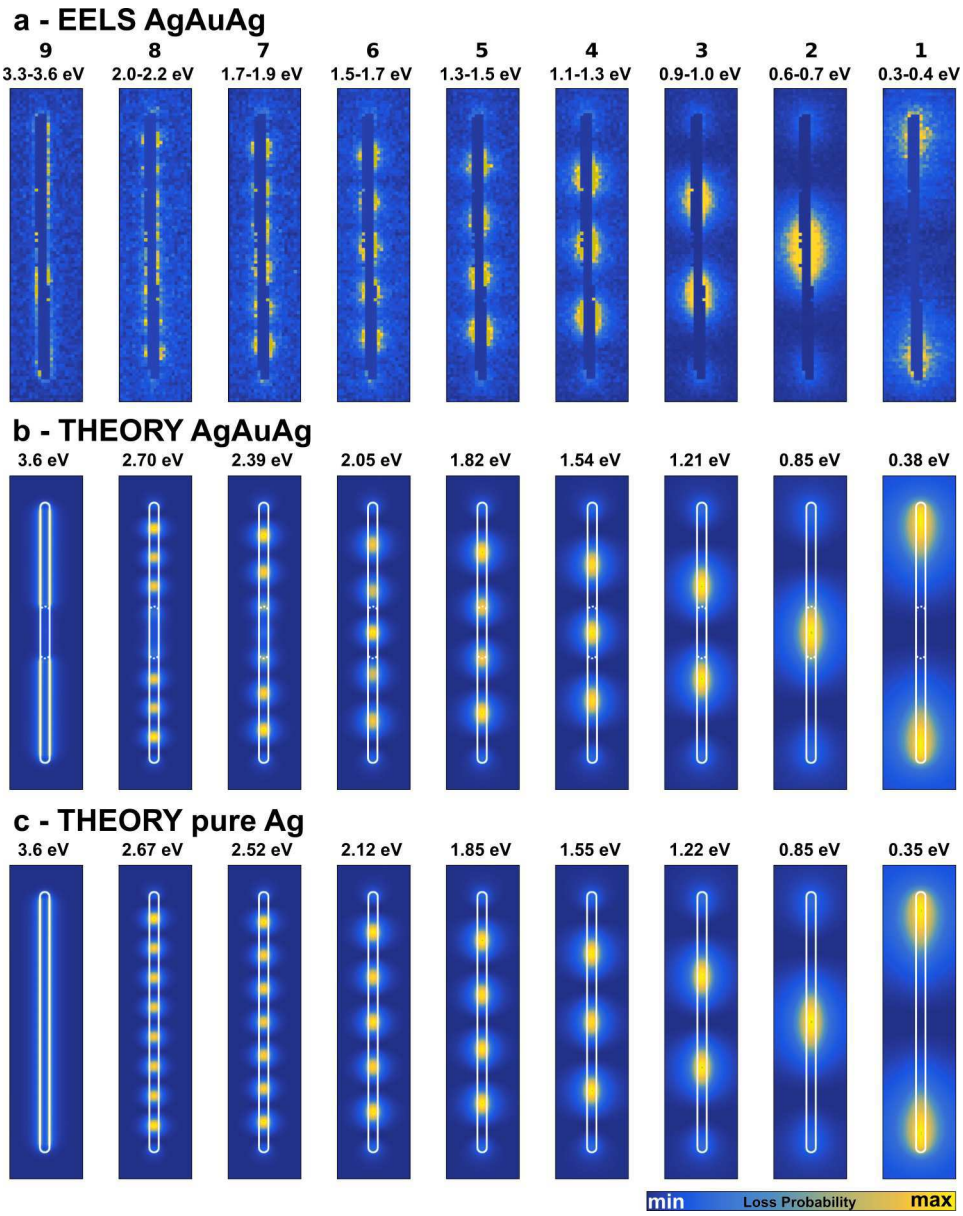

Figure IV.6.: Near-field characterization of exemplary long AgAuAgNW. (a) Spatial distribution of plasmon modes for a long AgAuAgNW (AgEn = 5.3) as measured by EELS; the numbers refer to the same modes as in the vis-NIR spectrum of **Figure IV.4a**. (b) BEM simulations of EELS maps associated to the plasmon modes shown in (a), for a NW containing the PT-AuNR core. (c) Simulations for an AgNW with the same dimensions. The simulated maps are normalized to the maximum intensity in each case. The silver (gold) surface is indicated with solid (broken) white lines in the calculated maps.

experimental EELS maps (**Figure IV.6a**). Since the NIR response of gold and silver is similar, as they both behave as Drude's metals, and the interband transition contributes marginally in this spectral region, the low energy plasmon position should not change significantly between a pure Au and a pure AgNW; nonetheless we expect to observe additional broadening in the case of gold, since it shows higher intrinsic damping losses compare to silver (71 *vs.* 21 meV). In **Supporting Figure A.IV.9** we investigate this point with a new set of calculation relative to a pure Au NWs. In conjunction with a higher broadening, we observed a reduction in the plasmon extinction cross section. Subsequently, the PT-AuNR core can only be identified in the higher-

order modes, which involve a large intensity in the central NW region, while their high energies involve very different and relatively moderate values of the dielectric functions of the two metals. Interestingly, the second-order mode, which also has a large weight in the center of the NW, appears at a sufficiently low energy as to feel a similar response from both gold and silver, as we argued above, and consequently, the calculated energies of this mode in the long NWs are similar with and without the PT-AuNR core. For such low order modes, the NW acts as a whole plasmonic entity. On the contrary, the vacuum/silver interface plasmon is both experimentally and theoretically localized on the silver parts only. For this mode, corresponding to high wave vectors (short wavelengths), the plasmons feel differently each metal, and consequently the gold and silver parts act as two separated plasmonic entities in this regime.

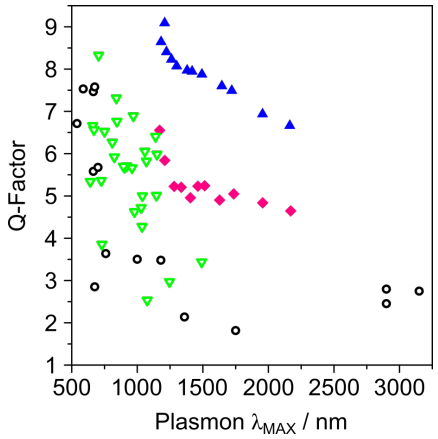

Figure IV.7.: Comparison of the quality factor of vis-NIR plasmons reported in the literature for different nanoparticles preparation: lithography (black opened circles) and wet-chemistry (green opened triangles). These are compared with the one that we obtained for the AgAuAgNWs, both experimentally (pink diamonds) and from calculations (blue triangles).[59–71]

In conclusion, the synthesis of AgAuAg bimetallic nanowires has been largely improved by enforcing living growth conditions to the deposition of silver on the tip of pentatwinned Au nanorods, which allowed us to achieve high quality colloidal dispersions with remarkably low polydispersity. As a result, the plasmon bands observed in colloidal NW dispersions are much narrower than those reported for other types of both lithographic and colloidal nanoparticles within the same IR spectral range (see **Figure IV.7**). The measured quality factor (*i.e.*, the ratio of plasmon energy to spectral energy FWHM, which is equal to $\frac{1}{2\pi}$ times the number of plasmon oscillations before the near-field intensity is attenuated by a factor 1⁄e) is in fact reasonably close to the calculated one for NWs of well defined size, and as we discuss above, the difference between these two is well explained in terms of the experimental finite size distribution, thus emphasizing our understanding of the optical response of the NWs in terms of the local permittivities of gold and silver. The new protocol provides the opportunity to fine tune the NWs length up to the micrometer scale (AR > 100), and the obtained optical antennas displayed a large number of plasmonic modes that spread over the entire UV-vis-IR region (up to 9 detectable modes directly in the colloidal suspension). The role of the gold cores on the optical response was carefully investigated by EELS, and we demonstrated that it does not interfere with plasmon propagation along the NW surface, whilst its influence is limited to higher energy modes. The procedure opens up new possibilities to exploit plasmon resonances in the near and middle IR regions.

Methods

Materials. Benzyldimethylhexadecylammonium chloride (BdaC), hexadecyltrimethylammonium bromide (CtaB, $\geq$99%), hexadecyltrimethylammonium chloride (CtaC, 25 wt% in water), hydrogen tetrachloroaurate trihydrate ($HAuCl_4 \cdot 3\ H_2O$, $\geq$99.9%), silver nitrate ($AgNO_3$, $\geq$99.9%), L-ascorbic acid ($AscH_2$, $\geq$99%), deuterium oxide (D_2O, 99.9 atom% D), sodium borohydride ($NaBH_4$, 99%) and trisodium citrate ($\geq$98%) were purchased from Aldrich. All chemicals were used as received. Milli-Q water (resistivity 18.2 MΩcm at 25 °C) was used in all experiments. All glassware was washed with aqua regia, rinsed with water, sonicated three times for 3 min with Milli-Q water, and dried before use.

PT-AuNR synthesis. The pentatwinned gold nanorod synthesis was adopted from the protocol of Pérez-Juste *et al.* with some minor modifications.[49] These changes mainly refer to an increase of $NaBH_4$ concentration during citrate-capped seed growth to improve reproducibility and increase of $AscH_2$ concentration during AuNR growth to improve the final yield. 3.5 nm citrate-capped Au seeds. Briefly, 20 mL of a 0.125 mM $HAuCl_4$, 0.25 mM trisodium citrate aqueous solution was prepared and stirred for 10 minutes at room temperature. Next, 600 µL of a freshly prepared 0.1 M $NaBH_4$ solution was added quickly under vigorous stirring. After 2 minutes the stirring rate was reduced and the seeds were aged 40 min under slow stirring at room temperature. To ensure for complete removal of excessive $NaBH_4$ the solution was stirred at 40–45 °C for another 15 minutes. 5.5 nm CtaB-capped Au seeds. A 5 mL growth solution was prepared consisting of 40 mM CtaB and 0.125 mM $HAuCl_4$. The Au(III) was reduced to Au(I) with 12.5 µL of a 0.1 M $AscH_2$ solution (f.c. 0.25 mM), indicated by a fast color change from yellow-orange to transparent. Then 835 µL of the citrate-capped Au seeds was added quickly and the solution was mixed by hand-shaking thoroughly. The 5.5 nm CtaB-capped Au seeds were aged for 3 h at 23 °C prior final overgrowth. PT-AuNR synthesis. A 500 mL growth solution was prepared containing 8 mM CtaB and 0.125 mM $HAuCl_4$. The solution was thermostated at 20 °C. Next 1560 µL of a 0.1 M $AscH_2$ (f.c. 0.313 mM) was added and gently stirred leading to a clearance of the solution. Finally, 750 µL of 5.5 nm CtaB-capped Au seeds was added quickly and mixed thoroughly. The solution was thermostated at 20 °C overnight.

PT-AuNR purification. Purification was carried out as described by Scarabelli *et al.*[50] For PT-AuNRs of length and width ca. 200 nm and 30 nm, respectively, the final surfactant concentration was set to 0.1 M through the addition of 67.5 mL of a 25 wt% CtaC solution, leading to flocculation and sedimentation overnight. The supernatant was discarded and the sediment containing the NRs was redispersed in a 10 mM BdaC solution to obtain a final Au(0) concentration of 0.25 mM (measured using the absorbance at 400 nm).[51,52]

AgAuAgNW synthesis. 20 mL of the purified PT-AuNR solution containing 10 mM BdaC and 0.25 mM Au(0) was heated to 60 °C. $AgNO_3$ (0.004 M in water) and $AscH_2$ (0.016 M in 20 mM BdaC, in order to keep the BdaC concentration constant) were added continuously in separate syringes by a syringe pump with a rate of 0.24 mol of Ag(I) per mol of Au(0) per hour (effective rate starting at 300 µL/h) under slow stirring at 60 °C. Samples of 1 mL were taken

after defined time frames and the effective rate adjusted to maintain the rate of 0.24 mol of Ag(I) per mol of Au(0) per hour during the whole experiment (see **Supporting Table A.IV.3** for the effective rates). For UV-vis-NIR measurements beyond the water limit at around 1350 nm, the path length was reduced using a 1 mm cuvette and water was exchanged by deuterated water to reduce vibrational modes and consequently reduce overall extinction. The samples were washed 3 times by centrifugation (1000–3000 rpm) and redispersing in deuterated water (concentrating the sample down to 400 µL) to allow UV-vis-NIR measurements in the range of 300–2500 nm in a 1 mm pathway cuvette to be performed.

Spectroscopic and TEM Characterization. Transmission electron microscopy (TEM) images were collected with a JEOL JEM1400PLUS instrument operating at 120 kV with carbon-coated 400 square mesh copper grids. All samples were centrifuged twice before blotting on the grid to reduce surfactant concentration. Optical extinction spectra were recorded using an Agilent Cary 5000 UV-vis-NIR spectrophotometer in deuterated water. All the presented UV-vis-NIR spectra were multiplied by the respective dilution factors to facilitate comparison of the data. HAADF-STEM images and electron tomography series were acquired using an aberration corrected cubed FEI Titan 60–300 electron microscope operated at 200 kV. For the reconstruction of the series the Total Variation Minimization technique (TVM) was used. EELS plasmon maps, were acquired using a monochromated double aberration corrected cubed FEI Titan 50–80 electron microscope operated at 300 kV and yielding an energy resolution of 0.12 eV. For the analysis of the two EELS datasets, first a Richardson-Lucy deconvolution of the zero-loss peak from the data was performed and then the zero-loss peak was fitted and subtracted from the result, by using Hyperspy.[72] Since the points of the map passing over the rod still present a large background due to multiple phonon scattering, and are also noisier due to the lower counts, reducing the signal quality from those areas, a mask was used in the place of the NR.[73]

Electromagnetic and EELS simulations. Optical extinction spectra, electric near-field intensity maps, and EELS intensities are calculated by solving the Maxwell equations in the presence of either an external light plane wave or an electron point charge moving with constant velocity (v=0.78c, corresponding to an acceleration voltage of 300 kV), respectively. The extinction calculations are averaged over NW orientations and light polarizations. For EELS, the electron is incident along a direction normal to the long wire axis. For simplicity, the wires are simulated as axially symmetric rods of the same volume as the actual PT-NW, using the boundary-element method and exploiting the axial symmetry of the particles, as described elsewhere.[48] More precisely, the outer gold and silver NW interfaces are modeled as circular cylinders with hemispherical caps. The radius of the silver wire is considered to be 2 nm larger than that of the gold core. The latter has a length (diameter) of 210 nm (34 nm) in the simulations of **Figure IV.3** and 180 nm (32 nm) in **Figure IV.4–IV.6**. Gold and silver are represented by their tabulated frequency-dependent complex dielectric functions.[74] The NWs are considered to be in vacuum ($\varepsilon = 1$) for EELS and in deuterated water ($\varepsilon = 1 - 0.30637\lambda^2/(\lambda^2 + 47.26686) + 0.74659.\lambda^2/(\lambda^2 - 0.00893)$, where λ is the free-space light wavelength in microns under optical illumination[75]) for optical extinction.

Acknowledgments. LML-M acknowledges funding from the European Research Council Advanced Grant PLASMAQUO (No. 267867) and from the Spanish MINECO (grant MAT2013-46101-R). SB acknowledges funding from ERC Starting Grant COLOURATOMS (335078). The research leading to these results has received funding from the European Union Seventh Framework Programme under Grant Agreements 312483 (ESTEEM2) and 262348 (ESMI). MM, MT, and AF acknowledge funding from the European Research Council starting grant METAMECH (No 306686). MT was supported by the Elite Network Bavaria in the frame of the Elite Study Program 'Macromolecular Science' and funded *via* a grant for PhD candidates according to Bavarian elite promotion law (BayEFG).

References

[1] S. Kawata, A. Ono, P. Verma, “Subwavelength colour imaging with a metallic nanolens”, *Nature Photonics* **2008**, *2*, 438–442.

[2] C. L. Cortes, W. Newman, S. Molesky, Z. Jacob, “Quantum nanophotonics using hyperbolic metamaterials”, *Journal of Optics* **2012**, *14*, 063001.

[3] V. M. Shalaev, “Optical negative-index metamaterials”, *Nature Photonics* **2007**, *1*, 41–48.

[4] G. Lu, H. De Keersmaecker, L. Su, B. Kenens, S. Rocha, E. Fron, C. Chen, P. Van Dorpe, H. Mizuno, J. Hofkens, J. A. Hutchison, H. Uji-i, “Live-Cell SERS Endoscopy Using Plasmonic Nanowire Waveguides”, *Advanced Materials* **2014**, *26*, 5124–5128.

[5] A. McLintock, C. A. Cunha-Matos, M. Zagnoni, O. R. Millington, A. W. Wark, “Universal Surface-Enhanced Raman Tags: Individual Nanorods for Measurements from the Visible to the Infrared (514–1064 nm)”, *ACS Nano* **2014**, *8*, 8600–8609.

[6] G. Y. Tonga, K. Saha, V. M. Rotello, “25th Anniversary Article: Interfacing Nanoparticles and Biology: New Strategies for Biomedicine”, *Advanced Materials* **2014**, *26*, 359–370.

[7] M.-F. Tsai, S.-H. G. Chang, F.-Y. Cheng, V. Shanmugam, Y.-S. Cheng, C.-H. Su, C.-S. Yeh, “Au Nanorod Design as Light-Absorber in the First and Second Biological Near-Infrared Windows for *in Vivo* Photothermal Therapy”, *ACS Nano* **2013**, *7*, 5330–5342.

[8] S. Mubeen, J. Lee, N. Singh, S. Krämer, G. D. Stucky, M. Moskovits, “An autonomous photosynthetic device in which all charge carriers derive from surface plasmons”, *Nature Nanotechnology* **2013**, *8*, 247–251.

[9] S. Sarina, E. R. Waclawik, H. Zhu, “Photocatalysis on supported gold and silver nanoparticles under ultraviolet and visible light irradiation”, *Green Chemistry* **2013**, *15*, 1814.

[10] J. Gu, Y.-W. Zhang, F. (Tao, “Shape control of bimetallic nanocatalysts through well-designed colloidal chemistry approaches”, *Chemical Society Reviews* **2012**, *41*, 8050.

[11] C. J. DeSantis, A. C. Sue, M. M. Bower, S. E. Skrabalak, “Seed-Mediated Co-reduction: A Versatile Route to Architecturally Controlled Bimetallic Nanostructures”, *ACS Nano* **2012**, *6*, 2617–2628.

[12] F.-R. Fan, D.-Y. Liu, Y.-F. Wu, S. Duan, Z.-X. Xie, Z.-Y. Jiang, Z.-Q. Tian, “Epitaxial Growth of Heterogeneous Metal Nanocrystals: From Gold Nano-octahedra to Palladium and Silver Nanocubes”, *Journal of the American Chemical Society* **2008**, *130*, 6949–6951.

[13] M. Jin, H. Zhang, J. Wang, X. Zhong, N. Lu, Z. Li, Z. Xie, M. J. Kim, Y. Xia, “Copper Can Still Be Epitaxially Deposited on Palladium Nanocrystals To Generate Core–Shell Nanocubes Despite Their Large Lattice Mismatch”, *ACS Nano* **2012**, *6*, 2566–2573.

[14] C. J. DeSantis, S. E. Skrabalak, “Core Values: Elucidating the Role of Seed Structure in the Synthesis of Symmetrically Branched Nanocrystals”, *Journal of the American Chemical Society* **2013**, *135*, 10–13.

[15] S. E. Habas, H. Lee, V. Radmilovic, G. A. Somorjai, P. Yang, “Shaping binary metal nanocrystals through epitaxial seeded growth”, *Nature Materials* **2007**, *6*, 692–697.

[16] N. Li, P. Zhao, D. Astruc, "Anisotropic Gold Nanoparticles: Synthesis, Properties, Applications, and Toxicity", *Angewandte Chemie International Edition* **2014**, *53*, 1756–1789.

[17] C. S. Ah, S. D. Hong, D.-J. Jang, "Preparation of Au-core Ag-shell Nanorods and Characterization of Their Surface Plasmon Resonances", *The Journal of Physical Chemistry B* **2001**, *105*, 7871–7873.

[18] S. Hong, Y. Choi, S. Park, "Shape Control of Ag Shell Growth on Au Nanodisks", *Chemistry of Materials* **2011**, *23*, 5375–5378.

[19] S. Gómez-Graña, B. Goris, T. Altantzis, C. Fernández-López, E. Carbo-Argibay, A. G. Martínez, N. Almora-Barrios, N. Lopez, I. Pastoriza-Santos, J. Perez-Juste, S. Bals, G. Van Tendeloo, L. M. Liz-Marzán, "Au@Ag Nanoparticles: Halides Stabilize {100} Facets", *The Journal of Physical Chemistry Letters* **2013**, DOI 10.1021/jz401269w.

[20] E. C. Le Ru, J. Grand, I. Sow, W. R. C. Somerville, P. G. Etchegoin, M. Treguer-Delapierre, G. Charron, N. Félidj, G. Lévi, J. Aubard, "A Scheme for Detecting Every Single Target Molecule with Surface-Enhanced Raman Spectroscopy", *Nano Letters* **2011**, *11*, 5013–5019.

[21] T. Ming, H. Chen, R. Jiang, Q. Li, J. Wang, "Plasmon-Controlled Fluorescence: Beyond the Intensity Enhancement", *The Journal of Physical Chemistry Letters* **2012**, *3*, 191–202.

[22] S. Bagheri, H. Giessen, F. Neubrech, "Large-Area Antenna-Assisted SEIRA Substrates by Laser Interference Lithography", *Advanced Optical Materials* **2014**, *2*, 1050–1056.

[23] D. Seo, C. I. Yoo, J. Jung, H. Song, "Ag−Au−Ag Heterometallic Nanorods Formed through Directed Anisotropic Growth", *Journal of the American Chemical Society* **2008**, *130*, 2940–2941.

[24] Q. Li, R. Jiang, T. Ming, C. Fang, J. Wang, "Crystalline structure-dependent growth of bimetallic nanostructures", *Nanoscale* **2012**, *4*, 7070.

[25] E. Carbó-Argibay, B. Rodríguez-González, I. Pastoriza-Santos, J. Pérez-Juste, L. M. Liz-Marzán, "Growth of pentatwinned gold nanorods into truncated decahedra", *Nanoscale* **2010**, *2*, 2377–2383.

[26] P. Muhlschlegel, "Resonant Optical Antennas", *Science* **2005**, *308*, 1607–1609.

[27] M.-W. Chu, V. Myroshnychenko, C. H. Chen, J.-P. Deng, C.-Y. Mou, F. J. García de Abajo, "Probing Bright and Dark Surface-Plasmon Modes in Individual and Coupled Noble Metal Nanoparticles Using an Electron Beam", *Nano Letters* **2009**, *9*, 399–404.

[28] J. Dorfmüller, R. Vogelgesang, W. Khunsin, C. Rockstuhl, C. Etrich, K. Kern, "Plasmonic Nanowire Antennas: Experiment, Simulation, and Theory", *Nano Letters* **2010**, *10*, 3596–3603.

[29] V. K. Valev, A. V. Silhanek, B. De Clercq, W. Gillijns, Y. Jeyaram, X. Zheng, V. Volskiy, O. A. Aktsipetrov, G. A. E. Vandenbosch, M. Ameloot, V. V. Moshchalkov, T. Verbiest, "U-Shaped Switches for Optical Information Processing at the Nanoscale", *Small* **2011**, *7*, 2573–2576.

[30] G. Baffou, R. Quidant, “Thermo-plasmonics: using metallic nanostructures as nano-sources of heat”, *Laser & Photonics Reviews* **2013**, *7*, 171–187.

[31] A. L. Koh, K. Bao, I. Khan, W. E. Smith, G. Kothleitner, P. Nordlander, S. A. Maier, D. W. McComb, “Electron Energy-Loss Spectroscopy (EELS) of Surface Plasmons in Single Silver Nanoparticles and Dimers: Influence of Beam Damage and Mapping of Dark Modes”, *ACS Nano* **2009**, *3*, 3015–3022.

[32] M. Kociak, O. Stéphan, “Mapping plasmons at the nanometer scale in an electron microscope”, *Chemical Society Reviews* **2014**, *43*, 3865–3883.

[33] M. Liu, T.-W. Lee, S. Gray, P. Guyot-Sionnest, M. Pelton, “Excitation of Dark Plasmons in Metal Nanoparticles by a Localized Emitter”, *Physical Review Letters* **2009**, *102*, DOI 10.1103/PhysRevLett.102.107401.

[34] X. Wang, Z. Zhang, G. V. Hartland, “Electronic Dephasing in Bimetallic Gold−Silver Nanoparticles Examined by Single Particle Spectroscopy”, *The Journal of Physical Chemistry B* **2005**, *109*, 20324–20330.

[35] S.-H. Ahn, D.-S. Kim, D. Seo, W. Choi, G.-R. Yi, H. Song, Q.-H. Park, Z. H. Kim, “Localized plasmon resonances of bimetallic AgAuAg nanorods”, *Physical Chemistry Chemical Physics* **2013**, *15*, 4190–4194.

[36] D. Denkova, N. Verellen, A. V. Silhanek, V. K. Valev, P. V. Dorpe, V. V. Moshchalkov, “Mapping Magnetic Near-Field Distributions of Plasmonic Nanoantennas”, *ACS Nano* **2013**, *7*, 3168–3176.

[37] J. Dorfmüller, R. Vogelgesang, R. T. Weitz, C. Rockstuhl, C. Etrich, T. Pertsch, F. Lederer, K. Kern, “Fabry-Pérot Resonances in One-Dimensional Plasmonic Nanostructures”, *Nano Letters* **2009**, *9*, 2372–2377.

[38] R. L. Olmon, P. M. Krenz, A. C. Jones, G. D. Boreman, M. B. Raschke, “Near-field imaging of optical antenna modes in the mid-infrared”, *Optics Express* **2008**, *16*, 20295.

[39] L. Douillard, F. Charra, Z. Korczak, R. Bachelot, S. Kostcheev, G. Lerondel, P.-M. Adam, P. Royer, “Short Range Plasmon Resonators Probed by Photoemission Electron Microscopy”, *Nano Letters* **2008**, *8*, 935–940.

[40] H. Okamoto, K. Imura, “Visualizing the Optical Field Structures in Metal Nanostructures”, *The Journal of Physical Chemistry Letters* **2013**, *4*, 2230–2241.

[41] E. J. R. Vesseur, R. de Waele, M. Kuttge, A. Polman, “Direct Observation of Plasmonic Modes in Au Nanowires Using High-Resolution Cathodoluminescence Spectroscopy”, *Nano Letters* **2007**, *7*, 2843–2846.

[42] O. Nicoletti, M. Wubs, N. A. Mortensen, W. Sigle, P. A. van Aken, P. A. Midgley, “Surface plasmon modes of a single silver nanorod: an electron energy loss study”, *Optics Express* **2011**, *19*, 15371.

[43] D. Rossouw, M. Couillard, J. Vickery, E. Kumacheva, G. A. Botton, “Multipolar Plasmonic Resonances in Silver Nanowire Antennas Imaged with a Subnanometer Electron Probe”, *Nano Letters* **2011**, *11*, 1499–1504.

[44] B. S. Guiton, V. Iberi, S. Li, D. N. Leonard, C. M. Parish, P. G. Kotula, M. Varela, G. C. Schatz, S. J. Pennycook, J. P. Camden, "Correlated Optical Measurements and Plasmon Mapping of Silver Nanorods", *Nano Letters* **2011**, *11*, 3482–3488.

[45] B. Rodríguez-González, F. Attouchi, M. F. Cardinal, V. Myroshnychenko, O. Stéphan, F. J. García de Abajo, L. M. Liz-Marzán, M. Kociak, "Surface Plasmon Mapping of Dumbbell-Shaped Gold Nanorods: The Effect of Silver Coating", *Langmuir* **2012**, *28*, 9063–9070.

[46] In *IUPAC Compendium of Chemical Terminology*, (Eds.: M. Nič, J. Jirát, B. Košata, A. Jenkins, A. McNaught), IUPAC, Research Triagle Park, NC, **2009**.

[47] F. J. García de Abajo, A. Howie, "Relativistic Electron Energy Loss and Electron-Induced Photon Emission in Inhomogeneous Dielectrics", *Physical Review Letters* **1998**, *80*, 5180–5183.

[48] F. J. García de Abajo, A. Howie, "Retarded field calculation of electron energy loss in inhomogeneous dielectrics", *Physical Review B* **2002**, *65*, 115418.

[49] J. Pérez-Juste, L. M. Liz-Marzán, S. Carnie, D. Y. C. Chan, P. Mulvaney, "Electric-Field-Directed Growth of Gold Nanorods in Aqueous Surfactant Solutions", *Advanced Functional Materials* **2004**, *14*, 571–579.

[50] L. Scarabelli, M. Coronado-Puchau, J. J. Giner-Casares, J. Langer, L. M. Liz-Marzán, "Monodisperse Gold Nanotriangles: Size Control, Large-Scale Self-Assembly, and Performance in Surface-Enhanced Raman Scattering", *ACS Nano* **2014**, *8*, 5833–5842.

[51] L. Scarabelli, M. Grzelczak, L. M. Liz-Marzán, "Tuning Gold Nanorod Synthesis through Prereduction with Salicylic Acid", *Chemistry of Materials* **2013**, *25*, 4232–4238.

[52] J. Rodríguez-Fernández, J. Pérez-Juste, P. Mulvaney, L. M. Liz-Marzán, "Spatially-Directed Oxidation of Gold Nanoparticles by Au(III)−CTAB Complexes", *The Journal of Physical Chemistry B* **2005**, *109*, 14257–14261.

[53] Y. Yang, W. Wang, X. Li, W. Chen, N. Fan, C. Zou, X. Chen, X. Xu, L. Zhang, S. Huang, "Controlled Growth of Ag/Au Bimetallic Nanorods through Kinetics Control", *Chemistry of Materials* **2013**, *25*, 34–41.

[54] M. Tebbe, C. Kuttner, M. Mayer, M. Maennel, N. Pazos-Perez, T. A. König, A. Fery, "Silver-Overgrowth Induced Changes in Intrinsic Optical Properties of Gold Nanorods: From Non-Invasive Monitoring of Growth Kinetics to Tailoring Internal Mirror Charges", *The Journal of Physical Chemistry C* **2015**, DOI 10.1021/acs.jpcc.5b03155.

[55] S. Zhang, L. Chen, Y. Huang, H. Xu, "Reduced linewidth multipolar plasmon resonances in metal nanorods and related applications", *Nanoscale* **2013**, *5*, 6985–6991.

[56] B. Goris, W. Van den Broek, K. J. Batenburg, H. Heidari Mezerji, S. Bals, "Electron tomography based on a total variation minimization reconstruction technique", *Ultramicroscopy* **2012**, *113*, 120–130.

[57] F. J. García de Abajo, "Optical excitations in electron microscopy", *Reviews of Modern Physics* **2010**, *82*, 209–275.

[58] R. Gómez-Medina, N. Yamamoto, M. Nakano, F. J. G. d. Abajo, "Mapping plasmons in nanoantennas via cathodoluminescence", *New Journal of Physics* **2008**, *10*, 105009.

[59] V. Bastys, I. Pastoriza-Santos, B. Rodríguez-González, R. Vaisnoras, L. M. Liz-Marzán, "Formation of Silver Nanoprisms with Surface Plasmons at Communication Wavelengths", *Advanced Functional Materials* **2006**, *16*, 766–773.

[60] X. Ye, C. Zheng, J. Chen, Y. Gao, C. B. Murray, "Using Binary Surfactant Mixtures To Simultaneously Improve the Dimensional Tunability and Monodispersity in the Seeded Growth of Gold Nanorods", *Nano Letters* **2013**, *13*, 765–771.

[61] X. Ye, L. Jin, H. Caglayan, J. Chen, G. Xing, C. Zheng, V. Doan-Nguyen, Y. Kang, N. Engheta, C. R. Kagan, C. B. Murray, "Improved Size-Tunable Synthesis of Monodisperse Gold Nanorods through the Use of Aromatic Additives", *ACS Nano* **2012**, *6*, 2804–2817.

[62] L. Vigderman, E. R. Zubarev, "High-Yield Synthesis of Gold Nanorods with Longitudinal SPR Peak Greater than 1200 nm Using Hydroquinone as a Reducing Agent", *Chemistry of Materials* **2013**, *25*, 1450–1457.

[63] L. Scarabelli, M. Coronado-Puchau, J. J. Giner-Casares, J. Langer, L. M. Liz-Marzán, "Monodisperse Gold Nanotriangles: Size Control, Large-Scale Self-Assembly, and Performance in Surface-Enhanced Raman Scattering", *ACS Nano* **2014**, *8*, 5833–5842.

[64] F. Garwe, U. Huebner, T. Clausnitzer, E.-B. Kley, U. Bauerschaefer in, *Vol. 5955*, [Online; accessed 2015-07-05], **2005**, 59550T–59550T-8.

[65] M. Hentschel, M. Saliba, R. Vogelgesang, H. Giessen, A. P. Alivisatos, N. Liu, "Transition from Isolated to Collective Modes in Plasmonic Oligomers", *Nano Letters* **2010**, *10*, 2721–2726.

[66] N. Liu, M. L. Tang, M. Hentschel, H. Giessen, A. P. Alivisatos, "Nanoantenna-enhanced gas sensing in a single tailored nanofocus", *Nature Materials* **2011**, *10*, 631–636.

[67] S. Cataldo, J. Zhao, F. Neubrech, B. Frank, C. Zhang, P. V. Braun, H. Giessen, "Hole-Mask Colloidal Nanolithography for Large-Area Low-Cost Metamaterials and Antenna-Assisted Surface-Enhanced Infrared Absorption Substrates", *ACS Nano* **2012**, *6*, 979–985.

[68] S. Aksu, M. Huang, A. Artar, A. A. Yanik, H. Altug in, (Eds.: R. J. Martín-Palma, Y.-J. Jen, T. G. Mackay), [Online; accessed 2015-07-05], **2011**, pp. 810405–810405-6.

[69] S. Aksu, A. A. Yanik, R. Adato, A. Artar, M. Huang, H. Altug, "High-Throughput Nanofabrication of Infrared Plasmonic Nanoantenna Arrays for Vibrational Nanospectroscopy", *Nano Letters* **2010**, *10*, 2511–2518.

[70] D. Weber, J. Katzmann, F. Neubrech, T. Härtling, A. Pucci, "Spectral tuning of IR-resonant nanoantennas by nanogap engineering", *Optical Materials Express* **2011**, *1*, 1301.

[71] J. Aizpurua, P. Hanarp, D. S. Sutherland, M. Käll, G. W. Bryant, F. J. García de Abajo, "Optical Properties of Gold Nanorings", *Physical Review Letters* **2003**, *90*, 057401.

[72] F. de la Peña, M.-H. Berger, J.-F. Hochepied, F. Dynys, O. Stephan, M. Walls, "Mapping titanium and tin oxide phases using EELS: An application of independent component analysis", *Ultramicroscopy* **2011**, *111*, 169–176.

[73] D. Rossouw, G. A. Botton, “Resonant optical excitations in complementary plasmonic nanostructures”, *Optics Express* **2012**, *20*, 6968.

[74] P. B. Johnson, R. W. Christy, “Optical Constants of the Noble Metals”, *Physical Review B* **1972**, *6*, 4370–4379.

[75] S. Kedenburg, M. Vieweg, T. Gissibl, H. Giessen, “Linear refractive index and absorption measurements of nonlinear optical liquids in the visible and near-infrared spectral region”, *Optical Materials Express* **2012**, *2*, 1588.

IV.2 Aqueous Gold Overgrowth of Silver Nanoparticle

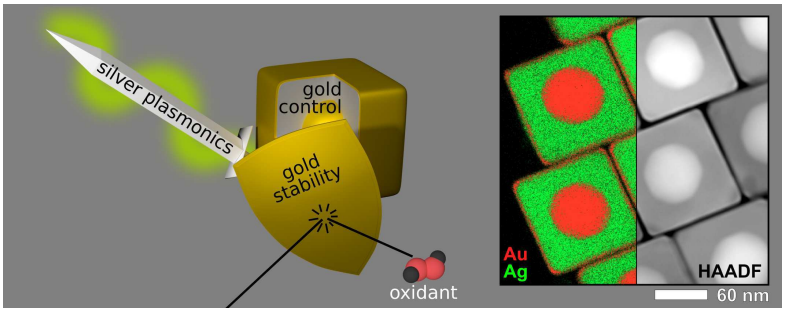

This section is based on the publication *Angewandte Chemie Int. Ed.* **2017**, *56*, 15866–15870. Adapted with permission. Copyright 2017, Wiley-VCH.

By Martin Mayer,[a,b,‡] Anja Maria Steiner,[a,‡] Falk Röder,[a,c] Petr Formanek,[a,c] Tobias A.F. König,[a,*] and Andreas Fery[a,b,d,*]

[a]Leibniz-Institut für Polymerforschung Dresden e.V., Institute of Physical Chemistry and Polymer Physics, Hohe Str. 6, 01069 Dresden, Germany
[b]Cluster of Excellence Center for Advancing Electronics Dresden, Technische Universität Dresden, 01062 Dresden, Germany
[c]Helmholtz-Zentrum Dresden-Rossendorf, Institute of Resource Ecology, Bautzner Landstraße 400, 01328 Dresden, Germany
[d]Department of Physical Chemistry of Polymeric Materials, Technische Universität Dresden, Hohe Str. 6, 01069 Dresden, Germany
‡ contributed equally
* corresponding author

Abstract. To date, it has not been possible to combine the high optical quality of silver particles with good chemical stability and synthetic convenience in a fully aqueous system, while simultaneously allowing chemical surface functionalization. The presented synthetic pathway opens up new possibilities for future developments in information, energy and medical technology where strong optical/electronic properties are crucial. Therefore, the advantages inherent to gold are fused with the plasmonic properties of silver in a fully aqueous Au/Ag/Au core-shell-shell system. These nanoparticles inherit low dispersity from their masked gold cores, yet simultaneously exhibit the strong plasmonic properties of silver. Protecting the silver surface with a sub-skin depth gold layer enables oxidant stability and functionality without altering the silver-controlled optical properties. This combines both worlds—optical quality and chemical stability—and furthermore it is not limited to a specific particle shape.

Gold and silver have emerged as the dominant metals for a vast range of plasmonic applications, *e.g.* optics,[1] sensing,[2] photocatalysis,[3,4] and therapeutics.[5] Based on the requirements of the targeted application, either gold or silver is selected due to their distinct advantages. Gold nanoparticles tend to be chosen for their well-controlled synthesis which results in the accessibility of a variety of well-defined shapes. Moreover, gold surfaces are inert to oxidation, while also allowing chemical functionalization. Therefore, the majority of plasmonics-based breakthroughs, *e.g.* the plasmon ruler,[2] photothermal cancer therapy,[6] chiral dichroic effects,[7] or DNA nanotechnology,[8] have actually been implemented using gold particles. Plasmonic silver nanoparticles, on the other hand, hold great potential due to their plasmonic properties. This prospective utility arises from the dielectric constant of silver, *i.e.*, low damping, excitation over the entire visible spectrum and beyond (>330 nm), and strong plasmonic coupling, ultimately resulting in more pronounced plasmonic effects and higher quality factors. Due to the complementary advantages of these two metals, combining the plasmonic properties of silver with the superior stability and functionality of gold would be tremendously advantageous for the development of plasmonics. However, silver colloids are difficult to synthesize: reaction control and reproducibility are often poor and silver particles tend to oxidize after preparation.[9,10]

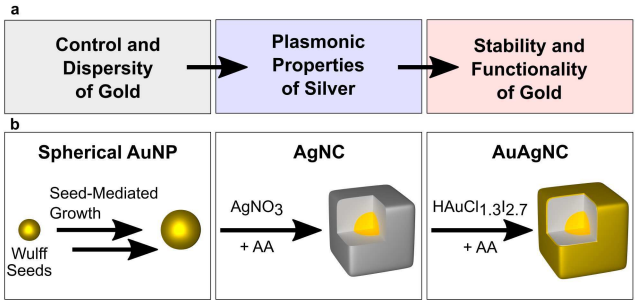

Figure IV.8.: General synthesis pathway exemplarily realized by cubic-shaped nanoparticles. (a) The controlled and well-established seeding of gold as well as its stable and functional surface chemistry are merged with the strong plasmonic properties of silver. (b) Exemplarily: synthesis of spherical single-crystalline AuNSps by seed-mediated growth. Next, facet-selective silver overgrowth to form AgNCs. Finally, gold overgrowth to yield a homogeneous, sub-skin depth gold layer (AuAgNCs).

Commonly, control over silver synthesis is achieved by polyol-reactions in organic solvents.[11] On the one hand, these methods are well-established and even enable gold overgrowth,[12,13] but on the other hand, they can also introduce environmental and synthetic drawbacks, as recently described in detail by Xia and coworkers.[14] Most notably, passivation of the noble metal surface with the long-chain polymer tends to hinder further surface modifications. Here, we show an alternative pathway to overcome this major bottleneck by utilizing short-chain surfactant ligands and a water-based synthesis. Due to the entropic mobility of the short-chain ligands, the active metal surface can easily be modified with a range of functionalities, *e.g.* DNA[15] or conductive polymers.[16] Thus, we developed a general approach to achieve the monodispersity, chemical accessibility, and oxidant stability inherent to gold nanocrystals, while maintaining the advantageous plasmonic properties of silver (**Figure IV.8**).
To exemplify this combination of properties, we use a cubic morphology, since the corners tend to enhance the chemical and plasmonic sensitivity. The synthetic pathway is schematically illustrated in **Figure IV.8b**. The use of gold seeds enables the controlled synthesis of various silver

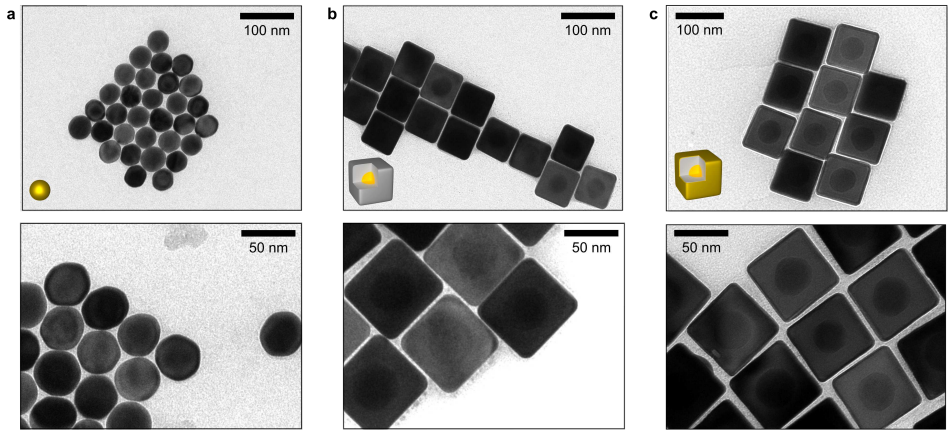

Figure IV.9.: TEM images of the intermediate particles and the final gold protected silver nanocubes (AuAgNCs). Single-crystalline spherical AuNSps (a) are synthesized by three-step seed-mediated growth. Bimetallic AgNCs (gold core, silver cubical shell, (b) are formed by epitaxial silver overgrowth. Gold protected AuAgNCs (c) are obtained by subsequent gold overgrowth of Ag colloids.

morphologies in aqueous dispersions,[17] and therefore, we selected the seed-mediated growth of Wulff seeds to spherical single-crystalline gold nanoparticles (AuNSps).[18] Exploiting these AuNSps as seeds for silver overgrowth *via* facet-selective capping then enables the preparation of silver nanocubes (AgNCs)[a] with sharp edges, a narrow size distribution, and high yield.[19–21] Finally, we achieved a thin gold shell by overgrowth with a Au(III)-iodide complex resulting in AuAgNCs. The gold shell ensures oxidant stability and simultaneously facilitates a variety of chemical functionalization protocols in aqueous dispersions,[22–24] for which we show a proof of concept (**Figure IV.9**). The exemplarily synthesized AuAgNCs show that the low dispersity of the initial gold seeds and the sharp edges of the AgNCs can be intrinsically passed on to the gold protected nanoparticles. The homogeneity of the achieved AuAgNCs was analyzed *via* high-angle annular darkfield transmission electron microscopy (HAADF-TEM) supported by energy dispersive X-ray (EDX) elemental mapping, as shown in **Figure IV.10a**. The gold shell and core can easily be distinguished, and by overlaying the elemental maps of gold and silver, one can see that the gold shells are smooth, conformal and homogeneous around the inner AgNCs.

To ensure a homogeneous shell, it is crucial to balance the kinetics and reduction potentials of silver, gold and reducing agent. Since gold is the most noble metal, and consequently predetermined as protective layer, the required Au(III) precursor salt ($HAuCl_4$) naturally gets reduced by less noble metals.[25,26] This so-called galvanic replacement reaction needs to be completely suppressed by fast reduction of the Au(III) precursor complex and, even more crucial, by lowering the complex's reduction potential. Control over the fast reduction kinetics is achieved by tuning the excess of reducing agent and the temperature (see Methods). Introducing iodide into the precursor complex sufficiently decreases the reduction potential of the gold complex,[27,28] suppressing both etching and galvanic replacement. Since iodide is able to strongly absorb onto gold surfaces, an over-abundance leads to capping of the surface and thus, to retardation of the reduction kinetics.[29] Balancing the iodide/chloride ratio in the Au(III) complex and externally tuning the kinetics by controlled addition of this gold complex leads to an optimized gold shell.

[a]Note: For the sake of simplicity the gold core is neglected in the nomenclature of AgNCs.

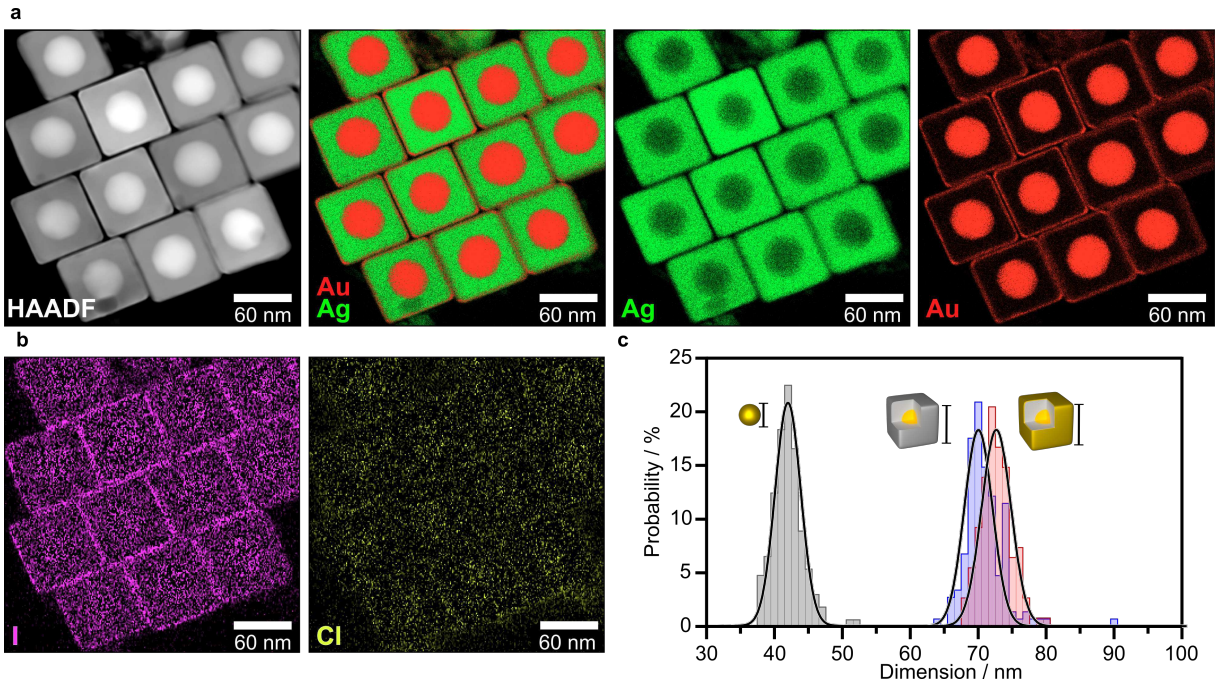

Figure IV.10.: Elemental and statistical evaluation of the overgrowth mechanism. (a) HAADF-TEM image and EDX elemental mappings of silver and gold content in the final AuAgNCs. (b) EDX elemental mapping of iodine (purple) and chlorine (green-yellow) indicating the passivation of the facets by iodide. (c) Histograms of the particle dimensions (diameter for AuNSps 41.3 ± 2.6 nm and edge length for AgNCs 69.7 ± 2.9 nm and AuAgNCs 71.9 ± 3.1 nm).

Since the iodide complexes more strongly with gold than chloride, a quantitative formation of the mixed complex can be assumed.[30] In **Figure IV.10b** the ambivalent role of iodide and the competitive replacement of chloride on the gold surface can be clearly identified by EDX mapping. The particle surface is covered predominantly by iodide, although the concentration of chloride is 20 times greater in the synthesis. The influence of the deployed iodide/chloride ratio on the gold overgrowth is shown in the **Supporting Figure A.IV.11**. The histograms of particle dimensions (see **Figure IV.10c**) summarize the morphological evolution. Starting from the narrowly-distributed single-crystalline AuNSps, the size increases from 41.3 ± 2.6 nm (diameter) to 69.7 ± 2.9 nm (edge length) upon silver overgrowth. During this process the initial dispersity is preserved, while the epitaxial silver growth leads to selective formation of defined shapes. Thus, AgNC with sharp edges are formed (see **Figure IV.9** & **Supporting Figure A.IV.10**). In regard to alternative AgNC synthesis procedures, shape-precision is on par with the state-of-the-art,[14,31,32] and high yields (>90%) are reached under mild conditions and quantitative silver conversion.

Subsequent gold overgrowth results in marginal increment of the edge length by 2 nm and precision of the overgrowth process is revealed by the insignificant change in dispersity during the growth of the protective gold shell. Sharp corners are critical to the sensitivity of the plasmonic system, and therefore edge rounding was evaluated. Negligible rounding of edges was measured after gold overgrowth, suggesting that no corner-specific etching occurs and sharp corners are retained (**Figure IV.11**, for example, the HAADF-TEM image in **Figure IV.9a** and **Supporting Figure A.IV.10**).

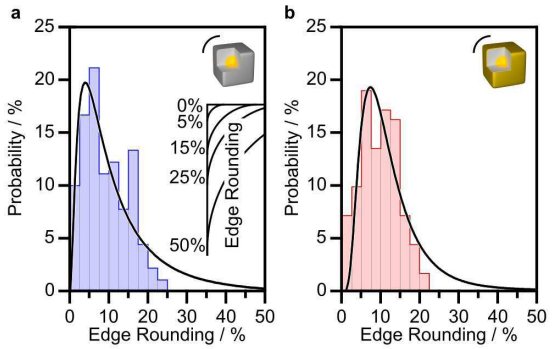

Figure IV.11.: Analysis of the edge rounding. (a) AgNCs (9.3% ± 4.7%) and (b) AuAgNCs (9.4% ± 4.2%) by TEM image analysis of edge length and diagonal length of over 100 particles and calculation of edge rounding for each particle, as defined in equation IV.3. 0% corresponds to a perfect cube; 50% to a perfect sphere (see inset).

The effect of the stepwise overgrowth on optical properties was examined by UV-vis-NIR spectroscopy. **Figure IV.12a** shows the normalized extinction spectra measured for each step in the synthesis pathway. For the spherical AuNSps used as seeding particles, a plasmon resonance peak at a wavelength of 528 nm is observable, and the increased extinction below 515 nm can be assigned to the interband-gap of gold. After silver overgrowth, the predominant mode is shifted to 512 nm. Importantly, the absorption signature of the Au interband transition has vanished. Additional higher-order plasmonic modes arising from the properties of pure AgNCs are found from 350 nm to 450 nm, which indicates low dispersity as well as sharpness of the cube-corners.[33] These features are confirmed by TEM analysis and electromagnetic simulations (see **Supporting Figure A.IV.13**). Thus, the gold core does not influence the plasmonics, and an extinction spectrum resembling that of pure AgNCs is observed.[20,21] After gold overgrowth, the dominant

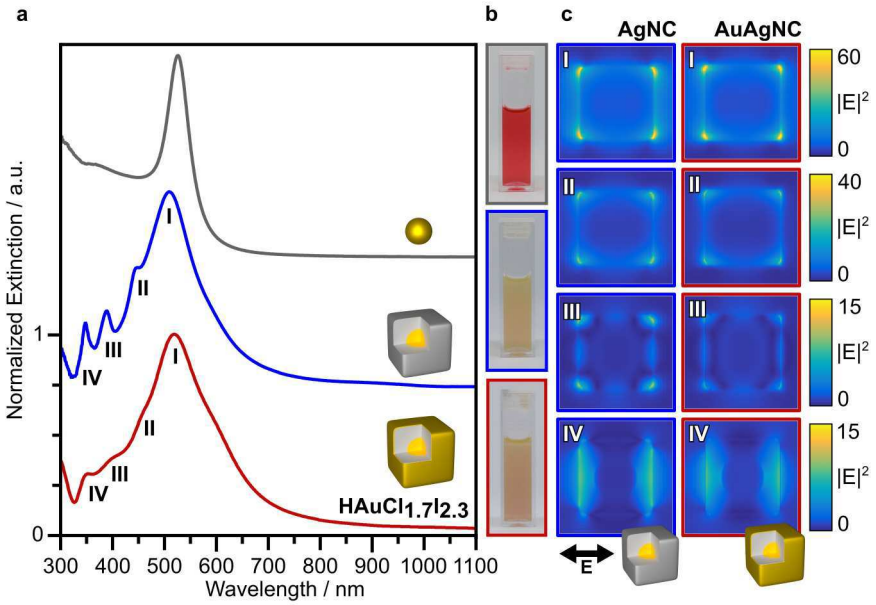

Figure IV.12.: Evolution of plasmonic spectra throughout the synthesis. UV-vis-NIR spectra (a) and photographs of the corresponding colloidal dispersions (b) for single-crystalline gold cores (gray, top), AgNCs (blue, middle), and the final gold-protected AuAgNCs (red, bottom). Electromagnetic simulations of the integrated electric field $|E|^2$ (c) for AgNCs (blue, left) and AuAgNCs (red, right) for the different observable plasmonic modes (I–IV).

plasmonic mode does not shift significantly. Since the overall changes in morphology for the final Au-overgrowth step are minor, variations in plasmonic properties can primarily be attributed to differences in the dielectric functions of gold and silver. Due to the damping of gold, the higher-order modes are less pronounced, but still clearly observable. Since the shell thickness is well below the skin depth for gold, the plasmonics are dominated by the inner AgNCs (see related electromagnetic simulations in the **Supporting Figure A.IV.14 & A.IV.15**), and the characteristic dip of the interband of silver is not damped out by the addition of gold. Comparing the colors of the colloidal dispersions in **Figure IV.12b**, the gold cores show the typical red color, whereas the AgNCs as well as the AuAgNCs have a characteristic yellow-orange color. Since the near-field behavior is the basis for many practical applications,[26,34] the electrical field enhancement was determined using numerical simulations (see **Figure IV.12c**). Comparing the electrical fields of pure AgNCs with the gold coated AuAgNCs the predominant dipolar mode (I) reveals nearly unaffected (99.4%) and also the higher modes clearly show the predicted nature of AgNCs (96.7%, 62.7%, 67.3%, (II–IV) respectively).[33] This behavior of the electrical fields can also be transferred to other particle morphologies, *e.g.,* nanorods, as shown in **Figure IV.13b**.

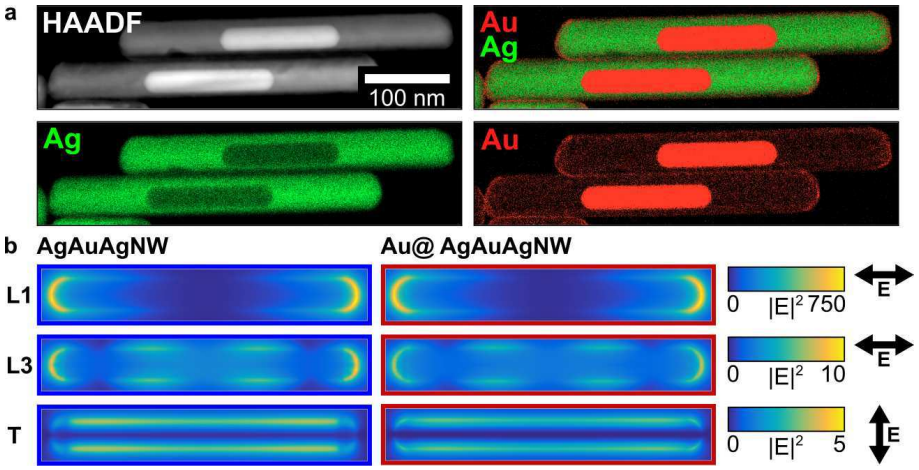

Figure IV.13.: Elemental mapping and electromagnetic simulations for Au@ AgAuAgNWs. (a) HAADF-TEM image and EDX elemental mappings of silver and gold content in the final gold overgrown AgAuAgNWs. (b) Electromagnetic simulations of the integrated electric field $|E|^2$ for pure silver nanorods (left) and gold coated nanorods (right) for all observable (*i.e.*, bright) modes. The electric field enhancement factor of the corresponding modes is almost uninfluenced by the gold coating (97.7%, 86.4% and 77.1% for L1, L3 and T, respectively).

While the morphological as well as the plasmonic properties of AgNCs remain almost unaffected by the overgrowth of a thin homogeneous gold layer, this step has strong effects on the chemical properties of the nanoparticles. The main challenge for applications is stability against oxidants. To test this, we selected an aqueous solution of hydrogen peroxide (H_2O_2) as strong oxidant, commonly used to selectively etch silver.[12] **Figure IV.14a** serves as reference for the fast etching process of AgNCs under the oxidative conditions of a 0.1 vol% hydrogen peroxide solution. After only 5 min, the extinction spectrum blue-shifts and its intensity drops. After 30 min, only the plasmonic response of the gold cores remains, indicating complete removal of silver. In contrast, the extinction spectra of gold-protected AuAgNCs (see **Figure IV.14b**) are completely uninfluenced by a 10-fold greater hydrogen peroxide concentration (1 vol%) maintained for several months. This indicates resistance to even strong oxidants.

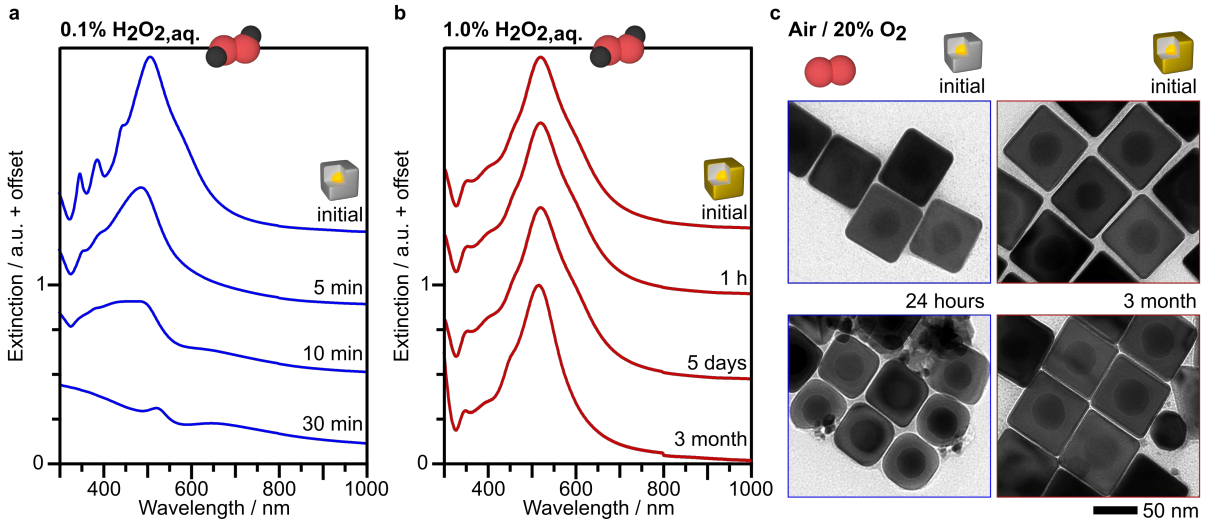

Figure IV.14.: Long-term oxidant stability in dispersed and dried states. (a) Spectral shifts due to fast oxidation of unprotected AgNCs within 30 min by 0.1 vol% hydrogen peroxide solution. (b) Absence of spectral changes for AuAgNCs despite the presence of 1 vol% hydrogen peroxide solution for over 3 months. All spectra are normalized to the initial intensity. (c) Morphological stability in air / 20% O_2 for AgNCs and AuAgNCs on the same TEM grid.

In terms of applications, the stability of silver particles against air (*e.g.* oxygen) plays a particularly important role, and thus, the influence of long-term air exposure was examined more closely. In **Figure IV.14c**, this was studied for AgNCs (left) and AuAgNCs (right) *via* TEM. Unprotected AgNCs clearly developed edge rounding after 24 h. In direct comparison, no degradation or morphological changes were observed for AuAgNCs even after 3 months.

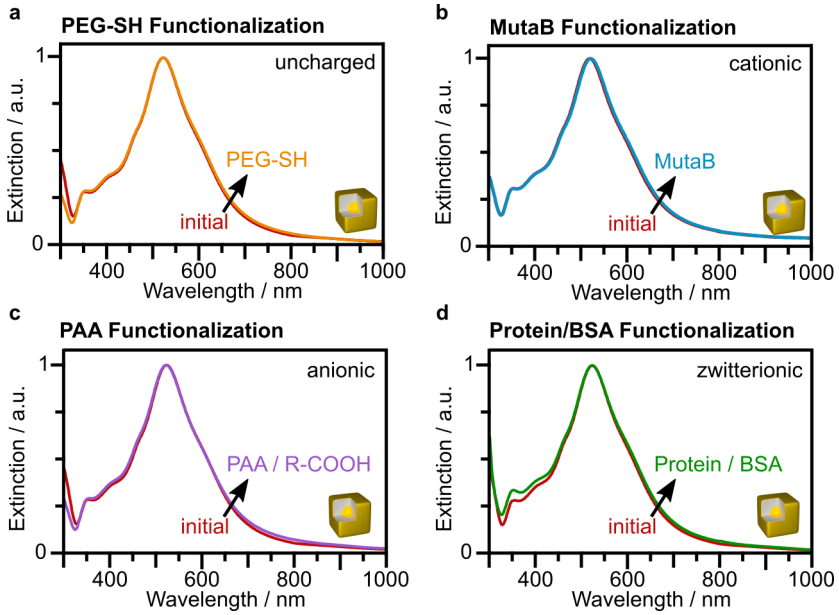

Figure IV.15.: Functionalization of AuAgNCs. Upon functionalization with PEG-SH (polyethylenglycol, 5000 g/mol, a), short-chain ligand (11-mercaptoundecyl)trimethylammonium bromide, MutaB, b), low-molecular weight polyacrylic acid (PAA, 5200 g/mol, c) as well as protein (BSA, d) only minor changes in the extinction spectra are observable, which can be attributed to the difference in absorption of the ligands in the UV range. All spectra are normalized to the initial intensity and plotted without offset.

Additionally, it is worth mentioning that byproducts, *e.g.* tetrahedra, are also generally stabilized, indicating that the gold-passivation protocol is robust toward various facet orientations and can likely be extended to the full range of morphologies accessible for silver colloids in aqueous systems, *e.g.* for AgAuAgNWs, as shown in **Figure IV.13**.
Despite the noble character of gold, surface variability can be achieved based on its strong binding to a variety of functional anchor groups (R-SH, R-NH_2/R-NR_2^2, R-COOH, ...) without being etched or oxidized by the ligand and the ligand-exchange-conditions. To exemplify this, we functionalized AuAgNCs with a short-chain thiol-anchored ligand (11-mercaptoundecyl)trimethylammonium bromide, MutaB, anionic), a low-molecular weight polyethylenglycol (PEG, uncharged) and polyacrylic acid (PAA, cationic), and a protein (BSA, zwitterionic) demonstrating replacement of the stabilizing surfactant without altering the extinction spectrum, as shown in **Figure IV.15**. Such ligand-exchange treatments are critical for most real-world applications, where direct contact between metal and functional coating is required.[35]

In summary, we have developed a synthetic pathway to successfully combine the benefits of silver and gold in a fully aqueous plasmonic system. The overall particle distribution and morphology were initially controlled by an optically masked gold core, and the superior optical properties of silver were protected with a sub-skin depth gold layer. This wet-chemical approach opens new possibilities in scalable bottom-up fabrication, especially integration with plasmonics applications requiring long-term stability. Exploiting the advantages of silver-based plasmonics boosts the sensitivity, but the oxidation resistance and chemical functionality of the fully-accessible noble metal surface is maintained. In combination with the nanometer precision of colloidal self-assembly, a renewed prominence of bottom-up materials for optoelectronics, light harvesting, photocatalysis, sensing and therapeutics can be expected.

Methods

Materials. Ascorbic acid ($AscH_2$, $C_6H_8O_6$, >99%), hexadecyltrimethylammonium chloride (CtaC, 25 wt% in water), hydrogen tetrachloroaurate ($HAuCl_4$, >99.9%), hydrogen peroxide (30 vol%), (11-mercaptoundecyl)trimethylammonium bromide (MutaB, $C_{14}H_{32}BrNS$)), potassium iodide (KI, >99.5%), silver nitrate ($AgNO_3$, 99.9999%) and sodium borohydride ($NaBH_4$, 99%) were obtained from Sigma Aldrich. Hexadecyltrimethylammonium bromide (CtaB, 99%) was received from Merck KGaA. All chemicals and solvents were used as received. Purified water (Milli-Q-grade, 18.2 MΩcm at 25 °C) was used in all preparations. Metal precursor salts were continuously added by a syringe pump system from HLL (model LA120) and fully-siliconized winged infusion sets (Vasuflo; 0.8 × 19 mm; Luer-Lock; 30 cm tube).

Nanoparticle synthesis

In each step, full control over the growth kinetics was ensured by temperature control and dropwise addition using a syringe-pump dispenser.[21] With these measures, side-reactions and non-selective metal reduction were prevented. During the gold overgrowth, fast reduction of the supplied gold(III) precursor was ensured by an excess of reducing agent and elevated temperature. To establish statistical relevance, we measured the distribution of particle morphologies by TEM image analysis (see **Figure IV.9** and **Figure IV.10c**) of at least 150 particles at each

step of the synthesis. Starting from the narrowly-distributed single-crystalline AuNSps, the size increases from 41.3 ± 2.6 nm (diameter) to 69.7 ± 2.9 nm (edge length) upon addition of the silver precursor. This represents an increase of the calculated particle volume by a factor of 9. However, due to partial twinning of the initial Wulff seeds, the AgNCs are accompanied by a small amount of 5–10% tetrahedral and twinned byproducts (see **Supporting Figure A.IV.10**). Subsequent gold overgrowth results in a marginal increment of the edge length from 69.7 ± 2.9 nm to 71.9 ± 3.1 nm representing a small volume increase of 10%. Precision of the overgrowth process is revealed by the insignificant change in dispersity from 4.1% to 4.3% during the growth of the protective gold shell.

Single-crystalline gold Wulff seeds. To 4.7 mL of a 0.1 M CtaB solution, 25 µL of 50 mM $HAuCl_4$ (f.c. 0.266 mM) were added and slowly stirred for 10 min at 32 °C to form the gold precursor complex. Subsequently, 300 µL of a freshly prepared 10 mM $NaBH_4$ were injected under vigorous stirring and stirring was continued for 30 seconds. Prior to the next overgrowth step, the seeds were aged for 25 min at 32 °C to ensure reproducibility and complete deposition of $NaBH_4$.

Single-crystalline spherical gold nanoparticles (AuNSps). Aqueous solutions of CtaC (200 mM, 40 mL), $AscH_2$ (100 mM, 30 mL), and 1 mL of the initial, CtaB-capped Wulff seeds were mixed in a 100 mL beaker. Afterwards, an aqueous $HAuCl_4$ solution (0.5 mM, 40 mL) was quickly injected under stirring (350 rpm). The reaction was allowed to continue at room temperature (RT) for 15 min. These 8 nm gold colloids were collected by centrifugation at 15000 rcf for 1 h and washed with water. For the further growth to 41 nm, the obtained nanospheres were dispersed in 10 mL of an aqueous CtaC solution (10 mM). Thereafter, aqueous solutions of CtaC (50 mM, 200 mL), $AscH_2$ (1 M, 780 µL) and 2.5 mL of the concentrated 8 nm AuNSp solution were mixed. Additionally, 400 mL of a growth solution including $HAuCl_4$ (1.5 mM) and CtaC (55 mM) was prepared and tempered at 45 °C. Next, the growth solution was added dropwise using a syringe pump system at an injection rate of 0.5 mL/min. The reaction was allowed to continue for 12 h at RT after the injection was finished. The final product was collected by centrifugation at 320 rcf for 40 min and washed twice using a 10 mM CtaC solution. For further use, the nanoparticles were redispersed in 15 mL of aqueous CtaC solution (10 mM).

Silver nanocubes (AgNCs with gold core). Silver overgrowth of gold cores was adopted from Mayer *et al.* with minor optimization to the new system.[21] In this process, 25 mL of the 41 nm AuNSp (0.15 mM Au(0)) in 10 mM CtaC was heated to 65 °C. To avoid excess of reactants $AgNO_3$ (10 mM) and $AscH_2$ (40 mM) were added continuously in separate syringes at a rate of 0.333 mol Ag(I) per mol Au(0) and per hour (effective rate 500 µL/h) under slow stirring. At a Ag/Au ratio of one (3 h, f.c. 0.15 mM Ag(I)), the $AscH_2$ concentration was reduced to 10 mM to keep the $AscH_2$/Ag ratio constant. 70 nm silver cubes were received at an Ag/Au ratio of 8 (24 h, f.c. 0.9 mM Ag(I)). After cooling to RT, the AgNCs were centrifuged twice (300 rcf; 1 h) and redispersed in 10 mM CtaC.

Gold overgrowth of silver nanocubes (AuAgNCs). For thin gold coatings, a 12 mL growth solution containing 10 mM CtaC, 125 mM AscH_2 and AgNCs (0.6 mM Ag(0), 0.075 mM Au(0), 6 mL of the as-synthesized concentration) was heated to 65 °C. Next, 20 mL of a 0.125 mM $HAuCl_4$ solution complexed with 0.3 mM KI resulting in the formation of $HAuCl_{1.7}I_{2.3}$ were continuously added at a rate of 2 mL/h under slow stirring. After complete addition, AuAgNCs were centrifuged (300 rcf; 30 min) and redispersed in 1 mM CtaC to remove excessive reactants. Oxidant stability test with hydrogen peroxide. To 1.931 mL of AuAgNC solution in 1 mM CtaC, 69 µL of a 30 vol% hydrogen peroxide solution were added (f.c. 1%) and UV-vis spectra were measured after distinct times. For AgNCs, it was necessary to reduce the oxidant concentration to allow for UV-vis spectroscopy. Consequently, the hydrogen peroxide stock solution was diluted to 3 vol% to yield a final concentration of 0.1 vol%.

Ligand exchange with MutaB. For the functionalization, 1 mg of MutaB was dissolved in 2 mL of the NC solution (f.c. 1 mM CtaC and 0.5 mg/mL MutaB) and incubated for 24 h. Subsequently, the surfactant (CtaC) and excessive MutaB were removed by repeated centrifugation (300 rcf; 30 min) and redispersion in water.

Characterization

Transmission electron microscopy (TEM) measurements were performed with a Libra200 (Zeiss, Germany) with an acceleration voltage of 200 kV. For TEM analysis, 1 mL nanoparticle solutions were concentrated to 100 µL *via* centrifugation, and they were washed twice to reduce the surfactant concentration below the critical micelle concentration (CMC). Subsequently, 2–5 µL of these solutions were dried on a 300 mesh copper grid with carbon film. In the statistical evaluation, plus/minus values noted in the text represent standard deviations taken from the Gaussian fits.

Sharp corners are critical to the sensitivity of the plasmonic system, and therefore edge rounding, ER, was evaluated from the diagonal length, DL, and edge length, EL, using the expression

$$\mathrm{ER} = \frac{\mathrm{EL}/\sqrt{2} - \mathrm{DL}/2}{\mathrm{EL}(\sqrt{2}-1)} \tag{IV.3}$$

Negligible rounding of edges, from 9.3% to 9.4% (**Figure IV.11**), was measured after treatment of AgNCs with the gold(III) precursor salt, suggesting that no corner-specific etching occurs and sharp corners are retained (see, for example, the HAADF-TEM image in **Supporting Figure A.IV.10**)

High-angle annular darkfield scanning transmission electron microscopy and energy dispersive X-ray mappings (HAADF-STEM and EDX) were conducted with a FEI Talos F200X (FEI, USA) operated at 200 kV and equipped with Super-X-EDX detector (Bruker, USA) of 0.9 sr effective solid angle. We further employed a high-visibility-low-background specimen holder for minimized X-ray shadowing. HAADF was performed at a camera length of 98 mm and 2 µs dwell time at 0.8 nA probe current. For the reconstruction of the elemental maps, we applied the energies of the following absorption edges Ag-Lα, Au-Mα-β, Cl-Kα and I-Lα. The EDX data were corrected for background using Bruker Esprit software.

UV-vis-NIR spectra were recorded on a Cary 5000 spectrophotometer (Agilent, USA) and subsequently background corrected by subtraction of a water reference. If not stated otherwise, all spectra were normalized to the maximal intensity of the plasmonic peak.

Numerical electromagnetic simulations were performed by the finite-difference time-domain method (FDTD) using the commercial software FDTD Solutions (ver. 8.11.422, Lumerical Solutions Inc., Canada). For the dielectric properties of silver, a CRC approximation by Hagemann *et al.* was used; for gold, data from Johnson and Christy was used.[36,37] Two meshes were used for the simulation: The nanocubes were simulated with a 0.5 nm mesh to reduce artifacts on the rounded edges, while the surrounding empty space was meshed with 4 nm. AgNCs and AuAgNCs were modeled according to their experimental dimensions and edge rounding. Consequently, for AuAgNCs, the AgNCs were extended by the gold layer, while keeping all other properties constant. To determine the field distributions the model was simulated at the wavelengths of the absorption maxima of the corresponding plasmonic modes (see **Supporting Figure A.IV.14** for the respective wavelengths). Electric field enhancement distributions were integrated along the incident q-vector in order to equally consider edges and corners. All simulations reached a convergence of 10^{-6} before reaching 300 fs simulation time.

Acknowledgments. We thank Kenneth D. Harris from the National Research Council Canada for valuable discussion of the manuscript. This study was funded by the European Research Council under grant ERC-2012-StG 306686 (METAMECH: Template-assisted assembly of METAmaterials using MECHanical instabilities) and the Deutsche Forschungsgemeinschaft (DFG) within the Cluster of Excellence 'Center for Advancing Electronics Dresden' (cfaed). Financial support for TAFK provided by Volkswagen Stiftung Freigeist-Fellowship, grant no. 92 902 is gratefully acknowledged. The use of HZDR Ion Beam Center TEM facilities and the support by its staff is gratefully acknowledged. In particular, we acknowledge the funding of TEM Talos by the German Federal Ministry of Education and Research (BMBF), Grant No. 03SF0451 in the framework of HECMP.

References

[1] J. A. Fan, C. Wu, K. Bao, J. Bao, R. Bardhan, N. J. Halas, V. N. Manoharan, P. Nordlander, G. Shvets, F. Capasso, "Self-assembled plasmonic nanoparticle clusters", *Science* **2010**, *328*, 1135–8.

[2] N. Liu, M. Hentschel, T. Weiss, A. P. Alivisatos, H. Giessen, "Three-dimensional plasmon rulers", *Science* **2011**, *332*, 1407–10.

[3] H. A. Atwater, A. Polman, "Plasmonics for improved photovoltaic devices", *Nat Mater* **2010**, *9*, 205–13.

[4] S. Linic, P. Christopher, D. B. Ingram, "Plasmonic-metal nanostructures for efficient conversion of solar to chemical energy", *Nature Materials* **2011**, *10*, 911–21.

[5] R. R. Arvizo, S. Bhattacharyya, R. A. Kudgus, K. Giri, R. Bhattacharya, P. Mukherjee, "Intrinsic therapeutic applications of noble metal nanoparticles: past, present and future", *Chemical Society Reviews* **2012**, *41*, 2943–70.

[6] X. Huang, I. H. El-Sayed, W. Qian, M. A. El-Sayed, "Cancer cell imaging and photothermal therapy in the near-infrared region by using gold nanorods", *Journal of the American Chemical Society* **2006**, *128*, 2115–20.

[7] W. Ma, L. Xu, A. F. de Moura, X. Wu, H. Kuang, C. Xu, N. A. Kotov, "Chiral Inorganic Nanostructures", *Chemical Reviews* **2017**, *117*, 8041–8093.

[8] C. A. Mirkin, R. L. Letsinger, R. C. Mucic, J. J. Storhoff, "A DNA-based method for rationally assembling nanoparticles into macroscopic materials", *Nature* **1996**, *382*, 607–9.

[9] A. Desireddy, B. E. Conn, J. Guo, B. Yoon, R. N. Barnett, B. M. Monahan, K. Kirschbaum, W. P. Griffith, R. L. Whetten, U. Landman, T. P. Bigioni, "Ultrastable silver nanoparticles", *Nature* **2013**, *501*, 399–402.

[10] M. Erol, Y. Han, S. K. Stanley, C. M. Stafford, H. Du, S. Sukhishvili, "SERS Not To Be Taken for Granted in the Presence of Oxygen", *Journal of the American Chemical Society* **2009**, *131*, 7480–7481.

[11] Y. Sun, Y. Xia, "Shape-controlled synthesis of gold and silver nanoparticles", *Science* **2002**, *298*, 2176–9.

[12] X. Sun, J. Kim, K. D. Gilroy, J. Liu, T. A. Konig, D. Qin, "Gold-Based Cubic Nanoboxes with Well-Defined Openings at the Corners and Ultrathin Walls Less Than Two Nanometers Thick", *ACS Nano* **2016**, *10*, 8019–25.

[13] Y. Yang, J. Liu, Z. W. Fu, D. Qin, "Galvanic replacement-free deposition of Au on Ag for core-shell nanocubes with enhanced chemical stability and SERS activity", *Journal of the American Chemical Society* **2014**, *136*, 8153–6.

[14] S. Zhou, J. Li, K. D. Gilroy, J. Tao, C. Zhu, X. Yang, X. Sun, Y. Xia, "Facile Synthesis of Silver Nanocubes with Sharp Corners and Edges in an Aqueous Solution", *ACS Nano* **2016**, *10*, 9861–9870.

[15] F. N. Gur, F. W. Schwarz, J. Ye, S. Diez, T. L. Schmidt, "Toward Self-Assembled Plasmonic Devices: High-Yield Arrangement of Gold Nanoparticles on DNA Origami Templates", *ACS Nano* **2016**, *10*, 5374–82.

[16] Y. Kim, J. Zhu, B. Yeom, M. Di Prima, X. Su, J. G. Kim, S. J. Yoo, C. Uher, N. A. Kotov, "Stretchable nanoparticle conductors with self-organized conductive pathways", *Nature* **2013**, *500*, 59–63.

[17] S. Gomez-Grana, B. Goris, T. Altantzis, C. Fernandez-Lopez, E. Carbo-Argibay, A. Guerrero-Martinez, N. Almora-Barrios, N. Lopez, I. Pastoriza-Santos, J. Perez-Juste, S. Bals, G. Van Tendeloo, L. M. Liz-Marzan, "Au@Ag Nanoparticles: Halides Stabilize 100 Facets", *Journal of Physical Chemistry Letters* **2013**, *4*, 2209–2216.

[18] Y. Q. Zheng, X. L. Zhong, Z. Y. Li, Y. N. Xia, "Successive, Seed-Mediated Growth for the Synthesis of Single-Crystal Gold Nanospheres with Uniform Diameters Controlled in the Range of 5-150 nm", *Particle & Particle Systems Characterization* **2014**, *31*, 266–273.

[19] Z. Y. Bao, W. Zhang, Y.-L. Zhang, J. He, J. Dai, C.-T. Yeung, G.-L. Law, D. Y. Lei, "Interband Absorption Enhanced Optical Activity in Discrete Au@Ag Core–Shell Nanocuboids: Probing Extended Helical Conformation of Chemisorbed Cysteine Molecules", *Angew Chem Int Ed* **2017**, *56*, 1283–1288.

[20] Y. Ma, W. Li, E. C. Cho, Z. Li, T. Yu, J. Zeng, Z. Xie, Y. Xia, "Au@Ag core-shell nanocubes with finely tuned and well-controlled sizes, shell thicknesses, and optical properties", *ACS Nano* **2010**, *4*, 6725–34.

[21] M. Mayer, L. Scarabelli, K. March, T. Altantzis, M. Tebbe, M. Kociak, S. Bals, F. J. Garcia de Abajo, A. Fery, L. M. Liz-Marzan, "Controlled Living Nanowire Growth: Precise Control over the Morphology and Optical Properties of AgAuAg Bimetallic Nanowires", *Nano Letters* **2015**, *15*, 5427–37.

[22] E. Galati, M. Tebbe, A. Querejeta-Fernandez, H. L. Xin, O. Gang, E. B. Zhulina, E. Kumacheva, "Shape-Specific Patterning of Polymer-Functionalized Nanoparticles", *ACS Nano* **2017**, *11*, 4995–5002.

[23] W. G. Kreyling, A. M. Abdelmonem, Z. Ali, F. Alves, M. Geiser, N. Haberl, R. Hartmann, S. Hirn, D. J. de Aberasturi, K. Kantner, G. Khadem-Saba, J. M. Montenegro, J. Rejman, T. Rojo, I. R. de Larramendi, R. Ufartes, A. Wenk, W. J. Parak, "In vivo integrity of polymer-coated gold nanoparticles", *Nature Nanotechnoloy* **2015**, *10*, 619–23.

[24] L. Vigderman, P. Manna, E. R. Zubarev, "Quantitative replacement of cetyl trimethylammonium bromide by cationic thiol ligands on the surface of gold nanorods and their extremely large uptake by cancer cells", *Angewandte Chemie International Edition* **2012**, *51*, 636–41.

[25] F. Gao, M. Sun, W. Ma, X. Wu, L. Liu, H. Kuang, C. Xu, "A Singlet Oxygen Generating Agent by Chirality-dependent Plasmonic Shell-Satellite Nanoassembly", *Advanced Materials* **2017**, *29*, 1606864.

[26] M. J. Schnepf, M. Mayer, C. Kuttner, M. Tebbe, D. Wolf, M. Dulle, T. Altantzis, P. Formanek, S. Forster, S. Bals, T. A. F. König, A. Fery, "Nanorattles with tailored electric field enhancement", *Nanoscale* **2017**, *9*, 9376–9385.

[27] C. Gao, Z. Lu, Y. Liu, Q. Zhang, M. Chi, Q. Cheng, Y. Yin, "Highly stable silver nanoplates for surface plasmon resonance biosensing", *Angewandte Chemie International Edition* **2012**, *51*, 5629–33.

[28] L. M. Liz-Marzan, M. Grzelczak, "Growing anisotropic crystals at the nanoscale", *Science* **2017**, *356*, 1120–1121.

[29] M. Liu, K. D. Gilroy, H. C. Peng, M. Chi, L. Guo, Y. Xia, "The effect of surface capping on the diffusion of adatoms in the synthesis of Pd@Au core-shell nanocrystals", *Chemical Communications* **2016**, *52*, 13159–13162.

[30] L. Scarabelli, A. Sanchez-Iglesias, J. Perez-Juste, L. M. Liz-Marzan, "A "Tips and Tricks" Practical Guide to the Synthesis of Gold Nanorods", *Journal of Physical Chemistry Letters* **2015**, *6*, 4270–9.

[31] A. Klinkova, E. M. Larin, E. Prince, E. H. Sargent, E. Kumacheva, "Large-Scale Synthesis of Metal Nanocrystals in Aqueous Suspensions", *Chemistry of Materials* **2016**, *28*, 3196–3202.

[32] Q. Zhang, W. Li, C. Moran, J. Zeng, J. Chen, L. P. Wen, Y. Xia, "Seed-mediated synthesis of Ag nanocubes with controllable edge lengths in the range of 30-200 nm and comparison of their optical properties", *Journal of the American Chemical Society* **2010**, *132*, 11372–8.

[33] S. Zhang, K. Bao, N. J. Halas, H. Xu, P. Nordlander, "Substrate-induced Fano resonances of a plasmonic nanocube: a route to increased-sensitivity localized surface plasmon resonance sensors revealed", *Nano Letters* **2011**, *11*, 1657–63.

[34] F. Gao, M. Sun, L. Xu, L. Liu, H. Kuang, C. Xu, "Biocompatible Cup-Shaped Nanocrystal with Ultrahigh Photothermal Efficiency as Tumor Therapeutic Agent", *Advanced Functional Materials* **2017**, *27*, 1700605.

[35] M. L. Brongersma, N. J. Halas, P. Nordlander, "Plasmon-induced hot carrier science and technology", *Nature Nanotechnology* **2015**, *10*, 25–34.

[36] H.-J. Hagemann, W. Gudat, C. Kunz, "Optical constants from the far infrared to the x-ray region: Mg, Al, Cu, Ag, Au, Bi, C, and Al_2O_3", *Journal of the Optical Society of America* **1975**, *65*, 742.

[37] P. B. Johnson, R. W. Christy, "Optical Constants of the Noble Metals", *Physical Review B* **1972**, *6*, 4370–4379.

IV.3 Tailoring the Plasmonics of Silver Nanoparticles

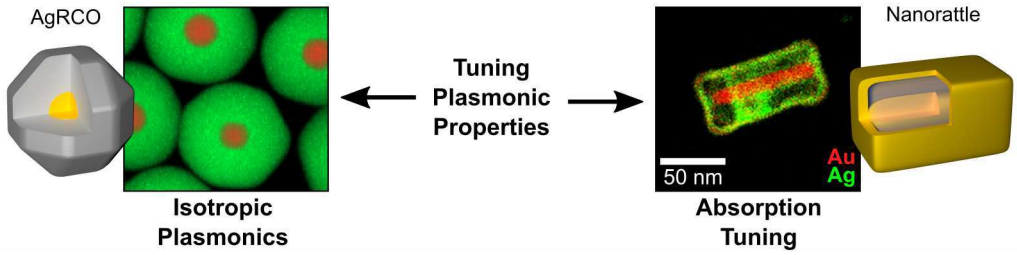

This section is based on the publications *Chemistry of Materials* **2019**, *31*, 2822–2827 and *Nanoscale* **2017**, *9*, 9376–9385.

By Anja Maria Steiner,[a,b,‡] Martin Mayer,[a,b,‡] Daniel Schletz,[a] Daniel Wolf,[c] Petr Formanek,[a,d] René Hübner,[a,d] Martin Dulle,[e] Stephan Förster,[e] Tobias A.F. König,[a,b,*] and Andreas Fery[a,b,f,*]

and

by Max J. Schnepf,[a,‡‡] Martin Mayer,[a,b,‡‡] Christian Kuttner,[a,b] Moritz Tebbe,[g] Daniel Wolf,[c] Martin Dulle,[e] Thomas Altantzis,[h] Petr Formanek,[a] Stephan Förster,[e] Sara Bals,[h] Tobias A.F. König,[a,b,*] and Andreas Fery[a,b,f,*]

[a]Leibniz-Institut für Polymerforschung Dresden e.V., Institute of Physical Chemistry and Polymer Physics, Hohe Str. 6, 01069 Dresden, Germany
[b]Cluster of Excellence Center for Advancing Electronics Dresden, Technische Universität Dresden, 01062 Dresden, Germany
[c]IFW Dresden, Institute for Solid State Research, Helmholtzstr. 20, 01069 Dresden, Germany
[d]Helmholtz-Zentrum Dresden-Rossendorf, Institute of Resource Ecology, Bautzner Landstraße 400, 01328 Dresden, Germany
[e]JCNS-1/ICS-1, Forschungszentrum Jülich GmbH, Wilhelm-Johnen-Straße, 52428 Jülich
[f]Department of Physical Chemistry of Polymeric Materials, Technische Universität Dresden, Hohe Str. 6, 01069 Dresden, Germany
[g]Physical Chemistry II, University of Bayreuth, Universitätsstr. 30, 95440 Bayreuth, Germany
[h]EMAT, University of Antwerp, Groenenborgerlaan 171, 2020 Antwerp, Belgium
‡ contributed equally
‡‡ contributed equally
* corresponding author

This section provides a brief insight into further tweaking of the morphology, and thereby the plasmonics, of silver colloids by an additional oxidative reaction step. There are numerous reasons requiring to tweak the plasmonics, *e.g.*, in order to match to targeted applications or a specific spectral window. Herein, the focus lies on extending the spectral range into the violet and/or to efficiently increase the absorption cross section of silver colloids.

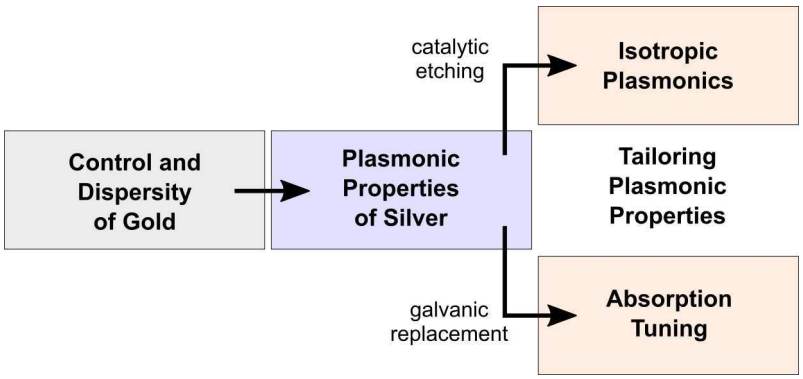

Figure IV.16.: General synthesis concept for the tuning of the plasmonic response. Starting from well-defined silver colloids, the plasmonics can be tuned by changing the particle morphology. By a catalytic etching process isotropic response can be achieved by transforming the morphology of nanocubes to rhombicuboctahedra. Alternatively, by galvanic replacement an internal cavity is formed by etching of cuboids to rattles. The cavity allows to tailor the internal electric field and renders the particles absorption dominated.

As summarized in **Figure IV.16**, this can be achieved by oxidative reaction conditions. On the one hand, facet-selective etching decreases efficiently the anisotropy of silver colloids, resulting in plasmonically isotropic rhombicuboctahedra. On the other hand, by galvanic replacement reactions a plasmonic cavity is formed. The cavity of the resulting axisymmetric nanorattles features a dominating absorption cross section and high electric field enhancement.

Nanoparticles with rhombicuboctahedral shape and isotropic plasmonics

For fundamental studies, but also plasmonic applications, spherical silver colloids are highly important due to their isotropic plasmonic response and simple geometry. Although plasmonic properties are more pronounced in anisotropic or pointy particles, *e.g.,* in nanorods, nanocubes, or nanostars, fundamental plasmonic effects are more intuitive and simple for isotropic particles. Thus, the complex coupling behavior between colloids can be deconvolved to comprehensible models in the case of spheres,[1,2] since the complexity of the individual particles is reduced to a minimum (for example see also **Section V.2**). As a consequence, any additional effects can be contributed to the plasmonic coupling and the influence of the isolated colloid can be excluded.[3] For gold nanoparticles, a variety of well-established synthesis protocols exists resulting in almost perfectly spherical particles.[4–7] However, the plasmonics of gold is limited to the range beyond its interband transition (wavelengths above 515 nm) and additionally, gold is quiet lossy compared to silver.[8–10] In terms of plasmonics, silver is able to extend over the complete visible spectrum (>330nm)[11] and features a remarkable high quality factor for lower wavelengths, thus, making it the superior plasmonic material.[12,13] This spectral range is of particular interest for several applications, since it matches to absorption band gaps of typical metal oxides.[14,15]

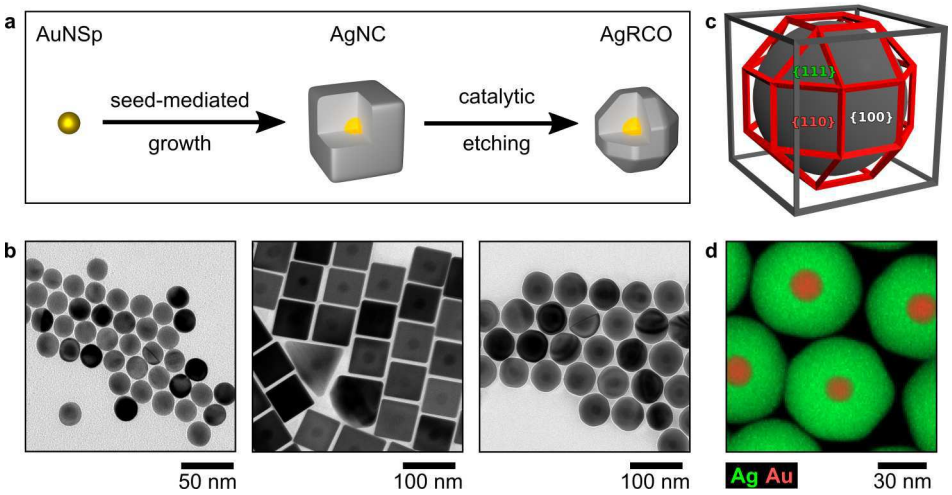

Figure IV.17.: Synthetic pathway to rhombicuboctahedral shaped nanoparticles *via* catalytic etching. (a) AgNC are synthesized by facet-selective silver overgrowth of single-crystalline spherical AuNSp. These AgNCs are then catalytically etched to rhombicuboctahedra (AgRCOs). (b) TEM images of intermediate particles (left: AuNSp; middle: AgNCs) and the obtained AgRCOs (right). (c) 3D sketch of a rhombicuboctahedron to visualize the particle geometry. (d) EDX element distributions of silver and gold in the AgRCOs. Adapted with permission.[16] Copyright 2019, American Chemical Society.

However, the defined synthesis of isotropically behaving silver colloids in aqueous media with low dispersity, (almost perfect) spherical shape, and narrow linewidth of the plasmonics is neither fully controlled nor understood. On one hand, for seed-mediated growth, there is a lack of protocols, which yield single-crystalline and monodisperse seeds.[17,18] On the other hand, silver tends to form low-index crystal facets during growth, resulting in anisotropic nanoparticles with sharp corners.[17,19–21] Thus, isotropic particles are not achievable by common synthetic approaches relying on facet capping and controlled kinetics.[21] To overcome this limitation, oxidative etching can increase the symmetry of the particles by chemically removing the corners and edges.[22,23] As sketched in **Figure IV.17a**, the plasmonics can be rendered isotropic by catalytically etching of well-defined silver nanocubes with a copper-based process.[23–25]
As described in the previous **Sections IV.1 & IV.2**, a single-crystalline gold sphere was employed for silver overgrowth to yield narrowly distributed AgNCs.[19,20] In order to also mask the gold core in the final quasi-spherical shape, comparably small gold particles (22 nm) were selected as seed. In the next step, the corners and edges of the AgNCs were etched by a copper catalyst. The evolution of particles and the elemental composition of the final particle are summarized in **Figure IV.17b&d**.
Whilst a spherical-like shape is typically described in such processes,[23,26,27] we are able to show, that preferentially silver rhombicuboctahedra (AgRCOs) are formed featuring well-defined low-index facets. This morphology, as visualized in **Figure IV.17c**, marks the geometry with the highest ratio of low-index facets for a quasi-sphere, *i.e.*, the most-isotropic achievable shape. Thus, AgRCOs are the thermodynamically most stable product of this synthesis due to the efficient facet capping by chloride. The formation of low-index facts is accelerated by the identified simultaneous silver growth process, which is in equilibrium with the etching process. This balance between etching and growth is fundamental to all catalytic copper-based etching processes and inhibits the formation of high-index facets.

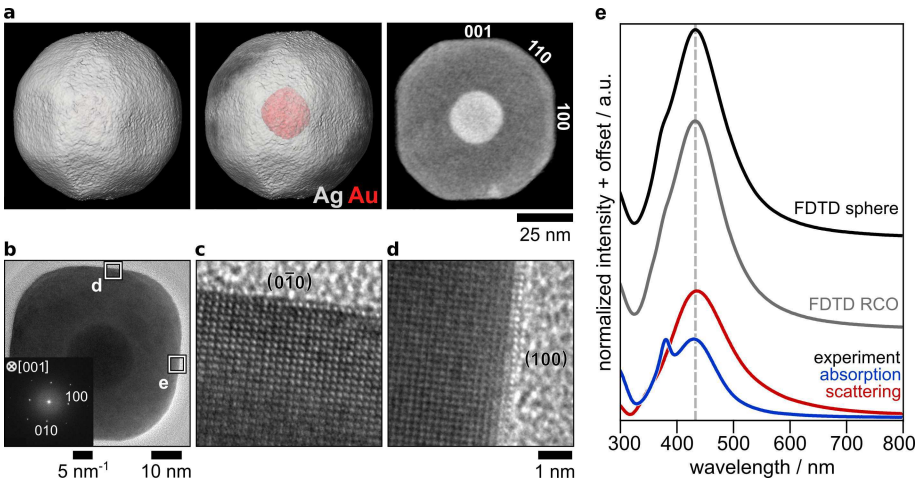

Figure IV.18.: Plasmonics and morphology of AgRCOs. (a–d) 3D iso-surface rendering of the reconstructed TEM tomogram and HRTEM proofing the rhombicuboctahedral shape and the formation of low-index facets. (e) Direct comparison of numerical simulations of a perfect spheres, comparable rhombicuboctahedron, and experimental measurements of the extinction (black) with the respective contribution of scattering (red) and absorption (blue). Adapted with permission.[16] Copyright 2019, American Chemical Society.

As shown in **Figure IV.18** in the 3D TEM tomogram and HRTEM, the morphology clearly is rhombicuboctahedral with well-shaped low-index facets, but the plasmonics behave strictly isotropic. Direct comparison to numerical simulations of a perfect sphere and a simulated RCO (**Figure IV.18e**) additionally reveals the outstanding low polydispersity, which was also determined *via* small angle X-ray scattering (SAXS) to be as low as 3.5%.
Considering the fact, that only isotropic silver particles are able to span into the violet (330–500 nm), the introduced monodisperse AgRCOs are able to extend the optical range due to their isotropic plasmonics. This system, thereby, opens up new possibilities in applications based on collective plasmonic coupling such as lasing,[28,29] photovoltaics,[30] and higher harmonic plasmonics.[31]

Axisymmetric nanorattles with tailored electric field enhancement

Plasmonic nanorattles are metallic core – metallic shell particles, in which the core is separated by a dielectric spacer from the shell.[32,33] To achieve such particle structures, galvanic replacement processes allow to fabricate nanorattles from various silver nanoparticles shapes, *e.g.,* spherical,[34,35] cubic,[36,37] cuboidal,[32] and octahedral.[33] In these particles a plasmonic cavity is formed between core and shell. Due to the resulting extraordinary high electric-field enhancement inside the cavity, nanorattles exhibit improved sensitivity for catalytic applications and plasmonic sensors.[34] In particular, the flat face-to-face contact of the cavity geometry ensures stronger and primarily, more homogeneous electric field enhancement compared to particles with high curvature. Additionally, the induced plasmonic cavity mode renders the particles absorption dominated, despite their size and material.
However, the core of the such nanorattles typically is freely movable inside the box or even worse, stuck to one side of the box. The undefined core position leads to a wide distribution of gap dimensions and as a result, the plasmonic peak is broadened and the respective field enhancement fluctuating.

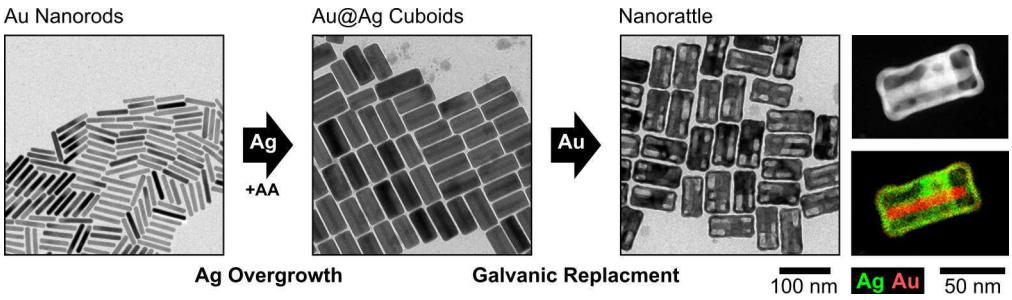

Figure IV.19.: Synthetic pathway to axisymmetric nanorattles by galvanic replacement. As shown in the TEM images, gold nanorods (left) are overgrown with silver (gold@silver cuboids; middle) to obtain axisymmetric nanorattles (right) *via* subsequent galvanic replacement, and EDX element distributions of silver and gold in the final nanorattle (bottom, with respective HAADF-STEM image on top. Adapted under the terms of CC-BY-NC license.[38] Copyright 2017, Royal Society of Chemistry.

In this study, these limitations are overcome by introducing axisymmetric fixation of the inner core to the outer box using state-of-the-art synthesis methods. By employing living silver overgrowth conditions, the obtained silver cuboids are almost exclusively grown into width, due to the facet selective silver deposition.[19,39] Thus, the gold core gets fixed to the outer shell at its tips during the kinetically-controlled galvanic replacement reaction, resulting in axisymmetric nanorattles.[33] This ensures a homogeneous and well-defined cavity size in the entire colloidal ensemble.
As presented in **Figure IV.19**, the synthetic approach starts with a single-crystalline gold nanorod, which in the end will be used as core. In the first step, the nanorod is selectively overgrown to gold@silver cuboids, analogous to **Sections IV.1 & IV.2**. Next, chloroauric acid is continuously added below the kinetic reaction limit in order to suppress etching of the silver shell and favor galvanic replacement. During galvanic replacement gold is reduced on the gold@silver cuboid surface forming a gold–silver alloy shell, as shown in the elemental distribution. For each reduced gold ion, three silver atoms are oxidized, thereby forming the cavity between the exterior gold–silver alloy shell and the inner gold nanorod core.[33,40,41]

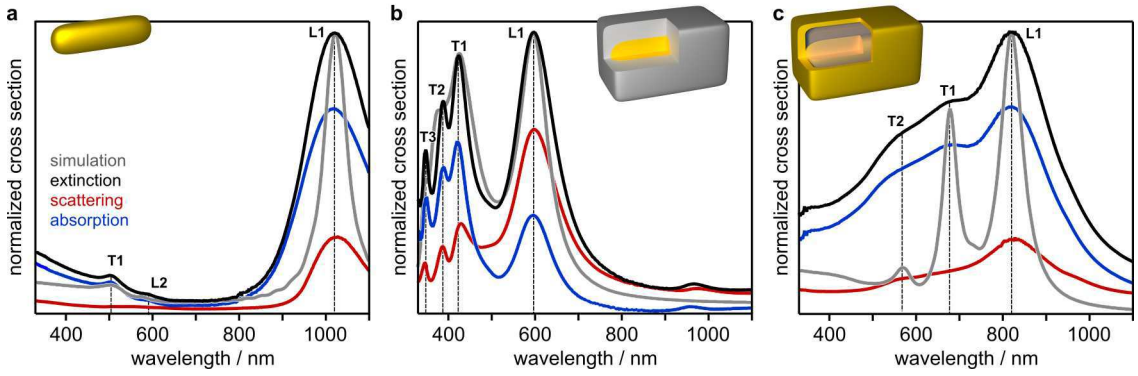

Figure IV.20.: Numerical simulation of the ensemble-averaged geometric model and comparison with absorption, scattering and extinction UV-vis-NIR spectroscopy. Optical response for (a) gold nanorods, (b) gold@silver cuboids, and (c) axisymmetric nanorattles. Numerical simulations (gray) and experimental extinction (black) with respective contribution of absorption (blue) and scattering (red). Adapted under the terms of CC-BY-NC license.[38] Copyright 2017, Royal Society of Chemistry.

The plasmonic evolution during the synthesis steps are shown in **Figure IV.20** by the extinction spectra with the respective contributions of absorption and scattering. The initial gold rod exhibits the predominant L1 mode, the first-order L2 mode, and the transversal T mode, which all are absorption dominated due to their rather small dimensions. Contrary, the longitudinal L1 mode of the cuboid is predominantly scattering and the T1··3 modes are mostly absorbing. As mentioned above, for final axisymmetric nanorattles, all modes are dominated by absorption. In particular, the cavity mode (T1) is almost exclusively absorbing the incident light and is featuring extraordinary high and homogeneous electric field enhancement inside of the plasmonic cavity. Since the final cavity size is directly controlled by the silver overgrowth step, the introduced synthesis protocol allows tailoring of the electric field enhancement, the absorption efficiency, and the spectral position of the cavity mode. For sensing and catalytic applications, an uniform wall thickness is important to ensure efficient coupling of light to the plasmonic cavity. This parameter is then controlled in the next step by the added amount of chloroauric acid.
Consequently, this reliable and up-scalable synthetic approach toward controlled axisymmetric nanorattles adds a further particle type to the in this thesis introduced silver-based building block library. By exploiting these particles in colloidal self-assembly, the intrinsic cavity could open up new possibilities to couple with collective optical effects resulting in novel metasurfaces.[42–45]

References

[1] A. M. Steiner, M. Mayer, M. Seuss, S. Nikolov, K. D. Harris, A. Alexeev, C. Kuttner, T. A. König, A. Fery, "Macroscopic Strain-Induced Transition from Quasi-infinite Gold Nanoparticle Chains to Defined Plasmonic Oligomers", *ACS Nano* **2017**, *11*, 8871–8880.

[2] P. Nordlander, C. Oubre, E. Prodan, K. Li, M. I. Stockman, "Plasmon Hybridization in Nanoparticle Dimers", *Nano Letters* **2004**, *4*, 899–903.

[3] N. J. Halas, S. Lal, W.-S. Chang, S. Link, P. Nordlander, "Plasmons in Strongly Coupled Metallic Nanostructures", *Chemical Reviews* **2011**, *111*, 3913–3961.

[4] N. G. Bastús, J. Comenge, V. Puntes, "Kinetically Controlled Seeded Growth Synthesis of Citrate-Stabilized Gold Nanoparticles of up to 200 nm: Size Focusing versus Ostwald Ripening", *Langmuir* **2011**, *27*, 11098–11105.

[5] M. R. Langille, M. L. Personick, J. Zhang, C. A. Mirkin, "Defining Rules for the Shape Evolution of Gold Nanoparticles", *Journal of the American Chemical Society* **2012**, *134*, 14542–14554.

[6] Y.-J. Lee, N. B. Schade, L. Sun, J. A. Fan, D. R. Bae, M. M. Mariscal, G. Lee, F. Capasso, S. Sacanna, V. N. Manoharan, G.-R. Yi, "Ultrasmooth, Highly Spherical Monocrystalline Gold Particles for Precision Plasmonics", *ACS Nano* **2013**, *7*, 11064–11070.

[7] Y. Zheng, X. Zhong, Z. Li, Y. Xia, "Successive, Seed-Mediated Growth for the Synthesis of Single-Crystal Gold Nanospheres with Uniform Diameters Controlled in the Range of 5-150 nm", *Particle & Particle Systems Characterization* **2014**, *31*, 266–273.

[8] P. B. Johnson, R. W. Christy, "Optical Constants of the Noble Metals", *Physical Review B* **1972**, *6*, 4370–4379.

[9] J. B. Khurgin, "How to deal with the loss in plasmonics and metamaterials", *Nature Nanotechnology* **2015**, *10*, 2 EP.

[10] F. Wang, Y. R. Shen, "General Properties of Local Plasmons in Metal Nanostructures", *Physical Review Letters* **2006**, *97*, DOI 10.1103/PhysRevLett.97.206806.

[11] H.-J. Hagemann, W. Gudat, C. Kunz, "Optical constants from the far infrared to the x-ray region: Mg, Al, Cu, Ag, Au, Bi, C, and Al_2O_3", *Journal of the Optical Society of America* **1975**, *65*, 742.

[12] M. Mayer, M. J. Schnepf, T. A. F. König, A. Fery, "Colloidal Self-Assembly Concepts for Plasmonic Metasurfaces", *Advanced Optical Materials* **2018**, 1800564.

[13] M. Rycenga, C. M. Cobley, J. Zeng, W. Li, C. H. Moran, Q. Zhang, D. Qin, Y. Xia, "Controlling the Synthesis and Assembly of Silver Nanostructures for Plasmonic Applications", *Chemical Reviews* **2011**, *111*, 3669–3712.

[14] K. Awazu, M. Fujimaki, C. Rockstuhl, J. Tominaga, H. Murakami, Y. Ohki, N. Yoshida, T. Watanabe, "A Plasmonic Photocatalyst Consisting of Silver Nanoparticles Embedded in Titanium Dioxide", *Journal of the American Chemical Society* **2008**, *130*, 1676–1680.

[15] P. Christopher, H. Xin, S. Linic, "Visible-light-enhanced catalytic oxidation reactions on plasmonic silver nanostructures", *Nature Chemistry* **2011**, *3*, 467–472.

[16] A. M. Steiner, M. Mayer, D. Schletz, P. Formanek, R. Hübner, M. Dulle, S. Förster, S. Bals, T. A. F. König, A. Fery, "Silver particles with rhombicuboctahedral shape and effective isotropic interactions with light", *Chemistry of Materials* **2019**, *31*, 2822–2827.

[17] S. Zhou, J. Li, K. D. Gilroy, J. Tao, C. Zhu, X. Yang, X. Sun, Y. Xia, "Facile Synthesis of Silver Nanocubes with Sharp Corners and Edges in an Aqueous Solution", *ACS Nano* **2016**, *10*, 9861–9870.

[18] N. G. Bastús, F. Merkoçi, J. Piella, V. Puntes, "Synthesis of Highly Monodisperse Citrate-Stabilized Silver Nanoparticles of up to 200 nm: Kinetic Control and Catalytic Properties", *Chemistry of Materials* **2014**, *26*, 2836–2846.

[19] M. Mayer, L. Scarabelli, K. March, T. Altantzis, M. Tebbe, M. Kociak, S. Bals, F. J. García de Abajo, A. Fery, L. M. Liz-Marzán, "Controlled Living Nanowire Growth: Precise Control over the Morphology and Optical Properties of AgAuAg Bimetallic Nanowires", *Nano Letters* **2015**, *15*, 5427–5437.

[20] M. Mayer, A. M. Steiner, F. Röder, P. Formanek, T. A. F. König, A. Fery, "Aqueous Gold Overgrowth of Silver Nanoparticles: Merging the Plasmonic Properties of Silver with the Functionality of Gold", *Angewandte Chemie International Edition* **2017**, *56*, 15866–15870.

[21] G. González-Rubio, T. M. de Oliveira, T. Altantzis, A. La Porta, A. Guerrero-Martínez, S. Bals, L. Scarabelli, L. M. Liz-Marzán, "Disentangling the effect of seed size and crystal habit on gold nanoparticle seeded growth", *Chemical Communications* **2017**, *53*, 11360–11363.

[22] C. Hanske, G. González-Rubio, C. Hamon, P. Formentín, E. Modin, A. Chuvilin, A. Guerrero-Martínez, L. F. Marsal, L. M. Liz-Marzán, "Large-Scale Plasmonic Pyramidal Supercrystals via Templated Self-Assembly of Monodisperse Gold Nanospheres", *The Journal of Physical Chemistry C* **2017**, *121*, 10899–10906.

[23] H. Jing, Q. Zhang, N. Large, C. Yu, D. A. Blom, P. Nordlander, H. Wang, "Tunable Plasmonic Nanoparticles with Catalytically Active High-Index Facets", *Nano Letters* **2014**, *14*, 3674–3682.

[24] W. Li, P. H. C. Camargo, L. Au, Q. Zhang, M. Rycenga, Y. Xia, "Etching and Dimerization: A Simple and Versatile Route to Dimers of Silver Nanospheres with a Range of Sizes", *Angewandte Chemie International Edition* **2010**, *49*, 164–168.

[25] X. Lin, S. Lin, Y. Liu, M. Gao, H. Zhao, B. Liu, W. Hasi, L. Wang, "Facile Synthesis of Monodisperse Silver Nanospheres in Aqueous Solution via Seed-Mediated Growth Coupled with Oxidative Etching", *Langmuir* **2018**, *34*, 6077–6084.

[26] F. Haber, J. Weiss, "The Catalytic Decomposition of Hydrogen Peroxide by Iron Salts", *Proceedings of the Royal Society A: Mathematical Physical and Engineering Sciences* **1934**, *147*, 332–351.

[27] B. Halliwell, J. M. Gutteridge, "Oxygen free radicals and iron in relation to biology and medicine: Some problems and concepts", *Archives of Biochemistry and Biophysics* **1986**, *246*, 501–514.

[28] A. I. Väkeväinen, R. J. Moerland, H. T. Rekola, A.-P. Eskelinen, J.-P. Martikainen, D.-H. Kim, P. Törmä, "Plasmonic Surface Lattice Resonances at the Strong Coupling Regime", *Nano Letters* **2014**, *14*, 1721–1727.

[29] W. Zhou, M. Dridi, J. Y. Suh, C. H. Kim, D. T. Co, M. R. Wasielewski, G. C. Schatz, T. W. Odom, "Lasing action in strongly coupled plasmonic nanocavity arrays", *Nature Nanotechnology* **2013**, *8*, 506–511.

[30] M. Karg, T. A. König, M. Retsch, C. Stelling, P. M. Reichstein, T. Honold, M. Thelakkat, A. Fery, "Colloidal self-assembly concepts for light management in photovoltaics", *Materials Today* **2015**, *18*, 185–205.

[31] Q. Ai, L. Gui, D. Paone, B. Metzger, M. Mayer, K. Weber, A. Fery, H. Giessen, "Ultra-narrow Second-Harmonic Resonances in Hybrid Plasmon-Fiber Cavities", *Nano Letters* **2018**, *18*, 5576–5582.

[32] Y. Khalavka, J. Becker, C. Sönnichsen, "Synthesis of Rod-Shaped Gold Nanorattles with Improved Plasmon Sensitivity and Catalytic Activity", *Journal of the American Chemical Society* **2009**, *131*, 1871–1875.

[33] L. Polavarapu, D. Zanaga, T. Altantzis, S. Rodal-Cedeira, I. Pastoriza-Santos, J. Pérez-Juste, S. Bals, L. M. Liz-Marzán, "Galvanic Replacement Coupled to Seeded Growth as a Route for Shape-Controlled Synthesis of Plasmonic Nanorattles", *Journal of the American Chemical Society* **2016**, *138*, 11453–6.

[34] J. A. Fan, K. Bao, L. Sun, J. Bao, V. N. Manoharan, P. Nordlander, F. Capasso, "Plasmonic mode engineering with templated self-assembled nanoclusters", *Nano Letters* **2012**, *12*, 5318–24.

[35] N. Gandra, C. Portz, S. Singamaneni, "Multifunctional Plasmonic Nanorattles for Spectrum-Guided Locoregional Therapy", *Advanced Materials* **2014**, *26*, 424–429.

[36] Y. Ma, W. Li, E. C. Cho, Z. Li, T. Yu, J. Zeng, Z. Xie, Y. Xia, "Au@Ag Core−Shell Nanocubes with Finely Tuned and Well-Controlled Sizes, Shell Thicknesses, and Optical Properties", *ACS Nano* **2010**, *4*, 6725–6734.

[37] J.-E. Park, S. Kim, J. Son, Y. Lee, J.-M. Nam, "Highly Controlled Synthesis and Super-Radiant Photoluminescence of Plasmonic Cube-in-Cube Nanoparticles", *Nano Letters* **2016**, *16*, 7962–7967.

[38] M. J. Schnepf, M. Mayer, C. Kuttner, M. Tebbe, D. Wolf, M. Dulle, T. Altantzis, P. Formanek, S. Förster, S. Bals, T. A. F. König, A. Fery, "Nanorattles with tailored electric field enhancement", *Nanoscale* **2017**, *9*, 9376–9385.

[39] M. Tebbe, C. Kuttner, M. Mayer, M. Maennel, N. Pazos-Pérez, T. A. Koenig, A. Fery, "Silver-Overgrowth-Induced Changes in Intrinsic Optical Properties of Gold Nanorods: From Noninvasive Monitoring of Growth Kinetics to Tailoring Internal Mirror Charges", *The Journal of Physical Chemistry C* **2015**, *119*, 9513–9523.

[40] B. Goris, L. Polavarapu, S. Bals, G. Van Tendeloo, L. M. Liz-Marzán, "Monitoring galvanic replacement through three-dimensional morphological and chemical mapping", *Nano Letters* **2014**, *14*, 3220–6.

[41] X. Zhuo, X. Zhu, Q. Li, Z. Yang, J. Wang, “Gold Nanobipyramid-Directed Growth of Length-Variable Silver Nanorods with Multipolar Plasmon Resonances”, *ACS Nano* **2015**, *9*, 7523–7535.

[42] S. Gómez-Graña, J. Pérez-Juste, R. A. Alvarez-Puebla, A. Guerrero-Martínez, L. M. Liz-Marzán, “Self-Assembly of Au@Ag Nanorods Mediated by Gemini Surfactants for Highly Efficient SERS-Active Supercrystals”, *Advanced Optical Materials* **2013**, *1*, 477–481.

[43] T. Thai, Y. Zheng, S. H. Ng, H. Ohshima, M. Altissimo, U. Bach, “Facile gold nanorod purification by fractionated precipitation”, *Nanoscale* **2014**, *6*, 6515–20.

[44] S. P. Burgos, R. de Waele, A. Polman, H. A. Atwater, “A single-layer wide-angle negative-index metamaterial at visible frequencies”, *Nature Materials* **2010**, *9*, 407–12.

[45] W. Fan, S. Zhang, B. Minhas, K. J. Malloy, S. R. J. Brueck, “Enhanced Infrared Transmission through Subwavelength Coaxial Metallic Arrays”, *Physical Review Letters* **2005**, *94*, 033902.

Chapter

Coupled Particle Assemblies

V.1 Self-Assembly of Macroscopic Magnetic Metasurfaces

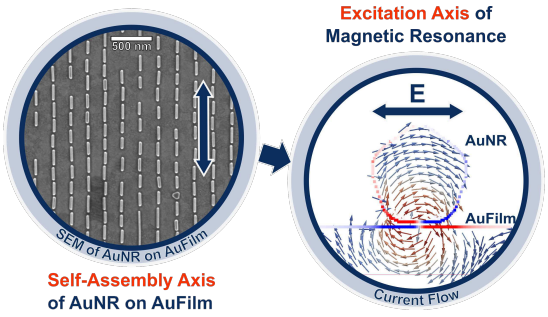

This section is based on the publication *Faraday Discussions* **2016**, *191*, 159–176.

By Martin Mayer,[a] Moritz Tebbe,[b] Christian Kuttner,[a,c] Max J. Schnepf,[a] Tobias A.F. König,[a,c,*] and Andreas Fery[a,c,d,*]

[a]Leibniz-Institut für Polymerforschung Dresden e.V., Institute of Physical Chemistry and Polymer Physics, Hohe Str. 6, 01069 Dresden, Germany
[b]Department of Physical Chemistry II, University of Bayreuth, Universitätsstr. 30, 95440 Bayreuth, Germany
[c]Cluster of Excellence Center for Advancing Electronics Dresden (cfaed), Technische Universität Dresden, 01062 Dresden, Germany
[d]Department of Physical Chemistry of Polymeric Materials, Technische Universität Dresden, Hohe Str. 6, 01069 Dresden, Germany
*corresponding author

Abstract. Template-assisted colloidal self-assembly is presented as a versatile approach for the fabrication of magnetic metasurfaces on macroscopic areas. The choice of anisotropic colloidal particle geometry, assembly pattern, and metallic film is based on rational design criteria, taking advantage of mirror-charge effects for gold nanorods placed on gold film. Monodisperse gold nanorods prepared utilizing wet-chemistry are arranged with high precision on wrinkled templates to form linear array-type assemblies and subsequently transferred to a thin gold film. Due to the obtained particle-to-film distance of 1.1 nm, the plasmonic mode of the nanorod is able to couple efficiently with the supporting metallic film, giving rise to a magnetic mode in the visible spectrum (721 nm). Conventional UV-vis-NIR measurements in close correlation with electromagnetic simulations provide evidence for the presence of a magnetic resonance on macroscopic area. The herein presented scalable lithography-free fabrication process paves the road toward colloidal functional metasurfaces with an optical response in the effective magnetic permeability.

Recent interest in designing metamaterials focuses on the step from 3D bulk materials to 2D metasurfaces, which feature similar optical features.[1–6] Metasurfaces are optical functional interfaces based on regular patterns of subwavelength repeating metaatoms (unit cells). The controlled arrangement of metaatoms allows engineering of novel optical devices based on controlled reflectance,[7,8] efficient energy transport and wave guiding,[9,10] as well as perfect lensing[11] and optical magnetism.[12] For many of these applications, the main challenge is the control of magnetic resonances in the visible optical range. The lack of magnetic response in natural optical materials[13] was first overcome by artificial magnetic resonances obtained for split-ring resonators in the micro-wave regime.[4] However for split-ring resonators, the limited scalability and saturation effects[14] deny their application in the visible optical range. Consequently, the fabrication of nanostructures with magnetic resonances remains a challenge especially on macroscopic areas. The design of such magnetic metasurfaces needs to be rationally linked to scalable fabrication techniques of hierarchical assemblies into quasi 2D-resonators.[6] The incident electric-field component induces oscillating charges within the resonators and, hence, gives rise to an effective magnetic moment; this excitation is commonly referred to as a magnetic resonance.[15–17] To achieve these effects, metasurfaces have to be built with nanometer precision.[18,19] Common fabrication techniques rely on lithographic methods, like e-beam lithography or ion-beam milling, which have several drawbacks, such as losses due to polycrystallinity and lack in resolution and scalability.[20–24] The colloidal bottom-up assembly approach which exploits the advantages of wet-chemically synthesized noble metal nanoparticles (*e.g.*, single-crystallinity, scalability) can provide alternatives to lithographic top-down techniques.[25–27] However, those approaches often rely on random particle deposition, which strongly limits the complexity of prepared unit cells and homogeneity of the obtained metasurfaces.[28–30] To boost the complexity of the fabricated metasurfaces, plasmonic nanoparticles are coupled to metallic films to form mirror charges in the emerging cavities.[8,9,31–33] Template-assisted convective self-assembly allows designing unit cells with high complexity and in a large variety by surface-alignment of nanoparticles in well-defined orientations. Such assemblies are only limited by the scalability and spatial resolution of the directing template.[34–36] In this work, we use a lithography-free colloidal bottom-up approach to fabricate a macroscopic magnetic metasurface. Plasmonic nanoparticles in close contact to a metallic film induce electric current loops due to mirrored charges at the substrate, which give rise to a magnetic mode. We provide theoretical explanations for the experimentally observed magnetic mode through electromagnetic modeling and conventional UV-vis-NIR spectroscopy. Anisotropic nanoparticles are used, due to the following reasons: The short axis of nanorods is used for magnetic mode excitation and their long axes serves for control over their orientation in template-assisted self-assembly. For the building block, we used tailored wet-chemical synthesis to obtain monodisperse, gold nanorods with defined crystalline facets (flat faces). Furthermore, due to a defined spacer material we obtain a reliable particle-to-film distance. By colloidal self-assembly, we were able to fabricate a macroscopic magnetic metasurface, which shows a clear signature of an effective magnetic permeability in the visible wavelength range. With this colloidal approach, we aim at a reliable method to make unique manipulation of light on the macroscale possible.

Design of the Metasurface Unit Cell

One of the central prerequisites to obtain a magnetic resonance is the induction of a circular oscillating current flow within the unit cell. This can be achieved by efficient coupling of the surface plasmon with the electric component of the incident light.[15,37] Isolated nanoparticles in solution inherently exhibit electric modes in the form of localized surface plasmon resonances, as indicated for an exemplary dipolar-isolated electric mode (EM) by its surface charges (**Figure V.1a**, electric mode).[38] Breaking the symmetry is achieved by coupling a plasmonic nanoparticle to a substrate. The emerging modes depend strongly on the substrate material, nanoparticle geometry and particle-to-film distance. In contrast to nanospheres, nanoparticles with flat faces are advantageous because of their larger contact area with the substrate, which results in narrow resonances and enhanced excitation.[39] The interaction of a nanoparticle with a dielectric substrate results in hybridized modes.[40] In contrary, when a particle is coupled to a metallic substrate, the dipolar mode induces a mirror charge pattern at the surface of the metallic film (**Figure V.1a**, magnetic mode (MM)).[41–43] These mirror charges may induce an electric current loop (current density J), as calculated by electromagnetic simulations. According to Ampère's circuital law, a magnetic moment is excited.

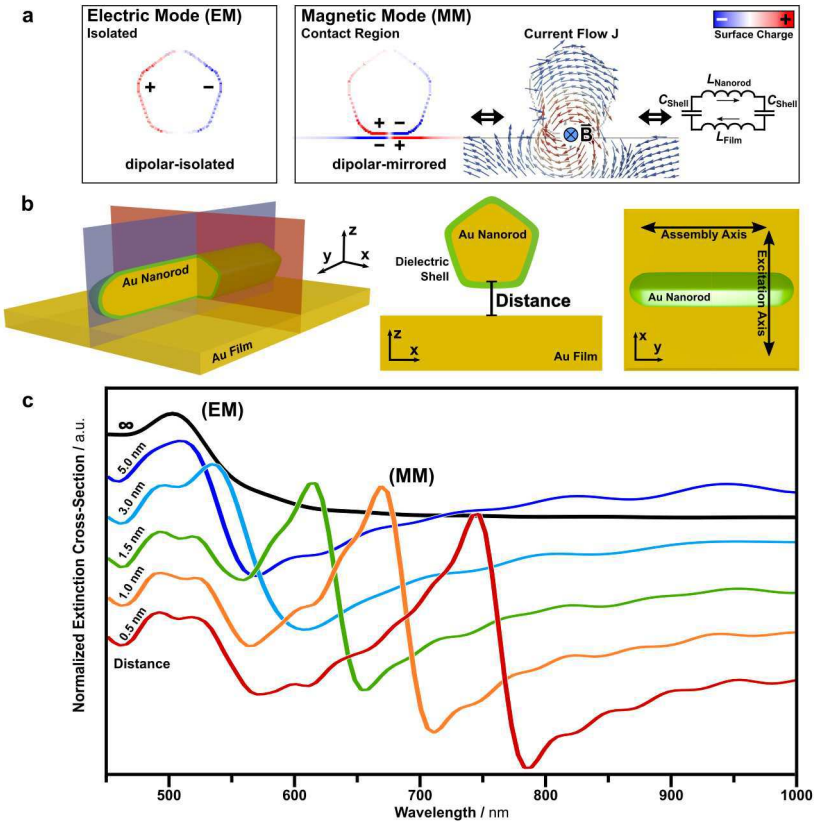

Figure V.1.: Evolution of magnetic modes – from electric to magnetic resonance through metallic film-coupled plasmonic nanoparticles. (a) Surface charge pattern of an electric mode (EM), magnetic mode (MM), characteristic electric current loop (flow J) and representative inductor-capacitor (LC) model for one unit cell. (b) Schematic representation of the unit cell: gold nanorods (160 nm × 30 nm) on a 40 nm thin gold film. The short axis of the nanorod is used for the excitation by linear polarized light (transversal mode) and the long axis is used for directing the assembly process. (c) Calculated extinction cross section at different particle-to-film distances, normalized against the bare gold film.

Recently, Wang *et al.* have numerically demonstrated that magnetic modes can be represented by an inductor-capacitor (LC) model. (**Figure V.1a**).[8] For film-coupled nanoparticles, the metal components act as inductors L, whereas the dielectric insulator acts as a capacitor C. Thus, the resonance wavelengths λ(MM) of the dipolar-mirrored mode (MM) can be expressed by the following equation:

$$\lambda_{MM} = 2\pi c\sqrt{L_{Nanorod}+L_{Film})C_{Shell}/2} \quad (V.1)$$

However, an analytical calculation by means of equation V.1 is not straightforward, since the inductance and the capacitance depend on the curvature and geometry of the nanoparticle. Nevertheless, the model provides an intuitive description of the counter-oscillating currents in the unit cell. Consequently, a metasurface can be designed based on film-coupled nanoparticles. We decided to design our magnetic metasurface based on film-coupled nanorods utilizing their short axis for magnetic mode excitation (transversal mode) and their long axes for providing orientational order upon self-assembly (**Figure V.1b**). The transversal magnetic mode is excited if the electric field component is in plane with the cross section of the unit cell (xz-plane, red). In contrast, the longitudinal magnetic mode, which could be excited with the electric field parallel to the long axis (yz-plane, blue), is significantly shifted outside the frequency range of visible light and will not be further discussed. **Figure V.1b** shows a schematic depiction of the proposed metasurface unit cell consisting of a nanoparticle as building block positioned over a metallic film. The capping agent of the nanoparticle serves as a thin dielectric shell. For observation of the magnetic mode with conventional spectroscopy methods, an array of well-aligned anisotropic nanoparticles is required. For colloidal metasurface design, 1D periodic arrangements are ideal as they provide collective alignment of nanorods along their long axis. At the same time, a distance of at least five nanorod radii between the lines will suppress grating effects.[44] Tip-to-tip coupling within nanorod lines is decoupled from transversal excitation and does not interfere with the induction of the magnetic resonance. Comprehensive numerical simulations of this unit cell clearly reveal, that the spectral position of the magnetic mode can be tailored by tuning the following four parameters: (I) dimensions and shape of the plasmonic nanoparticle; (II) refractive index of the dielectric spacer (*e.g.*, capping agent); (III) material of the plasmonic nanoparticle and (IV) coupling distance between the nanoparticle surface and the substrate. These four parameters need to be precisely balanced to provide a strong magnetic resonance within the visible spectrum. However, tuning of the first three parameters is limited by: (I) the dimension of the nanorods (approximately 30 nm in width);[45] (II) the index of refraction of the spacer material (roughly from 1.4 to 1.5 for polymeric materials);[46] (III) the limited choice in plasmonic metals. Silver as well as gold possess plasmonic properties in the optical range. However, even though silver features lower damping, offering narrower line-widths and higher intensities,[47,48] it is vulnerable against sulfidation and oxidation at air.[49] Consequently, we choose gold in the present study. In contrast, the particle-to-film separation can be controlled by the capping agent and an additional spacer layer at the substrate, *e.g.*, by layer-by-layer techniques.[50] In combination, the cavity size can be tailored with nanometer precision. Taking the limited range of optimization of the nanorod morphology and index of refraction of the building blocks into account, we will focus on the size of the nanoparticle-film cavity in order to further optimize the metasurface design. **Figure V.1c** shows the extinction cross section Q_{ext} of a nanorod at variable distance to a metal-

lic film. The extinction spectra were normalized against the transmission of the bare gold film ($Q_{ext} = -\log T_{coupled\ NR}/T_{Au\ film}$, with respective transmissons T). Owing to the transmission characteristics of gold, the extinction cross sections show a pseudo-resonance below the interband gap of gold (< 512 nm) and a pronounced increase in extinction toward lower energy. The isolated particle monomer, *i.e.* at infinite separation, shows a single plasmonic resonance (electric mode, EM). This transversal excitation corresponds to the electric mode as discussed above. Approaching the surface the dipolar electric mode is converted to a magnetic dipolar-mirrored mode (magnetic mode, MM) and a higher-order magnetic mode. This quadrupolar-mirrored mode is further discussed in the **Supporting Figure A.V.1**. The magnetic resonance shifts toward lower energy in comparison to the isolated electric mode. This characteristic red-shift is also known as plasmon ruler.[51] The spectral position of the magnetic mode is particularly sensitive to distance changes even in the angstrom range. Thus, the resonance frequency may be tuned over the entire optical range. To avoid effects like quantum tunneling, a minimum distance of 0.4 nm should be sustained.[52,53] These separations lie within the range of conventional capping agents.[54] Next, we will address the fabrication of suitable nanoparticles as building blocks.

Synthesis of Well-Defined Building Blocks

Gold nanorods possess intrinsic anisotropy in both their geometrical and optical properties. Thus, nanorods as well as their top-down lithographic equivalents are common building blocks in metamaterial fabrication, *e.g.*, as in the well-known double-bar setup.[15,18,55] The fabrication of hierarchical unit cells at high precision requires building blocks of well-defined size and shape (**Figure V.2**). High structural integrity is critical for the performance of the final system, because disorder and polydispersity in size and shape yield additional undesired resonance broadening. By wet-chemical bottom-up synthesis, a variety of monodisperse building blocks is accessible. In particular, the control over nanoparticle size, shape, and crystallinity allows for tailored morphological and optical properties.[56,57] The used pentatwinned nanorods were prepared by seed-mediated growth based on a modified protocol by Pérez-Juste *et al.*[45,58] combined with a supplemental purification step employing depletion forces.[59,60]

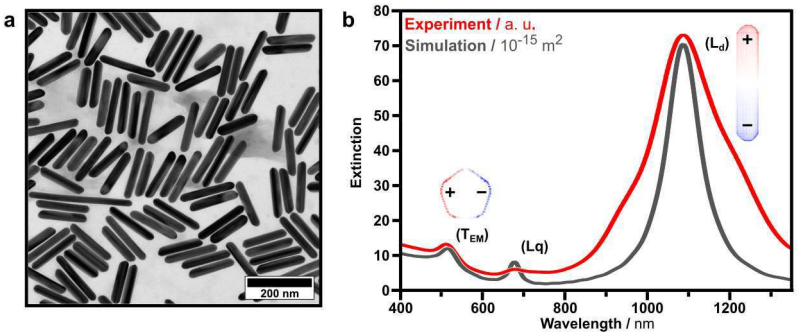

Figure V.2.: Gold nanorods in solution – nature of electric modes. (a) TEM of the purified gold nanorods with mean dimensions of 161.0 ± 14.8 nm in ⟨length⟩ and 30.2 ± 3.7 nm in ⟨width⟩, respectively. (b) Experimental (red) and simulated extinction spectra (black). The gold nanorods exhibit three electric plasmon resonances, which can be attributed to dipolar transversal (TEM, 512 nm), dipolar longitudinal (L_d, 1 087 nm) as well as quadrupolar longitudinal (L_q, 680 nm) modes. The corresponding surface charges of dipolar excitations are shown as insets.

With this method, pentatwinned gold nanorods can be produced which exhibit higher thicknesses and higher aspect ratios compared to the more commonly used single-crystalline gold nanorods.[61] Additionally, their pentagonal cross section and their flat sides are beneficial for substrate-supported effects due to the increased interaction areas. However, owing to the use of twinned seeds only 20% of the resulting nanoparticles are nanorods with the majority being in form of spherical and 2D by-products. These by-products need to be removed as they strongly impede with the bottom-up self-assembly of hierarchical unit cells. Consequently, a supplemental purification step is required to yield narrow distributions. Efficient separation can be achieved by exploiting depletion forces with additional surfactants acting as depletants, as published recently.[59,60] Here, the effective physical parameter is the interaction area – and, thus, the morphology of nanoparticles in solution. To avoid time-consuming screening for an adequate depletant (*i.e.*, surfactant) concentration, we measured a calibration curve which allows purifying pentatwinned gold nanorods depending on their longitudinal localized surface plasmon resonance (see **Supporting Figure A.V.2**). This purification protocol enables almost quantitative removal of spherical by-products and other morphologies. A second purification step is performed to remove longer and thinner nanorods to selectively tune and enhance the size-distribution. **Figure V.2** shows TEM images (a) and extinction spectra (b) of the synthesized and purified nanorod sample. The nanorods exhibited mean dimensions of 161.0 ± 14.8 nm in ⟨length⟩ and 30.2 ± 3.7 nm in ⟨width⟩ (for as-synthesized TEM images, UV-vis spectra and histograms of the size distribution, see **Supporting Figure A.V.2**). Consequently, the herein presented 3-step protocol is an ideal means to precisely tailor the aspect ratio of nanorods. The dipolar electric character of the transversal (TEM) and of the predominant longitudinal plasmon resonance (L_d) are depicted by their surface charges in **Figure V.2** (insets). For successful template-assisted convective assembly the wetting behavior of nanorods is critical. As shown recently by our group, surface chemistry providing enhanced wettability can be adjusted by surface functionalization with a hydrophilic protein shell.[21,55] Consequently, concentrated highly stable solutions of gold nanorods with bovine serum albumin (BSA)[21] as dielectric shells were obtained for subsequent assembly. In dry state, the BSA layer exhibit a shell thickness below 2 nm as we have shown in previous work. Consequently, these nanoparticles match the requirements for reliable template-assisted colloidal self-assembly. In the following, we focus on the self-assembly of nanorods into array-type structures.

Fabrication of Film-Coupled Nanorod Arrays as Magnetic Unit Cells

Controlled colloidal self-assembly of the nanoscale building blocks into the proposed magnetic unit cell is an important step toward a macroscopic magnetic metasurface (**Figure V.3**). Recently, we demonstrated the precise alignment of nanorods into well-defined 1D particle lines by template-assisted convective self-assembly employing wrinkled elastomeric substrates.[55] In a first fabrication step, the nanorods are assembled in form of tip-to-tip arrangements within the periodic structure of the wrinkle. In order to achieve periodic macroscopic alignment in single particle lines the templates need to be homogeneous on square-centimeter scales. The dimensions of its features are crucial and need to precisely match the nanorod dimensions (*i.e.*, width). The employed wrinkled templates are fabricated by plasma treatment of a macroscopic uniaxially stretched polydimethylsiloxane (PDMS) elastomer. The plasma treatment introduces a thin

oxidized film at the surface. Upon strain release, periodic wrinkles are formed due to mechanical mismatch between the substrate and the thin film.[62] The template periodicity is critical for controlling the period of the alignment. To avoid any grating effects the periodicity was chosen sufficiently large (see discussion above for more details). Thus, periodicity and amplitude were tuned to values of 210 nm and 40 nm, respectively.[62] Subsequently, the amplitude was reduced to 20 nm by additional plasma post-treatment without altering the periodicity to match the dimensions of the employed gold nanorods.[55] At the same time, the surface is hydrophilized sufficiently to enable subsequent nanoparticle assembly from aqueous solution (see plasma post-treatment calibration in the **Supporting Figure A.V.3**).

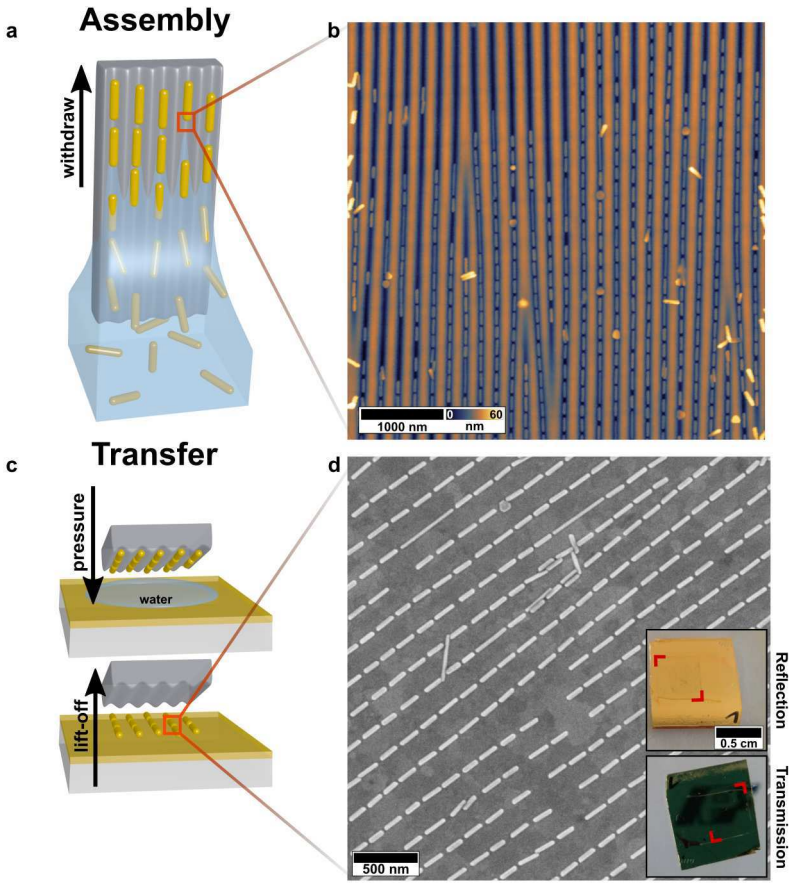

Figure V.3.: Macroscopic template-assisted self-assembly exploiting mechanical instabilities as templates. (a) Schematic template-assisted self-assembly process by dip coating of wrinkled templates from a highly concentrated gold nanorod solution. (b) AFM image of the self-assembled array of gold nanorods in the wrinkle template. (c) Schematic transfer process using wet-contact printing and subsequent lift-off of the emptied template. (d) SEM image of assembled structures transferred to a smooth gold film and photographs of the macroscopic substrate in reflection and transmission (upper and lower inset, respectively).

Nanorod assembly into single particle lines was achieved by dip coating. The unidirectional laminar flow promotes the orientation of the anisotropic particles along the major (long) axis. **Figure V.3a** displays schematically the self-assembly process. Macroscopic templates are withdrawn from a highly concentrated nanoparticle solution (2 mg/mL). During withdrawal, the nanorods are aligned into the channels by capillary forces within the confined meniscus (see **Figure V.3b**). Due to the confinement of the wrinkle structure, we are able to align the building blocks for a further transfer step.

In a second fabrication step, we use the wet-contact print method to transfer the pre-aligned anisotropic nanorods onto the gold film. The building blocks were transferred to a hydrophilized gold film while maintaining their orientational order. Utilizing template stripping a surface roughness of the gold film below 1 nm was achieved. Consequently, a uniform contact between nanorods and supporting gold film is provided. Quantitative transfer can be achieved applying wet-transfer printing of the prefilled templates and subsequent lift-off of the emptied template as schematically depicted in **Figure V.3c**. Contrary to the transfer to other surface materials,[55] an additional adhesion promoter is not required. The combination of van der Waals interactions between gold nanoparticle and gold film and gold-selective binding groups of the protein shell (*e.g.*, amine, thiol) is sufficient to guarantee a complete transfer. Thus, sufficient particle–substrate spacing is given solely by the thickness of the dried shell of the stabilizing agent at the nanorod surface. The successful transfer covers an area of 5 mm $\times$ 5 mm as evidenced by SEM micrographs and macroscopic photographs (see **Figure V.3d**).

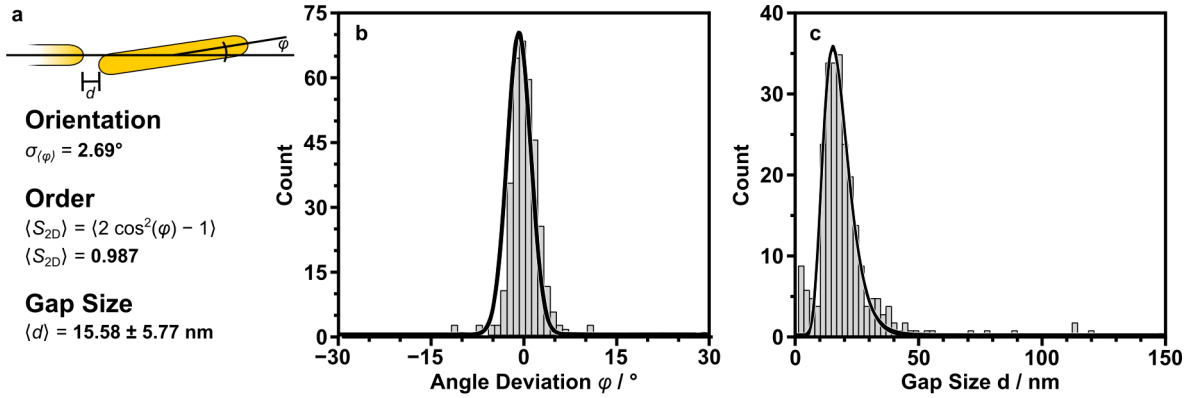

Figure V.4.: Statistical evaluation of the assembly. (a) Schematic depiction of the evaluated angle of deviation and gap size. The evaluation of over 360 individual nanorods reveals a standard deviation of the angle of 2.69°, resulting in a 2D-order parameter of 0.987. The mean gap size in line is 15.6 ± 5.8 nm. Histogram plots of the angle of deviation (b) and gap size (c).

The quality of the assembled structures was evaluated by statistical analysis of the position and orientation of particles in high magnification SEM images (360 individual nanorods, **Figure V.4**). The tip-to-tip particle spacing was determined to be 15.6 ± 5.8 nm within the lines and 209 ± 6 nm between neighboring lines, in-line with the template periodicity. The high structural precision of the assembly was evidenced by the averaged deviation Θ to the principle alignment direction $\langle\sigma_\Theta\rangle$ of only 2.69° corresponding to a 2D-order parameter $\langle S_{2D}\rangle$ of 0.99 ($\langle S_{2D}\rangle = \langle 2\cos^2[\Theta - 1]\rangle$). This large-yield and scalable method enabled us to fabricate a metasurface array of film-coupled nanorods on the macroscale. The following section will elucidate its optical characteristics.

Optical Characterization of Film-Coupled Nanorod Arrays

The optical properties of the macroscopic assemblies were investigated by conventional far-field UV-vis-NIR measurements. Since the magnetic resonance is dominated by absorption, spectrometry was performed in transmission geometry.[63] In order to allow spectroscopy in transmission, the thickness of the gold film was set to 34 nm (**Figure V.3d**, insets). In the visible

wavelength range, the magnetic mode is excited only if the polarized light is in plane with the cross section of the nanorod (transversal mode). Experimentally, this excitation was performed on a spot size of 4 mm $\times$ 4 mm by polarized spectroscopy measurements. **Figure V.5** shows the extinction spectrum normalized against the bare gold film.

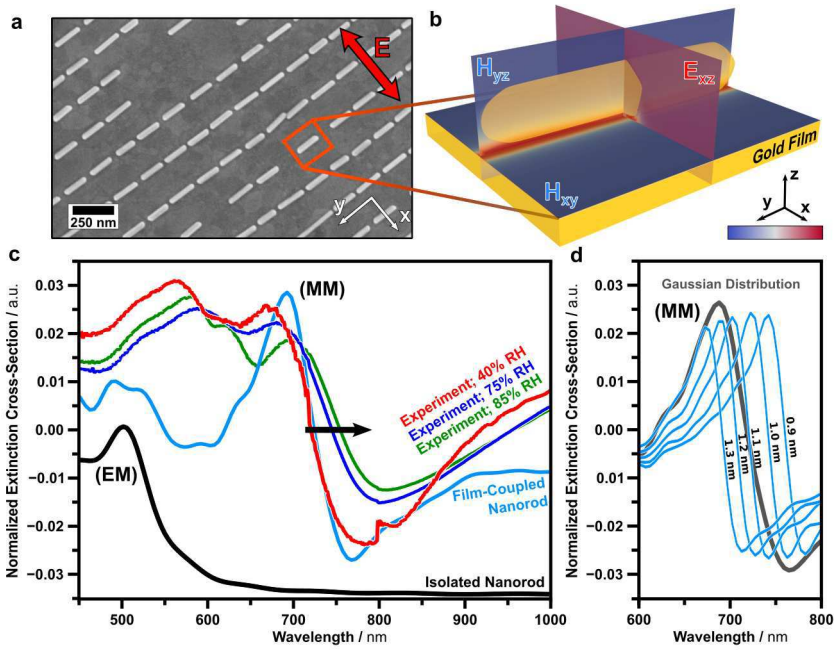

Figure V.5.: Macroscopic magnetic metasurface. (a) SEM image of the template-assisted self-assembled array of film-coupled nanorods. (b) Simulated magnetic ($|H|^2/|H_0|^2$, colored scale range from 1 to 4) and electric field intensity ($|E|^2/|E_0|^2$, colored scale range from 1 to 100) of the unit cell. (c) Experimentally observed UV-vis-NIR (red) and modeled (blue) extinction spectrum of the metasurface. Upon increment of the relative humidity (RH), the mode shifts to higher wavelengths (red 50% RH, blue 75% RH, green 85% RH). Modeled transversal extinction spectrum of an isolated nanorod (black, not to scale). (d) Modeled extinction spectra of the magnetic mode at various particle-to-film distances (0.9 nm to 1.3 nm) and averaged result.

Experimentally we observe the clear spectral signature of a magnetic mode (MM) with its peak intensity at 675 nm and point of inflexion at 721 nm (**Figure V.5c**). In addition, the quadrupolar-mirrored mode at 556 nm is present. The experimental observation is in excellent agreement with the modeling results of a film-coupled nanorod array (blue). The extinction cross section of an isolated nanorod in air (transversal excitation, black) indicates the position of the initial electric mode (EM). From the position of the magnetic mode (MM), a mean particle-to-film distance of 1.1 nm was extracted. This distance is still above the quantum tunneling limit of 0.4 nm.[52] The small deviation between experiment and modeling can be attributed to the high sensitivity toward particle-to-film distances. This influence is determined in **Figure V.5d** for various distance with 0.9 nm to 1.3 nm. This further emphasizes the high sensitivity of the mode for environmental variations. Consequently, macroscopic magnetic substrates may be tuned over the entire visible spectrum. In order to proof the high sensitivity of the magnetic mode, we changed the relative humidity around the sample. As shown in **Figure V.5c**, the magnetic mode shifts toward higher wavelengths, since the incorporation of water molecules results in an increased permittivity of the dielectric shell. A relative humidity change results in a sensitivity to humidity changes of 1.13 $^{\mathrm{nm}}/_{\%\,\mathrm{RH}}$. Remarkably, this plasmonic shift directly correlates to the protein conformational

changes of the BSA monolayer between the particle and the gold film. The conformational changes are only triggered by the humidity changes and could be possibly exploited to track other external or biological stimuli of proteins.

Effective Magnetic Properties of the Metasurface

To quantify the magnitude of the magnetic response of the metasurface, we modeled the effective optical properties using the S-parameter retrieval method established by D.R. Smith *et al.*[64] This method is in close analogy to the inductor-capacitor (LC) model (see equation V.1 and **Figure V.6a**). For this purpose, the anisotropic optical response must be calculated in forward and backward direction (S-parameters). The model was build based on the identical parameters (*i.e.*, nanorod dimensions, shell and film thickness, particle-to-film distance) as described above.

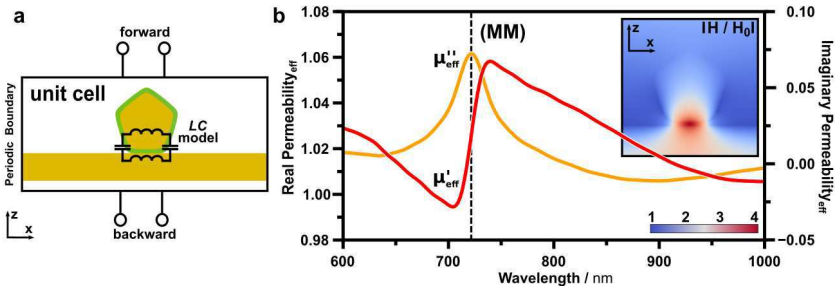

Figure V.6.: Effective magnetic properties of film-coupled nanorods. (a) Schematic representation of the S-parameter retrieval method and the inductor-capacitor (LC) model. The unit cell is treated as an effective media, since only the S-parameters are evaluated in forward and backward direction. (b) Calculated magnetic permeability for the film-coupled nanorod revealing the presence of a magnetic resonance and related magnetic field (inset).

Before we can understand the effective magnetic permeability of the unit cell, we will discuss the optical properties of the following building blocks: (I) gold nanorod monomer and (II) the bare gold film (**Supporting Figure A.V.4**). These steps are important to proof the stability of the S-parameter method in this frequency range. (I) The calculated effective electric permittivity of the bare gold film (40 nm thickness) agrees well with literature values (see methods part). (II) The optical properties of the individual gold nanorod monomer are of particular interest for colloidal optical metamaterial design, because the bulk real part of the permittivity of gold is always negative. Once the metallic particle is surrounded by dielectric, the real part of the permittivity turns positive, which is in well agreement with observation described in literature.[65] Adding a film to the nanorod will result in clear response in the complex magnetic permeability (**Figure V.6b**). The imaginary part of the permeability reveals the energetic location of the magnetic resonance through its characteristic peak at the point of inflexion of the extinction, whereas the real part shows the typical slope at the same energy. This relation is defined generally as Kramers-Kronig relation, which indicates the relation between absorption and dispersion, respectively. At the same energy, also an electric response was observed in the permittivity (**Supporting Figure A.V.4**). Consequently, the observed resonances show a mode characteristic for an electric and a magnetic resonance. This is not surprising due to the strong electromagnetic coupling of the plasmonic particle to the metallic film. We want to advice that the retrieved values below the interband gap of gold (< 515 nm) should be taken with caution. In this short wavelength regime the permittivity is in the non-radiative limit for a surface plasmon resonance, which renders the

response of the particle to a highly damped mode.[66] However, the signature of the magnetic mode is clearly revealed by the magnetic permeability. Consequently, the herein fabricated system represents a magnetic metasurface, which is capable to tune the effective permeability by the induction of a magnetic moment.

Conclusion

Within this study, we developed a scalable colloidal self-assembly approach toward magnetic metasurfaces using anisotropic metal nanoparticles coupled to a supporting noble metal film. The assembly was based on a rational design strategy, which used the short axis for magnetic mode excitation and the long axis for the template-assisted self-assembly process. In particular, our approach utilizes mirror charges induced by the gold nanorods into the gold film to excite a magnetic resonance. With this approach, we were able to identify a suitable unit cell geometry: (I) anisotropic building block with flat faces to ensure a large contact area to the supporting substrate; (II) suitable spacer material for well-defined nanoscale particle-to-film distance and (III) sufficient line-to-line spacing to neglect grating effects. The building blocks are assembled through a template-assisted colloidal self-assembly technique resulting in well-defined orientation and scalability. Applying nanoparticles with a thin homogeneous dielectric shell enabled us to realize a mean coupling distance of 1.1 nm. The 2D-order parameter was determined to be close to unity (0.99) clearly proofing the high potential of the employed convective self-assembly technique. Conventional UV-vis-NIR spectroscopy in close agreement with electromagnetic simulations was used to reveal the signature of the optical properties of the fabricated magnetic metasurface. The main target optical feature, the magnetic resonance, was identified at a wavelength of 721 nm. Retrieval of the effective optical properties (S-parameter method) clearly identified its presence and magnetic mode in absorption as well as dispersion. Achieving optical metasurface features on macroscopic areas requires assembly concepts that are robust in the sense that local variations are suppressed or can be tolerated. In the present study, we achieve robustness in several ways: First, the use of nanorods allows for control over orientational order by exploiting their intrinsic anisotropy (anisotropy in geometrical and optical properties), which is demonstrated by the high 2D-order parameter. In addition, line spacing (structure periodicity) much larger than the relevant particle length scale (in this case the particle width) grants robustness by suppressing undesired coupling between lines. Finally, the use of a defined nanoparticle coating as a spacer layer results in uniform particle-to-film distance. In terms of functionality, these aspects allow for extension of this concept to a functional magnetic metasurface. In particular, the high sensitivity of the film-coupled concept (sharp drop of the magnetic resonance) makes it interesting for sensing applications. To extend the functionality, for example, stimulus responsive polymers could be used as spacer layers and thus translate configurational changes into an optically detectable response. As a proof of concept we were able to track the conformational changes of the protein monolayer around the particles toward changes of the relative humidity of the environment. Thus, the proposed approach can be generalized toward the colloidal fabrication of functional optical metasurfaces on macroscopic area.

Methods

Materials. Ammonia hydroxide solution (NH_3, 25%), ascorbic acid ($AscH_2$, $C_6H_8O_6$, >99%), benzyldimethylhexadecylammonium chloride (BdaC), bovine serum albumin (BSA, 98%), hydrogen peroxide (H_2O_2, 30%), hydrogen tetrachloroaurate ($HAuCl_4$, >99.9%) and sodium borohydride ($NaBH_4$, 99%) were purchased from Sigma Aldrich. 1 M sodium hydroxide (NaOH) solutions and trisodium citrate ($Na_3C_6H_5O_7$, >99%) were supplied by Grüssing. Hexadecyltrimethylammonium bromide (CtaB, 99%) was received from Merck KGaA. Hexadecyltrimethylammonium chloride (CtaC, 99%) was supplied by Molekula. Sylgard 184 PDMS elastomer kit was purchased from Dow Corning. NOA81 UV Curing Optical Adhesive was supplied by Norland Products. Gold films were evaporated on RCA-SC1 cleaned silicon wafers. All chemicals and solvents were used as received. MilliQ-grade water (18.2 MΩcm, pH 8) was used as solvent in all preparations.

Pentatwinned Gold Nanorod Synthesis. The pentatwinned gold nanorod synthesis protocol was adopted from Pérez-Juste *et al.* with some recently published optimizations.[45,58] 3.5 nm sized citrate-capped gold seeds: Briefly, 20 mL of a 0.125 mM $HAuCl_4$, 0.25 mM trisodium citrate aqueous solution was prepared and stirred for 10 min at room temperature. Next, 600 µL of a freshly prepared 0.1 M $NaBH_4$ solution was added quickly under vigorous stirring. After 2 min, the stirring rate was reduced and the seeds were aged for 40 min under slow stirring at room temperature. To ensure complete removal of excessive $NaBH_4$, the solution was stirred at 40–45 °C for another 10 min. 5.5 nm-sized CtaB-capped gold seeds: 8 mL of a growth solution consisting of 40 mM CtaB and 0.125 mM $HAuCl_4$ was prepared. The Au(III) was reduced to Au(I) utilizing 20 µL of a 0.1 M $AscH_2$ solution (f.c. 0.25 mM). Then, 1333 µL of the citrate-capped gold seeds were added quickly and the solution was mixed 30 s by Vortex-Finger treatment thoroughly. The 5.5 nm-sized CtaB-capped gold seeds were aged for 3 h at 23 °C prior the final overgrowth step. Pentatwinned gold nanorod growth: 4 L of a growth solution containing 8 mM CtaB and 0.125 mM $HAuCl_4$ was prepared. The solution was thermostated at 20 °C for at least 30 min. Next, 12.5 mL of a 0.1 M $AscH_2$ solution (f.c. 0.313 mM) was added and gently stirred leading to a clearance of the solution within minutes. Finally, 6.67 mL of 5.5 nm-sized CtaB-capped seeds were added quickly and mixed thoroughly. For the nanorod growth, the solution was thermostated at 20 °C overnight.

Nanorod Purification. Nanorod purification was carried out analogous to the purification protocol by Scarabelli *et al.*[60] For pentatwinned gold nanorods of an averaged length and width of about 160 nm and 30 nm, respectively, the final surfactant (CtaC) concentration, determined by the calibration curve in **Supporting Figure A.V.2**, was set to 70 mM with a 25 wt% CtaC solution leading to selective flocculation and sedimentation overnight. The supernatant was discarded and the sediment containing the nanorods was redispersed in 12 mL of a 10 mM BdaC solution for the next purification step. The longer gold nanorods were slowly sedimented in a 10 mM BdaC solution in the course of 5 days. The targeted gold nanorods in the supernatant were collected and the longer nanorods in the precipitate discarded.

Ligand Exchange and Functionalization. For functionalization with BSA, the BdaC concentration of 6 mL of a pentatwinned gold nanorod solution was set to 0.5 mM (correlates to the critical micelle concentration CMC of BdaC) by repeated centrifugation at 1400 rcf for 30 min. Directly before functionalization, the surfactant concentration was reduced below the CMC to 0.25 mM by dilution. The nanorod solution was added quickly to a 30 mL BSA solution (pH 8, 10 mg/mL) containing 0.02 wt% trisodium citrate under sonication. After 20 min sonication, the solution was centrifuged at 1500 rcf for 45 min and the concentrated nanorods were redispersed in one drop of NaOH solution at a pH 11 and diluted with 30 mL BSA solution (pH 10, 1 mg/mL) containing 0.02 wt% trisodium citrate. Finally, after incubation overnight at 4 °C, the BSA-functionalized gold nanorods were washed 3 times at 1500 rcf for 45 min with NaOH solution at a pH value of 10.5 to remove excess protein. Subsequently the solution was concentrated to a gold concentration of 2 mg/mL.

Wrinkle Preparation as Templates. Wrinkled templates with a wavelength and amplitude of approximately 210 nm and 30 nm, respectively, were produced as described elsewhere.[55] Briefly, PDMS was prepared by casting 25 g of the mixture of cross-linker and pre-polymer (1:5 w/w) in a balanced polystyrene dish (10 cm × 10 cm). First, the PDMS was pre-cross-linked at room temperature for 24 h and afterwards cross-linked at 80 °C for 4 h. The final PDMS was cut into 1 cm × 4.5 cm stripes and individually stretched above the critical strain in a home-built stretching apparatus. Next, the stripes were plasma-treated for 1200 s in an oxygen atmosphere at 0.6–1.2 mbar and relaxed slowly after cooling to room temperature inducing wrinkle formation. The wrinkled PDMS substrates were cut into 1 cm × 0.7 cm templates. To adjust the amplitude to the desired value of 15–20 nm the substrate was post-treated with oxygen plasma at 0.6 mbar with a power of 100 W for 540 s (see calibration curve in **Supporting Figure A.V.3**). Finally, the templates were covalently fixed on plasma-activated glass stripes (6 mm × 76 mm) with the wrinkles oriented parallel to the long axis of the glass slides, which later act as fixture for the subsequent assembly process by dip-coating.

Substrates. Smooth gold film substrates were produced by template stripping. Therefore, a 34.19 ± 0.02 nm thick gold film was evaporated on a RCA SC-1 cleaned silicon wafer without adhesive agent. Afterwards, 1.5 cm × 1.5 cm glass slides were placed with 3 µL of NOA81 UV Curing Optical Adhesive and cured with an approximated energy exposure of 2 J/cm^2 from a hand-held UV light source followed by 12 h final curing at 50 °C. Finally, the glass slides were carefully stripped using a scalpel with the smooth gold film on top. The resulting gold films exhibited a root-mean-square roughness (RMS) of 0.38 nm and were spectral transparent within an optical window between 400 nm and 750 nm.

Convective Self-Assembly and Transfer. Template-assisted convective self-assembly of gold nanorods was performed by dip-coating as published recently by Tebbe *et al.*[55] Therefore, the wrinkled templates fixed on the glass stripe were clamped into the dip coater and moved into 1 cm × 1 cm glass cuvettes, which act as container. Afterwards, 600 µL of the gold nanorod solution (2 mg/mL, pH 10.5, BSA-stabilized) was poured slowly into the container. Assembly is performed by withdrawing of the template with a commercially available dip coater (DC/D/LM

system, KSV Instruments, Germany) at a speed of 10 µm/min. Transfer to the gold substrate was adopted from Hanske *et al.*[21] Briefly, the gold substrate was hydrophilized with oxygen plasma for 7 min (0.2 mbar, 100 Ws). The resulting hydrophilic gold substrate was wetted with 6 µL of a pH 10.5 NaOH solution and the nanorod-filled template was pressed with a pressure of 140 kPa on the substrate. After 5 h, the water was dried and the template was carefully lifted off.

Modeling and Numerical Simulation. A commercial-grade simulator from Lumerical Solutions, Inc. (FDTD Solutions, Version 8.11.442 on Linux x86_64) based on the finite-difference time-domain (FDTD) method was used to perform the calculations. The pentatwinned gold nanorods were modeled with a pentagonal cross section in water (constant index of refraction of 1.333) and a rounded cap to represent their true structure. Nanorod dimensions were set according to TEM analysis (see size distributions in **Supporting Figure A.V.2D–E**, 161 nm $\times$ 30 nm) and the rods are covered with a homogeneous 3 nm layer of BSA with a fixed index of refraction of 1.48. The edge rounding and tip length were rendered to agree with experimental UV-vis-NIR measurements of the purified nanorod solutions (10% and 11 nm, respectively). Assemblies were modeled with optimized gold nanorods on a gold substrate in air (constant index of refraction of 1). To emulate the dried state on the gold substrate, the thickness of the BSA layer was reduced to 1.5 nm. Considering the smoothness of the gold substrate and the good agreement with the experiment, the optical roughness of the film was neglected. On the basis of the experimental data of Johnson and Christy an approximating polynomial function for the optical constants of gold is used by the FDTD software (6 coefficients, 1 imaginary weight: 0.241 RMS error).[67] Zero-conformal-variant mesh refinement with a mesh size of 0.5 nm was used for best representation of the rounded structure in the cavity the mesh size was reduced to 0.1 nm. All simulations reached the automatic shut-off level of 10^{-6} before reaching 300 fs of simulation time. The simulation space was restricted by perfectly matched layers for isolated nanorods as boundary conditions and by periodic boundaries for the unit cell setup. The fields were normalized against the unit cell without the nanorod but with the gold film as reference. Therefore, the presented data include only the contribution of the nanorod whereas the contribution of the gold film serves as background. To calculate the effective optical properties of film-coupled nanorods, S-parameter extraction analysis from Lumerical Solutions Inc. was used. To retrieve the optical constants for the inhomogeneous asymmetric structure, we calculated the S11 and S22 parameters by simulating in forward and backward source direction at an automatic shut-off level of 10^{-7}, respectively.

Characterization.

Optical characterization of the solutions was performed in a 1 mm pathway cuvette without dilution at a Cary 5000 spectrometer (Agilent, USA) using the Cary Universal Measurement Accessory (UMA), which allowed to measure aqueous nanoparticle solutions in the range from 200 nm to 1 850 nm. The gold substrates were measured in transmission geometry on the Cary 5000 spectrometer (Agilent, USA) with an attached Cary Universal Measurement Accessory (UMA) at a spot size of 4 mm $\times$ 4 mm with linearly polarized light. The background was recorded on the same substrate prior transfer of the gold nanorods. The spot size was fixed to the same value for UV-vis and NIR detectors resulting in a slit width of 1 nm and 4 nm, respectively.

The gold substrate was characterized by variable-angle spectroscopic ellipsometry at incident angles from 45° to 85° in 5° steps in a wavelength range from 193 nm to 1690 nm using a RC2 (J.A. Woollam Co., USA) and fitted with CompleteEASE software package. AFM measurements of all substrates (wrinkled templates, gold films, assemblies in the wrinkled templates and nanorods transferred to the gold films) were performed with a Nanoscope Dimension V (Bruker, USA), operated in Tapping ModeTM. Al-coated silicon cantilevers (OTESPA, Bruker) with a stiffness of typically 35–47.2 N/m and typical resonance frequencies of 300 kHz were utilized.

TEM measurements of the gold nanoparticles at all relevant stages of the synthesis were performed on a Zeiss 922 OMEGA EFTEM at a voltage of 120 kV. Zero-loss filtered images were recorded using a bottom mounted Ultrascan 1000 (Gatan) CCD camera system. Gatan Digital Micrograph 3.9 for GMS 1.4 software was used for image acquisition. TEM samples were concentrated and the surfactant concentration (if present) was set to the corresponding critical micelle concentration. Droplets of 5 µL were dried on Quantifoil 300 mesh copper grid with carbon films placed on a hydrophobic film to trap the droplet during drying. For the determination of the mean particle dimensions 250 particles / sample were measured. SEM Measurements were recorded on a LEO 1530 FE-SEM (Zeiss, Germany) with in-lens and SE2 detectors using an acceleration voltage of 2–3 kV.

Acknowledgments. This study was funded by the European Research Council under grant ERC-2012-StG 306686 (METAMECH: Template-assisted assembly of METAmaterials using MECHanical instabilities). MT was supported by the Elite Network Bavaria within the framework of the Elite Study Program “Macromolecular Science” and funded *via* a grant for PhD candidates according to Bavarian elite promotion act (BayEFG).

References

[1] S. P. Burgos, R. de Waele, A. Polman, H. A. Atwater, “A single-layer wide-angle negative-index metamaterial at visible frequencies”, *Nat Mater* **2010**, *9*, 407–412.

[2] A. V. Kildishev, A. Boltasseva, V. M. Shalaev, “Planar Photonics with Metasurfaces”, *Science* **2013**, *339*, DOI 10.1126/science.1232009.

[3] J. B. Pendry, “Negative Refraction Makes a Perfect Lens”, *Physical Review Letters* **2000**, *85*, 3966–3969.

[4] J. B. Pendry, A. J. Holden, D. J. Robbins, W. J. Stewart, “Magnetism from conductors and enhanced nonlinear phenomena”, *Microwave Theory and Techniques IEEE Transactions on* **1999**, *47*, 2075–2084.

[5] D. R. Smith, W. J. Padilla, D. C. Vier, S. C. Nemat-Nasser, S. Schultz, “Composite medium with simultaneously negative permeability and permittivity”, *Phys Rev Lett* **2000**, *84*, 4184–7.

[6] N. Yu, F. Capasso, “Flat optics with designer metasurfaces”, *Nat Mater* **2014**, *13*, 139–150.

[7] G. M. Akselrod, T. Ming, C. Argyropoulos, T. B. Hoang, Y. Lin, X. Ling, D. R. Smith, J. Kong, M. H. Mikkelsen, “Leveraging Nanocavity Harmonics for Control of Optical Processes in 2D Semiconductors”, *Nano Letters* **2015**, *15*, 3578–3584.

[8] H. Wang, K. O’Dea, L. Wang, “Selective absorption of visible light in film-coupled nanoparticles by exciting magnetic resonance”, *Optics Letters* **2014**, *39*, 1457–1460.

[9] J. B. Lassiter, F. McGuire, J. J. Mock, C. Ciracì, R. T. Hill, B. J. Wiley, A. Chilkoti, D. R. Smith, “Plasmonic Waveguide Modes of Film-Coupled Metallic Nanocubes”, *Nano Letters* **2013**, *13*, 5866–5872.

[10] A. Rose, T. B. Hoang, F. McGuire, J. J. Mock, C. Ciracì, D. R. Smith, M. H. Mikkelsen, “Control of Radiative Processes Using Tunable Plasmonic Nanopatch Antennas”, *Nano Letters* **2014**, *14*, 4797–4802.

[11] S. Kawata, A. Ono, P. Verma, “Subwavelength colour imaging with a metallic nanolens”, *Nature Photonics* **2008**, *2*, 438–442.

[12] M. Kataja, T. K. Hakala, A. Julku, M. J. Huttunen, S. van Dijken, P. Torma, “Surface lattice resonances and magneto-optical response in magnetic nanoparticle arrays”, *Nature Communications* **2015**, *6*, DOI 10.1038/ncomms8072.

[13] A. Alù, N. Engheta, “The quest for magnetic plasmons at optical frequencies”, *Optics Express* **2009**, *17*, 5723–5730.

[14] J. Zhou, T. Koschny, M. Kafesaki, E. N. Economou, J. B. Pendry, C. M. Soukoulis, “Saturation of the Magnetic Response of Split-Ring Resonators at Optical Frequencies”, *Physical Review Letters* **2005**, *95*, 223902.

[15] G. Dolling, C. Enkrich, M. Wegener, J. F. Zhou, C. M. Soukoulis, S. Linden, “Cut-wire pairs and plate pairs as magnetic atoms for optical metamaterials”, *Optics Letters* **2005**, *30*, 3198–3200.

[16] D. Lin, P. Fan, E. Hasman, M. L. Brongersma, "Dielectric gradient metasurface optical elements", *Science* **2014**, *345*, 298–302.

[17] C. M. Soukoulis, M. Wegener, "Past achievements and future challenges in the development of three-dimensional photonic metamaterials", *Nature Photonics* **2011**, *5*, 523–530.

[18] Z.-G. Dong, H. Liu, M.-X. Xu, T. Li, S.-M. Wang, S.-N. Zhu, X. Zhang, "Plasmonically induced transparent magnetic resonance in a metallic metamaterial composed of asymmetric double bars", *Optics Express* **2010**, *18*, 18229–18234.

[19] N. I. Zheludev, "The Road Ahead for Metamaterials", *Science* **2010**, *328*, 582–583.

[20] H. Ditlbacher, A. Hohenau, D. Wagner, U. Kreibig, M. Rogers, F. Hofer, F. R. Aussenegg, J. R. Krenn, "Silver Nanowires as Surface Plasmon Resonators", *Physical Review Letters* **2005**, *95*, 257403.

[21] C. Hanske, M. Tebbe, C. Kuttner, V. Bieber, V. V. Tsukruk, M. Chanana, T. A. F. König, A. Fery, "Strongly Coupled Plasmonic Modes on Macroscopic Areas via Template-Assisted Colloidal Self-Assembly", *Nano Letters* **2014**, *14*, 6863–6871.

[22] N. Meinzer, W. L. Barnes, I. R. Hooper, "Plasmonic meta-atoms and metasurfaces", *Nature Photonics* **2014**, *8*, 889–898.

[23] G. V. Naik, V. M. Shalaev, A. Boltasseva, "Alternative Plasmonic Materials: Beyond Gold and Silver", *Advanced Materials* **2013**, *25*, 3264–3294.

[24] B. J. Wiley, D. J. Lipomi, J. Bao, F. Capasso, G. M. Whitesides, "Fabrication of Surface Plasmon Resonators by Nanoskiving Single-Crystalline Gold Microplates", *Nano Letters* **2008**, *8*, 3023–3028.

[25] Y. Cui, M. T. Björk, J. A. Liddle, C. Sönnichsen, B. Boussert, A. P. Alivisatos, "Integration of Colloidal Nanocrystals into Lithographically Patterned Devices", *Nano Letters* **2004**, *4*, 1093–1098.

[26] J.-S. Huang, V. Callegari, P. Geisler, C. Brüning, J. Kern, J. C. Prangsma, X. Wu, T. Feichtner, J. Ziegler, P. Weinmann, M. Kamp, A. Forchel, P. Biagioni, U. Sennhauser, B. Hecht, "Atomically flat single-crystalline gold nanostructures for plasmonic nanocircuitry", *Nature Communications* **2010**, *1*, 150.

[27] Z. Li, S. Butun, K. Aydin, "Touching Gold Nanoparticle Chain Based Plasmonic Antenna Arrays and Optical Metamaterials", *ACS Photonics* **2014**, *1*, 228–234.

[28] G. M. Akselrod, J. Huang, T. B. Hoang, P. T. Bowen, L. Su, D. R. Smith, M. H. Mikkelsen, "Large-Area Metasurface Perfect Absorbers from Visible to Near-Infrared", *Advanced Materials* **2015**, *27*, 8028–8034.

[29] W. Chen, M. Tymchenko, P. Gopalan, X. Ye, Y. Wu, M. Zhang, C. B. Murray, A. Alu, C. R. Kagan, "Large-Area Nanoimprinted Colloidal Au Nanocrystal-Based Nanoantennas for Ultrathin Polarizing Plasmonic Metasurfaces", *Nano Letters* **2015**, *15*, 5254–5260.

[30] M. J. Rozin, D. A. Rosen, T. J. Dill, A. R. Tao, "Colloidal metasurfaces displaying near-ideal and tunable light absorbance in the infrared", *Nature Communications* **2015**, *6*, DOI 10.1038/ncomms8325.

[31] H. Chen, T. Ming, S. Zhang, Z. Jin, B. Yang, J. Wang, "Effect of the Dielectric Properties of Substrates on the Scattering Patterns of Gold Nanorods", *ACS Nano* **2011**, *5*, 4865–4877.

[32] H. Chen, L. Shao, T. Ming, K. C. Woo, Y. C. Man, J. Wang, H.-Q. Lin, "Observation of the Fano Resonance in Gold Nanorods Supported on High-Dielectric-Constant Substrates", *ACS Nano* **2011**, *5*, 6754–6763.

[33] T. Maurer, P.-M. Adam, G. Lévêque, "Coupling between plasmonic films and nanostructures: from basics to applications", *Nanophotonics* **2015**, *4*, DOI 10.1515/nanoph-2014-0015.

[34] S. Ni, J. Leemann, H. Wolf, L. Isa, "Insights into mechanisms of capillary assembly", *Faraday Discussions* **2015**, *181*, 225–242.

[35] A. Rey, G. Billardon, E. Lortscher, K. Moth-Poulsen, N. Stuhr-Hansen, H. Wolf, T. Bjornholm, A. Stemmer, H. Riel, "Deterministic assembly of linear gold nanorod chains as a platform for nanoscale applications", *Nanoscale* **2013**, *5*, 8680–8688.

[36] X. Zhou, Y. Zhou, J. C. Ku, C. Zhang, C. A. Mirkin, "Capillary Force-Driven, Large-Area Alignment of Multi-segmented Nanowires", *ACS Nano* **2014**, *8*, 1511–1516.

[37] A. Vallecchi, M. Albani, F. Capolino, "Collective electric and magnetic plasmonic resonances in spherical nanoclusters", *Optics Express* **2011**, *19*, 2754–2772.

[38] C. F. Bohren, D. R. Huffman in *Absorption and Scattering of Light by Small Particles*, Wiley-VCH Verlag GmbH, **2007**, pp. 325–380.

[39] T. König, R. Kodiyath, Z. A. Combs, M. A. Mahmoud, M. A. El-Sayed, V. V. Tsukruk, "Silver Nanocube Aggregates in Cylindrical Pores for Higher Refractive Index Plasmonic Sensing", *Particle & Particle Systems Characterization* **2014**, *31*, 274–283.

[40] S. Zhang, K. Bao, N. J. Halas, H. Xu, P. Nordlander, "Substrate-Induced Fano Resonances of a Plasmonic Nanocube: A Route to Increased-Sensitivity Localized Surface Plasmon Resonance Sensors Revealed", *Nano Letters* **2011**, *11*, 1657–1663.

[41] D. E. Gómez, Z. Q. Teo, M. Altissimo, T. J. Davis, S. Earl, A. Roberts, "The Dark Side of Plasmonics", *Nano Letters* **2013**, *13*, 3722–3728.

[42] G. Lévêque, O. J. F. Martin, "Optical interactions in a plasmonic particle coupled to a metallic film", *Optics Express* **2006**, *14*, 9971–9981.

[43] A. Pors, S. I. Bozhevolnyi, "Plasmonic metasurfaces for efficient phase control in reflection", *Optics Express* **2013**, *21*, 27438–27451.

[44] M. B. Müller, C. Kuttner, T. A. F. König, V. V. Tsukruk, S. Förster, M. Karg, A. Fery, "Plasmonic Library Based on Substrate-Supported Gradiential Plasmonic Arrays", *ACS Nano* **2014**, *8*, 9410–9421.

[45] M. Mayer, L. Scarabelli, K. March, T. Altantzis, M. Tebbe, M. Kociak, S. Bals, F. J. García de Abajo, A. Fery, L. M. Liz-Marzán, "Controlled Living Nanowire Growth: Precise Control over the Morphology and Optical Properties of AgAuAg Bimetallic Nanowires", *Nano Letters* **2015**, *15*, 5427–5437.

[46] J. Mark, *Polymer Data Handbook*, Oxford University Press, **2009**.

[47] J. Becker, I. Zins, A. Jakab, Y. Khalavka, O. Schubert, C. Sönnichsen, "Plasmonic Focusing Reduces Ensemble Linewidth of Silver-Coated Gold Nanorods", *Nano Letters* **2008**, *8*, 1719–1723.

[48] N. Dmitruk, S. Malynych, I. Moroz, V. Kurlyak, "Optical Efficiency of Ag and Au Nanoparticles", *Semiconductor Physics Quantum Electronics & Optoelectronics* **2010**, *13*, 369–373.

[49] J. L. Elechiguerra, L. Larios-Lopez, C. Liu, D. Garcia-Gutierrez, A. Camacho-Bragado, M. J. Yacaman, "Corrosion at the Nanoscale: The Case of Silver Nanowires and Nanoparticles", *Chemistry of Materials* **2005**, *17*, 6042–6052.

[50] G. Decher, "Fuzzy Nanoassemblies: Toward Layered Polymeric Multicomposites", *Science* **1997**, *277*, 1232–1237.

[51] P. K. Jain, W. Huang, M. A. El-Sayed, "On the Universal Scaling Behavior of the Distance Decay of Plasmon Coupling in Metal Nanoparticle Pairs: A Plasmon Ruler Equation", *Nano Letters* **2007**, *7*, 2080–2088.

[52] J. A. Scholl, A. Garcia-Etxarri, G. Aguirregabiria, R. Esteban, T. C. Narayan, A. L. Koh, J. Aizpurua, J. A. Dionne, "Evolution of Plasmonic Metamolecule Modes in the Quantum Tunneling Regime", *ACS Nano* **2015**, DOI 10.1021/acsnano.5b06738.

[53] L. Yang, H. Wang, Y. Fang, Z. Li, "Polarization State of Light Scattered from Quantum Plasmonic Dimer Antennas", *ACS Nano* **2015**, DOI 10.1021/acsnano.5b07223.

[54] C. Kuttner, M. Chanana, M. Karg, A. Fery in *Macromolecular Self-Assembly*, (Ed.: O. V. Borisov), Wiley-VCH, **2015**.

[55] M. Tebbe, M. Mayer, B. A. Glatz, C. Hanske, P. T. Probst, M. B. Muller, M. Karg, M. Chanana, T. A. F. Konig, C. Kuttner, A. Fery, "Optically anisotropic substrates via wrinkle-assisted convective assembly of gold nanorods on macroscopic areas", *Faraday Discussions* **2015**, *181*, 243–260.

[56] E. C. Dreaden, A. M. Alkilany, X. Huang, C. J. Murphy, M. A. El-Sayed, "The golden age: gold nanoparticles for biomedicine", *Chemical Society Reviews* **2012**, *41*, 2740–2779.

[57] Y. Xia, Y. Xiong, B. Lim, S. E. Skrabalak, "Shape-Controlled Synthesis of Metal Nanocrystals: Simple Chemistry Meets Complex Physics?", *Angewandte Chemie International Edition* **2009**, *48*, 60–103.

[58] J. Pérez-Juste, L. M. Liz-Marzán, S. Carnie, D. Y. C. Chan, P. Mulvaney, "Electric-Field-Directed Growth of Gold Nanorods in Aqueous Surfactant Solutions", *Advanced Functional Materials* **2004**, *14*, 571–579.

[59] K. Park, H. Koerner, R. A. Vaia, "Depletion-Induced Shape and Size Selection of Gold Nanoparticles", *Nano Letters* **2010**, *10*, 1433–1439.

[60] L. Scarabelli, M. Coronado-Puchau, J. J. Giner-Casares, J. Langer, L. M. Liz-Marzán, "Monodisperse Gold Nanotriangles: Size Control, Large-Scale Self-Assembly, and Performance in Surface-Enhanced Raman Scattering", *ACS Nano* **2014**, *8*, 5833–5842.

[61] L. Scarabelli, A. Sánchez-Iglesias, J. Pérez-Juste, L. M. Liz-Marzán, “A “Tips and Tricks” Practical Guide to the Synthesis of Gold Nanorods”, *Journal of Physical Chemistry Letters* **2015**, *6*, 4270–4279.

[62] B. A. Glatz, M. Tebbe, B. Kaoui, R. Aichele, C. Kuttner, A. E. Schedl, H.-W. Schmidt, W. Zimmermann, A. Fery, “Hierarchical line-defect patterns in wrinkled surfaces”, *Soft Matter* **2015**, *11*, 3332–3339.

[63] U. K. Chettiar, A. V. Kildishev, T. A. Klar, V. M. Shalaev, “Negative index metamaterial combining magnetic resonators with metal films”, *Optics Express* **2006**, *14*, 7872–7877.

[64] D. R. Smith, D. C. Vier, T. Koschny, C. M. Soukoulis, “Electromagnetic parameter retrieval from inhomogeneous metamaterials”, *Physical Review E* **2005**, *71*, 036617.

[65] C. Rockstuhl, F. Lederer, C. Etrich, T. Pertsch, T. Scharf, “Design of an Artificial Three-Dimensional Composite Metamaterial with Magnetic Resonances in the Visible Range of the Electromagnetic Spectrum”, *Physical Review Letters* **2007**, *99*, 017401.

[66] M. Tebbe, C. Kuttner, M. Mayer, M. Maennel, N. Pazos-Perez, T. A. F. König, A. Fery, “Silver-Overgrowth-Induced Changes in Intrinsic Optical Properties of Gold Nanorods: From Noninvasive Monitoring of Growth Kinetics to Tailoring Internal Mirror Charges”, *The Journal of Physical Chemistry C* **2015**, *119*, 9513–9523.

[67] P. B. Johnson, R. W. Christy, “Optical Constants of the Noble Metals”, *Physical Review B* **1972**, *6*, 4370–4379.

V.2 Plasmon Band Formation and Delocalization in Quasi-Infinite Chains

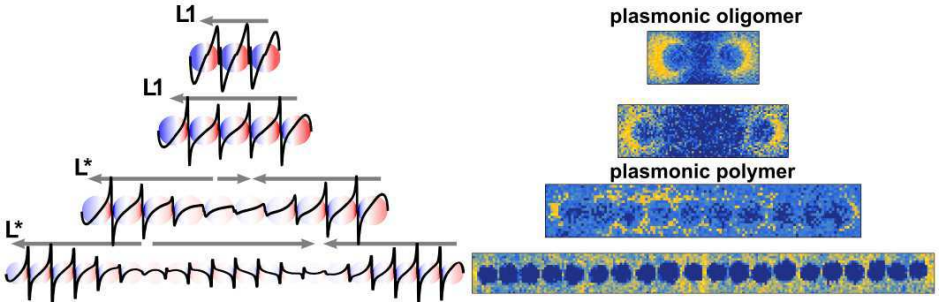

This section is based on the publication *Nano Letters* **2019**, 19, 3854–3862.

By Martin Mayer,[a,b] Pavel Potapov,[c] Darius Pohl,[b,d,e] Anja Maria Steiner,[a,b] Johannes Schultz,[c] Bernd Rellinghaus,[b,d,e] Axel Lubk,[c,*] Tobias A.F. König,[a,b,f,*] and Andreas Fery[a,b,f,*]

[a]Leibniz-Institut für Polymerforschung Dresden e.V., Institute of Physical Chemistry and Polymer Physics, Hohe Str. 6, 01069 Dresden, Germany
[b]Cluster of Excellence Center for Advancing Electronics Dresden (cfaed), Technische Universität Dresden, 01062 Dresden, Germany
[c]Leibniz-Institut für Festkörper- und Werkstoffforschung, Institute for Solid State Research, Helmholtzstr. 20, 01069 Dresden, Germany
[d]Leibniz-Institut für Festkörper- und Werkstoffforschung, Institute for Metallic Materials, Helmholtzstr. 20, 01069 Dresden, Germany
[e]Dresden Center for Nanoanalysis, Technische Universität Dresden, 01062 Dresden, Germany
[f]Department of Physical Chemistry of Polymeric Materials, Technische Universität Dresden, Hohe Str. 6, 01069 Dresden, Germany
*corresponding author

Abstract. Chains of metallic nanoparticles sustain strongly confined surface plasmons with relatively low dielectric losses. To exploit these properties in applications, such as waveguides, the fabrication of long chains of low disorder and a thorough understanding of the plasmon mode properties, such as dispersion relations, are indispensable. Here, wrinkled templates are used for directed self-assembly to assemble chains of gold nanoparticles. With this up-scalable method, chain lengths from two particles (140 nm) to 20 particles (1 500 nm) and beyond can be fabricated. Electron energy-loss spectroscopy supported by boundary element simulations, finite-difference time-domain, and a simplified dipole coupling model reveal the evolution of a band of plasmonic waveguide modes from degenerated single-particle modes in detail. In striking difference from plasmonic rod-like structures, the plasmon band is confined in excitation energy, which allows light manipulations below the diffraction limit. The non-degenerated surface plasmon modes show suppressed radiative losses for efficient energy propagation over a distance of 1 500 nm.

Localized surface plasmon resonances (LSPR) are self-sustaining resonances appearing when delocalized conduction band electrons of a metal are confined within a nanoparticle.[1,2] Plasmonic resonances are characterized by strong and localized electromagnetic field enhancement, which is strongly sensitive to the geometry and composition of the nanoparticle and the environment.[3] This makes them attractive for a wide range of applications, in which sub-wavelength control of electromagnetic fields from the infrared to ultraviolet range is crucial.[4] In particular, long metallic nanoparticle chains have been proposed for plasmonic waveguiding,[5] *i.e.*, photonic transport confined to the sub-micron and hence, sub-wavelength length scale, which is difficult to realize with optical devices.[6,7] In this length scale, plasmonic waveguides open up new strategies for signal transport due to their strong confinement and the high signal speed. It has been predicted through analytical and numerical studies, that regular nanoparticle chains support plasmon modes with distinct dispersion relations and hence, signal transmission velocities depending on the geometric parameters of the chain.[8] More recently, geometric modifications of the monopartite chain prototype, such as bipartite chains or zig-zag chains, are predicted to feature more complicated band structures including plasmonic band gaps as well as topological edge states.[9]

For the realization of such waveguides and the experimental proof of the predicted effects, however, energy dissipation in the metal and precise positional control of the metallic nanoparticles are still bottle necks. In particular, the intrinsic losses of the employed metals limit the overall performance of plasmonic waveguides.[10] However, smart assembly, resulting in finely-tuned particle coupling, can further lower the dissipation. For example, Liedl *et al.* recently showed low-dissipative and ultrafast energy propagation at a bimetallic chain with three 40 nm particles.[11] Various colloidal techniques, such as DNA origami[12] or self-assembly by chemical linkers,[13] are available to assemble noble metal nanoparticles into chains. In principle, infinitely long particle chains can be fabricated with these techniques, however, trade-offs in particle spacing, particle size or linear geometry must be accepted. In recent years, masks have been used for colloidal self-assembly to overcome the size limitation, which results into long-range energy transfer even around a micrometer-sized corner.[14] It has been shown, that above a rather undefined chain length, the so-called *infinite chain limit*, the longitudinal plasmonic modes converge to a non-zero asymptotic energy.[15,16] Consequently, the plasmonic response above this lengths differs from shorter chains because of the discrete nature of the chain and the finite coupling strength.[17] To make it easier to distinguish between them, chains above the *infinite chain limit* are referred to plasmonic polymers, whereas shorter chains are called plasmonic oligomers, in close analogy to organic polymer synthesis.[8,12]

Although the energy transport is principally improved by dark modes, which suffer significantly less from radiation losses than the bright ones, it is still a matter of debate, whether those dark modes are responsible for the transport.[18] Recently, methods for visualizing localized plasmons on the nanometer scale have emerged. These methods involve transmission electron microscopy (TEM) combined with electron energy-loss spectroscopy (EELS) with high energy resolution, which is now readily available in dedicated monochromated TEM instruments. Examples of successful application of TEM-EELS methods includes mapping LSPR modes in metallic nanocubes,[19] nanorods,[20–22] and nanospheres.[23,24]

In this section, long regular nanoparticle chains are fabricated, which allow for individual probing of local fields. By comprehensive spatially resolved electron energy loss studies, the plasmonic response is characterized. Here, we will particularly address the transition from individual single particle modes to plasmonic bands in quasi-infinite long chains, which has not been directly observed previously. Robust excitation of the plasmonic waveguide modes relies on recent developments in our groups: single crystalline wet-chemical synthesis,[25] and template-assisted colloidal self-assembly,[26] as well as improved electron energy-loss (EELS) characterization in the TEM,[27] and electromagnetic modeling.[18]

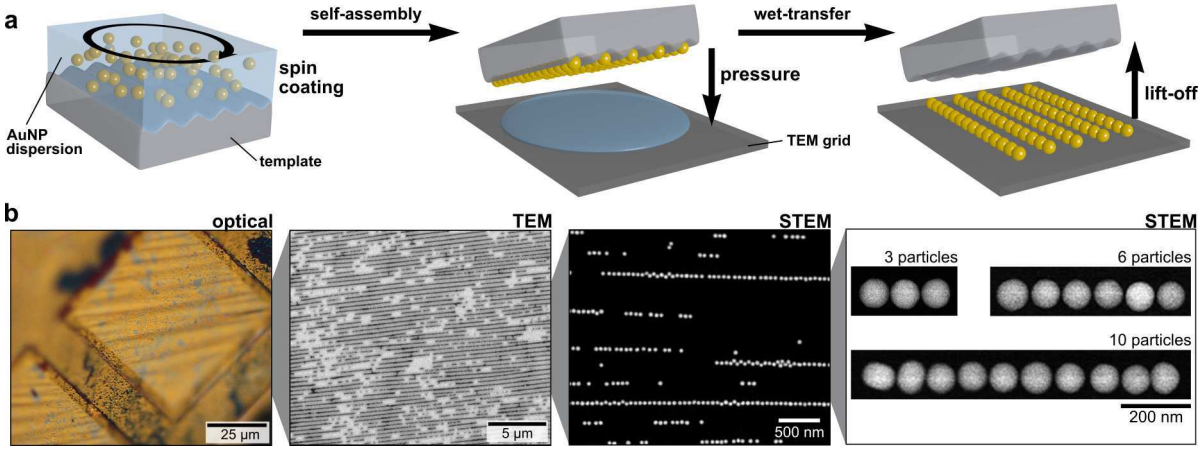

Figure V.7.: Large-area template-assisted self-assembly of various chain lengths and wet-transfer for spectroscopic (EELS) studies. (a) Schematic template-assisted colloidal self-assembly *via* spin coating, followed by wet-transfer printing on a TEM grid. (b) A microscope image, (S)TEM images and selective details (3, 6, and 10 particle chains) of the transferred gold particle chains.

Template-assisted colloidal self-assembly (**Figure V.7**) was used to fabricate colloidal nanoparticle chains (particle diameter of 70 nm) on micrometer scaled carbon coated TEM grids.[26,28,29] Since high optical quality, reproducibility and narrow size-distributions are crucial parameters, single crystalline spherical gold nanoparticles (AuNSp) were synthesized by seed-mediated growth, which comply with these requirements.[30,31] The highly linear assembly of these gold spheres into wrinkled elastomeric templates results in closely-packed chains with a homogeneous sub-2 nm spacing.[26,30] The obtained inter-particle distance relies, in this case, only on the well-defined thickness of the employed dielectric spacer, *i.e.*, in this case on the protein shell.[26] The resulting spacing can also be seen in the TEM images in **Figure V.7b**. The directed self-assembly process followed by wet-contact printing on the target structure (TEM grid) is outlined in **Figure V.7a**. Transfer to a TEM grid allows the spectroscopic study of the coherent plasmonic coupling in chains of different lengths (**Figure V.7b**), while maintaining the good filling rate (defined by chains per area) and close-packing of the nanoparticles within chains. In order to obtain close-packed chains with varying lengths and a slightly reduced density of chains on the sample, the pH of the colloidal nanoparticle solution was slightly reduced, as described in the experimental section. Thus, such assemblies mark the perfect test system to study the effects of various particle lengths with comparable properties in a combinatorial approach.

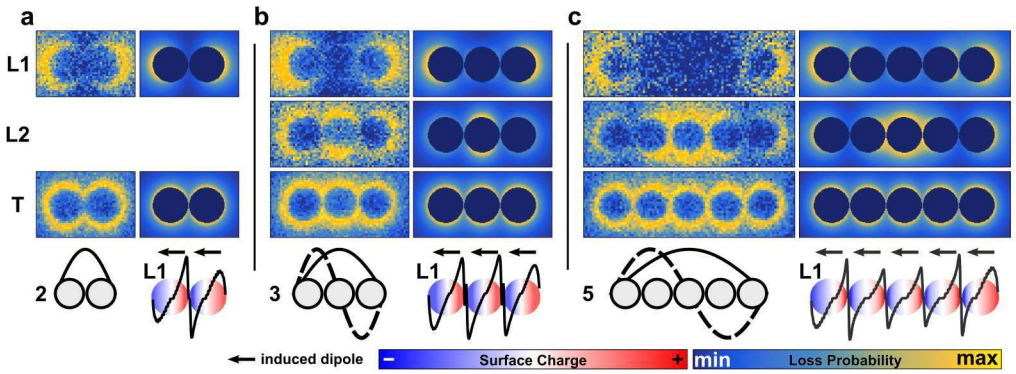

Figure V.8.: Theoretical and experimental plasmonic modes of a dimer (a), trimer (b) and pentamer (c). Schematic descriptions, integrated surface charge images and plots (black line) as well as corresponding dipole moments for simulated surface charge plots for the most dominant longitudinal modes. Experimental and simulated EELS maps of longitudinal and transversal modes.

The following investigates the transition from plasmonic monomer to polymer (*i.e.*, beyond the *infinite chain limit*) in detail. **Figure V.9** shows plasmonic oligomers, consisting of a number of nanoparticles well-below the *infinite chain limit*. The plasmonic properties for such short particle chains with up to five particles have been studied extensively by Mulvaney *et al.*[24] Electron energy-loss spectroscopy (EELS) in the TEM is nowadays a common approach to spatially image plasmons. In this method, the energy loss of a focused electron beam upon crossing the electric field of plasmons (excited by the evanescent field of the very same electron) is spectroscopically mapped with a focused electron beam, which at the same time, excites the plasmons. For short particle chains, several plasmon modes can be observed in the EELS maps and spectra (see also **Supporting Figure A.V.8**). By directly comparing experimentally observed maps of energy-loss with the electromagnetic simulations, the nature of the induced coupling interactions can be elucidated. This comparison allows for the identification of the plasmonic modes by their corresponding surface charges. Starting from a single particle (**Supporting Figure A.V.6**), the addition of a second particle (forming a dimer, **Figure V.9a**) induces hybridization.[32] Hence, the longitudinal modes split into a symmetric (L2) and antisymmetric (L1) one with higher and lower energy, respectively, compared to the fundamental (transversal) mode.[15,24] The maps of energy-loss and the derived surface charges reveal the lower energy antisymmetric mode. The higher energy L2 mode is not unambiguously detectable, because of its lower interaction with the electron beam (see below for details) and its larger damping by interband transitions.
By forming a trimer (**Figure V.9b**), the L1 mode shifts further to lower energies. Additionally the next order longitudinal L2 mode, with a node in the central particle, can be discerned from the transversal and L1 mode. The mutual cancellation of induced dipoles generates a net dipole moment of zero (even numbers of surface charge waves) rendering this L2 mode dark (*i.e.*, non-radiatively interacting with photons). The higher energetic L3 mode above the transversal mode is again damped by interband transitions. As the number of particles increases to five particles, the energetically lowest mode (L1) approaches the *infinite chain limit* already (see **Figure V.9c**). However, the induced longitudinal modes L1 and L2 can still be discerned and the surface charge waves cover the complete length of the chain.

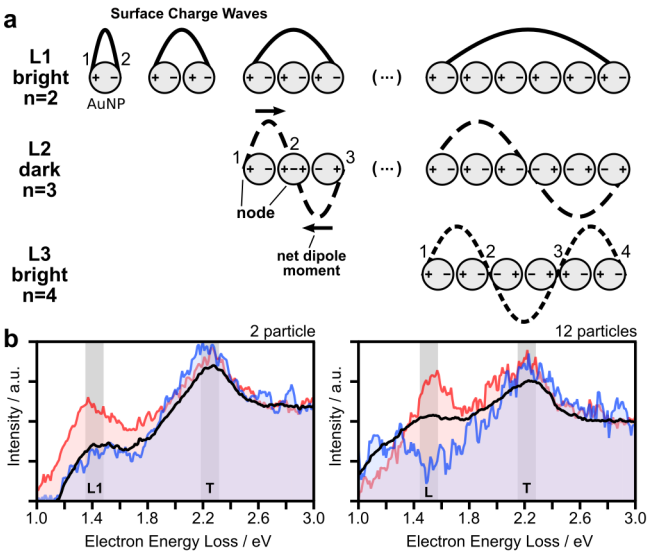

Figure V.9.: Definitions of the longitudinal plasmonic modes and their spectroscopic response. Schematic descriptions of the plasmonic modes along the geometric axis by surface charge (+/-), dipole moment (black line), net-dipole moment, node and surface charge wave (schematically representing the polarization field of the respective plasmonic modes) (a). Selected electron energy loss spectra (EELS) for 2 and 12 particles (b). The blue and red lines show the EELS response averaged over 10–40 pixels, and the black line represents the values averaged over all spectra of the scanned map.

By exciting such particle chains with an electromagnetic field, *e.g.*, a light wave or the evanescent field of a focused electron beam, collective localized surface plasmons are induced in the particle chain. The induced electron density oscillation results in a localized dipole moment of the single particles (defined by surface charges). At large inter-particle distances, these oscillations do not couple and are energetically degenerate. When the inter-particle distance is decreased far below the excitation wavelength, the localized dipole moments of the single particles couple, lifting the degeneracy. By extension, also higher order multipole moments couple, which becomes increasingly important at small particle distances. The following shows that the principal plasmonic behavior of nanoparticle chains can be well-described on the dipolar coupling level. In particular the dipoles oriented along the chain axis strongly couple coherently leading to a set of distinguishable longitudinal modes (**Figure V.8**). Therefore, similar to the electron wave function in a diatomic molecule, the energetically lowest coherent plasmonic mode in a plasmonic dimer (L1 at 1.4 eV / 885 nm) is an antisymmetric bonding mode (**Figure V.8b**). For longer the chains, several harmonics of the longitudinal mode can be excited (see also **Figure V.8a**), which are defined by the number of nodes (n). In this context, a node is defined by a zero dipole moment at a specific chain position and the longitudinal modes (Lm) are indexed by $m = n + 1$.[24] Using this definition, bright modes (non-zero overall dipole moment) occur at odd m and dark modes (zero overall dipole moment) at even m, respectively. **Figure V.8b** exemplarily shows two selected EEL spectra for chains with 2 and 12 particles. In contrast to rod like structures,[33] the excitation energy of the L1 mode in long chains converges at low energies, described as the *infinite chain limit*.[16] In literature, this limit is typically defined somewhere between 8 and 12 particles (see also a spectral visualization in **Supporting Figure A.V.5**).[15,16] In contrast, nanoparticle dipole moments, perpendicular to the chain axis, couple only weakly, resulting in (almost) degenerate transversal modes (marked as T at 2.2 eV / 560 nm).

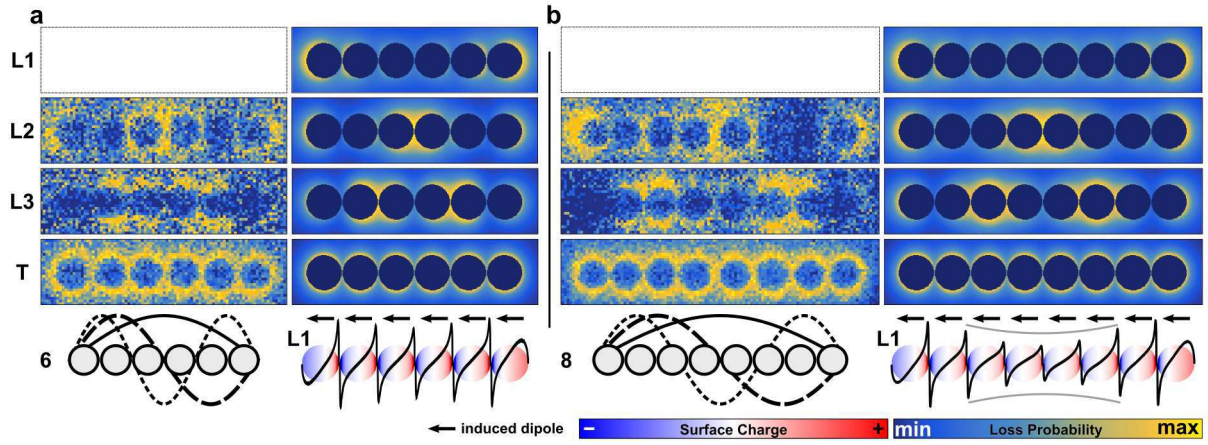

Figure V.10.: Particle chain length approaching the *infinite chain limit*. Schematic description, simulated surface charge plots of the lowest-order L1 mode and maps of energy-loss for all resolvable plasmonic modes (a–b; 6 and 8 particles, respectively; experimental results are shown on the left and simulated results on the right; the intensity of L1 modes was experimentally below the detection limit).

Approaching the *infinite chain limit*, the intensity of the fundamental longitudinal mode L1 shifts further to smaller energies and gradually vanishes (**Figure V.10**). Electromagnetic simulations reveal that this decrease can be ascribed to an increased damping due to intraband transitions (see **Supporting Figure A.V.10** for respective spectra). Above L2, the L3 mode becomes observable as identified by the number of nodes (n = 4).

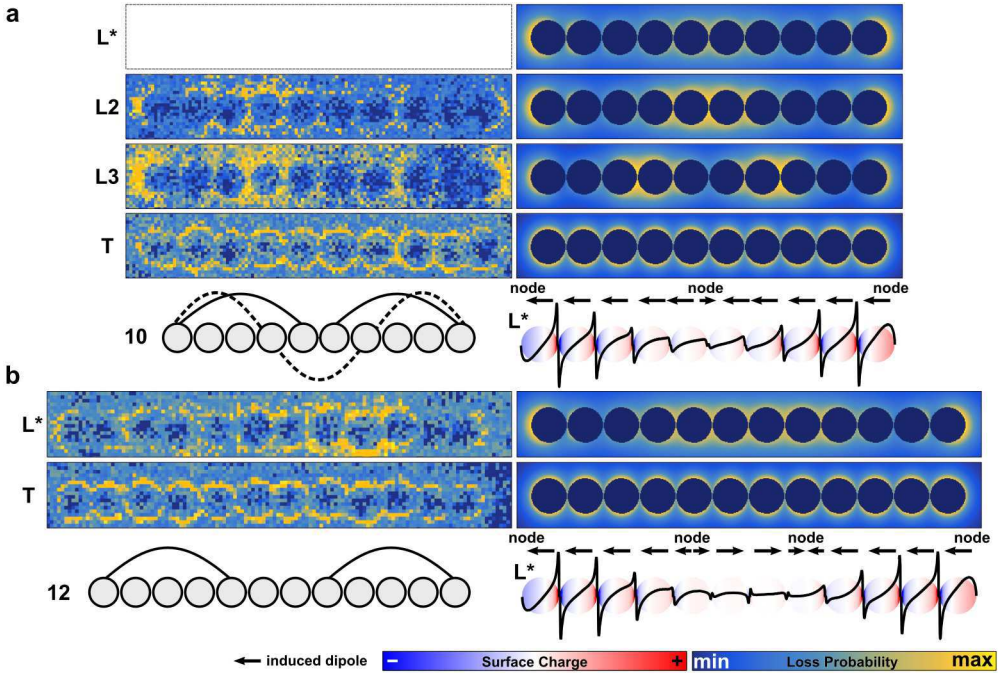

Figure V.11.: Particle chains close to the transition to quasi-infinite chains. Schemes, simulated surface charge plots (L*), and maps for electron energy loss for all selected plasmonic modes (a–b; 10 and 12 particles, respectively; experimental left and simulated right; the intensity of L1 modes for 10 particles was experimentally below the detection limit). For 10 particles (a), the L* mode is shaped in the simulations, but the higher modes (L2 and L3) are still isolated observable—marking thereby the transition from plasmonic oligomer to polymer. Note the localized increase of field strength around the small kink of the chain in (a) at the ninth particle of the chain.

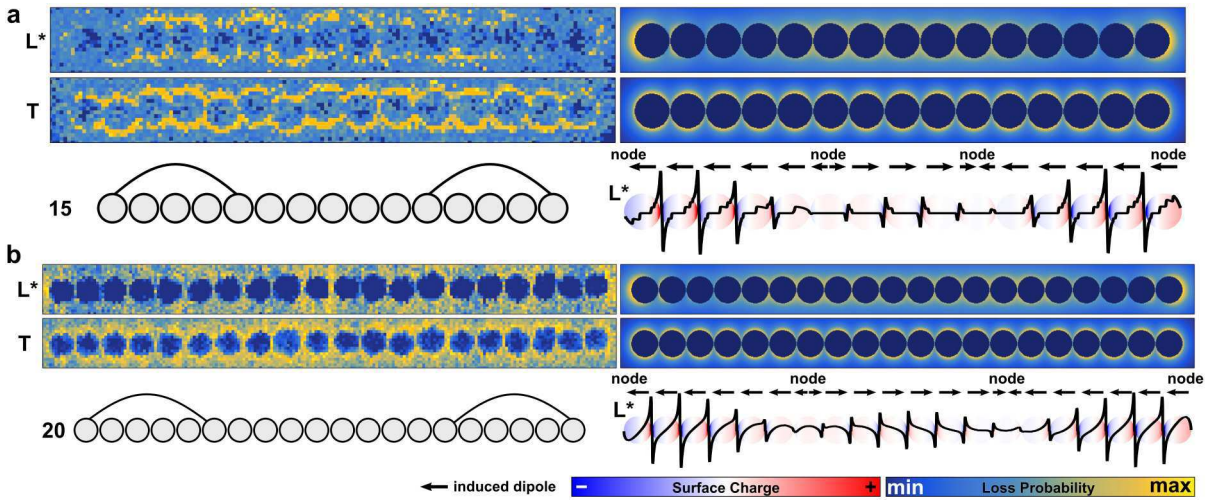

Figure V.12.: Particle chains beyond the *infinite chain limit*. Schemes, simulated surface charge plots (L*) and maps of energy-loss for all selected plasmonic modes (a–b; 15 and 20 particles, respectively; experimental left and simulated right).

When increasing the number of particles in a chain beyond the *infinite chain limit*, it becomes increasingly difficult or even impossible to discern pure Lm modes (**Figure V.11** & **V.12** for the maps of 10 and 15 particles), since more and more modes occupy the same spectral region. Indeed, instead of spectrally well-separated longitudinal modes, distinguished by their node number, a broad band of surface plasmon modes emerges (denoted by L*). This L* mode is characterized by two broad nodes close to the edge and a large maximum in between. The impact of the band formation on the surface charges is summarized in **Supporting Figure A.V.9**. The longest studied chain covers a distance of almost 1.5 μm, although there are much longer chains on the TEM grid (>30 particles) available. However, those particles tend to contain a certain degree of disorder, such as non-colinear alignment, distance variations, *etc.* These irregularities increasingly influence the mode formation by giving rise to localization effects, as already visible in **Figure V.11b** (see below for a more detailed discussion of this effect).

Figure V.13a summarizes the evolution of the excitation energy upon the transition from plasmonic oligomers to plasmonic polymers by plotting their peak position as a function of the chain length j. Significant scattering of the mode energies is observable, which is predominantly due to slight variations (disorder) of the observed chains. For instance, examining the L1 mode of the dimer, the latter consists of “kissing” spheres (**Figure V.9a**). Thus, leading to an enhanced interaction and hence, energy shift. The transversal mode is independent from the chain length within the error of the measurement. This indicates small coupling interactions between transversal dipoles and hence, the degeneracy of the corresponding single particle oscillations. In contrast, more and more longitudinal modes, separated in energy, appear with increasing chain length. Their energy decreases as the number of particles increases, approaching a lower boundary in the *infinite chain limit*. Eventually, the longitudinal modes energetically approach each other for plasmonic polymers, and superimpose (*i.e.*, degenerate) due to their finite lifetimes and hence, energy widths (**Figure V.13b**). Consequently, they cannot be discerned anymore (**Figure V.12**), forming an effective L* mode. This degenerated L* mode is defined by its characteristic in-phase

excitation at the chain ends and its characteristic superposition of multiple harmonic longitudinal modes in the central region. In the simplified sketch in **Figure V.13b**, the transition from isolated modes to the superimposed L* mode is visualized by an oscillating wave model.

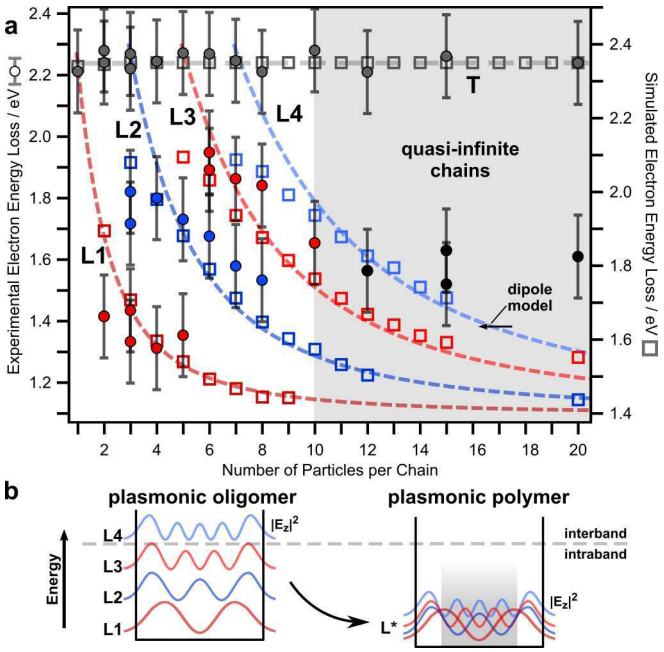

Figure V.13.: Study the transition from plasmonic oligomers to plasmonic polymers. Experimental (EELS filled circles) and BEM simulated (hollow squares) energies of the various longitudinal modes as a function of particle length (a). Dashed lines show the results of the coupled dipole model. Schematic description for the formation of the merged longitudinal plasmonic modes L* beyond the *infinite chain limit* (b).

The behavior of long particle chains differs from the reported plasmonic properties of long metallic rods, which support high-order harmonics with well-distinguishable energies.[20,21] To understand the plasmonics of long nanoparticle chains, simple coupled dipole model[8,9] have been used in the past (see Downing *et al.*[34] for a more elaborate quantum description). Accordingly, nanoparticle chains may be approximated by an assembly of discrete individual dipoles P_i for each sphere (index i). These dipoles weakly couple with their nearest neighbors by dipole-dipole interaction facilitated by the electric field propagator G_{ij} (see **Supporting Section A.V.1** for an explicit expression of the propagator), as described by the following self-consistent polarization model:

$$P_i(\omega) = \alpha(\omega)\left(E_{ext}(\omega) - \sum_{j=i\pm1} G_{ij}(\omega)P_j(\omega)\right). \tag{V.2}$$

Here, α denotes the (isotropic) single sphere polarizability and E_{ext} the external electric field associated to, *e.g.*, the electron beam. A plasmonic mode occurs at the poles of $(\alpha^{-1} - G)^{-1}$ (with $G \equiv \{G_{ij}\}$), which can be found by searching the zeros of $\det(1 - \alpha(\omega)G(\omega))$. However, $\alpha'(\omega)G(\omega)$ is generally non-Hermitian due to retardation and loss (*i.e.,* the complex nature of α), and α is a non-linear function in the complex plane. Therefore, exact zeros (*i.e.*, exact resonances) generally do not exist and maximal responses to external fields occur at the minima of the determinant in the complex plane ω, *i.e.*, at frequencies with imaginary part accounting for the finite lifetime of the plasmon mode. The above model is a simplified version of the

more general multiple elastic scattering of multipole expansions model (MESME),[35] which has been previously used to simulate SPR in nanoparticle chains.[36] Indeed, the small inter-particle distance also leads to significant quadrupole and even higher-order multipole interactions. Especially, the short distance interaction between nearest neighbors is increased in comparison to the simple dipole interaction model.

Here, the simple structure of the dipole model is exploited to analytically discuss several aspects of the long chain limit, not accessible by a full-scale numerical solution of Maxwell equation. First of all, by evaluating the eigenvalue problem $\bar{G}\bar{P}(\omega) = a\omega P(\omega)$ (see **Supporting Section A.V.1**), equation V.2 admits analytical solutions for the mode structure in arbitrary chain lengths, if the interaction to nearest neighbors (*i.e.* $j = i \pm 1$) is restricted, the inverse polarizability in the considered energy loss regime (*i.e.* $\alpha^{-1} \approx a\omega$) is linearized, and a ω-averaged propagator (*i.e.*, $G(\omega) \approx \bar{G}$) is used. In particular, the longitudinal mode energies are given by

$$\omega_l = \omega_0 - 2G_{xx}\cos\left(\frac{l\pi}{n+1}\right), \qquad l \in \{1,\ldots,n\} \tag{V.3}$$

with n denoting the number of particles. The corresponding polarizations read

$$P_{xj,l} = \sin\left(\frac{l\pi}{n+1}\right), \qquad l \in \{1,\ldots,n\} \tag{V.4}$$

with j being the particle index. Inserting the dipole field propagator and employing a polarizability derived from the dielectric function of gold,[37] the transverse mode is, however, too high in energy at 2.5 eV and the energy band is too narrow (0.5 eV) compared to the experiment. In order to obtain the band widths in reasonable agreement with experiment (*i.e.,* approximately taking higher-order multipole interactions into account), the coupling parameters were adapted to $G_{xx} \approx 800$ THz (3.3 eV / 375 nm) for the dipole aligned along the chain (see **Figure V.13a**). An indirect proof for the existence of higher-order multipole couplings is provided by the full-scale numerical solution of Maxwell's equation, which correctly reproduced the band width. The energy shift can be explained by the interaction with the carbon substrate. The latter acts as a reflecting half-plane for the electric field of the plasmon mode, introducing a second propagator (see again **Supporting Section A.V.1** for an explicit expression)

$$P_i(\omega) = \alpha(\omega)\left(E_{ext}(\omega) + \sum_{j\neq i} G_{ij}(\omega)P_j(\omega) + \sum_j G^{ref}_{ij}(\omega)P_j(\omega)\right). \tag{V.5}$$

Primarily, the reflected partial wave directly acts back on the emitting particle, giving rise to an additional self-interaction term $\alpha(\omega)G^{ref}_{ii}(\omega)P_j(\omega)$. This term leads to a renormalization of the polarization and hence, to a plasmon energy according to

$$P_i(\omega) = \frac{\alpha(\omega)}{1-\alpha(\omega)G^{ref}_{ii}(\omega)}\left(E_{ext}(\omega) + \sum_{j\neq i} G_{ij}(\omega)P_j(\omega)\right). \tag{V.6}$$

Numerical calculations using the dielectric function of carbon and the geometry of the gold particles show that this effect is sufficient to explain the red-shift of approximately 0.2 eV (see also Ref. [38]). In the full-scale solution of the Maxwell equations, an effective medium approach was employed to reproduce the red-shift. Considering the various involved approximations, the

agreement among full-scale simulations, the dipole model, and the experimental results is rather good (see **Figure V.13a**). The remaining differences to the experimental observed energies are ascribed to long-range coupling of the reflected wave (not included in our models) and deviations from the idealized geometry in the experiment, such as fluctuations in distance, shape, alignment, surface, *etc.* The latter can be subsumed under disorder effects. While the accurate description of disorder effects requires elaborate perturbation and renormalization schemes (for example, see Ref. [39] for a treatment within the self-consistent theory of Anderson localization), it is has been established that disorder in 1D systems always tends to localize the wave field with a characteristic exponential damping $|E| \sim \exp\left(\frac{|x-x_0|}{\xi(\eta)}\right)$ depending on the disorder strength η.[40] Upon close inspection of the investigated long chains, indeed, the localized excitations are close to geometric perturbations of the chain (*e.g.,* close to the kink in **Figure V.11b**); however, a larger sample base would be required to further elaborate this effect.

Next, the *infinite chain limit* is discussed using the discrete dipole model. The dipole coupling model describes analytically the formation of a continuous band of longitudinal modes with a dispersion relation (wave vector q) $\omega(q) = \omega_0 - 2G_{xx}\cos(qd)$ in the *infinite chain limit* (d denotes the inter-particle distance). However, due to the finite energy resolution and the finite lifetime (energy width) of the plasmon modes, only a supposition of harmonics can be excited (L* mode). Thus, the highest group velocity $v_{max} = [\partial\omega/\partial q]_{max} \approx 0.4c$ is reached around $q = {}^{2\pi}/_{4d}$, which corresponds to longitudinal plasmon modes close to the energy of the (non-dispersive) transverse mode. The group velocities decrease toward the longer wavelengths (and therefore lower excitation energies). Consequently, the group velocity and hence, the transport in the transversal mode is almost zero as the coupling $G_{yy,zz}$ between the transverse dipoles is very small. Finally, the analytical expressions for the net dipole moment are $p_x(q) = \frac{1}{qd}(1-\cos(qL))$ of the q-dependent modes (chain length L), which is a measure for the optical coupling strength of individual modes (*e.g.,* optically dark modes have a net moment zero). Accordingly, dark modes appear, whenever $q = \frac{2\pi n}{L}$ and the largest net dipole moment is realized in the long wavelength limit $q \to 0$. Furthermore, from the analytical band dispersion, the plasmonic density of states can be computed according to

$$DOS(\omega) = 2\frac{dq(\omega}{d\omega} = \left(G_{xx}d\sqrt{1-\left(\frac{\omega-\omega_0}{2G_{xx}}\right)^2}\right)^{-1}, \tag{V.7}$$

which also grows toward smaller excitation energies (more generally toward the band edge, which coincides the band minimum in this case). Consequently, we may conclude that the optical coupling ($\approx p \times DOS$) is maximal for lower excitation energies, where it is eventually bounded by increasing losses. Thus, treating more complicated chains (*e.g.,* with multipartite basis) including beyond-nearest neighbor interactions requires numerical schemes. However, for periodic arrangements such as the long chain, the use of Bloch's theorem greatly facilitates their implementation (see SI Section S1). In that case, equation V.2 reads

$$c_{a,\mu}(q,\omega) = \sum_{b\nu} D^{b\nu}_{a,\mu}(q,\omega)c_{b,\mu}(q,\omega) \tag{V.8}$$

With $c_a\mu$ (nanoparticle index in unit cell a, cartesian index μ) denoting the excitation coefficients of the Bloch waves $P_{a,\mu} = c_{a,\mu}(q,\omega)\exp(iqx_n)$ and $D^{b\nu}_{a,\mu}$ a dynamical coupling matrix. This formulation has been recently used to compute topological effects in Su-Schrieffer-Heeger model chains.[41]

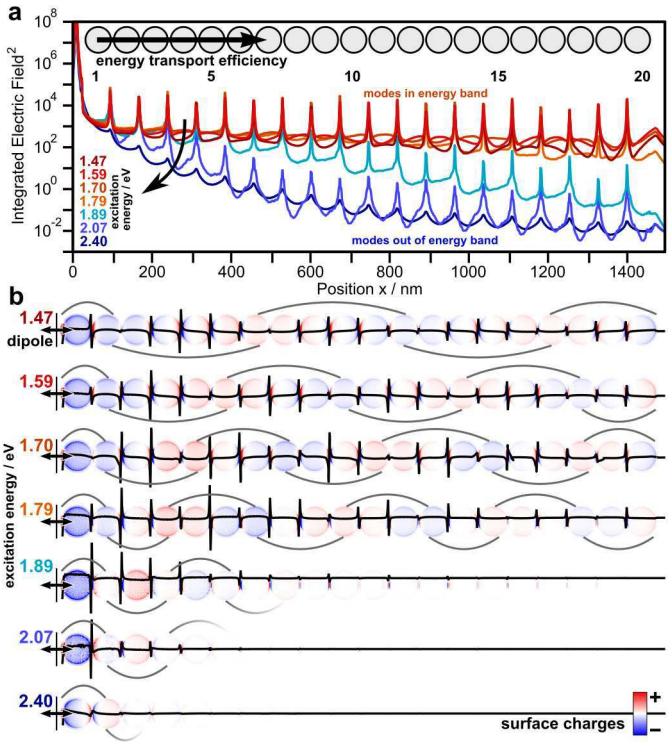

Figure V.14.: Energy-transport properties of plasmonic polymers (consisting of 20 nanoparticles). (a) Integrated electric field along the particle chain in respect to various dipole energies. (b) Corresponding integrated surface charge images (red-blue color scale) and surface charge waves (black lines).

To highlight the substantial importance of the degenerated L* mode in the plasmonics of linear particle chains, its impact on energy transport along such chains is briefly studied in the following. These considerations will also shine light on an important consequence of the non-Hermiticity (*i.e.,* lossy) nature of the plasmonic system by providing a characteristic length scale for the coherent coupling of the plasmonic modes. Plasmonic waveguiding is chosen because it is typically described as one of the most promising applications for linear particle chains.[11,18,42] Furthermore, the effect is dominated by near-field effects. As it has been suggested earlier, the previously observed degenerated modes have suppressed radiative losses, which may be further tuned by higher-multipole-order near field coupling terms (beyond dipole).[8,43–45] Finite-difference time-domain (FDTD) electromagnetic modeling were employed to quantify the energy transport properties (**Figure V.14**). As a simplified waveguiding experiment, a dipole source at one end of the particle chain is used as source. **Figure V.14a** visualizes the energy transport efficiency along the chain for all excitable modes by the integrated electric field (red indicating within and blue indicating out of the energy band).

The energetically highest mode (transversal, 2.42 eV, dark blue) exhibits a double exponential decay resulting in a theoretical damping factor of −1.83 dB / 50 nm. Longitudinal waveguiding modes above 1.8 eV (*i.e.*, not yet merged with the energy band) perform similar with a fast decay of the transported energy (blue, for the spectral overlap of the individual longitudinal modes see **Supporting Figure A.V.11b**). Contrary, degenerated modes overlapping with the energy band support efficient waveguiding with damping factors as low as −0.26 dB / 50 nm (for an excitation energy of 1.59 eV). For very small energies, however, the damping factor increases again. This behavior is consistent with previous studies[8] and can be explained by an optimal balance of group velocity (increasing toward higher energies) and radiative losses (decreasing toward high energies) in the sub-radiant above the super-radiant L1. In comparison to a comparable DNA-assembled waveguide, which is below the *infinite chain limit*, the herein observed damping by factor of 3 lower.[18]

Table V.1.: Plasmonic waveguide properties of different plasmonic modes (transverse mode: 2.42 eV and longitudinal modes: >2.42 eV; the mode size describes the radial drop to e^{-2}) of the integrated E^2 along the chain.

Excitation Energy / eV	**2.42**	**2.07**	**1.89**	**1.79**	**1.70**	**1.59**	**1.47**
Integrated E_0^2 (x_0 = 0 nm)	1071	1513	1925	1758	1679	1519	1171
Integrated E_N^2 (x_N = 1380 nm)	<0.01	<0.01	0.06	28	218	284	114
Damping / dB / 1380 nm	−50.41	−56.29	−45.04	−17.96	−8.86	−7.28	−10.10
Damping / dB / 50 nm	−1.83	−2.04	−1.63	−0.65	−0.32	−0.26	−0.37
Effective mode energy / eV	8.86	4.43	4.13	2.82	2.58	2.07	1.70
Effective mode size / nm	137	141	145	173	198	229	261

The properties of the supported waveguiding modes as well as the integrated electric fields E^2 at the first and last particle for each mode (necessary to calculate the damping factor) are listed in **Table V.1**. The induced surface charge waves (**Figure V.14b**) propagate with an effective energy along the particle chain, as visualized by the respective length of the wave package. Finally, the mode size perpendicular to the particle chains (energy E^2 at e^{-2} of the cross section) is critical for practical applications in order to avoid cross-talk between neighboring waveguides. The mode size for degenerated modes is below 300 nm, while for the non-degenerated modes it is 140 nm. However, in the real system disorder effects produce an additional localization (see discussion above), which may further increase the damping factor.

In summary, we directly observed the formation of hybridized plasmonic modes on linear nanoparticle chains as a function of the chain length ranging from one nanoparticle to the *infinite chain limit*. Plasmonic oligomers and polymers have been fabricated by template-assisted colloidal self-assembly yielding highly ordered chains with low disorder. Electron energy-loss spectroscopy and theoretical modeling allowed us to characterize the plasmonic mode transition between short chains (plasmonic oligomers) and long chains (plasmonic polymers). Plasmonic oligomers show well-separated, non-degenerated longitudinal modes and degenerated transverse modes. Beyond roughly 10 particles a band of longitudinal modes eventually emerges. This band exhibits a degenerated plasmonic waveguide mode signature with a large dispersion, which makes it suitable for long distance energy transport in the optimal band region. Theoretical simulations of the waveguiding performance suggest that the L* mode with a mode wavelength of 730 nm is able to transport energy with a damping of −0.26 dB / 50 nm at a mode cross sec-

tion size of 260 nm. Our findings pave the way for further exploitation of plasmonic nanoparticle chains as waveguides and photonic devices. For example, the waveguide mode can be intervened at each contact point by inserting materials such as fluorescent emitters[46] and organic[47] or smart polymers[48] to further modulate and enhance the radiative properties of the plasmonic waveguide.[49] Of particular interest is the coupling at end points of the chain, which sustain particular edge states that may be tuned by complex chain geometries (*e.g.*, bipartite chains). Furthermore, the presented approach opens up new possibilities to study combinatorically the plasmonics of multimetallic chains or chains with multiply particle morphologies within one chain.

Methods

Synthesis, template-assisted colloidal self-assembly, and wet-transfer to carbon-coated TEM grid. Synthesis of single-crystalline spherical gold nanoparticles with a diameter of 70.5 ± 1.2 nm by a three-step seed-mediated growth approach, and template-assisted self-assembly into wrinkled PDMS templates *via* spin-coating of protein (BSA) coated particle solutions (12 mg/mL [Au^0]) was performed as published elsewhere.[30] The pH of the nanoparticle solution was adjusted to pH 10 in order to produce closely-packed particle lines in non-completely filled templates.

Transfer of the in the grooves of the template assembled particle chains was performed by wet-contact-printing. The 3 nm carbon-film coated TEM grid (copper, 300 square meshes) was incubated in a PEI-solution (1 mg/ml, 1800 g/mol, linear) for 1 h, and subsequently washed with purified water (Purified water, Milli-Q-grade, 18.2 MΩ cm at 25 °C). For the transfer, a 2 μL water droplet (pH 10) was placed on the TEM grid, the particle-filled PDMS-stamp was pressed onto the grid with a constant pressure of 100 kPa and left for drying under environmental control (23 °C, 55% relative humidity). After drying (4 h), the stamp was carefully removed leaving the nanoparticle chains on the carbon film of the grid.

STEM EELS characterization. STEM scanning and EELS spectrum-imaging was performed in the probe-corrected Titan^3 operating at 300 kV. The microscope was equipped with a Tridiem energy filter and a Wien monochromator operating in the accelerating mode, which ensured the energy resolution of 100–120 meV. However, in the real system disorder effects produce an additional localization (see discussion above), which may further increase the damping factor.

The spectrum-images were acquired with a beam current 200 pA and dwell time 25 ms. For each chain of gold particles, 4–7 runs of spectrum-imaging were performed followed by the summation of the data cubes with accounting for the spatial drift between runs. The obtained spectra were corrected for the energy instabilities and the zero-loss peak was then removed by using the reference profile collected in a separate run without any sample object. An example of spectra treatment is shown in **Supporting Figure A.V.7**. Finally, the distinct peaks in the low-loss region of spectra were recognized and their energy positions and magnitude were fitted using the non-linear least square (NLLS) procedure. The integrated area under each fitted peak was plotted as a function of the beam position giving rise to maps of the probability for plasmon excitation, *i.e.*, maps of energy-loss.

Electromagnetic simulations. Simulations of electron energy loss spectra and mappings were performed using the Matlab MNPBEM13 toolbox,[50] which is based on the boundary element method (BEM) by García de Abajo.[51] Each sphere of the chain was approximated by triangulation (400 vertices per particle). The dimensions and positions of the gold nanospheres were selected according to the experimental size (70.5 ± 1.2 nm) and spaced with a distance of 1.5 nm. The dielectric properties of gold were taken from Johnson and Christy.[37] An effective medium of n = 1.2 is selected to emulate the air/substrate interface. The energy of the simulated electron beam was set to the experimental accelerating voltage of the TEM (300 kV). For each particle chain several spectra were evaluated in the energy range from 1–3 eV at different (not overlapping) electron beam positions to ensure excitation of all possible plasmonic modes EELS mappings were performed at selected energy levels and were simulated by 1.5 nm meshing of the electron beam. The respective spectra are summarized in **Supporting Figure A.V.10**.

For energy transfer / waveguiding simulations a commercial-grade simulator based on the finite-difference time-domain method (FDTD) was used to perform the calculations (Lumerical Inc., Canada, v8.22).[52] For the broadband and single mode excitation for energy transport, a dipole source for the specific wavelength range (short pulse length of 3 fs, E = 1–4 eV; λ = 300–1300 nm, see spectra in **Supporting Figure A.V.11a**) and single wavelength to probe individual modes (long pulse length of 18 fs) was used with a distance of 15 nm to the first particle, respectively. To extract the exact peak positions from the spectra, the internal multipeak-fitting function of IGOR Pro 7 (WaveMetrics, USA) was used. The mode size of the modes was defined by integrating of E^2 along the particle line and radially defining the $1/e^2$ decay of the E^2 field. For the FDTD simulations, the same refractive index data, nanoparticle dimension, inter particle distance, and materials constants were used as in the BEM simulations. Perfectly matched layers in all principal directions as boundary conditions, zero-conformal-variant mesh refinement and an isotropic mesh overwrite region of 1 nm were used. All simulations reached the auto shut-off level of 10^{-5} before reaching 150 fs of simulation time.

Acknowledgments. This project was financially supported by the Volkswagen Foundation through a Freigeist Fellowship to TAFK. AL has received funding from the European Research Council (ERC) under the Horizon 2020 research and innovation program of the European Union (grant agreement no. 715620). PLP acknowledges funding from DFG 'Zukunftskonzept' (F-003661-553-Ü6a-1020605).

References

[1] J. B. Khurgin, "How to deal with the loss in plasmonics and metamaterials", *Nat Nanotechnol* **2015**, *10*, 2–6.

[2] K. A. Willets, R. P. Van Duyne, "Localized Surface Plasmon Resonance Spectroscopy and Sensing", *Annual Review of Physical Chemistry* **2007**, *58*, 267–297.

[3] K. M. Mayer, J. H. Hafner, "Localized Surface Plasmon Resonance Sensors", *Chemical Reviews* **2011**, *111*, 3828–3857.

[4] M. Rycenga, C. M. Cobley, J. Zeng, W. Li, C. H. Moran, Q. Zhang, D. Qin, Y. Xia, "Controlling the Synthesis and Assembly of Silver Nanostructures for Plasmonic Applications", *Chemical Reviews* **2011**, *111*, 3669–3712.

[5] M. L. Brongersma, J. W. Hartman, H. A. Atwater, "Electromagnetic energy transfer and switching in nanoparticle chain arrays below the diffraction limit", *Physical Review B* **2000**, *62*, R16356–R16359.

[6] J. R. Krenn, "Watching energy transfer: Nanoparticle waveguides", *Nature Materials* **2003**, *2*, 210–211.

[7] F. Vetrone, F. Rosei, "A low-loss origami plasmonic waveguide", *Science* **2017**, *357*, 452–453.

[8] B. Willingham, S. Link, "Energy transport in metal nanoparticle chains via sub-radiant plasmon modes", *Optics Express* **2011**, *19*, 6450.

[9] D. E. Gómez, Y. Hwang, J. Lin, T. J. Davis, A. Roberts, "Plasmonic Edge States: An Electrostatic Eigenmode Description", *ACS Photonics* **2017**, *4*, 1607–1614.

[10] J. B. Khurgin, "How to deal with the loss in plasmonics and metamaterials", *Nature Nanotechnology* **2015**, *10*, 2.

[11] E.-M. Roller, L. V. Besteiro, C. Pupp, L. K. Khorashad, A. O. Govorov, T. Liedl, "Hotspot-mediated non-dissipative and ultrafast plasmon passage", *Nature Physics* **2017**, *13*, 761–765.

[12] S. J. Tan, M. J. Campolongo, D. Luo, W. Cheng, "Building plasmonic nanostructures with DNA", *Nature Nanotechnology* **2011**, *6*, 268–276.

[13] A. Klinkova, R. M. Choueiri, E. Kumacheva, "Self-assembled plasmonic nanostructures", *Chemical Society Reviews* **2014**, *43*, 3976.

[14] D. Solis, A. Paul, J. Olson, L. S. Slaughter, P. Swanglap, W.-S. Chang, S. Link, "Turning the Corner: Efficient Energy Transfer in Bent Plasmonic Nanoparticle Chain Waveguides", *Nano Letters* **2013**, *13*, 4779–4784.

[15] S. J. Barrow, A. M. Funston, D. E. Gómez, T. J. Davis, P. Mulvaney, "Surface Plasmon Resonances in Strongly Coupled Gold Nanosphere Chains from Monomer to Hexamer", *Nano Letters* **2011**, *11*, 4180–4187.

[16] L. S. Slaughter, L.-Y. Wang, B. A. Willingham, J. M. Olson, P. Swanglap, S. Dominguez-Medina, S. Link, "Plasmonic polymers unraveled through single particle spectroscopy", *Nanoscale* **2014**, *6*, 11451–11461.

[17] S. A. Maier, P. G. Kik, H. A. Atwater, “Observation of coupled plasmon-polariton modes in Au nanoparticle chain waveguides of different lengths: Estimation of waveguide loss”, *Applied Physics Letters* **2002**, *81*, 1714–1716.

[18] F. N. Gür, C. P. T. McPolin, S. Raza, M. Mayer, D. J. Roth, A. M. Steiner, M. Löffler, A. Fery, M. L. Brongersma, A. V. Zayats, T. A. F. König, T. L. Schmidt, “DNA-Assembled Plasmonic Waveguides for Nanoscale Light Propagation to a Fluorescent Nanodiamond”, *Nano Letters* **2018**, *18*, 7323–7329.

[19] O. Nicoletti, F. de la Peña, R. K. Leary, D. J. Holland, C. Ducati, P. A. Midgley, “Three-dimensional imaging of localized surface plasmon resonances of metal nanoparticles”, *Nature* **2013**, *502*, 80.

[20] S. M. Collins, O. Nicoletti, D. Rossouw, T. Ostasevicius, P. A. Midgley, “Excitation dependent Fano-like interference effects in plasmonic silver nanorods”, *Physical Review B* **2014**, *90*, 155419.

[21] D. Rossouw, M. Couillard, J. Vickery, E. Kumacheva, G. A. Botton, “Multipolar plasmonic resonances in silver nanowire antennas imaged with a subnanometer electron probe”, *Nano Letters* **2011**, *11*, 1499–504.

[22] B. Schaffer, K. Riegler, G. Kothleitner, W. Grogger, F. Hofer, “Monochromated, spatially resolved electron energy-loss spectroscopic measurements of gold nanoparticles in the plasmon range”, *Micron (Oxford England : 1993)* **2009**, *40*, 269–273.

[23] S. J. Barrow, S. M. Collins, D. Rossouw, A. M. Funston, G. A. Botton, P. A. Midgley, P. Mulvaney, “Electron Energy Loss Spectroscopy Investigation into Symmetry in Gold Trimer and Tetramer Plasmonic Nanoparticle Structures”, *ACS Nano* **2016**, *10*, 8552–8563.

[24] S. J. Barrow, D. Rossouw, A. M. Funston, G. A. Botton, P. Mulvaney, “Mapping Bright and Dark Modes in Gold Nanoparticle Chains using Electron Energy Loss Spectroscopy.”, *Nano Letters* **2014**, *14*, 3799–3808.

[25] M. Mayer, A. M. Steiner, F. Röder, P. Formanek, T. A. F. König, A. Fery, “Aqueous Gold Overgrowth of Silver Nanoparticles: Merging the Plasmonic Properties of Silver with the Functionality of Gold”, *Angewandte Chemie International Edition* **2017**, *56*, 15866–15870.

[26] C. Hanske, M. Tebbe, C. Kuttner, V. Bieber, V. V. Tsukruk, M. Chanana, T. A. F. Konig, A. Fery, “Strongly Coupled Plasmonic Modes on Macroscopic Areas via Template-Assisted Colloidal Self-Assembly”, *Nano Letters* **2014**, *14*, 6863–6871.

[27] J. Krehl, G. Guzzinati, J. Schultz, P. Potapov, D. Pohl, J. Martin, J. Verbeeck, A. Fery, B. Büchner, A. Lubk, “Spectral field mapping in plasmonic nanostructures with nanometer resolution”, *Nature Communications* **2018**, *9*, DOI 10.1038/s41467-018-06572-9.

[28] M. Mayer, M. Tebbe, C. Kuttner, M. J. Schnepf, T. A. F. König, A. Fery, “Template-assisted colloidal self-assembly of macroscopic magnetic metasurfaces”, *Faraday Discussions* **2016**, *191*, 159–176.

[29] M. Tebbe, M. Mayer, B. A. Glatz, C. Hanske, P. T. Probst, M. B. Müller, M. Karg, M. Chanana, T. A. F. König, C. Kuttner, A. Fery, "Optically anisotropic substrates via wrinkle-assisted convective assembly of gold nanorods on macroscopic areas", *Faraday Discussions* **2015**, *181*, 243–260.

[30] A. M. Steiner, M. Mayer, M. Seuss, S. Nikolov, K. D. Harris, A. Alexeev, C. Kuttner, T. A. F. Konig, A. Fery, "Macroscopic Strain-Induced Transition from Quasi-infinite Gold Nanoparticle Chains to Defined Plasmonic Oligomers", *ACS Nano* **2017**, *11*, 8871–8880.

[31] Y. Zheng, X. Zhong, Z. Li, Y. Xia, "Successive, Seed-Mediated Growth for the Synthesis of Single-Crystal Gold Nanospheres with Uniform Diameters Controlled in the Range of 5-150 nm", *Particle & Particle Systems Characterization* **2014**, *31*, 266–273.

[32] P. Nordlander, C. Oubre, E. Prodan, K. Li, M. I. Stockman, "Plasmon Hybridization in Nanoparticle Dimers", *Nano Letters* **2004**, *4*, 899–903.

[33] M. Mayer, L. Scarabelli, K. March, T. Altantzis, M. Tebbe, M. Kociak, S. Bals, F. J. García de Abajo, A. Fery, L. M. Liz-Marzán, "Controlled Living Nanowire Growth: Precise Control over the Morphology and Optical Properties of AgAuAg Bimetallic Nanowires", *Nano Letters* **2015**, *15*, 5427–5437.

[34] C. A. Downing, G. Weick, "Topological collective plasmons in bipartite chains of metallic nanoparticles", *Physical Review B* **2017**, *95*, 125426.

[35] F. J. García de Abajo, "Interaction of Radiation and Fast Electrons with Clusters of Dielectrics: A Multiple Scattering Approach", *Physical Review Letters* **1999**, *82*, 2776–2779.

[36] W. Cai, R. Sainidou, J. Xu, A. Polman, F. J. García de Abajo, "Efficient Generation of Propagating Plasmons by Electron Beams", *Nano Letters* **2009**, *9*, 1176–1181.

[37] P. B. Johnson, R. W. Christy, "Optical Constants of the Noble Metals", *Physical Review B* **1972**, *6*, 4370–4379.

[38] J. Waxenegger, A. Trügler, U. Hohenester, "Plasmonics simulations with the MNPBEM toolbox: Consideration of substrates and layer structures", *Computer Physics Communications* **2015**, *193*, 138–150.

[39] A. Lubatsch, J. Kroha, K. Busch, "Theory of light diffusion in disordered media with linear absorption or gain", *Physical Review B* **2005**, *71*, 184201.

[40] N. F. Mott, W. D. Twose, "The theory of impurity conduction", *Advances in Physics* **1961**, *10*, 107–163.

[41] S. R. Pocock, X. Xiao, P. A. Huidobro, V. Giannini, "Topological Plasmonic Chain with Retardation and Radiative Effects", *ACS Photonics* **2018**, *5*, 2271–2279.

[42] S. Lal, S. Link, N. J. Halas, "Nano-optics from sensing to waveguiding", *Nature Photonics* **2007**, *1*, 641.

[43] J. J. Choquette, K.-P. Marzlin, B. C. Sanders, "Superradiance, subradiance, and suppressed superradiance of dipoles near a metal interface", *Physical Review A* **2010**, *82*, DOI 10.1103/PhysRevA.82.023827.

[44] C. Ropers, D. J. Park, G. Stibenz, G. Steinmeyer, J. Kim, D. S. Kim, C. Lienau, "Femtosecond Light Transmission and Subradiant Damping in Plasmonic Crystals", *Physical Review Letters* **2005**, *94*, DOI 10.1103/PhysRevLett.94.113901.

[45] M. I. Stockman, S. V. Faleev, D. J. Bergman, "Localization versus Delocalization of Surface Plasmons in Nanosystems: Can One State Have Both Characteristics?", *Physical Review Letters* **2001**, *87*, DOI 10.1103/PhysRevLett.87.167401.

[46] M. J. Schnepf, Y. Brasse, F. R. Goßler, A. M. Steiner, J. Obermeier, M. Lippitz, A. Fery, T. A. König, "Single Particle Spectroscopy of Radiative Processes in Colloid-to-Film-Coupled Nanoantennas", *Zeitschrift fur Physikalische Chemie* **2018**, *232*, 1593–1606.

[47] C. Stelling, C. R. Singh, M. Karg, T. A. F. König, M. Thelakkat, M. Retsch, "Plasmonic nanomeshes: their ambivalent role as transparent electrodes in organic solar cells", *Scientific Reports* **2017**, *7*, DOI 10.1038/srep42530.

[48] K. Volk, J. P. S. Fitzgerald, P. Ruckdeschel, M. Retsch, T. A. F. König, M. Karg, "Reversible Tuning of Visible Wavelength Surface Lattice Resonances in Self-Assembled Hybrid Monolayers", *Advanced Optical Materials* **2017**, *5*, 1600971.

[49] M. Mayer, M. J. Schnepf, T. A. F. König, A. Fery, "Colloidal Self-Assembly Concepts for Plasmonic Metasurfaces", *Advanced Optical Materials* **2019**, *7*, 1800564.

[50] U. Hohenester, A. Trügler, "MNPBEM – A Matlab toolbox for the simulation of plasmonic nanoparticles", *Computer Physics Communications* **2012**, *183*, 370–381.

[51] F. J. García de Abajo, J. Aizpurua, "Numerical simulation of electron energy loss near inhomogeneous dielectrics", *Physical Review B* **1997**, *56*, 15873–15884.

[52] Lumerical Inc., CA, **2018**, http://www.lumerical.com/tcad-products/fdtd/ (visited on 11/06/2018).

Chapter

Conclusion

VI

Starting with one of the first descriptions of plasmonic effects in 1857 by Michael Faraday, the development and innovation of plasmonics connected with colloidal science. Thus, advances in the field of plasmonics also rely on the intrinsic properties of colloidal particles. One of the most tangible examples is a simple spherical gold nanoparticle, whose shape is not accessible by top-down methods, but results in distinct properties due to its isotropy. Along this line, the objective of this thesis was to explicitly focus on the intrinsic advantages of colloids and the resulting plasmonics: The three-dimensionality of colloidal nanoparticles in combination with their tunable dielectric ligand shell. In this context, my contribution spans this research field by concentrating on the design of adequate colloidal particles and the fundamental understanding of the plasmonics of self-assembled structures made from three-dimensional particles. In order to investigate the plasmonics of coupled particle assemblies, colloidal self-assembly was used as a versatile tool to fabricate suitable structures with nanometer precision and in dimensions, which allow for statistically relevant or even combinatorial approaches. Accordingly, this thesis is divided into two main chapters: design of colloidal building blocks (Chapter IV) and coupled particle assemblies (Chapter V).

From the plasmonic point of view, silver is the superior material due to its high quality factor and accessibility of the complete optical range. But the so-far available synthetic protocols typically result in a broad size and morphology distribution and in general, silver lacks chemical stability. **Chapter IV** introduced a general synthetic protocol for silver colloids aiming to comply with the high required particle quality for colloidal self-assembly and to countervail the intrinsic vulnerability of silver.

In **Section IV.1**, crystallinity, shape control, and also dispersity in size, has been rigorously improved for the resulting silver nanoparticles by enforcing the concept of *controlled living growth conditions*. The synthetic concept was introduced for the example of the controlled silver overgrowth of pentatwinned gold nanorods used as seed cores. The thereby yielded colloidal dispersions of nanowires featured a remarkably high quality and low polydispersity.
By establishing a constant silver deposition rate on the tips of pentatwinned gold nanorods, the lengths of the silver-gold-silver nanowires increased linearly in time with nanometer control. Therefore, the obtained one-dimensional growth process could be linked with classical polymerization processes, enabling us to generalize the concept.
In general, this concept exploits well-defined gold nanoparticles as seeds for a kinetically and thermodynamically controlled overgrowth process. As a result, the line width of the plasmonic modes of the colloidal ensemble is much narrower than for comparable lithographic or colloidal nanoparticle systems within the same spectral range. The experimental quality factor is in fact reasonably close to its theoretical limit, and the difference between them is explained by the experimental finite size distribution.
In the exemplified case of nanowires, the developed protocol provides the possibility to fine-tune the nanowire length up to the several micrometers. Thus, the obtained colloids represent optical antennas that posses a large number of plasmonic modes spreading over the entire UV-vis-IR region. For example for 900 nm long nanowires, distinguishable plasmonic modes up to the eighth order could be directly detect in the colloidal dispersion. The comprehensive electron

energy loss spectroscopy investigation demonstrated, that the gold core does not interfere with the plasmon propagation along the nanowire, whilst its influence is limited to higher energy modes.

Next, the introduced concept of *controlled living silver growth* was further generalized to another morphology in **Section IV.2** and extended with the overgrowth of an additional gold shell. Thus, the developed synthetic pathway successfully combines all benefits of silver and gold in a fully aqueous system. This was achieved by initially controlling the overall particle distribution and morphology *via* an optically masked gold core, and the superior optical properties of silver were chemically protected with a inert gold layer of sub-skin depth thickness.
Experimentally, the synthetic steps were exemplified for a cubic shape. Its sharp corners and edges exhibit high plasmonic and morphological sensitivity toward the influence of the gold core, the gold shell, and the resulting chemical stability.
By using single crystalline gold nanospheres as seeds, the *controlled living silver growth* results in silver nanocubes with low polydispersity and remarkably sharp corners. In the next step, these cubes were coated with a sub-skin depth gold shell aiming to chemically protect the silver. Since gold overgrowth can result in etching of the silver or in galvanic replacement reactions, the reaction conditions needed to be precisely balanced. This was achieved by similar reaction conditions as for the silver overgrowth, but additionally to the kinetic and thermodynamic control, the reduction potential of the employed gold precursor complex needs to be adjusted. By introducing a finely-tuned iodide amount in the gold-salt complex, the reduction potential of gold was sufficiently reduced. Thus, all side or etching reactions could be successfully suppressed resulting in a homogeneous gold layer with a thickness of 1.1 nm, corresponding to approximately three atom layers of gold. p While optical spectroscopy and electromagnetic simulations could show the negligible effect of the gold shell on the plasmonic properties, the gold shell proved full chemical stability in long-term experiments against oxidation in dispersed and dried state. Furthermore, due to the short-chain ligands in the aqueous media, the noble metal surface is accessible for chemical functionalization and the gold layer hinders etching of the silver by the employed ligands. Later on, the concept was successfully transferred to silver nanowires without the need to alter the protocol.
This wet-chemical synthetic approach opens new possibilities in scalable bottom-up fabrication, especially integration with plasmonics applications requiring long-term stability. By *controlled living silver growth* conditions the control over the size distribution and morphology control were pushed to a quality complying with the requirements for colloidal self-assembly. Additionally exploitation of the advantages of silver-based plasmonics boosts the sensitivity, while maintaining the oxidation resistance and chemical functionality of the fully-accessible gold surface by the gold coating.

Plasmonic coupling in colloidal systems differs distinctively from top-down fabricated substrates. These differences are mainly based on the three-dimensional character of colloids and the accessibility to much smaller interparticle distances limited only by the dielectric shell. **Chapter V** described the plasmonics of coupled particle assemblies with focus on the intrinsic features of colloidal particles. Template-assisted self-assembly was used as tool to fabricate the presented systems. Within this chapter, the complexity of the coupling increased gradually from local to collective effects.

In **Section V.1**, a macroscopic magnetic metasurface was fabricated by template-assisted colloidal self-assembly of gold nanorods supported by a gold mirror. The design concept utilizes mirror charges induced by the gold nanorods in the gold film with the aim to excite locally the required magnetic resonance. Due to the low coupling distance of the gold nanorod to the mirror, the achieved magnetic resonance was detectable in an isolated spectral range and by conventional optical spectroscopy (*i.e.,* UV-vis-NIR). The obtained small coupling distance of this metasurface relied on the thin and homogeneous protein shell of the employed pentatwinned gold nanorods. In combination with their pentagonal cross section, this system exhibited a robust and reproducible coupling geometry allowing up-scaling to square millimeters sized samples.
In more detail, alignment *via* wrinkle-assisted self-assembly allowed to macroscopically orient wet-chemically synthesized gold nanorods with an extraordinary precision. The nanorods could be quantitatively transferred on a thin, semi-transparent gold film by wet-contact printing. Assembly into linear particle arrays ensured high filling of the substrate, while transversal excitation of the nanorod avoided cross-talk between neighboring unit cells—thus, efficiently separating the geometric and the excitation axis. Evaluation of SEM images revealed an average deviation from the main orientation axis below 2.7° resulting in an averaged two-dimensional order parameter $\langle S_{2D} \rangle$ close to unity (0.99).
As proven by conventional UV-vis-NIR spectroscopy matched with electromagnetic simulations, the assembly technique yielded a low mean coupling distance of 1.1 nm with a standard deviation of 0.2 nm. The induced Fano-like signature of the magnetic resonance was identified at a wavelength of 721 nm. Exemplarily, the line shape of the magnetic mode was exploited to show its high sensitivity to external stimuli. The hydrophilic nature of the employed protein shell is capable to change the surrounding dielectric media by swelling upon relative humidity changes. Consequently, the sensitivity of the magnetic mode can be used to track the effect of environmental changes to the conformational changes of the protein monolayer around the particles. Finally, the circulating current oscillation between nanorod and gold film is indeed able to locally tune the effective magnetic permeability, as shown by electromagnetic simulations for the magnetic resonance.

Section V.2 focused on the gradual transition from local to collective coupling for linear monopartite chains of plasmonic particles. In striking difference to plasmonic rod-like structures, the induced plasmonic modes approach a certain limit in excitation energy (*infinite chain limit*), which allows light manipulation below the diffraction limit. Thus, these chains are promising plasmonic waveguides because of their strong field confinement and (relatively) low dielectric losses. This was achieved by exploiting the spherical shape and the thin dielectric shell of the employed particles, whereby the cross section of the coupling geometry was efficiently reduced to a point and

the inter-particle distance set to a homogeneous distance of approximately 1.5 nm, respectively. To be more precise, wrinkle-assisted directed self-assembly was used to create highly ordered chains of different lengths. Particle chains spanning the range from two particles (140 nm) up to 20 particles (1500 nm) were fabricated with this method. The plasmonic mode transition between short chains (plasmonic oligomers) and long chains (plasmonic polymers) was comprehensively characterized by electron energy-loss spectroscopy and theoretical modeling. Plasmonic oligomers revealed non-degenerated plasmonic L-modes, while long particle chains showed the clear signature of a degenerated plasmonic L* mode. With a simplified dipole coupling model, the presence and nature of the non-degenerated and degenerated plasmonic modes for the different chain lengths could be explained. By the degeneracy, the resulting near-field plasmonics can now be exploited to clearly distinguish between plasmonic oligomers (L-modes) and plasmonic polymers (L* modes).
The degenerated surface plasmon mode shows suppressed radiative losses for efficient energy propagation even for over long distances. Thus, all possible plasmonic waveguide modes in a long nanoparticle chain (1500 nm) were studied, as a proof of concept experiment. Theoretical simulations of the energy transport performance suggest, that the L* mode with an excitation wavelength of 730 nm is able to transport energy with a damping of -0.26 dB/50 nm at a mode size of 260 nm. The potential of the such a colloidal particle chain is that the waveguide can be intervened at each contact point and thus, functionality and tunability can be introduced.

In summary, this thesis aimed to highlight, emphasize, and especially, elucidate the three-dimensional properties of colloidal nanoparticles in, and for, colloidal plasmonic systems. The novel introduced synthesis concept for stable silver nanoparticles with various morphologies potentially will further enhance the plasmonic properties of colloidal systems. The combination of the high quality factor of silver with the variability of an exchangeable dielectric shell can be exploited to harvest stronger coupling interactions or to introduce responsiveness.
The fundamental understanding of the near-field effects of plasmonically coupled colloids opens up new possibilities to rationally introduce colloidal assemblies into various applications. These applications may include the as aforementioned use in sensing or energy transport topics, but also smart metasurfaces with emergent properties or smart polarimeters with tunable strong plasmonic chirality are within reach. Finally, combining the advantages of silver-based plasmonics with coupled plasmonic systems *via* colloidal self-assembly will further enhance the targeted plasmonic features and allow to spectrally tune the optics to match respective applications. In a broader perspective, the obtained deeper comprehension of the near-field properties and introduction of the specially designed building blocks holds great potential to couple the resulting collective plasmonic systems to non-plasmonic effects.
These could be, for example, photonic systems, materials with active gain, or catalytic metals. The first example may result in extraordinary quality factors and line widths. The second one in reduced losses and plasmonic lasing. In the last example, plasmonics could be used to boost and promote the catalytic activity of other metals and systems. Consequently, several other scientific fields and applications may profit from the well-designed collective plasmonic effects of colloidal building blocks.

Chapter

Appendix A

The information and figures in the Appendix are published in the Supporting Information of the underlying publications and are adapted within the respective permissions.

A.IV Design of Colloidal Building Blocks

1. Controlled Living Silver Growth

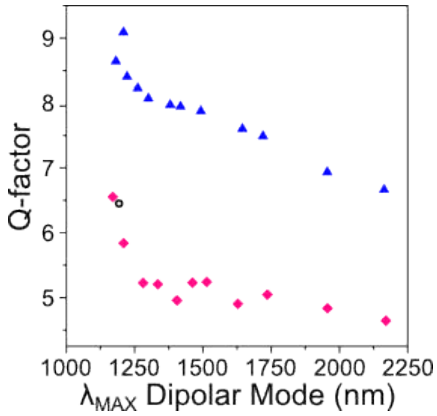

Figure A.IV.1.: Evolution of the QF during living nanowire growth. Experimentally (pink diamonds) we observed an exponential decrease in QF as a function of the dipole mode position. This trend was confirmed by BEM calculations (blue triangles). Interestingly the theoretical values are only 25% higher and show a similar decay rate, confirming the low polydispersity of AgAuAgNWs throughout the entire reaction. The black circle is the QF of the starting PT-AuNRs solution.

Table A.IV.1.: Summary of the TEM analysis relative to **Figure IV.3a**. It should be noticed that the NWs thickness increases at early growth stages, but then remains constant throughout all the experiment. The last two samples (AgEn=3.82 and 8.59) are not shown in **Figure IV.3a** for clarity.

AgEn	Thickness / nm	Length / nm	AR	Ag length per tip / nm	Dipole LSPR λ_{MAX} / nm
//	34 ± 1	210 ± 10	6.1 ± 0.4	//	1192
0.24	38 ± 1	220 ± 10	5.7 ± 0.5	3 ± 1	1170
0.36	38 ± 1	230 ± 10	6.0 ± 0.4	7 ± 2	1210
0.48	38 ± 1	240 ± 10	6.3 ± 0.5	17 ± 4	1281
0.60	38 ± 1	250 ± 20	6.7 ± 0.5	24 ± 4	1335
0.72	38 ± 1	270 ± 20	7.1 ± 0.5	33 ± 6	1405
0.84	39 ± 2	280 ± 20	7.3 ± 0.7	39 ± 8	1462
0.96	37 ± 2	300 ± 20	8.1 ± 0.7	50 ± 10	1514
1.20	38 ± 1	340 ± 20	8.9 ± 0.5	61 ± 9	1628
1.44	37 ± 2	360 ± 30	9.7 ± 0.9	75 ± 9	1736
1.92	38 ± 2	420 ± 30	11 ± 1	100 ± 10	1956
2.40	37 ± 2	470 ± 40	13 ± 2	130 ± 20	2170
5.76	38 ± 2	820 ± 90	21 ± 3	300 ± 40	//[a]
11.52	39 ± 3	1500 ± 200	39 ± 7	660 ± 90	//[a]

[a]The dipole resonance was red-shifted beyond the detection limit of the instrument

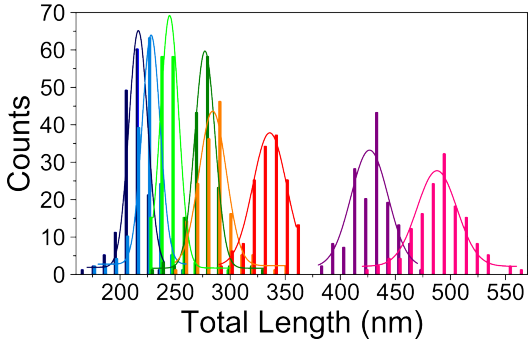

Figure A.IV.2.: Statistical length evaluation of TEM images. Total length distribution histograms of the 8 samples discussed in **Figure IV.3**A. The colors are the same as in **Figure IV.3a**. Histograms were obtained by measuring 150 NRs for each sample.

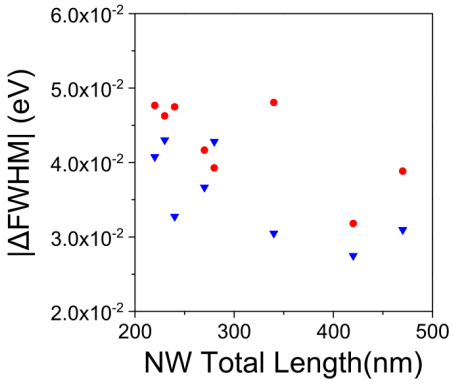

Figure A.IV.3.: Increase in plasmon FWHM due to the finite size distribution of the NWs. We compare the following two quantities: (1) difference of FWHM in experiment minus theory (red circles); (2) estimate of increase in FWHM extracted from the standard deviation of NW lengths observed in TEM images, multiplied by the derivative of the plasmon energy with respect to NW length (blue triangles). We only show results for the lowest-order plasmon mode. This figure confirms that the observed (moderate) increase in FWHM of experiment compared with theory is fully attributable to the finite distribution of NW lengths.

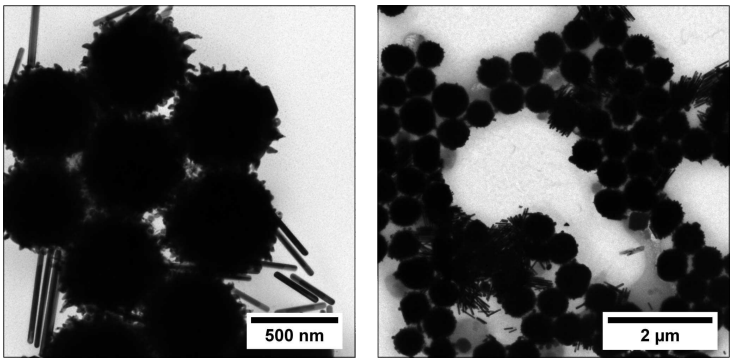

Figure A.IV.4.: AgCl particles observed upon drying when a higher addition rate was used for NW synthesis. The formation of these particles is likely due to accumulation of AgCl in the growth solution

Table A.IV.2.: Summary of TEM analysis of NWs obtained using a higher addition rate (see **Figure IV.3c**). The selective deposition of silver is less efficient, as seen from a double increment of NWs thickness compared to living growth conditions (see **Table A.IV.1**).

AgEn	Thickness / nm	Length / nm	AR	Ag length per tip / nm	Dipole LSPR λ_{MAX} / nm
//	33 ± 1	182 ± 10	5.4 ± 0.3	//	1078
0.36	37 ± 2	193 ± 9	5.3 ± 0.4	5.1 ± 0.4	1061
0.73	38 ± 1	201 ± 11	5.3 ± 0.4	9.1 ± 0.7	1076
1.46	38 ± 2	208 ± 19	5.4 ± 0.6	13.0 ± 0.7	1143
1.84	39 ± 1	228 ± 12	5.8 ± 0.4	23 ± 2	1187
2.58	39 ± 2	266 ± 22	6.8 ± 0.6	42 ± 4	1288
3.33	40 ± 1	300 ± 19	7.6 ± 0.6	59 ± 4	1364
4.08	40 ± 1	313 ± 28	7.8 ± 0.9	65 ± 7	1468
4.84	39 ± 1	313 ± 23	8.1 ± 0.7	65 ± 6	1567
5.60	39 ± 2	362 ± 26	9.3 ± 0.9	90 ± 9	1685
6.54	39 ± 1	406 ± 23	10.5 ± 0.7	112 ± 7	1850
7.49	39 ± 1	451 ± 31	12 ± 1	134 ± 12	2036
8.26	39 ± 2	489 ± 28	13 ± 1.2	153 ± 14	2232
8.74	41 ± 2	898 ± 57	22 ± 2	358 ± 30	//[a]

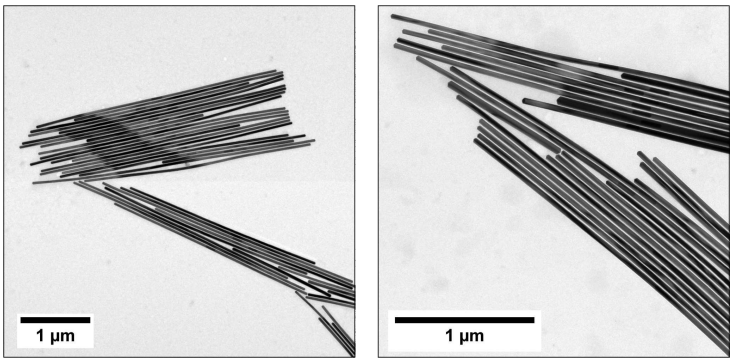

Figure A.IV.5.: TEM images of AgAuAg NWs after 7 days of growth (AgEn=40.32). The average dimensions are: 3.4 ± 0.6 µm in length, 37 ± 2 nm in thickness, corresponding to an average Ag length per tip of 1.6 ± 0.2 µ, and an aspect ratio of 90 ± 10.

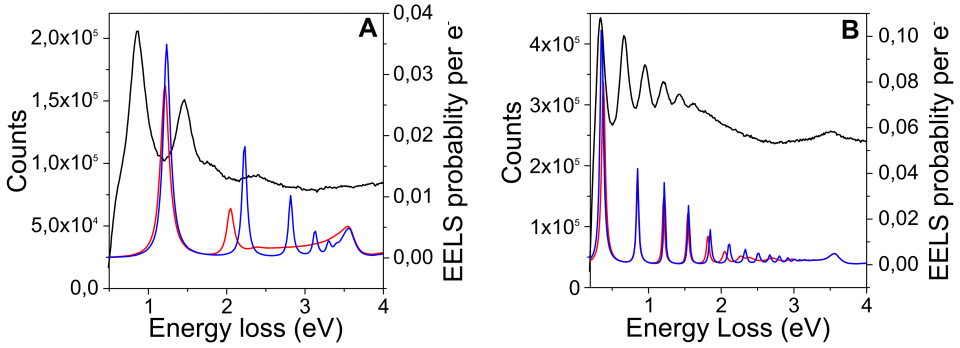

Figure A.IV.6.: Experimental EELS spectra (black) and calculated spectra, in the presence (red) and absence (blue) of the gold core. The Experimental spectra were background corrected to eliminate the zero-loss peak. (A) AgEn=0.5. (B) AgEn=5.3.

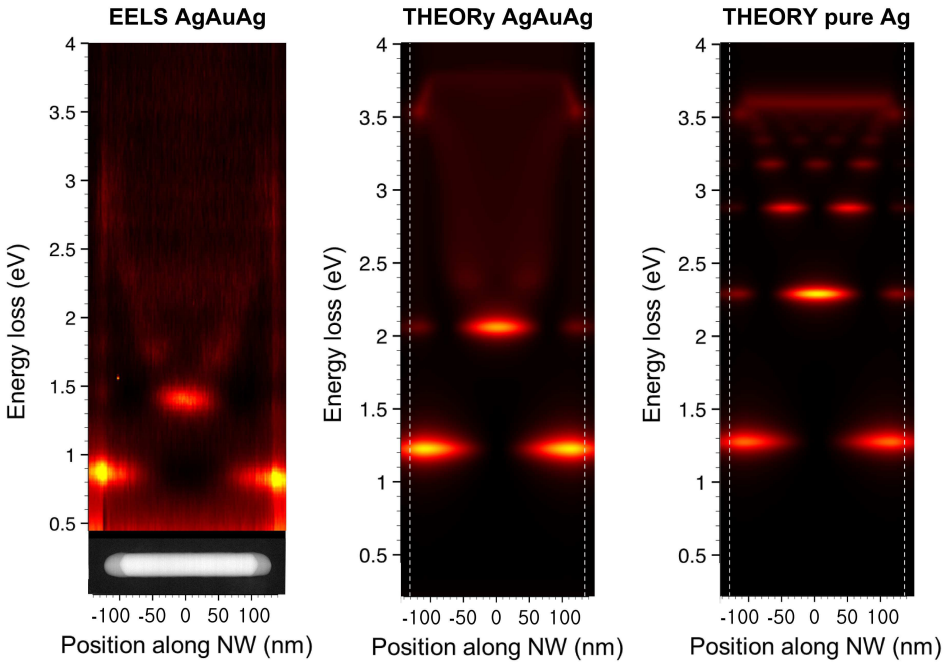

Figure A.IV.7.: Experimental and calculated EELS data as a function of energy for the sample with AgEn=0.5

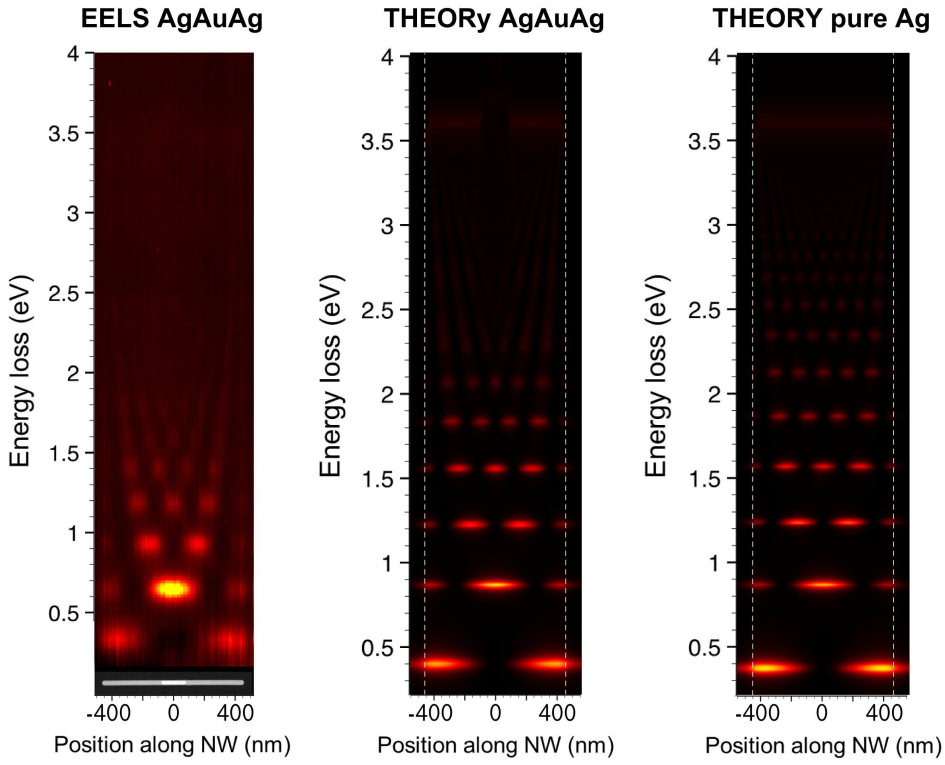

Figure A.IV.8.: Experimental and calculated EELS data as a function of energy for the sample with AgEn=5.3

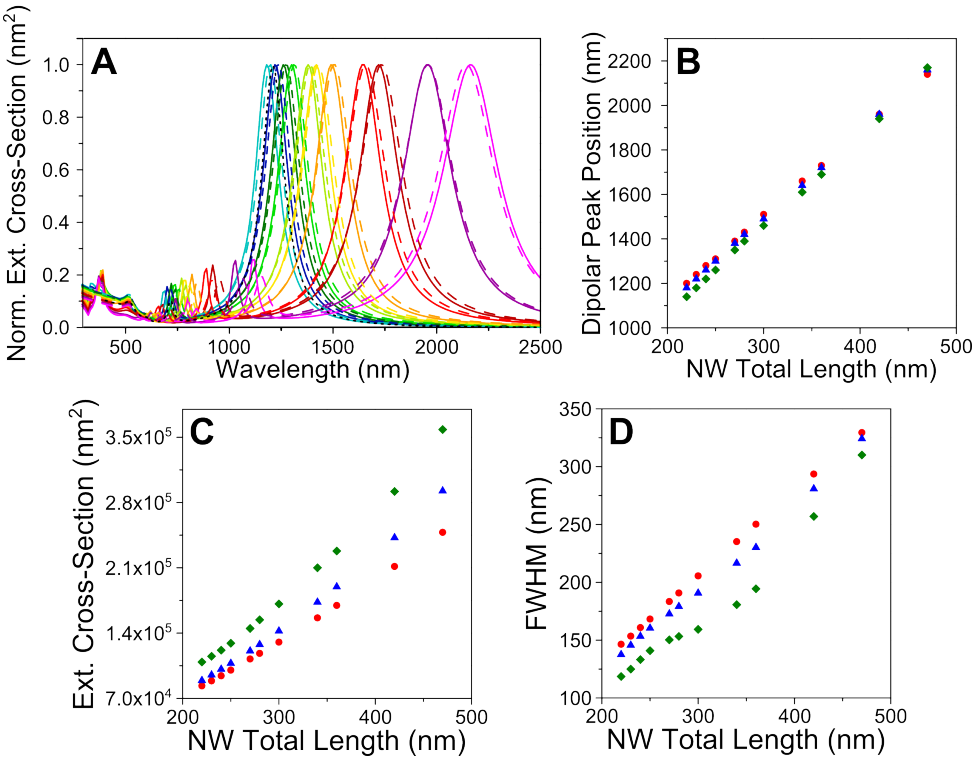

Figure A.IV.9.: Comparison between Experiment and monometallic and bimetallic NWs. (A) calculated (BEM) extinction spectra of AgAuAg (solid curves) and pure Au (dashed curves) NWs with dimensions corresponding to the experimental ones (same color code used for **Figure IV.3**). (B–D) Comparison between pure Au (red circles), pure Ag (green diamonds) and bimetallic AgAuAg NWs (blue triangles) for: dipolar peak position (B), extinction cross section (C) and FWHM (D).

Table A.IV.3.: Effective addition rates used for the experiment shown in **Figure IV.3**. The starting volume was 20 mL, with [Au_0] = 0.25 mM. For each sample we extracted 1 mL and adjusted the effective rate (µL, blue column) keeping constant the Ag added per Au mol per hour (orange column) at a value of 0.24.

Sample	Au_0 / mol	V_{AgNO_3} added / mL	Rate µL/h	Ag added / mol_{Au_0} / h	Time / h	AgEn
1	5.00×10^{-6}	1.50×10^{-1}	300.0	0.24	0.50	0.12
2	4.75×10^{-6}	7.13×10^{-2}	285.2	0.24	0.75	0.18
3	4.51×10^{-6}	6.76×10^{-2}	270.6	0.24	1.00	0.24
4	4.27×10^{-6}	1.28×10^{-1}	256.0	0.24	1.50	0.36
5	4.03×10^{-6}	1.21×10^{-1}	241.6	0.24	2.00	0.48
6	3.79×10^{-6}	1.14×10^{-1}	227.5	0.24	2.50	0.60
7	3.56×10^{-6}	1.07×10^{-1}	213.5	0.24	3.00	0.72
8	3.33×10^{-6}	9.99×10^{-2}	199.8	0.24	3.50	0.84
9	3.10×10^{-6}	9.31×10^{-2}	186.2	0.24	4.00	0.96
10	2.88×10^{-6}	1.73×10^{-1}	172.8	0.24	5.00	1.20
11	2.66×10^{-6}	1.60×10^{-1}	159.8	0.24	6.00	1.44
12	2.45×10^{-6}	2.94×10^{-1}	147.0	0.24	8.00	1.92
13	2.25×10^{-6}	2.70×10^{-1}	134.9	0.24	10.00	2.40
14	2.06×10^{-6}	1.73	123.4	0.24	24.00	5.76
15	1.91×10^{-6}	2.75	114.7	0.24	48.00	11.15

2. Aqueous Gold Overgrowth of Silver Nanoparticle

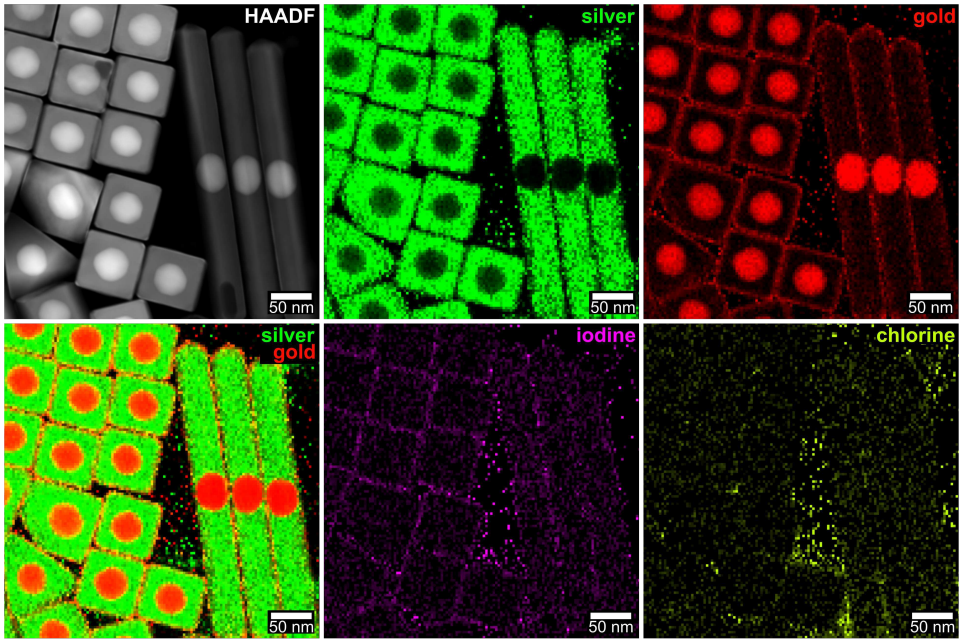

Figure A.IV.10.: HAADF-TEM and mapped EDX images of AuAgNCs and byproducts. Due to partially uncontrollable twinning of the Wulff seeds byproducts (wires and tetrahedra) are also formed. The gold overgrowth protocol allows facet-unselective and homogeneous overgrowth of all morphologies as obvious in the EDX map of gold. Selective absorption of the iodide and displacement of chloride on the gold surface, which ultimately leads to passivation, is observed in the respective EDX maps by the accumulation of iodine on the shell.

A.IV.1. Optical Characterization and Synthesis Optimization

For spherical AuNSps, a narrow plasmon resonance peak at a wavelength of 528 nm is observable in the extinction, and the increased extinction below 515 nm can be assigned to the interband-gap of gold.[1] After silver overgrowth, the predominant mode is shifted to 512 nm. For an optimized gold overgrowth, the dominant plasmonic mode shifts slightly to an excitation wavelength of 519 nm (see **Figure A.IV.11**). This 7 nm shift is caused mainly by the plasmonic polarizability of the gold shell, but also by the 2.2 nm size increment.

In **Figure A.IV.11b&c** (without and with offset, respectively) the influence of the iodide/chloride ratio can be tracked by varying the amount of potassium iodide added. Without iodide, an additional plasmonic mode (600–800 nm) appears which can be assigned to galvanic replacement of silver by the $HAuCl_4$ complex. The replacement-induced etching of the corners results in reduction of the higher plasmonic modes. On the other extreme, complete replacement of chloride in the precursor complex ($HAuI_4$) leads to drastically reduced shell-growth kinetics caused by strong adsorption of the excess iodide to the particle facets.[2] Thus, galvanic replacement occurs as indicated by the peak at 600–700 nm. With the mixed complex, $HAuCl_{2.8}I_{1.2}$, these effects are already reduced, however, galvanic replacement is not fully suppressed and some etching of the corners is apparent. With the complex $HAuCl_{1.7}I_{2.3}$, both etching of the corners

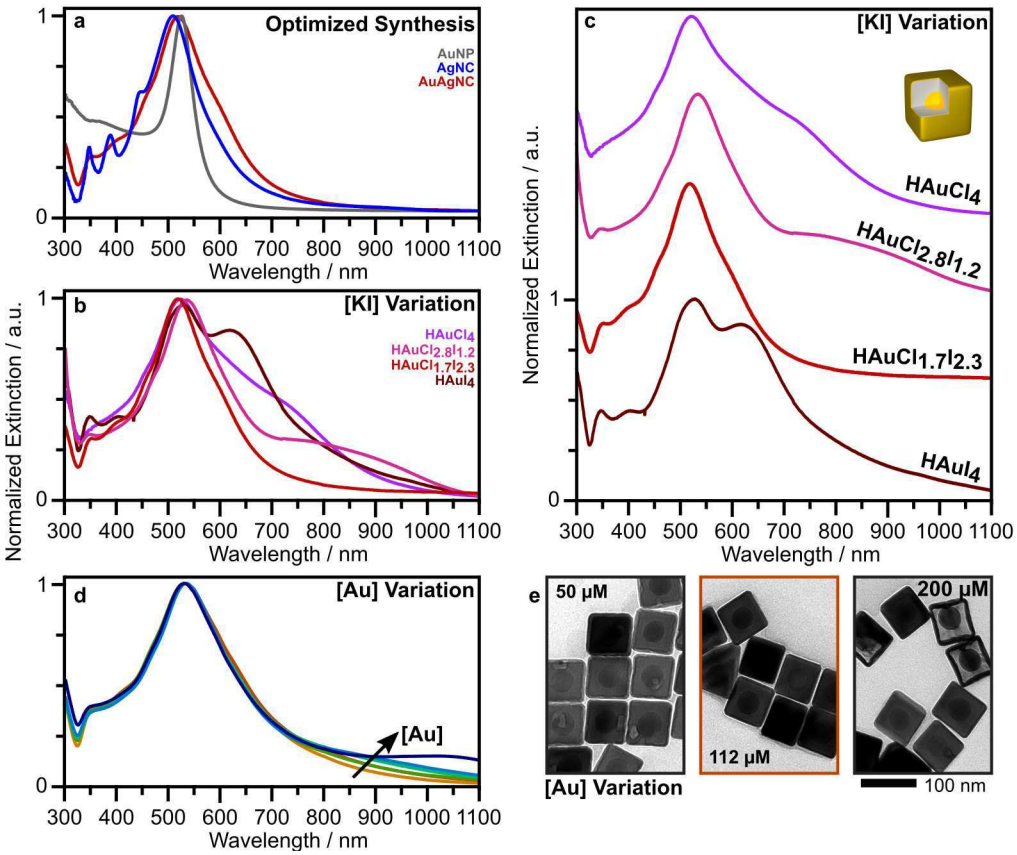

Figure A.IV.11.: Plasmonic evolution of the optimized synthesis and variation of the key reactant concentrations. (a) Extinction spectra of each step of the optimized synthesis plotted without offset. (b,c) Extinction spectra upon variation of the iodide concentration during gold overgrowth plotted without and with offset, respectively. (d,e) Extinction spectra and TEM images at distinct gold volumes with a fixed potassium iodide concentration of 0.3 mM: at 50 µM Au(III) no homogeneous and closed gold shell; homogeneous and closed stage at 112 µM of Au(III); occurrence of galvanic replacement at of 200 µM of Au(III).

and galvanic replacement are minimized, since the reduction potential is balanced with the passivation of the particle facets by iodide (see **Figure A.IV.10** and **Figure IV.10** in **Section IV.2** for details of iodide absorption indicated by EDX).

Fixing this balanced iodide/chloride ratio, the quantity of continuously added $HAuCl_{1.7}I_{2.3}$ complex also affects the formation of the gold shell. As depicted in the TEM images in **Figure A.IV.11e** (left), an insufficient amount results in holey shells. After achieving complete enclosure (**Figure A.IV.11e**, middle), additional precursor damps the kinetics by iodide adsorption and ultimately leads to the formation of rattle particles by galvanic replacement (**Figure IV.15e**, right). The minor spectral changes based on variations in the quantity of gold salt added can be seen in **Figure A.IV.11d**.

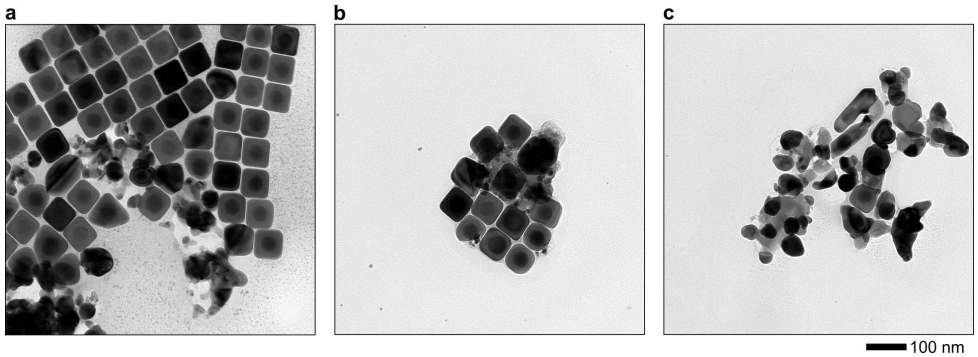

Figure A.IV.12.: Oxidation of pure AgNCs after 24h in air. Further TEM images of AgNCs to show the influence of air on pure AgNCs. A descent amount of AgNCs lose fast their corners and consequently minimizes the corroding surface, which hinders further oxidation (a). Contrary, another part is completely crumbling into pieces (c).

A.IV.2. Electromagnetic Simulations

Numerical electromagnetic simulations (FDTD) were performed on pure AgNCs and pure AuNCs—as theoretical references—and AuAgNCs. With increasing edge length of AgNCs (see **Figure A.IV.13a** and peak positions in **Figure A.IV.14b**, green) the predominant dipolar LSPR shifts linearly to higher wavelength and the higher modes become more dominant. For pure AuNCs the LSPR is shifted to the red (above the interband gap of gold) and does not show any higher modes (see **Figure A.IV.14c**). With increasing size this dipolar mode shifts also linearly to higher wavelengths (see **Figure A.IV.14b**, blue). In case of the AuAgNCs (see **Figure A.IV.13c**) the size of the inner AgNC was kept constant and the gold shell was gradually increased. While the LSPR shifts non-linearly to higher wavelengths, the initial higher modes slowly disappear due to the increased damping of gold.

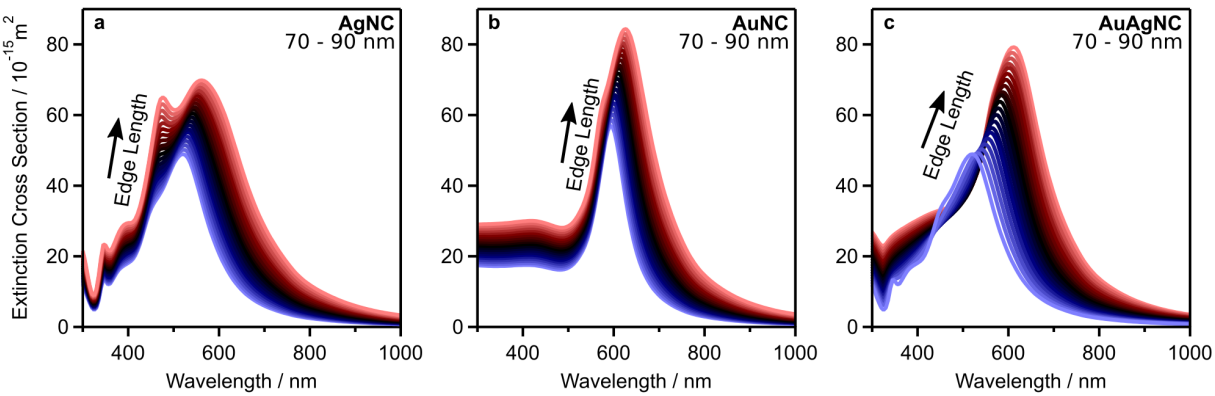

Figure A.IV.13.: Numerical simulations (FDTD) of (a) AgNCs, (b) AuNCs, and (c) AuAgNCs from 70 nm to 90 nm edge length. The edge rounding was set to a constant value of 9%

By direct comparison of the simulated and experimental extinction spectra (**Figure A.IV.14a**) the dominant dipolar mode and the position of all modes can be matched by taking the experimental details into account (size, edge rounding and gold shell thickness). However, due to overestimation of damping in the used dielectric constant of bulk silver,[3] the higher modes are more pronounced in the experiments.

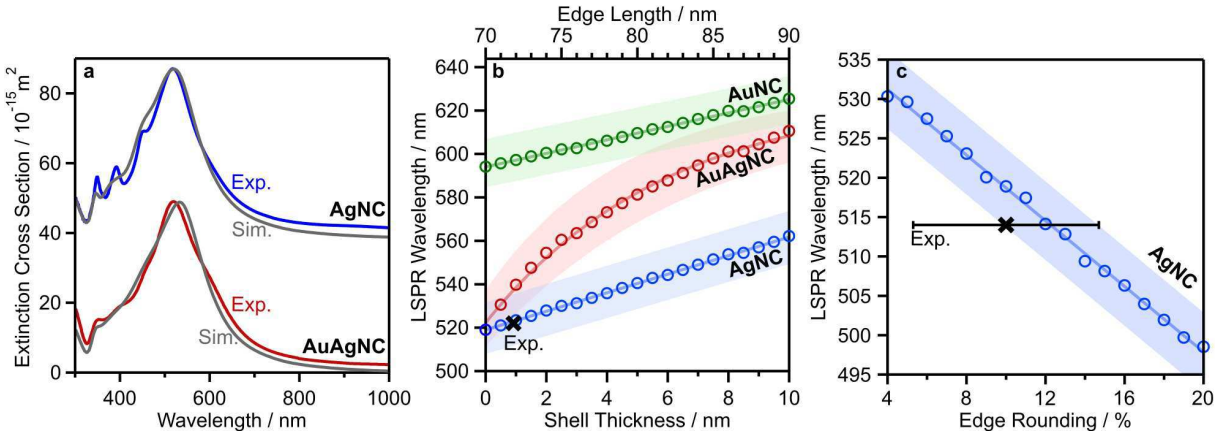

Figure A.IV.14.: Comparison of experimental UV-vis spectra with respective numerical simulations (FDTD) and wavelengths used for the simulation of the electric field distributions (gray lines in (a); 520 nm, 465 nm, 390 nm, and 345 nm, respectively). (b) LSPR peak positions of AgNCs, AuNCs, and AuAgNCs for increasing gold shell thickness. (c) LSPR peak positions of AgNCs for increasing edge rounding.

By tracing the peak positions of all nanocubes in **Figure A.IV.14b** the AuAgNCs converge from pure AgNCs to pure AuNCs, while increasing the gold shell thickness to 10 nm. The experimental peak position of gold overgrown nanocubes (shell thickness of 1.1 nm) matches to pure AgNCs due to deviations from the bulk dielectric constants of gold and silver (**Figure A.IV.14b&c**).[1,4]

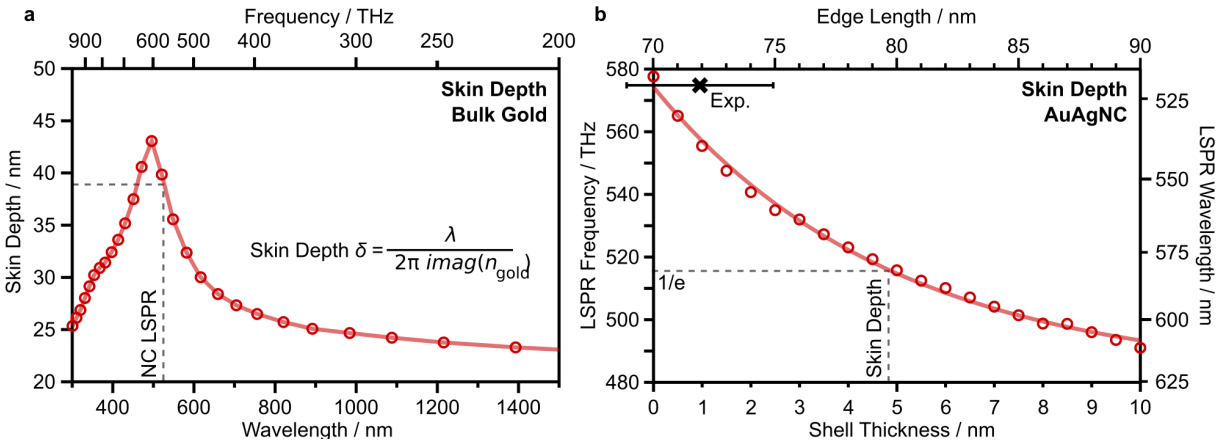

Figure A.IV.15.: Theoretical skin depth of gold. (a) bulk gold; (b) on the basis of the transition from AgNC to AuNC.

For bulk materials the skin depth of a surface plasmon polaritons is described in **Figure A.IV.15a** yielding a theoretical skin depth of 39 nm for gold at a wavelength of 517 nm. Based on the exponential transition (plotted against frequency) from a pure AgNC to pure AuNC we derived a more suitable effective skin depth by a 1/e decay (**Figure A.IV.15b**). This effective simulation results in a skin depth for the described system of 4.9 nm. In both cases, the experimental shell thickness of 1.1 nm is well below this limit.

A.V Coupled Particle Assemblies

1. Self-Assembly of Macroscopic Magnetic Metasurfaces

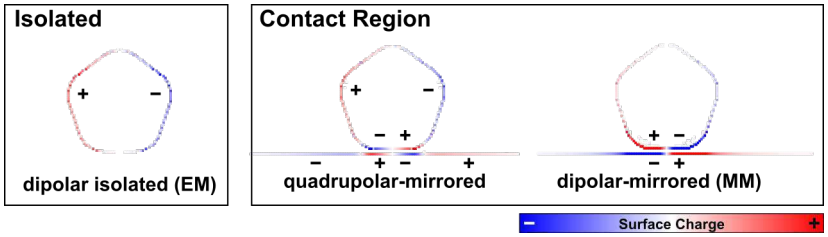

Figure A.V.1.: Surface charge plots of the isolated dipolar mode (EM) and the two emerging modes in the contact region. Contrary to the quadrupolar-mirrored mode at higher energies, the dipolar-mirrored mode (MM) induces a confinement of the charges in the contact area.

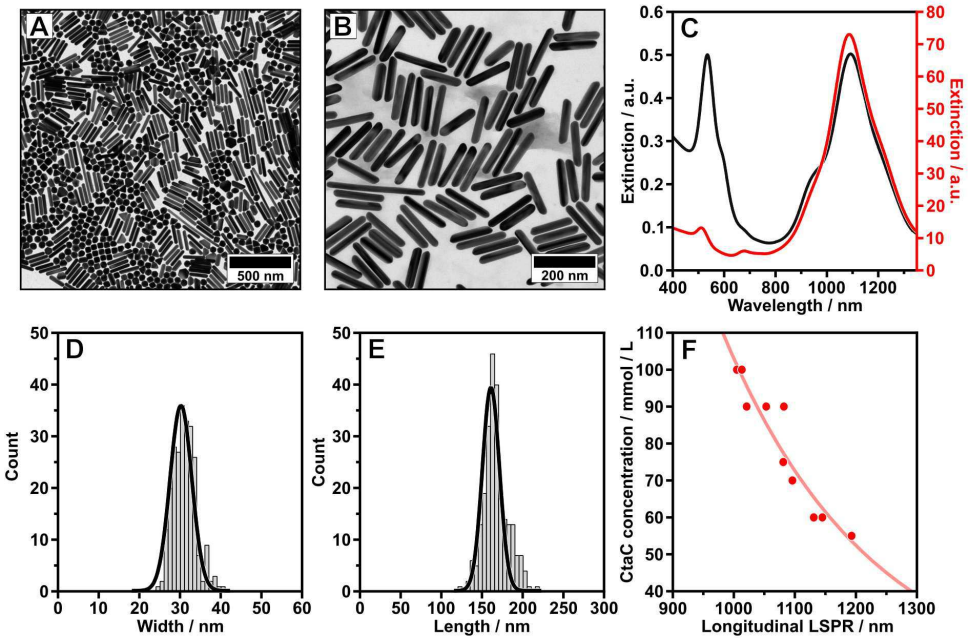

Figure A.V.2.: Nanorod Synthesis. TEM image of the as-synthesized (A) and of the purified (B) pentatwinned gold nanorod solution. (C) Respective UV-vis-NIR spectra. Histogram plot of the evaluation of the width (D) and length (E) (N > 250): 161.0 ± 14.8 nm in ⟨length⟩ and 30.2 ± 3.7 nm in ⟨width⟩. (F) Calibration plot for the required CTAC concentration to purify gold nanorods depending on their longitudinal plasmon resonance. The empirical fit (blue) can be used to assign an appropriate surfactant concentration without the need of TEM study or concentration screening. For in detail explanations of the purification process please see **Section IV.1**.

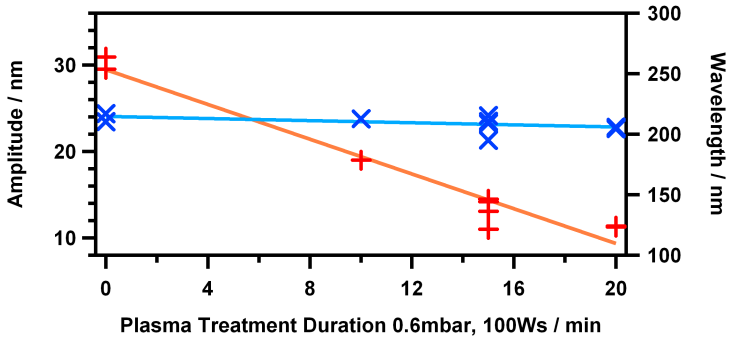

Figure A.V.3.: Plasma post-treatment calibration. To match the template dimensions to the nanorod dimension for the template-assisted self-assembly process, the amplitude of the wrinkled substrate needs to be reduced by an additional plasma treatment. The amplitude (red) is reduced linearly with plasma dose, while the wavelength (blue) remains constant.

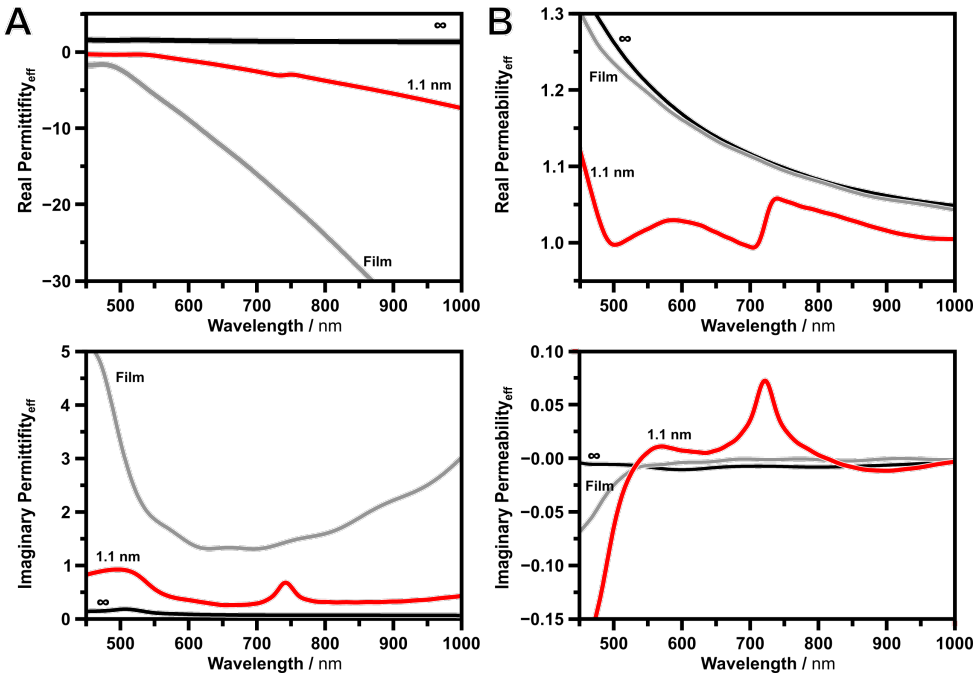

Figure A.V.4.: Calculated effective electric permittivity (A) and effective magnetic permeability (B) for a gold nanorod monomer (infinite separation from gold film, black), gold film only (gray) and film coupled nanorod at a distance of 1.1 nm (red).

2. Plasmon Band Formation and Delocalization in Quasi-Infinite Chains

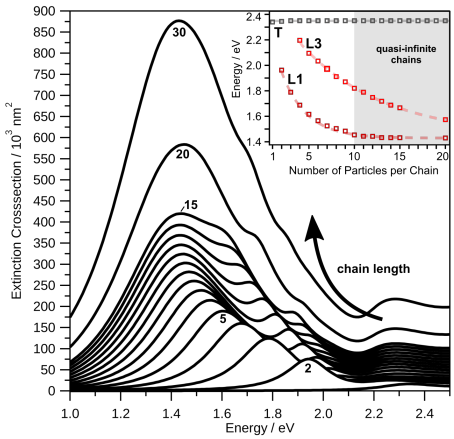

Figure A.V.5.: *Infinite chain limit* by plane wave excitation. By steadily increasing the chain lengths the excitation wavelengths shift to longer wavelengths, *i.e.*, lower energies. As shown in the inset, the longitudinal L1 mode converges to certain energy. In literature, this typically defines the *infinite chain limit* and is reached at about 10–12 particles.[5,6] Whereas at 20, the L3 superimposes with the L1 and becomes negligible Thus, in the *infinite chain limit*, the assembly sustains a band of plasmon modes.

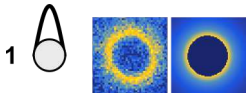

Figure A.V.6.: EELS probability map of an isolated gold nanoparticle. The single particle exhibits a basic LSPR mode at 2.25 eV, which identifies as transversal mode for particle chains (>1 particle), as shown in the main text.

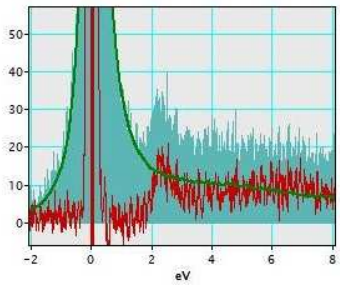

Figure A.V.7.: Example illustrating the treatment of low-loss EELS spectra. The raw spectra (filled) is aligned to zero energy by the Non-Linear Least Square (NLLS) fitting. The reference profile of a zero-loss peak (green curve) is deduced by averaging about thousand spectra collected far away from the gold particles, *i.e.* consisting of no plasmon excitations. Each individual spectrum was aligned to zero energy by the NLLS fitting before averaging. Then, the reference profile is normalized to the intensity of the raw spectra and subtracted from the latter resulting in the plasmon excitation spectrum (red curve). Note that plasmon peaks are typically of 3 orders of magnitude weaker than the zero-loss peak, thus the subtraction might be inaccurate in the vicinity of the zero energy where the tiny differences in the peak profile and its exact energy position are visible. In the present work, we discarded the energy range below 1 eV.

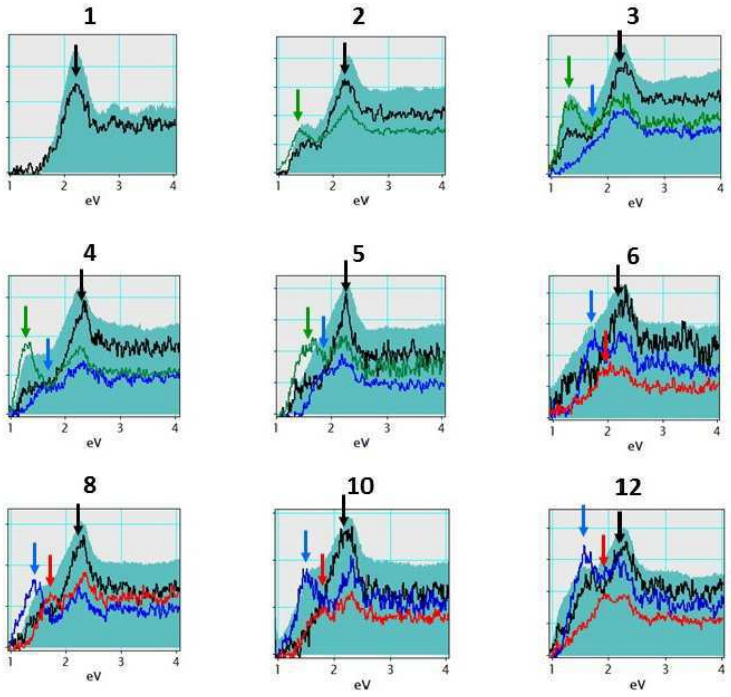

Figure A.V.8.: Examples of low-loss EELS spectra from spectrum-imaging of chains with a different number of gold nanoparticles. The number of particles in the chain is displayed on top of each spectrum. Filled profiles show the spectra averaged over the whole area of spectrum-images while green, blue and red curves show examples of the spectra picked from the selected parts of spectrum-images (averaged over the area of 10–40 pixels). Arrows denote the central positions of the different peaks eventually recognized in spectra.

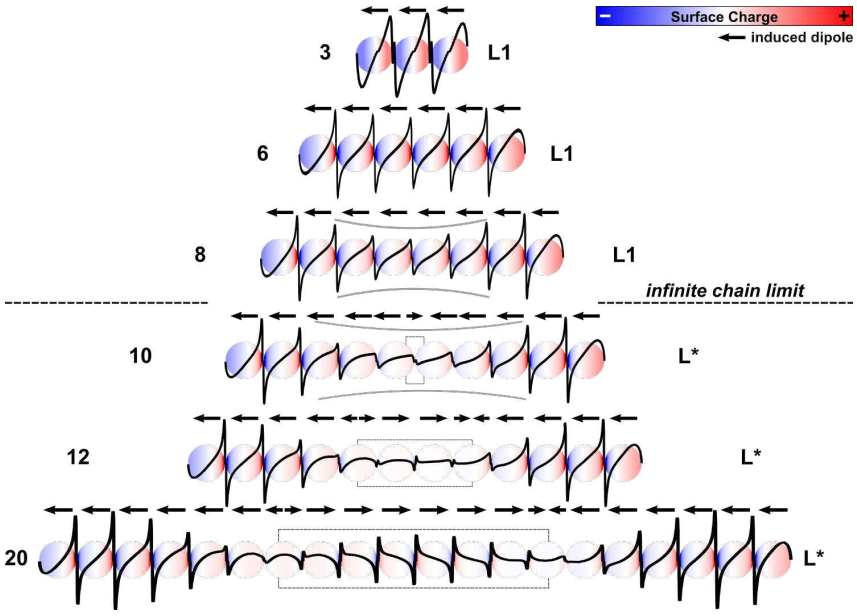

Figure A.V.9.: Simulated surface charge plots of the lowest-order mode (L1 or L*, respectively) for direct comparison. By increasing the chain length, at roughly 10 particles a pinch-off of the induced dipole moment in the center can be observed, which indicates the superposition of the L1 and L3 mode and the formation of the plasmon band ($\geq$10 particles, as indicated by the dotted box).

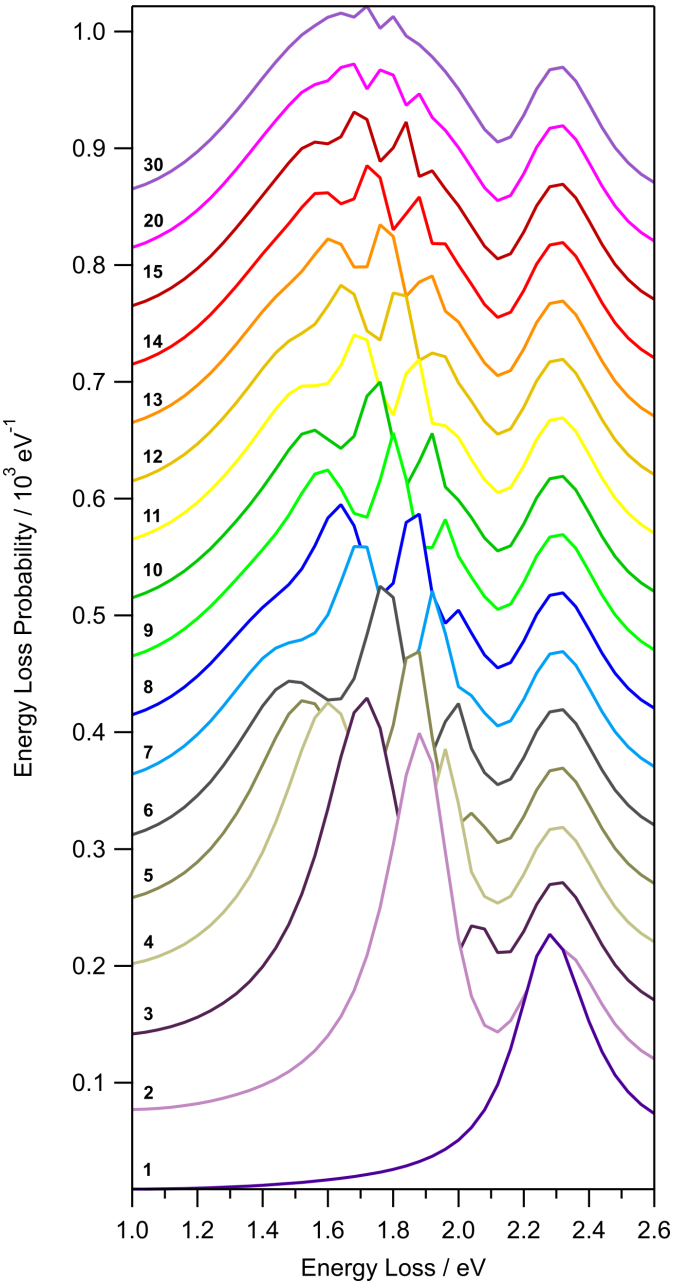

Figure A.V.10.: Simulated EELS spectra from 1 to 30 particles. The exciting electron beam was placed 50 nm from the terminal gold particle in longitudinal direction. Due to increasing damping of gold toward lower energies, the L1 mode becomes indistinguishable above 8 particles (where it appears as a small shoulder at 1.4 eV). Beyond 10 particles higher order Lm modes superimpose, thereby forming the L* mode.

For the transversal mode, the calculations predict a minor shift of 0.04 eV to higher energies due to its anti-bonding character.[7] The respective bonding mode is dark and consequently not observed. The shift is, however, not detected in experiments because it is far below the measurement accuracy. Consequently, the transversal mode consists of only weakly coupled individual particle modes. In contrast, both, experiments and simulations, suggest that the energies of all longitudinal modes decrease with increasing the number of particles in a chain.

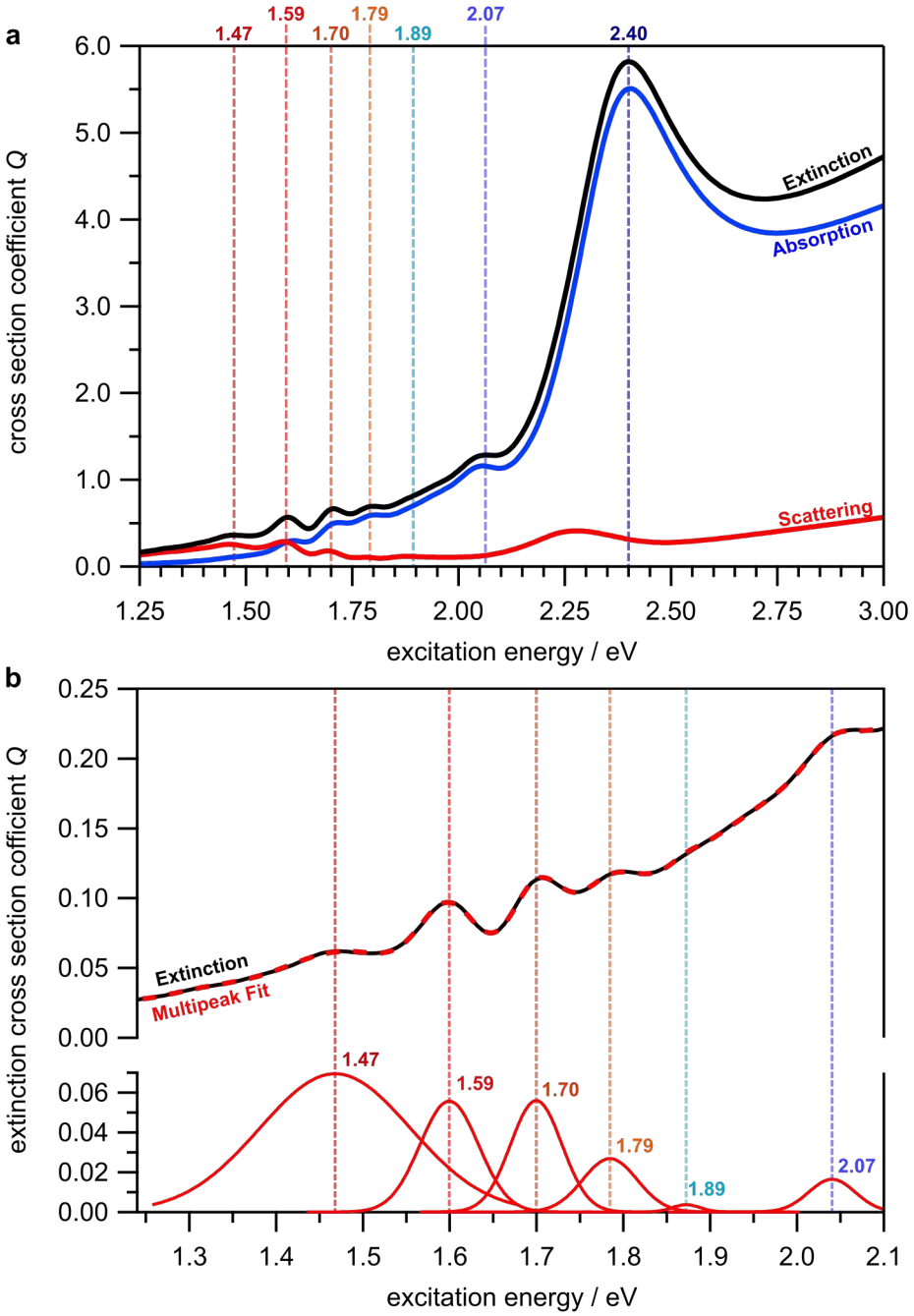

Figure A.V.11.: Plasmonic polymer spectrum (FDTD simulation) excited by a dipole source. In order to probe the energetic position of waveguiding modes in a particle chain consisting of 20 particles a broadband dipole source was placed at the end of the chain and the extinction, absorption, and scattering coefficient was computed (a). The dashed lines highlight the spectral position of the modes (picked according to the absorption peak positions), which are used for the waveguiding simulations in the main text. The role of the overlapping modes is visualized by multipeak-fitting of the extinction spectrum (b). The efficient waveguiding modes feature a significant overlap with the neighboring modes, thereby forming the energy band.

A.V.1. Discrete Dipole Model

In the following some more details of the discrete dipole model are provided including explicit expressions for the propagators and derivations of the main results noted in the main text. The propagator for the dipole radiation including retardation effects reads

$$G_{i,j}(\omega) = \frac{e^{ikr_{ij}}}{4\pi\varepsilon_0}\left\{\frac{k^2}{r_{ij}}\left(\hat{r}_{ij}\otimes\hat{r}_{ij}\right) + \left(1-ikr_{ij}\right)\frac{3\hat{r}_{ij}\otimes\hat{r}_{ij}-1}{r_{ij}^3}\right\}. \tag{A.V.1}$$

The corresponding expression $G_{ij,ref}(\omega)$ for the reflected fields is noted in the book of Novotny and Hecht (cf. Eq. 10.16).[8] Restricting the discrete dipole model do nearest neighbor interactions, taking into account the dominating diagonal coupling only, and linearizing the polarization within the frequency regime considered

$$\left(\alpha_0^{-1} + \alpha\omega + \sum_{j=i\pm1} G_{xx}(\omega)\right) P_{x,i}(\omega) = E_{x,ext}(\omega). \tag{A.V.2}$$

permits to find the longitudinal modes as the eigenvectors of the following $n \times n$ (with n being the number of nanoparticles) coupling matrix (here the constant a is absorbed into the G_{xx} and α_0^{-1})

$$\begin{pmatrix} \alpha_0^{-1} & G_{xx} & \cdots & & 0 \\ G_{xx} & \alpha_0^{-1} & & & \\ \vdots & & \ddots & & \vdots \\ & & & \alpha_0^{-1} & G_{xx} \\ 0 & & \cdots & G_{xx} & \alpha_0^{-1} \end{pmatrix} \tag{A.V.3}$$

This matrix has tridiagonal Toeplitz structure with n eigenvalues

$$\omega_k = \omega_0 - 2G_{xx}\cos\frac{l\pi}{n+1}, \qquad l \in \{1,\ldots,n\} \tag{A.V.4}$$

and corresponding eigenvectors (particle index vector j)

$$P_l = \sin\frac{jl\pi}{n+1}, \qquad l \in \{1,\ldots,n\} \tag{A.V.5}$$

denoted by j. In the *infinite chain limit* $n \gg 1$ ($L = n\Delta x$), the analytic dispersion relation reads $\omega(q) = \omega_0 - 2g_{xx}\cos(q\Delta)$. Thus, a band of eigenvalues with $\omega_{min} = \omega_0 - 2G_{xx}$ emerges, whose width may be controlled by the dipole coupling strength (*e.g.*, particle distance). Finally, the optical coupling strength per mode is given by the analytical expressions for the net dipole moment

$$P(q) = \sum_j P_j(q) \approx \int_0^L \sin(qx)\,dx = \frac{1}{qd}\left(1-\cos(qL)\right) \tag{A.V.6}$$

of the q-dependent modes (*e.g.*, optically dark modes have a net dipole moment of zero). Accordingly, dark modes appear, whenever $q = \frac{2\pi n}{L}$ and the largest net dipole moment is realized in the long wavelength limit $q \to 0$ (bright and dark modes highlighted in red and blue in **Figure V.13a** in **Section V.2**, respectively). In combination with the analytical expression for density of states (DOS) of 1D longitudinal states in the *infinite chain limit*:

$$DOS(\omega) = 2\frac{dq(\omega)}{d\omega} = \frac{1}{G_{xx}\Delta x}\frac{1}{\sqrt{1-\left(\frac{\omega-\omega_0}{2G_{xx}}\right)^2}}, \tag{A.V.7}$$

which also grows toward the minimal excitation energy, we may conclude that the integrated optical coupling proportional to the product $P \times DOE$ is maximal at the lower edge of the band, which is readily observed in the numerical calculations (**Figure A.V.5**).

We finally sketch the derivation of the general expression for discrete dipole model of on infinite periodic lattices. To this end we write the position vector of the nanoparticles $r_i = r_a + r_n$ as a superposition of a basis vector within the unit cell (index a) and the unit cell position (index n). Using this convention, the dipole propagator reads $G_{\mu\nu}(r_i - r_j, \omega) = G^{b\nu}_{a,\mu}(n - n', \omega)$. The discrete dipole model (equation V.2) can now be partly diagonalized by inserting the Bloch wave *ansatz* for the nanoparticles polarization vectors (Cartesian index ω) $P_{a,\mu}(r_n, q, \omega) = c_{a\mu}(q, \omega)\exp(iqr_n)$ into equation V.2 yielding

$$c_{a\mu}(q, \omega) = \sum_b \alpha_b(\omega) \sum_{n'\nu} G^{b\nu}_{a\mu}(n - n', \omega) e^{-iq(r_n - r_{n'})} c_{b\nu}(q, \omega) \tag{A.V.8}$$

Noting that the sum on the right-hand side is independent of n due to the translational invariance of the lattice we can finally write

$$c_{a\mu}(q, \omega) = \sum_{b\nu} \underbrace{\alpha_b(\omega) \sum_n G^{b\nu}_{a\mu}(n, \omega) e^{iqr_n}}_{D^{b\nu}_{a\mu}(q,\omega)} c_{b\nu}(q, \omega). \tag{A.V.9}$$

Consequently, surface plasmon resonances in periodic lattices of nanoparticles can be found by evaluating the minima of $\det(1 - D(q, \omega))$.

References

[1] H.-J. Hagemann, W. Gudat, C. Kunz, “Optical constants from the far infrared to the x-ray region: Mg, Al, Cu, Ag, Au, Bi, C, and Al_2O_3”, *Journal of the Optical Society of America* **1975**, *65*, 742.

[2] L. Scarabelli, A. Sanchez-Iglesias, J. Perez-Juste, L. M. Liz-Marzan, “A "Tips and Tricks" Practical Guide to the Synthesis of Gold Nanorods”, *Journal of Physical Chemistry Letters* **2015**, *6*, 4270–9.

[3] M. Tebbe, C. Kuttner, M. Mayer, M. Maennel, N. Pazos-Perez, T. A. König, A. Fery, “Silver-Overgrowth Induced Changes in Intrinsic Optical Properties of Gold Nanorods: From Non-Invasive Monitoring of Growth Kinetics to Tailoring Internal Mirror Charges”, *The Journal of Physical Chemistry C* **2015**, 9513–9523.

[4] P. B. Johnson, R. W. Christy, “Optical Constants of the Noble Metals”, *Physical Review B* **1972**, *6*, 4370–4379.

[5] A. M. Steiner, M. Mayer, M. Seuss, S. Nikolov, K. D. Harris, A. Alexeev, C. Kuttner, T. A. König, A. Fery, “Macroscopic Strain-Induced Transition from Quasi-infinite Gold Nanoparticle Chains to Defined Plasmonic Oligomers”, *ACS Nano* **2017**, *11*, 8871–8880.

[6] L. S. Slaughter, B. A. Willingham, W.-S. Chang, M. H. Chester, N. Ogden, S. Link, “Toward Plasmonic Polymers”, *Nano Letters* **2012**, *12*, 3967–3972.

[7] B. Willingham, D. W. Brandl, P. Nordlander, “Plasmon hybridization in nanorod dimers”, *Applied Physics B* **2008**, *93*, 209–216.

[8] L. Novotny, B. Hecht, *Principles of Nano-Optics*, Cambridge University Press, **2006**.

Acknowledgments / Danksagung

An dieser Stelle möchte ich mich gerne bei allen bedanken, die zum Gelingen dieser Arbeit beigetragen haben. Die letzten 4 Jahre waren geprägt von vielen kleinen und großen Veränderungen, Ereignissen, und schönen Momenten.
All diese Momente habe ich mit viele, vielen Personen erlebt, die mich ein Stück von diesem langen Weg begleitet haben und mir so die Reise erleichtert haben. In den folgenden wenigen Zeilen möchte ich mich ausnahmslos bei all diesen Menschen bedanken, auch wenn sie in der Kürze dieser Danksagung vielleicht nicht namentlich erwähnt werden.

An erster Stelle gilt mein besonderer Dank meinem Doktorvater Prof. Dr. **Andreas Fery**. Danke, dass Du mich in den letzten (insgesamt über 7) Jahren immer unterstützt hast und stets eine offene Bürotür hattest, wenn ich dringend kurzfristigen Input benötigt habe! Du hast mir ermöglicht diese Arbeit anzufertigen und mir dabei die Möglichkeit gegeben, selbständig, kreativ, und frei zu arbeiten/forschen, selbst wenn es nicht immer “Deine” Themengebiete waren.

Auch bei Dr. **Tobias A.F. König** möchte ich mich herzlich bedanken! Vielen Dank für Deine Hilfsbereitschaft, Dein mit mir geteiltes Wissen, Deine Weltsicht als Physiker ;) und dass Du immer ein offenes Ohr für meine Probleme, Sorgen, und Fragen hattest—als erfahrener Kollege und Mentor, und nicht als typischer (2.) Betreuer! Danke!

Einen herzlichen Dank auch **Janett Forkel** dafür, dass Du so gut um uns kümmerst und uns dadurch viele Prozesse/Problemchen am IPF erspart hast und danke Dr. **Petr Formanek**, dass Du von der wissenschaftlichen Seite das IPF und Dresden für mich geöffnet hast!

An die **AG Fery**, die **AG König**, kurz all meinen **Kollegen**: vielen Dank für die gemeinsame Zeit, den Spaß, den gemeinsamen Aktivitäten, den Zusammenhalt, den vielen und auch produktiven Kaffeepausen, und der schönen Zeit.
Dr. **Nicole Vilbrandt**, Dr. **Ye Yu**, und **Patrick Probst**, danke für die produktiven Diskussionen! Danke an **Daniel Schletz** und **Fabian Goßler** für die meist unterhaltsamen (wenn auch oft sehr anstrengenden und stets sinnlosen) Themen und Diskussionen.
Einen besonderen Dank an Dr. **Dana Schwarz**, **Bernhard Glatz**, und **Maximillian Seuß** für Eure Unterstützung, den Spaß, und fürs regelmäßige mich aus der “alles-dreht-sich-um-Plasmonik”-Box zu befreien!

Danke an meine **Freunde** und **Bekannten**, die mittlerweile teils in der ganzen Welt verteilt sind und Entschuldigung an Euch, dass ich mich so selten melde. Besonderen Dank an **Philipp Mangold**, auch wenn wir oft länger keinen Kontakt haben, bist Du als Freund doch da—vor allem in Momenten, in denen ich einen guten Freund brauche!
An dieser Stelle auch danke an **Maike Till** für die aufbauenden Worte und Motivation in der letzten Phase meiner Promotion und auch für Deine äußerst hilfreichen Anmerkungen und Korrekturen!

Ein großes Danke an **Anja Maria Steiner**! Es hat mir die letzten Jahre sehr, sehr viel Freude gemacht mit Dir so eng zusammen zu arbeiten und zu diskutieren, mit Dir (viel) Kaffee zu trinken, mit Dir eine Zeit lang in der WG zu wohnen, und einfach kurz, Zeit mit Dir zu verbringen. Ohne Dich würde diese Arbeit (und die Zeit hier in Dresden) nicht so sein, wie sie ist. Dankeschön!

Yannic Brasse und **Inga Melnyk**, ehrlich gesagt, weiß ich nicht, wie ich mich jemals angemessen für die letzten Jahre bei Euch bedanken soll bzw. kann. Deswegen hier nur ein kurzes, aber von ganzem Herzen kommendes DANKESCHÖN!

Ganz zum Schluss möchte ich mich bei meiner **Familie**, meiner **Mutter**, meinem **Vater**, meiner Tante, **Helga**, und bei **Ramona** und **Christian** bedanken! Danke, dass ich darauf vertrauen kann, dass Ihr immer und in jeder Situation für mich da seid und danke, dass Ihr mich immer unterstützt und an mich glaubt!

Nochmals **Danke** an Euch alle!

Erklärung & Versicherung

Hiermit versichere ich, dass ich die vorliegende Arbeit ohne unzulässige Hilfe Dritter und ohne Benutzung anderer als der angegebenen Hilfsmittel angefertigt habe; die aus fremden Quellen direkt oder indirekt übernommenen Gedanken sind als solche kenntlich gemacht. Die Arbeit wurde bisher weder im Inland noch im Ausland in gleicher oder ähnlicher Form einer anderen Prüfungsbehörde vorgelegt.

Die vorliegende Arbeit wurde von September 2015 bis Juli 2019 am Leibniz-Institut für Polymerforschung Dresden e.V. unter der Betreuung von Prof. Dr. Andreas Fery (Betreuender Hochschullehrer) und Dr. Tobias A.F. König (Betreuender Young Investigator) durchgeführt.

11. Juli 2019, Martin Mayer